UNIVERSIDAD COMPLUTENSE DE MADRID
FACULTAD DE CIENCIAS FÍSICAS

TESIS DOCTORAL

Espectroscopía de estrellas FGKM para la explotación científica de la búsqueda de exoplanetas con CARMENES

Spectroscopy of FGKM-type stars for the scientific exploitation of the CARMENES exoplanet search

MEMORIA PARA OPTAR AL GRADO DE DOCTOR

PRESENTADA POR

Emilio Gómez Marfil

Directores

David Montes Gutiérrez
Hugo Martín Tabernero Guzmán

Madrid

Universidad Complutense de Madrid
Facultad de Ciencias Físicas

Tesis Doctoral

Espectroscopía de estrellas FGKM para la explotación científica
de la búsqueda de exoplanetas con CARMENES

Spectroscopy of FGKM-type stars for the scientific exploitation
of the CARMENES exoplanet search

Memoria para optar al grado de Doctor
presentada por

Emilio Gómez Marfil

Directores

Prof. Dr. David Montes Gutiérrez
Dr. Hugo Martín Tabernero Guzmán

Madrid, diciembre 2021

[...]
El cielo
suculento
no solo tuvo nubes,
no solo espacio con olor a oxígeno,
sino una piedra terrestre
aquí y allá, brillando,
convertida en paloma,
convertida en campana,
en magnitud, en viento
penetrante:
en fosfórica flecha, en sal del cielo.

Pablo Neruda, *Las piedras del cielo*

Acknowledgements

Madrid, 20th December 2021

In memory of my grandmother

Contents

List of Figures

List of Tables

Abstract

Introduction

The increased interest that sparks the search for exoplanets over the last few years has resulted in the design of high-resolution spectrographs such as CARMENES, installed at the 3.5 m telescope in the Calar Alto Observatory in Almería (Spain), in order to improve the radial-velocity measurements and, thus, to help detect Earth-type planets around stars other than the Sun. Among these, M dwarfs constitute ideal candidates given their ubiquity in the solar neighbourhood, low temperatures, and low masses, which favours detections by both the radial-velocity and transit techniques.

In this context, the determination of stellar atmospheric parameters is an essential step to characterise exoplanet systems and to shed light on their formation and evolution by means of compared planetology, which tries to link the properties of exoplanets with those of their host stars. In particular, the CARMENES instrument, by virtue of its high resolution and simultaneous spectral coverage in the optical and near-infrared wavelength regions, not only provides key information for the analysis of cool stars, but it also opens up the opportunity to revisit classical techniques, such as the equivalent width method and spectral synthesis, to assess the impact of the near-infrared region on the computation of stellar parameters.

Aims and results

The prime objective of the PhD thesis is the photospheric characterisation of FGKM-type stars observed with the CARMENES instrument in the context of its stellar library and guaranteed time observations programme. For this aim, the equivalent width method and spectral synthesis technique were employed on high-resolution, high-S/N spectra in the optical ($R = 94600$, $\lambda \sim 5200$–9600 Å) and the near-infrared ($R = 80400$, $\lambda \sim 9600$–17100 Å). Spectra of FGK-type stars were characterised with the StePar code as an implementation of the equivalent width method, while M-dwarf spectra were analysed with the SteParSyn code, a Bayesian implementation of spectral synthesis following a Markov chain Monte Carlo approach. Both codes are well suited for the precise computation of the stellar atmospheric parameters of late-type stars, namely the effective temperature $T_{\rm eff}$, the surface gravity $\log g$, and the stellar metallicity [M/H], where [Fe/H] is often used as a proxy. As an integral part of the study, different model atmospheres, including MARCS, BT-Settl, and PHOENIX-ACES, and radiative transfer codes, including `turbospectrum` and MOOG, were employed.

The analysis resulted in homogenised sets of stellar parameters for 65 FGK-type stars and 343 M dwarfs observed with CARMENES. The inclusion of the near-infrared region led to the selection of 653 Fe I and 23 Fe II lines useful for the equivalent width method, which more than doubles the number of lines typically used in classical studies restricted to the optical region. In the same way, 75 magnetically-insensitive Ti I and Fe I lines were selected for the analysis of M dwarfs with spectral synthesis, along with the TiO γ and ϵ bands. To avoid any degeneracy in the M-dwarf parameter space, prior probability distributions in effective temperature and surface gravity were imposed, based on the comprehensive, multi-band photometric data available for the sample. Furthermore, with the aim of serving as a reference point to validate the spectroscopic determinations of the stellar atmospheric parameters, several subsets of stars included in the samples have been highlighted, including the *Gaia* benchmark stars, FGK+M and M+M binary systems, and M dwarfs with interferometrically measured angular diameters.

Conclusions

The STEPAR code has proved to be a robust implementation of the equivalent width method for the analysis of FGK-type stars with spectral types between F6 and K4. As additional limitations of the method, it is required that the spectra have a signal-to-noise ratio above 20 and a spectral resolution greater than 30 000 to prevent a suboptimal placement of the continuum level, allow for the resolution of spectral lines and correctly measure the equivalent widths of the lines. For the same reason, doubled-lined spectroscopic binaries and stars with rotational velocities greater than $15 \, \mathrm{km \, s^{-1}}$ have to be excluded.

Close examination of the impact of the near-infrared Fe I and Fe II lines on parameter determinations in FGK-type stars from the CARMENES stellar library has revealed a broader T_{eff} scale that appears to be linked to a higher sensitivity of these near-infrared lines to T_{eff}. However, the scarcity of Fe II lines in the near-infrared region prevented an analysis relying on this window alone. In general, there is good agreement with the parameter determinations from the literature, particularly with the 14 *Gaia* benchmark stars included in the sample.

The methodology used for the analysis of the M dwarfs is best suited in the range from M0.0 V to M7.0 V, but not beyond, due to the scarcity of Ti I and Fe I lines and the insensitivity of the TiO bands to T_{eff} as a result of dust formation. Even though the derived T_{eff} scale is in good agreement with the literature, large discrepancies in the [Fe/H] scales arise, probably as a result of the different methodologies considered. Nonetheless, there is agreement with the metallicity distribution of FGK-type stars in the solar neighbourhood and good correlation with the kinematic membership of the targets in the Galactic populations. Lastly, excellent agreement in T_{eff} is found for M dwarfs with interferometric angular diameter measurements, as well as in [Fe/H] between the components in the FGK+M and M+M systems included in the M-dwarf sample.

Resumen

Introducción

El creciente interés que despierta la búsqueda de exoplanetas ha conducido en los últimos años al desarrollo de espectrógrafos de alta resolución como CARMENES, instalado en el telescopio de 3.5 m del observatorio de Calar Alto en Almería (España), con el objetivo de mejorar las medidas de velocidad radial y permitir la detección de planetas de tipo terrestre alrededor de estrellas distintas al Sol. Entre ellas, las estrellas enanas de tipo M constituyen candidatos ideales dada su ubicuidad en el vecindario solar, sus bajas temperaturas y bajas masas, lo que favorece las detecciones mediante las técnicas de velocidad radial y de tránsitos.

En este contexto, la determinación de los parámetros atmosféricos estelares es un paso crucial para caracterizar los sistemas de exoplanetas y para arrojar luz sobre su formación y evolución mediante la planetología comparada, que pretende relacionar las propiedades de los exoplanetas con las de sus estrellas anfitrionas. En particular, el instrumento CARMENES, gracias a su alta resolución y su cobertura espectral simultánea en el óptico y el infrarrojo cercano, no solo proporciona información valiosa para el análisis de las estrellas frías, sino que también da la oportunidad de volver a evaluar técnicas clásicas, como el método de las anchuras equivalentes y la síntesis espectral, para estimar el impacto de la región infrarroja cercana en el cálculo de parámetros estelares.

Objetivos y resultados

El objetivo principal de la tesis doctoral es la caracterización fotosférica de estrellas de tipos FGKM observadas con CARMENES en el contexto de la librería estelar y el programa de observaciones de tiempo garantizado del instrumento. Para ello, se han empleado tanto el método de anchuras equivalentes como la técnica de síntesis espectral sobre espectros de alta resolución en el óptico ($R = 94600$, $\lambda \sim 5200$–$9600\,\text{Å}$) y en el infrarrojo cercano ($R = 80400$, $\lambda \sim 9600$–$17100\,\text{Å}$). Los espectros de estrellas de tipo FGK se han caracterizado con el código StePar como implementación del método de anchuras equivalentes, mientras que los espectros de estrellas de tipo M se han analizado con el código StParSyn, una implementación bayesiana de la síntesis espectral basada en cadenas de Markov Monte Carlo. Ambos códigos son adecuados para una determinación precisa de los parámetros atmosféricos estelares de estrellas de tipo tardío, en particular la temperatura efectiva T_{eff}, la gravedad superficial $\log g$, y la metalicidad estelar [M/H], donde [Fe/H] suele usarse como proxy. Como parte integral del estudio, se han empleado diferentes modelos de atmósfera, entre ellos los modelos MARCS, BT-Settl y PHOENIX-ACES, y diferentes códigos de transferencia radiativa, como `turbospectrum` y MOOG.

El análisis ha permitido determinaciones homogéneas de parámetros estelares para 65 estrellas de tipo FGK y 343 enanas de tipo M observadas con CARMENES. La inclusión del infrarrojo ha conducido a la selección de 653 y 23 líneas de Fe I y Fe II, respectivamente, útiles para el método de anchuras equivalentes. Esto significa doblar el número de líneas usadas típicamente en estudios clásicos restringidos a la región óptica. De la misma manera, 75 líneas de Ti I y Fe I, magnéticamente insensibles, han sido cuidadosamente seleccionadas, junto con las bandas γ y ϵ de TiO, para el análisis de las enanas de tipo M con síntesis espectral. Para evitar degeneraciones en el espacio de parámetros característico de las enanas de tipo M, se han impuesto distribuciones de probabilidad a priori en temperatura efectiva y gravedad superficial basadas en la información fotométrica multibanda disponible para la muestra. Además, con el objetivo de servir como punto de referencia para

validar las determinaciones espectroscópicas de los parámetros atmosféricos estelares, se han puesto de relieve diferentes submuestras de especial interés, como las estrellas de referencia *Gaia*, los sistemas binarios FGK+M y M+M, así como las enanas de tipo M con medidas interferométricas del diámetro angular.

Conclusiones

El código StePar ha demostrado ser una implementación robusta del método de anchuras equivalentes para el análisis de estrellas de tipos FGK comprendidas entre F6 y K4. Como limitaciones adicionales del método, se requiere una relación señal-ruido mayor que 20 y una resolución espectral superior a 30 000 para prevenir un posicionamiento incorrecto del continuo, permitir la resolución de las líneas y medir sus anchuras equivalentes de manera adecuada. Por el mismo motivo, han de excluirse binarias espectroscópicas de líneas dobles así como estrellas con velocidades de rotación superiores a 15 km s^{-1}.

El estudio del impacto de las líneas infrarrojas de Fe I y Fe II en la determinación de parámetros de estrellas de tipo FGK seleccionadas de la librería estelar de CARMENES ha revelado una escala en T_{eff} más profunda que parece estar vinculada a una mayor sensibilidad de estas líneas infrarrojas a T_{eff}. Sin embargo, la escasez de líneas de Fe II en la región infrarroja ha impedido un análisis que dependa de esta ventana únicamente. En general, se observa una buena concordancia con las determinaciones de parámetros de la literatura, en particular con las 14 estrellas de referencia *Gaia* incluidas en la muestra.

La metodología empleada para el análisis de las enanas de tipo M ha resultado adecuada en el rango M0.0 V a M7.0 V, pero no más allá, debido a la escasez de líneas de Ti I y Fe I y a la insensibilidad de las bandas de TiO a T_{eff} como resultado de la formación de polvo. Aunque la escala de T_{eff} obtenida concuerda con las de la literatura, se observan grandes discrepancias entre las escalas de [Fe/H], probablemente como resultado de las diferentes metodologías empleadas. No obstante, hay congruencia con la distribución de metalicidad en estrellas de tipo FGK en el vecindario solar y buena correlación con la pertenencia cinemática de las estrellas a las poblaciones de la Galaxia. Por último, se encuentra buena concordancia en T_{eff} para enanas de tipo M con determinaciones interferométricas del diámetro angular, así como en [Fe/H] entre las componentes en sistemas binarios FGK+M y M+M incluidos en la muestra de enanas M.

1 Introduction

1.1 Spectroscopy of FGK-type stars and M dwarfs

Stars are long-lived sources of heat and light as a result of the nuclear reactions that take place inside their cores under extreme physical conditions (Hubeny & Mihalas, 2014). Photons released in such reactions traverse the stellar interior until they emerge from the surface after millions of years (Stix, 2003). The many physical interactions that photons face in this journey imprint distinct signatures in the stellar spectra that render it possible to infer particularly interesting physical and chemical properties that characterise the stellar atmosphere. Among them are the effective temperature, T_{eff}, the surface gravity, $\log g$, the metallicity, [M/H], and the chemical abundances of individual atomic species. A summary of the main properties of each spectral type can be found in Table 1.1, while a thorough description of the observational foundations of stellar spectroscopy can be found in Hubeny & Mihalas (2014).

In particular, the spectroscopic analysis of FGK-type stars and M dwarfs has profound implications in many astrophysical contexts. For instance, large stellar spectroscopic surveys thrive on the ubiquity of late-type stars to pave the way for a better understanding of the structure and evolution of the Milky Way (Nordström et al., 2004; Jofré et al., 2019). In particular, M dwarfs stand out as excellent tracers of the chemical and dynamical history of the Galaxy since their lifetimes far exceed the Hubble time (Bochanski et al., 2010). Among these surveys are the RAdial Velocity Experiment (RAVE, Steinmetz et al., 2006), the APO Galactic Evolution Experiment (APOGEE, Allende Prieto et al., 2008), the *Gaia*-ESO Survey (GES, Gilmore et al., 2012), the GALactic Archeology with Hermes (GALAH, De Silva et al., 2015), the LAMOST Experiment for Galactic Understanding and Exploration (LEGUE, Deng et al., 2012), the Sloan Extension for Galactic Understanding and Exploration (SEGUE, Lee et al., 2008), the WHT Enhanced Area Velocity Explorer (WEAVE, Dalton et al., 2018), and the 4-metre Multi-Object Spectroscopic Telescope (4MOST, de Jong et al., 2019).

Despite their intrinsic dimness and higher activity levels compared to FGK-type stars, M dwarfs also enjoy increasing popularity in exoplanet surveys as potential hosts on account of their ubiquity in the solar neighbourhood, their low masses, and their low temperatures (Tal-Or et al., 2018), all of which favours radial-velocity detections of Earth-mass planets within their habitability zone, i.e. where liquid water can be sustained (Scalo et al., 2007). Consequently, the census of exoplanet-harbouring stars has soared over the last decades as a result of space missions such as CoRoT (Convection, Rotation and planetary Transits, Auvergne et al., 2009), *Kepler* (Koch et al., 2010; Borucki et al., 2010), and TESS (Transiting Exoplanet Survey Satellite, Ricker et al., 2014), as well as ground-based, high-resolution instruments including the High Accuracy Radial velocity Planet Searcher (HARPS, Mayor et al., 2003), HARPS North (HARPS-N, Cosentino et al., 2012), the Calar Alto high-Resolution search for M dwarfs with Exoearths with Near-infrared and optical Echelle Spectrographs (CARMENES, Quirrenbach et al., 2018), the SPectropolarimètre InfraROuge (SPIROu, Artigau et al., 2014), the InfraRed Doppler instrument (IRD, Kotani et al., 2014), the Habitable-zone Planet Finder (HPF, Mahadevan et al., 2014), MAROON-X (Seifahrt et al., 2020), HIRES (Vogt et al., 1994), GIARPS (Claudi et al., 2018), the Near Infra Red Planet Searcher (NIRPS, Wildi et al., 2017), and the Echelle Spectrograph for Rocky Exoplanet- and Stable Spectroscopic Observations (ESPRESSO, Pepe et al., 2021), among others. In this context, the spectroscopic analysis of M dwarfs is absolutely crucial as a way to accurately determine the position of the habitable zone

TABLE 1.1. Summary of the spectral sequence (Reid & Hawley, 2005; Hubeny & Mihalas, 2014).

Spectral type	T_{eff} [K]	M [$M_\odot$]	R [$R_\odot$]	L [$L_\odot$]	Frequency [a]
O	$\geq 30\,000$	≥ 17.4	≥ 7.2	$\geq 38\,000$	~0.00003 %
B	9 500–30 000	2.9–17.4	2.7–7.2	43–38 000	~0.1 %
A	7 200–9 500	1.6–2.9	1.5–2.7	5.8–43	~0.6 %
F	6 000–7 200	1.05–1.6	1.05–1.5	1.3–5.8	~3 %
G	5 100–6 000	0.79–1.05	0.85–1.05	0.4–1.3	~7.5 %
K	3 800–5 100	0.60–0.79	0.62–0.85	0.05–0.4	~12 %
M	2 300–3 800	0.075–0.60	0.08–0.62	0.00015–0.072	~76 %

Notes. [a]Frequency in the solar neighbourhood for stars brighter than absolute magnitude +16 per 10 000 pc^3 (Ledrew, 2001).

(Selsis et al., 2007; Kopparapu et al., 2013), and to contrain the masses and radii of detected exoplanets (Torres et al., 2012; Santos et al., 2013; Brewer et al., 2016; Sousa et al., 2018; Schweitzer et al., 2019), their composition (Maldonado et al., 2020; Ishikawa et al., 2020), and the atmospheres of transiting exoplanets to account for the centre-to-limb variation and the Rossiter-McLaughlin effect (Czesla et al., 2015; Borsa & Zannoni, 2018; Hoeijmakers et al., 2018; Casasayas-Barris et al., 2020). A precise determination of the stellar atmospheric parameters of M dwarfs is also particularly relevant to planet formation theories that attempt to explain the observed occurrence rate of exoplanets (Johnson et al., 2010; Howard et al., 2012; Buchhave et al., 2012; Sabotta et al., 2021) and selection effects (Winn & Fabrycky, 2015).

In broad terms, the advent of high-resolution spectrographs with coverage in the near-infrared wavelength region, such as CARMENES, SPIRou, IRD, HPF, and NIRPS, has opened up a unique opportunity to test and expand classical spectroscopic techniques that have long been restricted to the optical wavelength region (see e.g. Andreasen et al., 2016). Naturally, access to the near-infrared wavelength region significantly increases the number of spectral features that can potentially be useful for these techniques. This, in turn, helps to maximise spectral information and, thus, to circumvent possible shortcomings caused by atmospheric modelling (i.e. the synthetic gap, see Passegger et al., 2020). However, the near-infrared is also fraught with molecular features caused by the Earth's atmosphere, which raises the need for adequate yet complex telluric modelling and correction (Nagel, 2019). To make matters worse, the effects of the stellar magnetic field on the line profiles are also amplified in the near-infrared wavelength region (Shulyak et al., 2019; Passegger et al., 2019).

Spectroscopic techniques aimed at stellar atmospheric parameter determination generally focus on three fundamental parameters, namely the effective temperature T_{eff}, surface gravity $\log g$, and stellar metallicity [M/H], where [Fe/H] is often used as a proxy. Among these techniques are the equivalent width (EW) method and spectral synthesis. A short description of these techniques, fully implemented in the STEPAR[1] (Tabernero et al., 2019) and STEPARSYN[2] (Tabernero et al., 2021b) codes, respectively, is presented in the following sections.

1.1.1   The equivalent width (EW) method and the STEPAR code

The equivalent width (EW) of a spectral line is formally defined as (Hubeny & Mihalas, 2014):

$$\text{EW} = \int_{\lambda_1}^{\lambda_2} \left(1 - \frac{F(\lambda)}{F_{\text{c}}(\lambda)} \right) d\lambda, \tag{1.1}$$

---

[1]https://github.com/hmtabernero/StePar
[2]https://github.com/hmtabernero/SteParSyn
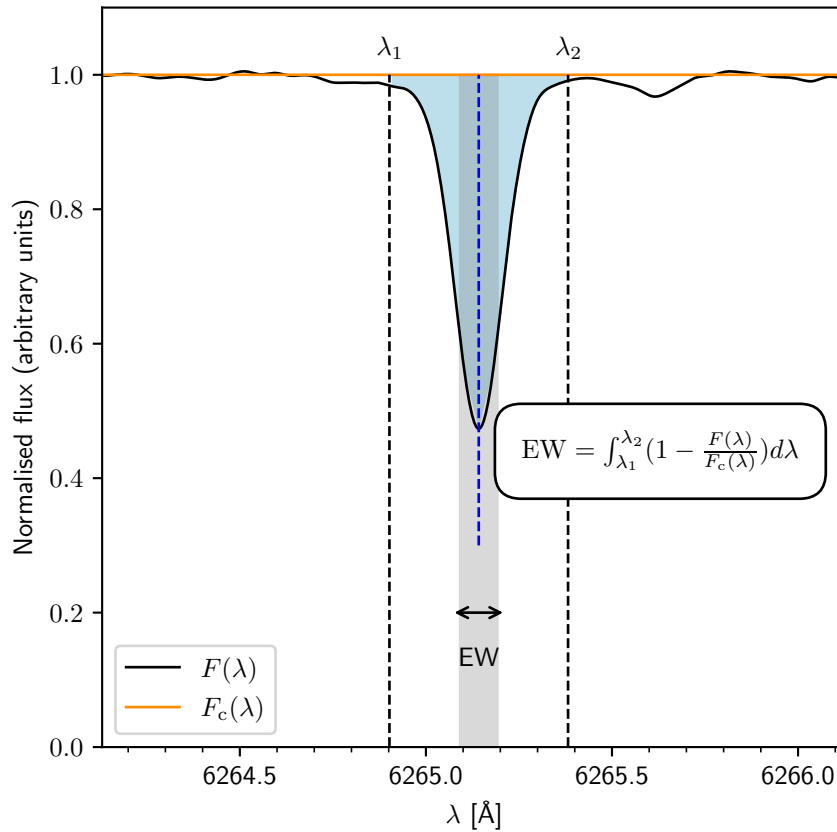
FIGURE 1.1. Illustration of the equivalent width of a spectral line. The Fe I line at 6265.13 Å in a NARVAL spectrum of the Sun taken from Blanco-Cuaresma et al. (2014c) is shown. The blue and black vertical dashed lines are the central wavelength of the line and the integration limits for the equivalent width computation, respectively. We note that the blue and grey shaded regions cover, by definition, equal areas.

where $F(\lambda)$ is the flux measured at wavelength λ in the line, and $F_c(\lambda)$ is the continuum flux at that wavelength (see Fig. 1.1). The measurement of EWs is usually done in an automated fashion with software tools such as TAME[3] (Kang & Lee, 2012), DAOSPEC[4] (Stetson & Pancino, 2008), ARES[5] (Sousa et al., 2007, 2015), or the `EWComputation` module[6] (Soto & Jenkins, 2018; Soto et al., 2021).

Line profiles appear as a result of thermal and collisional processes that take place in the stellar atmospheres. For instance, thermal processes widen the spectral lines by cause of the random motions of the atoms absorbing the light (i.e. Doppler effect). The combination of both thermal and collisional processes leads to a complex change in the equivalent width of spectral lines. EWs are usually analysed with a curve of growth, which relates, by means of the Saha and Boltzmann equations, the EW information from many lines simultaneously to the number of absorbers along the line of sight. In other words, EWs can be used for estimating the chemical abundances of individual elements and molecules present in a stellar atmosphere. The basic equations of line analysis under local thermodynamic equilibrium (LTE) that relate EWs and chemical abundances are widely discussed in many literature sources and will not be repeated here (see e.g. Hubeny & Mihalas 2014). These equations are implemented in a variety of codes, for instance WIDTH9[7] (Kurucz, 2005) and

---

[3] http://astro.suu.ac.kr/~kwkang/tame
[4] http://www.cadc-ccda.hia-iha.nrc-cnrc.gc.ca/en/community/STETSON/daospec/
[5] http://www.astro.up.pt/~sousasag/ares/
[6] https://github.com/msotov/EWComputation
[7] http://kurucz.harvard.edu/programs/width

MOOG[8] (Sneden, 1973).

Imposing excitation and ionisation equilibria conditions on a set of neutral and ionised lines with measured EWs assuming LTE constitutes one of the most common, accurate, and fastest methods to determine the stellar atmospheric parameters (T_{eff}, $\log g$, and [Fe/H]) of FGK-type stars. Spectral features considered for this purpose usually are weak metallic lines, typically Fe I and Fe II lines (Gonzalez & Lambert, 1996; Gonzalez et al., 2001; Sato et al., 2003; Santos et al., 2004; da Silva et al., 2006; Tabernero et al., 2012, 2017; Tsantaki et al., 2013; Mortier et al., 2014; Andreasen et al., 2016). The stellar atmospheric parameters can be derived as follows:

- Effective temperature. The optimal value of T_{eff} associated with a given spectrum can be derived by imposing excitation equilibrium, that is, by assuming that no correlation exists between the abundance and the excitation potential (χ) of the neutral iron lines. The reasoning goes as follows. According to the Boltzmann equation, the number of electrons populating each energy level is a function of T_{eff}, so that assuming a wrong T_{eff} would require different abundances to match spectral lines with different values of χ. For example, higher abudances would be required to match the line profiles of low-χ transitions if a too large value of T_{eff} were used, since this value would underpopulate the lower energy levels. The reverse is also true. Therefore, a wrong T_{eff} value would naturally translate into a correlation or an anticorrelation between the abundances and χ, depending on whether the wrong T_{eff} value is too small or too large, respectively.

- Surface gravity. Ionisation equilibrium states that the same abundance should be retrieved from lines of two ionisation stages for any given species. Since surface gravity directly determines the amount of pressure in the photosphere, any change in $\log g$ would translate into variations in the ionised lines, which are very sensitive to the electronic pressure.

- Metallicity. It can be derived as the mean abundance given by all iron lines, once excitation and ionisation equilibria conditions are met. Generally, [Fe/H] is assumed to be a good proxy of the overall metallicity, [M/H], even if iron is not the most abundant element in stars (Asplund et al., 2009).

In addition to T_{eff}, $\log g$, and [Fe/H], it is important to highlight the micro-turbulent velocity, ξ, which is introduced as an ad hoc parameter in the EW method to break any correlation between the iron abundance and line strength. The micro-turbulent velocity essentially adds an extra broadening to account for convection in the photosphere, which is generally not well described by one-dimensional, static model atmospheres.

Lastly, among the publicly available implementations of the EW method are ARES+MOOG (Sousa et al., 2008; Santos et al., 2013), FAMA[9] (Magrini et al., 2013), GALA[10] (Mucciarelli et al., 2013), FUNDPAR (Saffe, 2011), SPECIES[11] (Soto & Jenkins, 2018; Soto et al., 2021), and StePar[12] (Tabernero et al., 2019). For the purposes of this PhD thesis, the StePar code was adopted. Unlike other implementations of the EW method such as GALA or FAMA, StePar employs the Nelder-Mead optimisation algorithm, which is fast and can converge in very few iterations. On average, StePar takes between 2 and 5 minutes to reach a solution for any given star, depending on its actual position in the FGK parameter space.

---

[8] https://www.as.utexas.edu/~chris/moog.html
[9] http://cdsarc.u-strasbg.fr/viz-bin/qcat?J/A+A/558/A38
[10] http://www.cosmic-lab.eu/gala/gala.php
[11] https://github.com/msotov/SPECIES/
[12] https://github.com/hmtabernero/StePar

1.1.2 Spectral synthesis and the STEPARSYN code

The main idea behind the spectral synthesis technique is to find the synthetic spectrum that best matches the observed spectrum by means of a minimisation algorithm (Valenti & Fischer, 2005). For this aim, the most common approach is to adopt a grid of synthetic spectra that is already available in the literature (e.g. PHOENIX-ACES, Husser et al., 2013) or to compute it from scratch by assuming a set of model atmospheres, for instance MARCS (Gustafsson et al., 2008) or ATLAS9 (Kurucz, 1993), plus the line data required to solve the radiative transfer equation (accesible through e.g. the VALD3[13] database, Ryabchikova et al., 2015, and references therein) and, finally, to obtain the emergent flux. The radiative transfer equation can be solved by means of different programs such as MOOG (Sneden, 1973), SYNTHE[14] (Kurucz, 2005) or `turbospectrum`[15] (Plez, 2012). Caveats about the use of the radiative transfer codes that are available in the literature can be found in Blanco-Cuaresma (2019).

Grids of synthetic spectra usually cover wide portions of the parameter space under analysis. As an example, Figs. 1.2 and 1.3 show the effect of $T_{\rm eff}$, $\log g$ and [Fe/H] in the synthetic spectra, using BT-Settl model atmospheres (Allard et al., 2012). It is important to note that degeneracies naturally arise, that is, several combinations of stellar parameters yield synthetic spectra that show very good agreement with the observed spectra, although some of them might correspond to unphysical values (Passegger et al., 2018). This is particularly relevant in the M-dwarf regime, where independent methods are often imposed to break such degeneracy between the parameters, especially $\log g$ (Rojas-Ayala et al., 2012; Passegger et al., 2018, 2019).

Many implementations of the spectral synthesis technique are publicly available in the literature, including the APOGEE Stellar Parameter and Chemical Abundance Pipeline[16] (ASPCAP, García Pérez et al., 2016), FERRE[17] (Allende-Prieto, 2015), MINESweeper[18] (Cargile et al., 2020), MyGIsFOS[19] (Sbordone et al., 2014), The Payne[20] (Ting et al., 2019), Spectroscopy Made Easy[21] (SME, Piskunov & Valenti, 2017; Valenti & Piskunov, 1996), PySME (Wehrhahn, 2021), iSpec[22] (Blanco-Cuaresma et al., 2014b), FASMA[23] (Andreasen et al., 2017; Tsantaki et al., 2020), and BACCHUS[24] (Masseron et al., 2016). For the purposes of this PhD thesis, the STEPARSYN code[25] (Tabernero et al., 2021b) was adopted. STEPARSYN is a state-of-the-art Bayesian implementation of spectral synthesis written in Python that is particularly designed to map the posterior probability distribution of the stellar atmospheric parameters associated with a given spectrum following a Markov chain Monte Carlo (MCMC) approach. A comprehensive description of the code can be found in Tabernero et al. (2021b). Therefore, only a brief overview will be presented in the following. The code has already been used in different astrophysical contexts, including the characterisation of stars in open clusters (Lohr et al., 2018; Alonso-Santiago et al., 2019), stars in galaxies of the Local Group (Tabernero et al., 2018), the first super-AGB candidate in our Galaxy (VX Sgr, Tabernero et al., 2021a), and exoplanet host stars belonging to the ESPRESSO guaranteed time observations programme (Borsa et al., 2021; Demangeon et al., 2021).

---

[13]http://vald.astro.uu.se/
[14]http://kurucz.harvard.edu/programs/synthe
[15]https://github.com/bertrandplez/Turbospectrum2019
[16]https://www.sdss.org/dr14/irspec/aspcap
[17]http://hebe.as.utexas.edu/ferre
[18]http://github.com/pacargile/MINESweeper
[19]https://mygisfos.obspm.fr
[20]https://github.com/tingyuansen/The_Payne
[21]https://www.stsci.edu/~valenti/sme.html
[22]https://www.blancocuaresma.com/s/iSpec
[23]http://www.iastro.pt/fasma/
[24]http://www.ascl.net/1605.004
[25]https://github.com/hmtabernero/SteParSyn
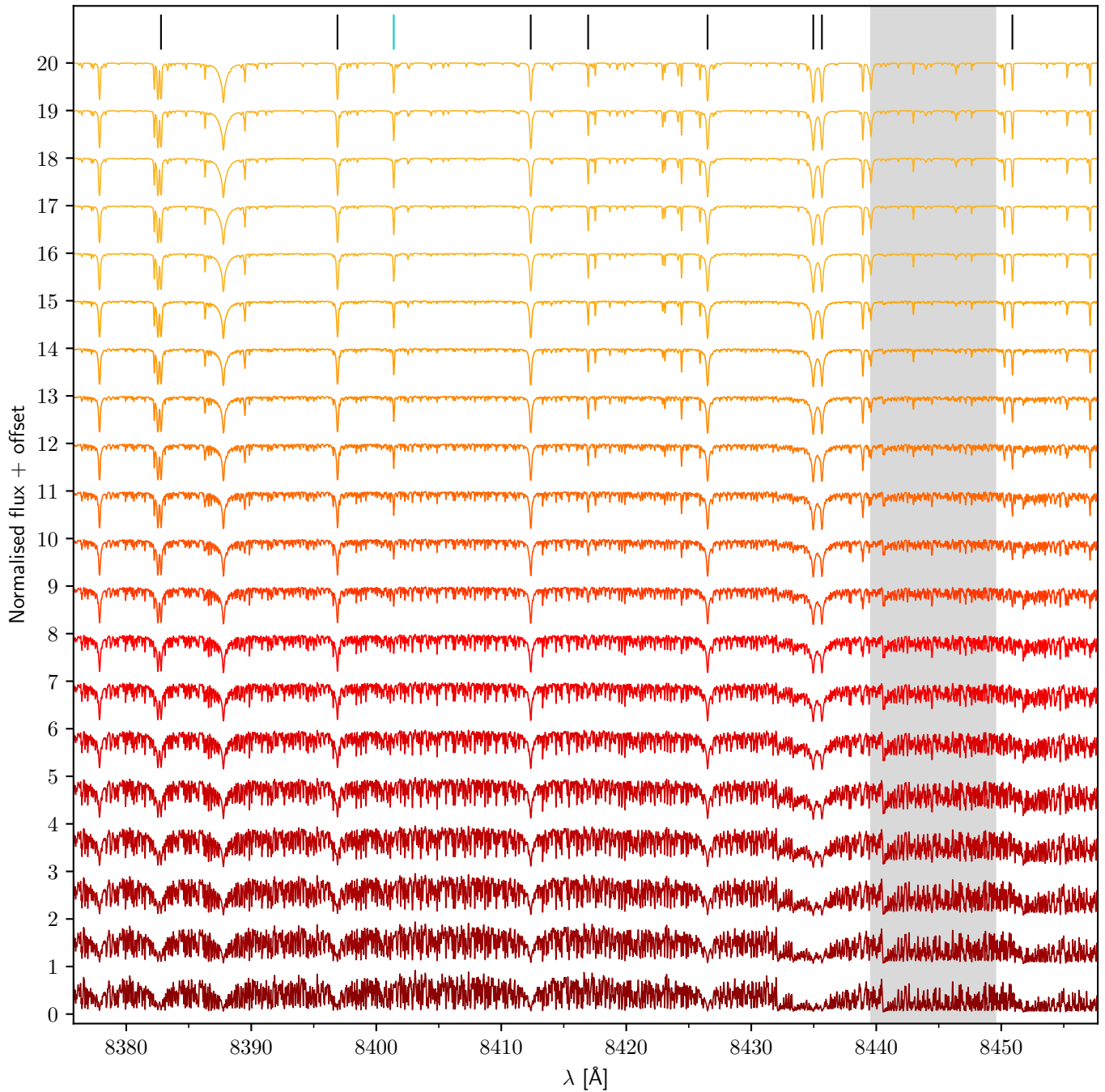
FIGURE 1.2. Impact of T_{eff} on synthetic spectra at infinite resolution in the range 8375.78–8457.72 Å. These were computed based on BT-Settl atmosphere models and `turbospectrum`. From top to bottom, T_{eff} ranges from 4500 K to 2600 K in steps of 100 K at constant $\log g$ and metallicity ($\log g = 5.0$ dex and [Fe/H] = 0.0 dex, respectively). Vertical lines at the top indicate Fe I (blue) and Ti I (black) lines used for comparison with the observed spectra. The TiO band head at ~8440 Å is also shown as a gray-shaded region.
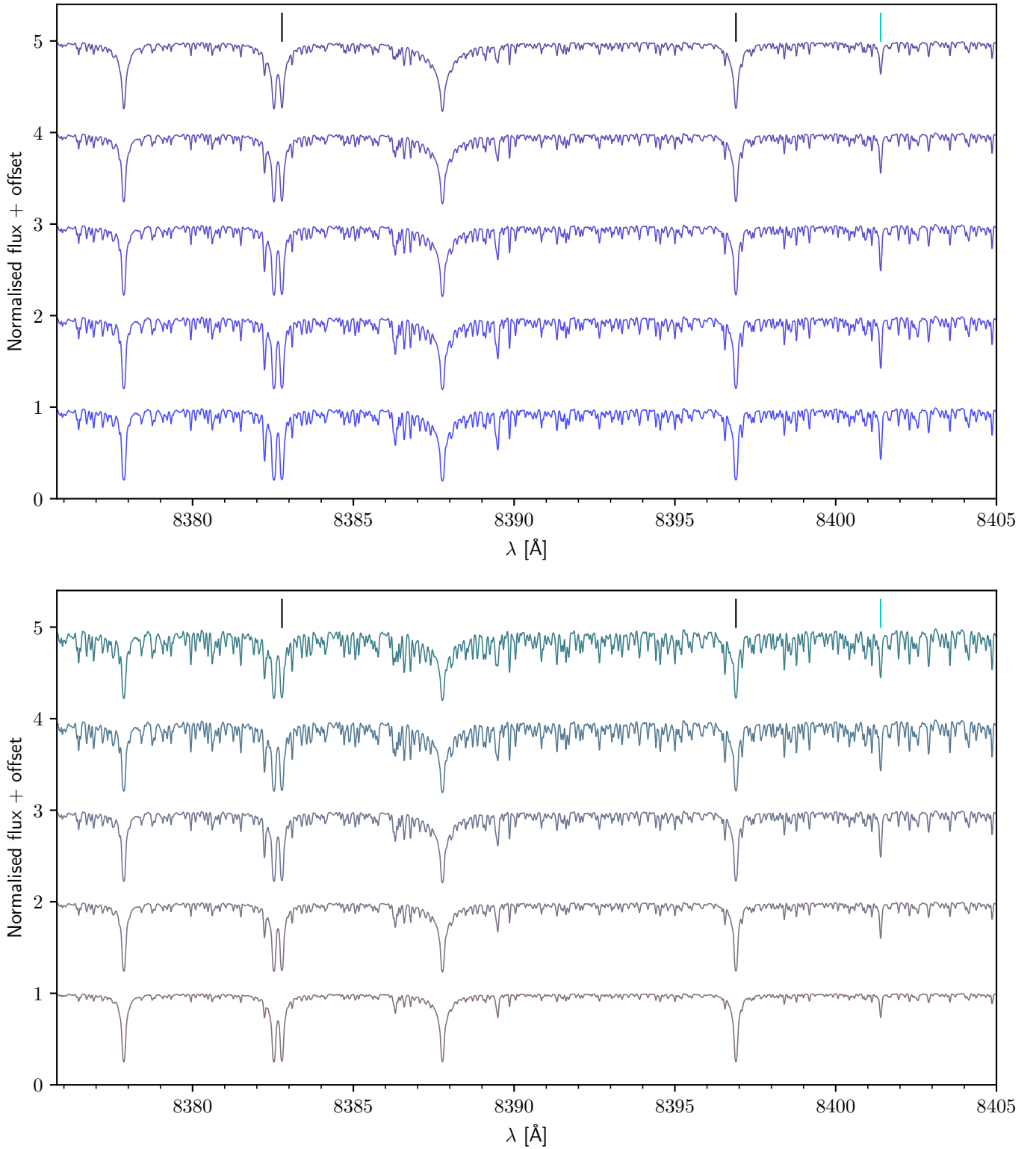
FIGURE 1.3. Impact of $\log g$ (top pannel) and [Fe/H] (bottom panel) on synthetic spectra in the range 8375.78–8405.00 Å. Symbols are the same as in Fig. 1.2. In the top pannel, $\log g$ increases from 4.0 dex (top) to 6.0 dex (bottom) in steps of 0.5 dex at constant T_{eff} and metallicity (T_{eff} = 3600 K and [Fe/H] = 0.0 dex, respectively). Wings of strong spectral lines become broader, as shown by the Fe I line at 8387.77 Å. In the bottom pannel, [Fe/H] decreases from 0.5 dex (top) to −1.0 dex (bottom), with intermediate values of 0.3 dex, 0.0 dex, and −0.5 dex, respectively, at constant T_{eff} and $\log g$ (T_{eff} = 3600 K and $\log g$ = 5.0 dex, respectively).

Besides the observed spectrum, the code takes a grid of synthetic spectra previously generated around certain spectral features of interest (i.e. atomic lines, molecular bands) as input. In order to find the starting point for the MCMC sampler, SteParSyn first performs a minimisation following the Trust Region Reflective algorithm implemented in the `curve_fit` function from the Python `scipy` package (Virtanen et al., 2020). The MCMC sampling is done with the Python package `emcee` (Foreman-Mackey et al., 2013). In stark contrast to classical deterministic methods, SteParSyn can map the probability distribution of the stellar atmospheric parameters. In this manner, it is actually possible to detect any degeneracy in the parameter space and also to provide uncertainties based on the probability distributions. The likelihood function ($\log L$) used for SteParSyn to evaluate any given point of the parameter space is given by the following expression:

$$\log L = \sum_{\lambda} -0.5[(F_{\lambda}^{\mathrm{obs}} - F_{\lambda}^{\mathrm{syn}})/\sigma_{\lambda}]^2 - \log \sqrt{2\pi}\sigma_{\lambda}, \tag{1.2}$$

where $F_{\lambda}^{\mathrm{obs}}$, $F_{\lambda}^{\mathrm{syn}}$, and σ_{λ} are the observed flux, the synthetic flux, and the uncertainties in the observed flux, respectively.

The synthetic grid is composed of discrete points, making it impossible to cover the parameter space in a continuous manner. Conversely, the computation of synthetic spectra on the fly to evaluate any point in the parameter space is a computationally expensive task. An effective approach to overcome this issue is to compress and store the synthetic grid following a principal component analysis to save as much memory as possible while preserving the accuracy of interpolated spectra (see Mészáros & Allende Prieto, 2013). This approach relies on the fact that synthetic spectra are not fully independent and, therefore, can be described in terms of linear combinations, that is, the synthetic flux $F_{\lambda}^{\mathrm{syn}}$ can be rewritten as:

$$F_{\lambda}^{\mathrm{syn}} = \mu_{\lambda} + \sigma_{\lambda} \sum_{i=1}^{N_{\mathrm{c}}} w_i\,(T_{\mathrm{eff}}, \log g, [\mathrm{Fe/H}])\, e_{\lambda}^i, \tag{1.3}$$

where e_{λ}^i and w_i are the eigen-vectors and weight coefficients, respectively, given by the principal component analysis, while μ_{λ} and σ_{λ} represent a linear transformation of the synthetic grid.

1.1.3   Benchmark tests

Spectroscopic studies require rigorous benchmark tests to evaluate the reliability of the results (Jofré et al., 2014). These tests can be implemented in a number of ways. For example, assuming that stars behave as perfect blackbodies, it is possible to infer T_{eff} directly from the Stefan-Boltzmann law:

$$L = 4\pi R^2 \sigma T_{\mathrm{eff}}^4, \tag{1.4}$$

where L is the luminosity, R the radius, and σ the Stefan-Boltzmann constant. With knowledge of the limb-darkened angular diameter θ_{LD} and the bolometric flux F_{bol} (i.e. the total radiative flux from the star received at the Earth), Equation 1.4 can be rewritten as (Heiter et al., 2015a):

$$T_{\mathrm{eff}} = \left(\frac{F_{\mathrm{bol}}}{\sigma}\right)^{0.25} (0.5\,\theta_{\mathrm{LD}})^{-0.5} \tag{1.5}$$

Thus, T_{eff} can be obtained independently from spectroscopy if measurements of θ_{LD} and F_{bol} are available. Unfortunately, this information can only be accurately measured for a handful of stars close to the Sun (see e.g. Boyajian et al., 2012a,b).

In a similar manner, the surface gravity can be derived from the fundamental relation:

$$g = G \frac{M}{R^2},$$

(1.6)

where M is the stellar mass, R the stellar radius, and G the gravitational constant. The stellar radius, R, can be easily inferred from the limb-darkened angular diameter, θ_{LD}, and the parallax, π, via the following expression:

$$R = \frac{\theta_{LD}}{2\pi}$$

(1.7)

Unlike angular diameters, parallaxes are available for thousands of stars as a result of dedicated space missions such as *Hipparcos* (Perryman et al., 1997; van Leeuwen, 2007) and, more recently, *Gaia* (Gaia Collaboration et al., 2021). The stellar mass, however, can only be derived from evolutionary tracks (Demarque et al., 2004; Bertelli et al., 2009), from the study of binary systems, and asteroseismology (Heiter et al., 2015a). Nonetheless, it must be noted that uncertainties in stellar mass are far less important for determining surface gravities than the uncertainty in the stellar radii.

In particular, the *Gaia* benchmark stars (Jofré et al., 2014, 2015b, 2018; Heiter et al., 2015a) constitute a set of 34 FGKM-type stars covering a wide portion of the parameter space with highly accurate measurements of the stellar radius and bolometrix flux. As explained before, this renders it possible to infer their T_{eff} and $\log g$ fundamentally, that is, independently from spectroscopy. Hence, these stars are extremely useful since they can serve as calibrators for any spectrocopic method aimed at stellar parameter and chemical abundance studies. There is a series of papers devoted to characterising these stars in terms of T_{eff} and $\log g$ (Heiter et al., 2015a), metallicity (Jofré et al., 2014), and α and iron-peak elements (Jofré et al., 2015b). Furthermore, Blanco-Cuaresma et al. (2014c) published the stellar library[26] related to the *Gaia* benchmark stars, which includes a collection of high-resolution, high signal-to-noise (S/N) ratio spectra of these 34 stars taken with different instruments (i.e. NARVAL, HARPS, and UVES) in the 4800–6800 Å wavelength region.

Lastly, wide multi-star systems stand out as ideal benchmark tests for stellar metallicity since they are believed to be formed from the same molecular cloud, and, thus, be coeval and share similar chemical compositions (Montes et al., 2018). This has been showed to be the case in a number of studies focused on FGK+FGK binaries (see e.g. Desidera et al., 2004, 2006), FGK+M binaries (see e.g. Ishikawa et al., 2020), and M+M systems (see e.g. Antoniadis-Karnavas et al., 2020).

1.2 The CARMENES instrument

CARMENES, the Calar Alto high-Resolution search for M dwarfs with Exoearths with Near-infrared and optical Échelle Spectrographs (Quirrenbach et al., 2020) is a high-resolution, double-channel spectrograph installed at the 3.5 m telescope at Calar Alto Observatory (Almería, Spain). It consists of optical and near-infrared channels (hereafter VIS and NIR) that provide coverage in the wavelength regions 5200–9600 Å and 9600–17100 Å with spectral resolutions of $R = 94600$ and 80400, respectively (Quirrenbach et al., 2020). From 2016 until mid-2020, the CARMENES M-dwarf survey gathered more than 18 500 VIS and nearly 18 000 NIR spectra for a sample of 365 M dwarfs throughout 5000 hours of observing time in the context of its guaranteed time observations (GTO) programme (Quirrenbach et al., 2020). Fig. 1.4 shows the vacuum tank of the VIS channel located at the coudé room of the 3.5 m telescope at Calar Alto. A dedicated website[27] contains all the detailed information about the most relevant parameters of the instrument, open-time proposals, observing manuals, and comparable spectrographs in the optical and/or the near-infrared at 4 m-class telescopes or larger.

---

[26]https://www.blancocuaresma.com/s/benchmarkstars
[27]https://carmenes.caha.es

Although the main scientific goal of CARMENES is the detection and characterisation of Earth-mass planets around M dwarfs (see e.g. Trifonov et al., 2018, 2020; Zechmeister et al., 2019; Luque et al., 2019; González-Álvarez et al., 2020), the large number of observations of the M dwarfs that make up the GTO programme of the instrument also provides an excellent opportunity to probe into their nature in a statistically significant way (Reiners et al., 2018), that is, in terms of activity levels and indicators (Schöfer et al., 2019), magnetic fields (Shulyak et al., 2019), stellar parameters (Passegger et al., 2018, 2019; Schweitzer et al., 2019), and chemical abundances of different species (Abia et al., 2020; Shan et al., 2021).

The wavelength calibration of CARMENES spectra is carried out by means of two calibration units (one for each channel) made up of a combination of hollow cathode lamps and Fabry-Pérot interferometers (Schäfer et al., 2018). The resulting median instrumental precision in the VIS channel is $1.2 \, \text{m} \, \text{s}^{-1}$, whereas the NIR radial-velocity data show a larger scatter around $3.7 \, \text{m} \, \text{s}^{-1}$ (Bauer et al., 2020). It is also important to note that spectra taken with CARMENES exhibit a series of inter-order spectral gaps in the NIR channel that become increasingly wider towards its red end. Another series of intra-order gaps in the NIR channel also appear as a result of the space between the two 2048×2048 pixel HAWAII-2RG units in the NIR mosaic. All of these gaps are listed in Tables 1.2 and 1.3 and can be appreciated in Figs. B.1 (Marfil et al., 2020) and 4.3 (Marfil et al., 2021).

Lastly, since CARMENES operates in vacuum, for the purpose of this PhD thesis wavelengths were transformed onto an air wavelength scale, following the International Astronomical Union standard (Morton, 2000):

$$\lambda_{\text{air}} = \frac{\lambda_{\text{vacuum}}}{n}, \tag{1.8}$$

where n is the refraction index, which can be expressed as:

$$n = 1 + 8.34254 \times 10^{-5} + \frac{2.406147 \times 10^{-2}}{130 - s^2} + \frac{1.5998 \times 10^{-4}}{38.9 - s^2}, \tag{1.9}$$

where $s = 10^4/\lambda_{\text{vacuum}}$, with λ_{vacuum} in Å.
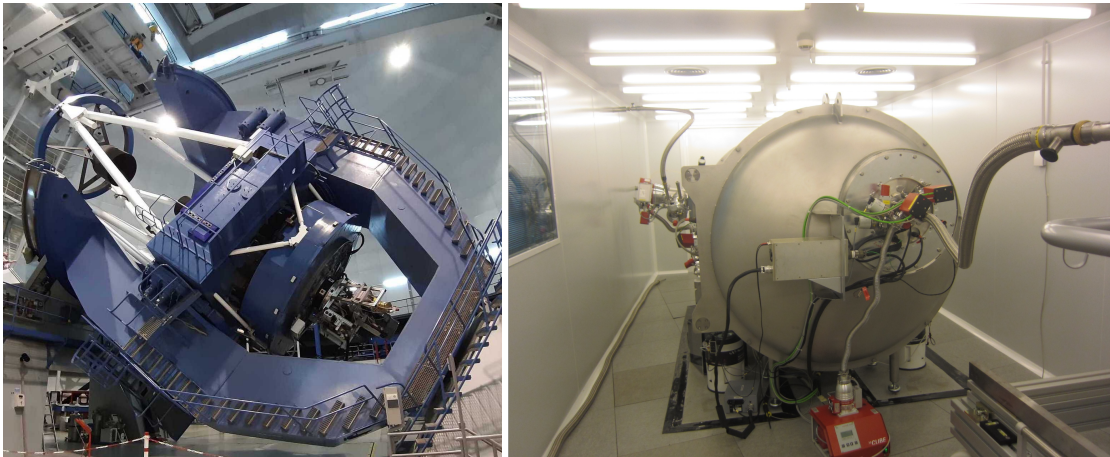
FIGURE 1.4. (*left*) Zeiss 3.5 m telescope at Calar Alto Observatory. Image credit: IAA-CSIC. Retrieved from https://www.iaa.csic.es. (*right*) Vacuum tank of the VIS channel of CARMENES at the coudé room. Image credit: the CARMENES consortium. Retrieved from https://carmenes.caha.es.

TABLE 1.2. Wavelength coverage of the CARMENES VIS échelle spectra

Order	λ_{min} [Å]	λ_{max} [Å]	$\Delta\lambda$ [Å]	Inter-order gap [Å]	Order	λ_{min} [Å]	λ_{max} [Å]	$\Delta\lambda$ [Å]	Inter-order gap [Å]
118	5171.4	5206.7	35.3	8.7	88	6887.9	7007.6	119.7	...
117	5215.4	5254.8	39.4	0.5	87	6967.0	7088.1	121.1	...
116	5255.3	5306.6	51.3	...	86	7048.1	7170.5	122.4	...
115	5297.6	5355.6	58.0	...	85	7131.0	7254.9	123.9	...
114	5339.0	5404.7	65.7	...	84	7215.9	7341.2	125.3	...
113	5383.6	5455.3	71.7	...	83	7302.8	7429.7	126.9	...
112	5429.7	5504.9	75.2	...	82	7391.9	7520.3	128.4	...
111	5477.0	5555.8	78.8	...	81	7483.1	7613.1	130.0	...
110	5524.5	5606.3	81.8	...	80	7576.7	7708.2	131.5	...
109	5573.3	5657.8	84.5	...	79	7672.6	7805.8	133.2	...
108	5622.9	5710.1	87.2	...	78	7771.0	7905.8	134.8	...
107	5673.5	5763.5	90.0	...	77	7871.9	8008.5	136.6	...
106	5725.7	5817.9	92.2	...	76	7975.5	8113.8	138.3	...
105	5778.6	5873.2	94.6	...	75	8081.8	8222.0	140.2	...
104	5832.8	5929.7	96.9	...	74	8191.0	8333.1	142.1	...
103	5887.8	5987.3	99.5	...	73	8303.2	8447.2	144.0	...
102	5943.6	6046.0	102.4	...	72	8418.6	8564.5	145.9	...
101	6001.2	6105.8	104.6	...	71	8537.2	8685.1	147.9	...
100	6061.3	6166.8	105.5	...	70	8659.1	8809.2	150.1	...
99	6122.5	6229.1	106.6	...	69	8784.6	8936.8	152.2	...
98	6185.0	6292.7	107.7	...	68	8913.8	9068.2	154.4	...
97	6248.7	6357.5	108.8	...	67	9046.9	9203.5	156.6	...
96	6313.8	6423.7	109.9	...	66	9183.9	9342.9	159.0	...
95	6380.3	6491.3	111.0	...	65	9325.2	9486.6	161.4	...
94	6448.2	6560.4	112.2	...	64	9471.0	9634.8	163.8	...
93	6517.5	6630.9	113.4	...					
92	6588.4	6703.0	114.6	...					
91	6660.8	6776.6	115.8	...					
90	6734.8	6851.9	117.1	...					
89	6810.5	6928.9	118.4	...					

Notes. Vacuum wavelengths in rest frame. Orders 63 to 58 are not included since they contain straylight.

1.2.1 The CARMENES stellar library

Libraries of stellar spectra, also known as stellar libraries, are a cornerstone for several branches in astrophysics. Broadly speaking, not only do they lay a strong foundation for the classification of stars and the derivation of their atmospheric parameters in relation to large spectroscopic surveys, but they are also an essential element in stellar population studies that endevour to unravel the secrets of galaxy formation and evolution (Sánchez-Blázquez et al., 2006). In particular, stellar libraries are highly useful for stellar spectral classification (Morgan & Keenan, 1973; Jaschek & Jaschek, 1990; Gray & Corbally, 2009; Gray, 2014; Gray et al., 2016), the study of unresolved stellar populations in globular clusters and galaxies inside and outside the Local Group (Worthey, 1994; Fioc & Rocca-Volmerange, 1997; Cenarro et al., 2001; Bruzual & Charlot, 2003; Zhang et al., 2005; Conroy et al., 2009; Percival et al., 2009; Vazdekis et al., 2012), the comparison with synthetic model spectra and calibration or validation of methods that aim at the determination of atmospheric parameters (T_{eff}, $\log g$, and [Fe/H]) and chemical abundances (Katz et al., 1998; Koleva et al., 2009; Wu et al., 2011; Tabernero et al., 2012; Bensby et al., 2014; Blanco-Cuaresma et al., 2014b; Jofré et al., 2014, 2015b; Allende Prieto, 2016), the study of the chromospheric activity in multi-wavelength observations via spectral subtraction (Montes & Martin, 1998; Montes et al., 2000; Frasca et al., 2003, 2006), the

TABLE 1.3. Wavelength coverage of the CARMENES NIR échelle spectra.

Order	$\lambda_{\min}$ [Å]	$\lambda_{\max}$ [Å]	$\Delta\lambda$ [Å]	Inter-order gap [Å]	Intra-order gap [Å]	Tellurics
63	9618.7	9782.1	163.4	...	6.0	Strong
62	9758.4	9939.9	181.5	...	6.1	Mild
61	9918.3	10102.9	184.6	...	6.2	Weak
60	10083.6	10271.2	187.6	...	6.3	Weak
59	10254.5	10445.3	190.8	...	6.4	Weak
58	10431.3	10625.4	194.1	...	6.5	Weak
57	10614.3	10811.8	197.5	...	6.7	Weak
56	10803.9	11004.9	201.0	...	6.8	Weak
55	11000.3	11205.0	204.7	...	6.9	Weak
54	11204.0	11412.5	208.5	...	7.0	Strong
53	11415.4	11627.8	212.4	3.0	7.1	Strong
52	11634.9	11851.4	216.5	7.2	7.3	Mild
51	11863.1	12083.7	220.6	11.7	7.4	Mild
50	12100.4	12325.4	225.0	16.6	7.6	Weak
49	12347.3	12576.9	229.6	21.9	7.7	Weak
48	12604.5	12839.0	234.5	27.6	7.9	Mild/weak
47	12872.7	13112.1	239.4	33.8	8.0	Weak
46	13152.6	13397.1	244.5	40.5	8.2	Weak
45	13444.9	13694.8	249.9	47.7	8.4	Strong
44	13750.5	14006.1	255.6	55.6	8.6	Strong
43	14070.3	14331.8	261.5	64.2	8.8	Strong
42	14405.3	14673.0	267.7	73.5	9.0	Mild
41	14756.6	15030.8	274.2	83.7	9.2	Mild
40	15125.6	15406.6	281.0	94.7	9.4	Weak
39	15513.4	15801.6	288.2	106.9	9.6	Weak
38	15921.7	16217.4	295.7	120.2	9.9	Weak
37	16352.1	16655.6	303.5	134.7	10.1	Weak
36	16806.3	17118.2	311.9	150.7	10.4	Weak

Notes. Vacuum wavelengths in rest frame. The inter-order gap refers to the spectral gap between the $(n-1)$th and the nth orders. The intra-order gap corresponds to the space between the two HAWAII-2RG units in the NIR mosaic.

definition of standard and prototype stars for spectroscopic studies in the Milky Way (Drew et al., 2005; Marigo et al., 2008; Lee et al., 2011; Milone et al., 2011; Damiani et al., 2014), the study of variable stars and composite systems, and the generation of radial-velocitiy templates and colour indices at arbitrary wavelengths and bandpasses (Cenarro et al., 2007; Coelho et al., 2007; Martins & Coelho, 2007; Bertone et al., 2008; Falcón-Barroso et al., 2011; de Laverny et al., 2012).

A large number of stellar libraries are publicly available in the literature in an attempt to cater to different astrophysical contexts. Among the most prominent stellar libraries with observed spectra are the X-Shooter Library[28] (XSL, Chen et al., 2014; Gonneau et al., 2020), the MILES library[29] (Sánchez-Blázquez et al., 2006; Falcón-Barroso et al., 2011), the *Gaia* benchmark stars[30] (Jofré et al., 2014, 2015b, 2018; Heiter et al., 2015a), the ELODIE library[31] (Soubiran et al., 1998; Prugniel & Soubiran, 2001), LAMOST[32] (Cui et al., 2012), the Indo-US library[33] (Valdes et al., 2004), and

---

[28]http://xsl.u-strasbg.fr/
[29]http://miles.iac.es/pages/stellar-libraries/miles-library.php
[30]https://www.blancocuaresma.com/s/benchmarkstars
[31]http://atlas.obs-hp.fr/elodie/
[32]http://www.lamost.org
[33]https://www.noao.edu/cflib

the MaNGA Stellar Library[34] (MaStar, Yan et al., 2019). Table 1.4 lists some of the most relevant and widely used stellar libraries, whereas the wavelength coverage, the resolution, and the number of stars in these libraries are illustrated in Fig. 1.5.

Prime among these is also the CARMENES stellar library (Caballero et al. in prep.), which gathers observations for a sample of 140 bright dwarfs, giants, and supergiants with spectral types from O4 to M6, including the Sun. Incidentally, it constitutes the first open time proposal made for the instrument. Fig. 1.6 shows the spectra around the infrared Ca II triplet in some representative main-sequence stars taken from the CARMENES stellar library. In contrast to other stellar libraries, the CARMENES stellar library provides a very high resolution and simultaneous coverage in the optical and near-infrared wavelength regions in a single exposure. As with all CARMENES observations, the spectra were reduced with `caracal` (Caballero et al., 2016b), which performs the bias correction, the order tracing, the flat-relative optimal extraction, and the wavelength calibration of the VIS and NIR spectra. The final product of the `caracal` pipeline is a fully reduced, wavelength-calibrated, one-dimensional spectrum for each spectral order, namely 61 spectra for the VIS channel, and 28 spectra for the NIR channel. The CARMENES stellar library is publicly available to the astronomical community through the Calar Alto Observatory Archive[35].

---

[34]https://www.sdss.org/dr16/mastar/
[35]http://caha.sdc.cab.inta-csic.es/calto/
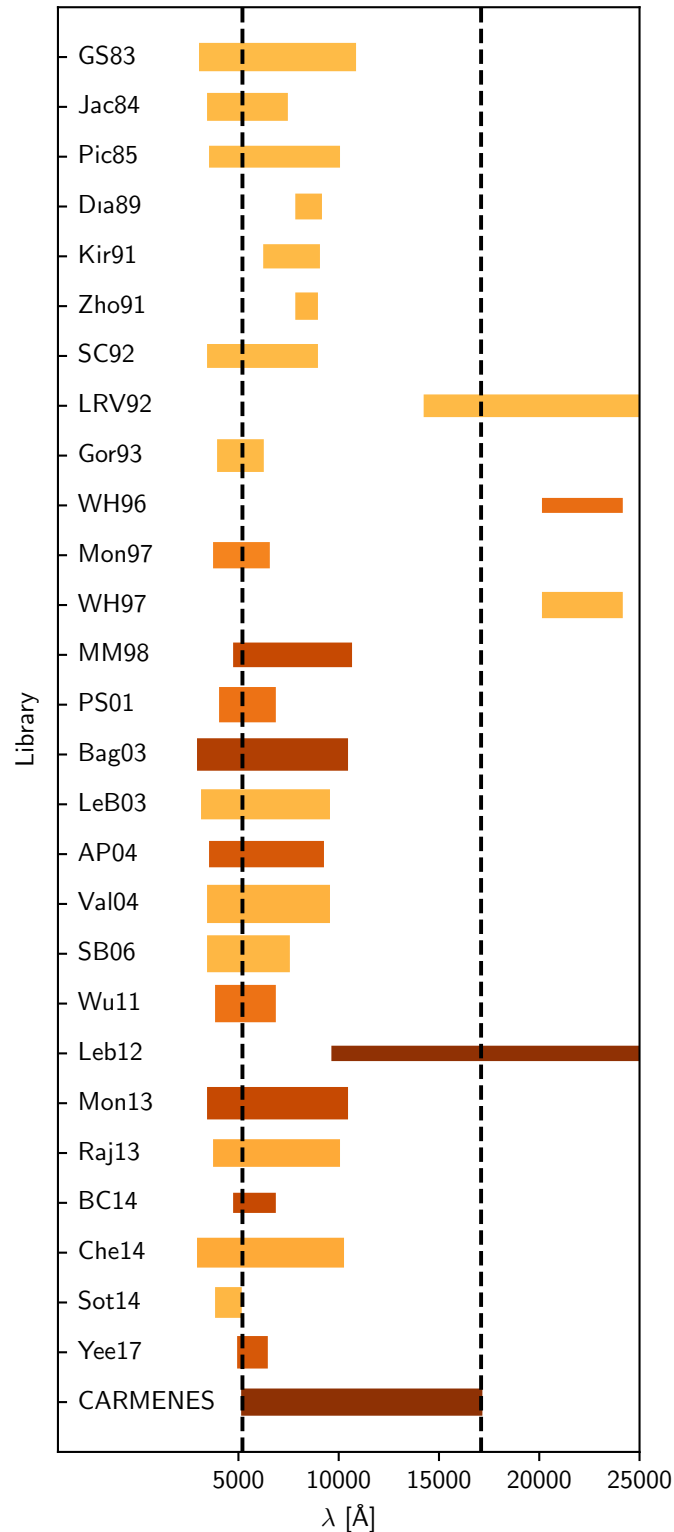
FIGURE 1.5. Wavelength coverage of the public stellar libraries listed in Table 1.4. The darker and wider the bands, the higher the resolution and the larger the number of stars, respectively. The CARMENES stellar library is shown at the bottom, exhibiting the highest spectral resolution and the only one having simultaneous coverage in the optical and near-infrared wavelength regions.
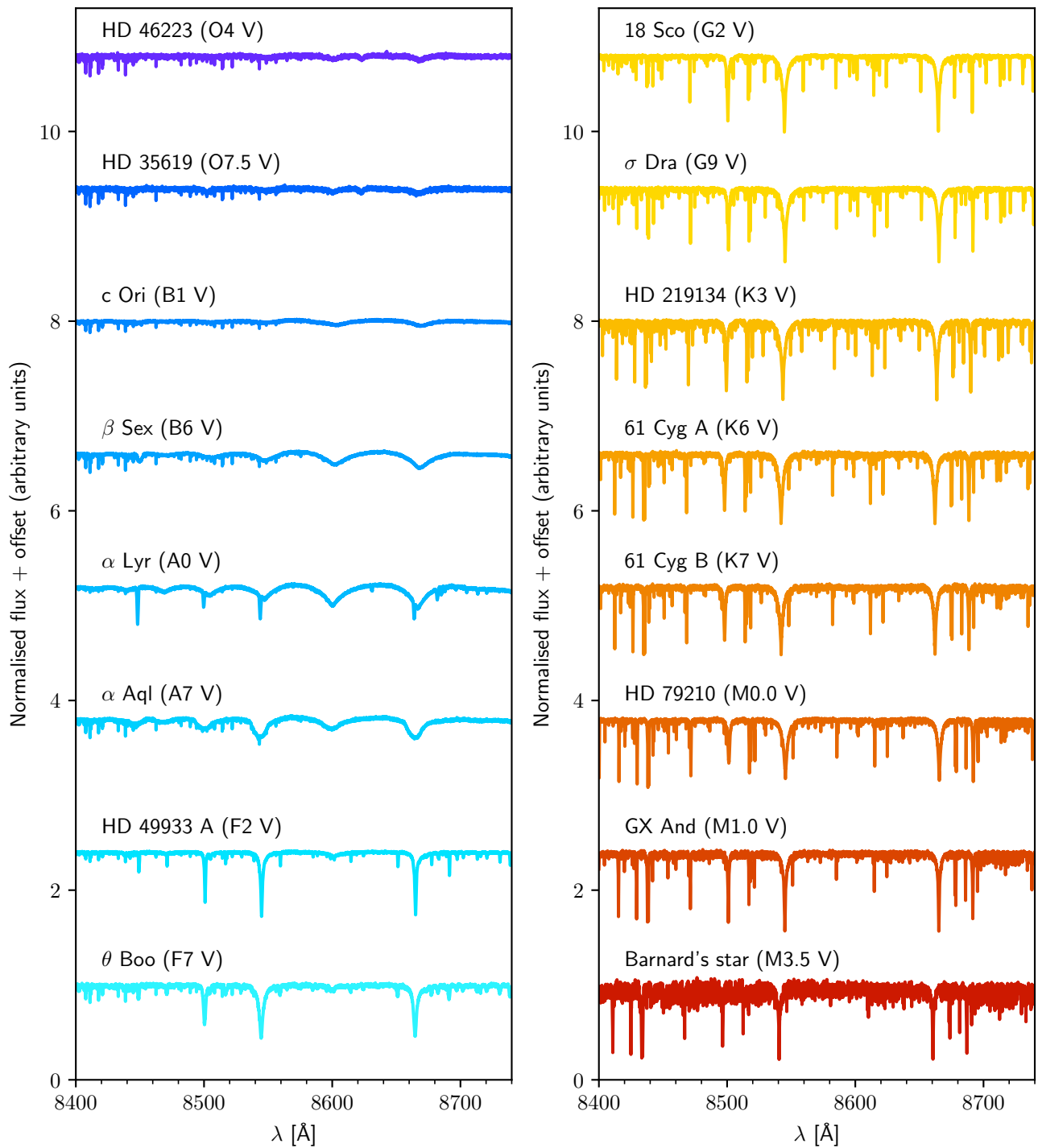
FIGURE 1.6. Close-up view around the infrared Ca II triplet at 8498, 8542, and 8662 Å in some representantive main-sequence stars with spectral types from 04 V to M3.5 V from the CARMENES stellar library.

TABLE 1.4. A selection of stellar spectral libraries.

Library	N_{stars}	Spectral types	Resolution	Wavelength range [Å]
Gunn & Stryker (1983)	175	O5–M8	160, 330	3130–10800
Jacoby et al. (1984)	161	O5–M7	1 500	3510–7427
Jones et al. (1984)	62	B0–M5	3 000	7000–10000
Pickles (1985)	200	O8–M6	500	3600–10000
Diaz et al. (1989) [a]	106	F5–M1	2 400	7900–9100
Kirkpatrick et al. (1991)	77	K5–M9	360, 800	6300–9000
Zhou (1991) [a]	144	F5–M7	4 200	7990–8680
Silva & Cornell (1992)	151	O5–M6	600	3510–8930
Lancon & Rocca-Volmerange (1992)	56	O6–M8	550	14280–25000
Gorgas et al. (1993) (Lick/IDS)	424	F3–M7	500	4000–6200
Wallace & Hinkle (1996)	12	F8–M6	45 000	20200–24100
Montes et al. (1997)	116	F0–M9	2 000, 32 000	3830–6500
Wallace & Hinkle (1997)	115	O4–M7	3 000	20000–24000
Montes & Martin (1998)	83	F2–M8	34 000, 70 000	4800–10600
Pickles (1998)	131	O5–M9	500	1150–25000
Soubiran et al. (1998) (ELODIE 1.0)	211	F5–K7	42 000	4400–6800
Jones (1998)	684	O6–M4	2 500	3820–4500, 4780–5450
Montes et al. (1999)	130	F0–M8	12 000	3800–10000
Munari & Tomasella (1999)	131	O4–M8	20 000	8500–8750
Lançon & Wood (2000)	80	AGB stars	1 100	5000–25000
Hinkle et al. (2000) (Arcturus)	1	K0 III	150 000	3727–9300
Prugniel & Soubiran (2001) (ELODIE 2.0)	709	O8–M3	42 000	4100–6800
Cenarro et al. (2001)	706	O6–M7	5 700	8348–9020
Bagnulo et al. (2003) (UVES-POP)	400	O4–M8	80 000	3040–10400
Le Borgne et al. (2003) (STELIB)	249	O5–M6	2 000	3200–9500
Allende Prieto et al. (2004) (S^{4}N)	118	A7–K4	50 000	3620–9210
Ivanov et al. (2004)	218	G0–M9	2 000, 3 000	14800–24500
Valdes et al. (2004) (Indo-US CFLIB)	1273	O5–M8	5 000	3460–9464
Takeda et al. (2005)	160	F2–K2	70 000	5000–8800
Gray et al. (2006) (NStars)	664	B5–M3	2 300	3800–4600
	1676		1 300	3800–4600
Sánchez-Blázquez et al. (2006) (MILES)	985	O7–M7	2 200	3525–7500
Luck & Heiter (2007)	140	F0–K5	60 000	4750–6850
	298		30 000	4000–8500
Rayner et al. (2009)	210	F0–T4	2 000	8000–50000
Sharon et al. (2010)	20	F4–M2	25 000	9500–11100
Sota et al. (2011) (GOSSS-N)	184	O2–B0	2 500	3740–5510
Wu et al. (2011) (ELODIE 3.2)	1070	O5–M7	42 000	3900–6800
Lebzelter et al. (2012) (CRIRES-POP)	13	B0–M7	96 000	9600–53000
Montes (2013)	400	F0–M8	40 000, 70 000	3500–10400
Rajpurohit et al. (2013)	152	K7–M9	10 000	5200–9500
Blanco-Cuaresma et al. (2014c)	34	F2–M4	70 000	4800–6800
Chen et al. (2014) (XSL)	237	O7–L2	10 000	3100–10185
Sota et al. (2014) (GOSSS-S)	258	O2–O9	2 500	3750–5600
Gonneau et al. (2016)	35	Carbon stars	10 000	3000–25000
Yee et al. (2017)	404	F1–M5	60 000	4990–6410
Carrasco et al. (2021) (MEGASTAR)	414	O6–M6	20 000	6420–6790, 8370–8885
CARMENES stellar library	140	O4–M6	94 600, 80 400	5200–17100

Notes. [a] They did not provide access to the spectra.
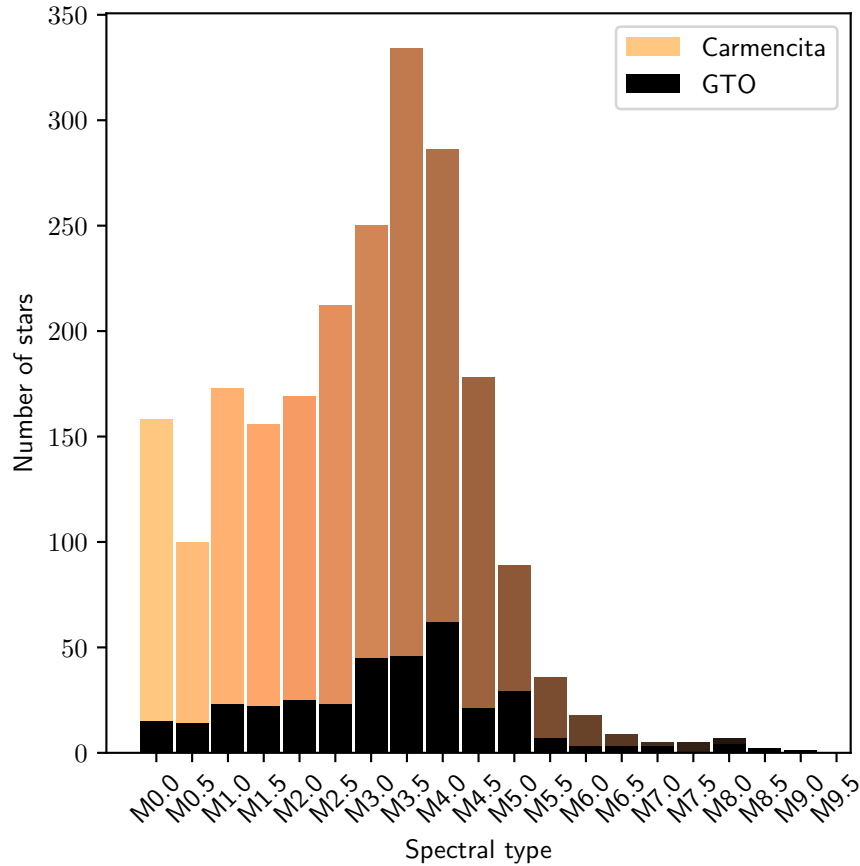
FIGURE 1.7. Distribution of spectral types in Carmencita (version 100) and the CARMENES GTO sample. Only M dwarfs with spectral types determined from spectroscopy are shown.

1.2.2 The CARMENES guaranteed time observations programme

M dwarfs that are included in the CARMENES GTO programme were selected from the CARMENES input catalogue, dubbed Carmencita (CARMENES Cool dwarf Information and daTa Archive), which constitutes a comprehensive record of several parameters of interest for around 2200 M dwarfs in the solar neighbourhood, including spectral types, kinematics, multiplicity, photometry, projected rotational velocities, and activity levels, among others. A complete overview of Carmencita can be found in Cortés-Contreras (2016) and a series of studies devoted to Carmencita (Alonso-Floriano et al., 2015; Cortés-Contreras et al., 2017; Jeffers et al., 2018; Díez Alonso et al., 2019; Cifuentes et al., 2020). Thus, only a short overview will be presented in the following.

M dwarfs in this input catalogue essentially fulfil two conditions (Alonso-Floriano et al., 2015):

- Targets must be observable from the Calar Alto Observatory (i.e. targets must have declinations $\delta > -23$ deg).

- Targets are the brightest amongst each spectral subtype according to their 2MASS J-band magnitude, so that all M dwarfs fainter than $J = 11.5$ mag are excluded.

A large number of sources and catalogues were revised to build Carmencita. Among them are the REsearch Consortium On Nearby Stars catalogue (RECONS, Winters et al., 2015, and references therein), Palomar/Michigan State University survey catalogue of nearby stars (PMSU, Gizis et al., 2002, and references therein), and other sources (e.g. Reid et al., 2008; Lépine et al., 2013). All stars

TABLE 1.5. Present and future spectrographs that are comparable to CARMENES [a].

Spectrograph	Resolution	Wavelength range [Å]	Reference
	Comparable spectrographs in the optical *and* near-infrared		
GIARPS	115 000, 50 000	3830–24500	Claudi et al. (2018)
NIRPS+HARPS	115 000, 100 000	3780–6910, 9500–18000	Bouchy et al. (2017)
HIRES@E-ELT	100 000	4000–18000	Marconi et al. (2020)
	Comparable spectrographs in the near-infrared		
Veloce	80 000	5800–9300	Gilbert et al. (2018)
CRIRES+	100 000	9500–52000	Dorn et al. (2016)
MAROON-X	80 000	5000–9200	Seifahrt et al. (2020)
NIRPS	100 000	9500–18000	Wildi et al. (2017)
SPIRou	73 500	9800–23500	Artigau et al. (2014)
HPF	55 000	8100–12800	Mahadevan et al. (2012, 2014)
IRD	70 000	9700–17500	Kotani et al. (2018)
GIANO-B	50 000	9000–24500	Origlia et al. (2014)
iSHELL	75 000	11000–53000	Rayner et al. (2016)
	Comparable spectrographs in the optical		
ESPRESSO	190 000	3780–7890	Pepe et al. (2021)
HORuS	25 000	3770–6910	Allende Prieto (2021)
HARPS-N	115 000	3830–6930	Cosentino et al. (2012)
PFS	190 000	3910–7340	Crane et al. (2010)
HARPS	115 000	3780–6910	Mayor et al. (2003)
HRS	120 000	3900–11000	Tull (1998)
UVES	110 000	3200–10500	Dekker et al. (2000)
HIRES@Keck	85 000	3000–10000	Vogt et al. (1994)

Notes. [a] High-resolution spectrographs with wide, simultaneous, spectral coverage at 4 m-class telescopes or larger.

in Carmencita have a unique identifier "Karmn JHHMMm^{+/−}DDd", where HHMMm^{+/−}DDd denote the truncated equatorial coordinates of the star, and J refers to the J2000.0 equinox. In some cases, the letters E/W or N/S are appended at the end of the Karmn identifier to distinguish binary pairs with similar equatorial coordinates.

The final selection of stars to be observed with CARMENES as part of its GTO programme was done in terms of priority flags based on stellar brightness and multiplicity (Cortés-Contreras, 2016). For instance, M dwarfs with physical companions closer than 5 arcsec were automatically discarded to avoid any potential contamination of the radial-velocity measurements caused by the gravitational pull of the companion. Furthermore, other classification schemes were also followed to ensure an equal distribution of the GTO targets into early-, mid-, and late-type M dwarfs to be observed with CARMENES. A histogram with spectral types in Carmencita and the CARMENES GTO sample is shown in Fig. 1.7.

Figs. 1.8 and 1.9 show the CARMENES spectrum of the M1.0 V star GX And (J00183+440) as an example of GTO target (for an order-merged, channel-merged spectrum of GX And, see e.g. Fig 4.3 from Marfil et al. 2021). As can be seen in Figs. 1.8 and 1.9 and according to Table 1.3, some orders (especially in the NIR channel) are affected by telluric absorption features. These features can be modelled and corrected with specific softwares tools such as `molecfit`[36] (Smette et al., 2015; Kausch et al., 2015), which incorporates the line-by-line radiative transfer code LBLRTM (Clough

---

[36] http://www.eso.org/sci/software/pipelines/skytools/molecfit

et al., 2005) and the HITRAN[37] molecular line list (Rothman et al., 2009). Once the individual spectra have been corrected for telluric absorption features, observations for the same star taken at different epochs can be stacked up to help enhance the overall S/N of the spectra (Nagel, 2019). Since hundreds of observations are taken for each GTO target, this step results in very high-S/N template spectra that are free from weak telluric absorption features and are, thus, optimal for any subsequent analysis, including parameter determination.

1.2.3 Present and future spectrographs comparable to CARMENES

Table 1.5 displays present and future spectrographs that are comparable to CARMENES in terms of wavelength coverage (i.e. optical and near-infrared spectrographs). Only high-resolution spectrographs with wide, simultaneous, spectral coverage at 4 m-class telescopes or larger are listed.

All of these spectrographs have been designed to support the ongoing search for extrasolar planets in close pursuit of increased velocity stability in order to achieve the best precision. The precision in radial velocity measurements can be as good as 25 m s^{-1} during a single night (ESPRESSO, Pepe et al., 2021) due to the natural limit established by photon noise and stellar jitter.

1.3 Aims and scope of the PhD thesis

The prime objective of this PhD thesis is the spectroscopic analysis of late-type stars observed with CARMENES. The work is divided into the analysis of FGK-type and M-dwarf CARMENES spectra by means of the EW method and spectral synthesis, respectively. For this purpose, the codes StePar (Tabernero et al., 2019) and SteParSyn (Tabernero et al., 2021b) have been used as robust implementations of these two techniques, along with atomic line lists optimised for the optical and near-infrared wavelength regions covered by CARMENES. The spectra analysed correspond to single observations from the CARMENES stellar library and template spectra for the CARMENES GTO targets. For this purpose, different radiative transfer codes, including MOOG (Sneden, 1973) and `turbospectrum` (Plez, 2012), and model atmospheres, including MARCS (Gustafsson et al., 2008), BT-Settl (Allard et al., 2012), and PHOENIX-ACES (Husser et al., 2013), have been employed.

Accurate determinations of stellar atmospheric parameters ($T_{\rm eff}$, $\log g$, and [Fe/H]) are crucial in the current era of dedicated spectroscopic surveys. They are also relevant in exoplanet research insofar as uncertainties in exoplanet properties, such as equilibrium temperatures, are generally dominated by uncertainties in the stellar properties of host stars (e.g. effective temperature and luminosity). Stellar atmospheric parameters also have a critical impact on chemical abundance determinations of host stars (Abia et al., 2020; Ishikawa et al., 2020; Shan et al., 2021), which are essential to a better understanding of exoplanet formation and composition (Dorn et al., 2015). Line selections carried out to perform such analyses are, for example, an asset for any present and future spectrograph sharing the same wavelength coverage as CARMENES (see Table 1.5). Accurate parameter determinations are in turn critical to deriving other parameters such as the stellar mass and radius (Schweitzer et al., 2019), on which determinations and constraints of planetary masses and radii rely (see e.g. Trifonov et al., 2020). In addition, dedicated exoplanet surveys often combine radial-velocity measurements and transit data for which accurate stellar atmospheric parameters are also strongly critical. In other words, the better host stars are characterised, the more insights can be gained into the properties of any potential exoplanet orbiting them.

Furthermore, recent studies show a trend between the stellar metallicity and the presence of giant planets orbiting around them (Johnson & Apps, 2009). Therefore, prior knowledge of stellar

---

[37]https://hitran.org

metallicity can be extremely useful for dedicated exoplanet surveys to maximise detections and also to shed light on planet formation mechanisms, namely the structure and evolution of protoplanetary disks, the formation of planetesimals, the accretion of exoplanets, and the orbital migration of growing planets, among others (Perryman, 2018).

Although the EW method is a fast way to compute the stellar atmospheric parameters, it is limited to the analysis of FGK-type stars. The reason behind this is that only in FGK-type spectra is there a significant number of Fe I and Fe II lines to impose equilibrium and ionisation conditions on. In particular, in the cool regime (i.e. K6 and later spectral types), Fe II become increasingly scarce or unfavourably blended with other lines, and the stellar continuum starts to fade away, which is essential to accurately measure EWs. For this reason, spectral synthesis emerges as an alternative to compute the stellar atmospheric parameters of M dwarfs.

Nonetheless, M-dwarf spectra are far more complex than those of FGK-type stars. The forests of lines that arise as a result of the low photospheric temperatures, coupled with strong magnetic fields and powerful stellar activity phenomena (Tal-Or et al., 2018; Shulyak et al., 2019), make it very hard to select spectral lines useful for accurate parameter determinations with spectral synthesis. Furthermore, the strong absorption features that are present in M-dwarf spectra severely distort the stellar continuum and makes it unfeasible to obtain reliable EW measurements, which are key to the EW method. In addition, some of the lines typically used in M-dwarf studies have been demonstrated to be affected by non-LTE effects, such as K I (Olander et al., 2021). Consequently, the precise derivation of M-dwarf atmospheric parameters is still very challenging and large discrepancies and uncertainties in the derived parameters from different methodologies, especially [Fe/H], still exist (Passegger et al., 2021).

As a way to ensure the reliability of the results, a sharp focus has been given to benchmark tests, including the *Gaia* benchmark stars (see e.g. Jofré et al., 2018), stars with interferometric angular measurements (Boyajian et al., 2012b; von Braun et al., 2014), and multi-star systems (Montes et al., 2018) included in the samples under analysis. These tests can help to detect systematic offsets that are inherent to any methodology.

In light of the above, the PhD thesis is structured as follows:

- Chapter 2 corresponds to the publication of the STEPAR code (Tabernero et al., 2019), the preferred implementation of the EW method that was employed for the analysis of the FGK-type spectra in the CARMENES stellar library included in Chapter 3. The purpose of Chapter 2 is to describe the key ingredients of the STEPAR code (i.e. the grid of model atmospheres, the radiative transfer code, the Fe I and Fe II line lists, the measurement of EWs, and the optimisation algorithm), its workflow, and overall performance on a selection of 23 *Gaia* benchmark stars selected from Blanco-Cuaresma et al. (2014c). General limitations of the EW method are also discussed. Even though STEPAR was already one of the 13 pipelines in the GES project, several shell and Python scripts had to be merged prior to the public release of the code. Therefore, the aim of this chapter is also to put the code to the test and to serve as a preliminary step for the analysis of the FGK-type stars from the CARMENES stellar library.

- Chapter 3 focuses on the results of the spectroscopic analysis carried out with the STEPAR code presented in Chapter 2 for a sample of 65 FGK-type stars selected from the CARMENES stellar library, as published in Marfil et al. (2020). The purpose of this chapter is two-fold: first, to expand previous studies, generally restricted to the optical wavelength range, into the near-infrared covered by CARMENES; second, to assess the potential impact that the inclusion of the near-infrared may have on parameter computations of FGK-type stars via the EW method. For this purpose, the 2017 version of the MOOG code (Sneden, 1973) along with a grid of MARCS model atmospheres (Gustafsson et al., 2008) were employed. EW measurements of the lines were done in an automated fashion with the `EWComputation` code (Soto & Jenkins, 2018; Soto et al., 2021). To expedite the search for Fe I and Fe II lines, four

different line lists were compiled after a careful literature search and a visual inspection of four reference spectra that are representative of metal-rich dwarfs, metal-poor dwarfs, metal-rich giants, and metal-poor giants. All line data were collected from the VALD3 database (Ryabchikova et al., 2015). Altogether, the four lists amount to 653 Fe I and 23 Fe II lines, which more than doubles the number of the lines typically used in classical studies restricted to the optical wavelength region. Finally, a sharp focus was also given to the exhaustive literature comparisons, especially the 14 *Gaia* benchmark stars (Jofré et al., 2014, 2015b, 2018; Heiter et al., 2015a) contained in the sample, in order to test the reliability of the results.

- Chapter 4 shifts the focus towards the application of the SteParSyn code (Tabernero et al., 2021b) as a Bayesian implementation of spectral synthesis on a sample of 343 M dwarfs observed with CARMENES in the context of its GTO programme, as published in Marfil et al. (2021). The use of SteParSyn for such an analysis allowed to circumvent the limitations of the StePar code in the analysis of very cool stars (i.e. later than K4), namely the absence of a well defined stellar continuum and the scarcity of useful Fe I and Fe II required for the EW method. For this purpose, a careful selection of 75 Ti I and Fe I lines with low magnetic sensitivity (i.e. low Landé factors, $g_{eff} < 1.5$ in the near-infrared) was carried out after the visual inspection of the spectra of three representantive early-, mid-, and late-type M dwarfs, namely GX And (M1.0 V), Luyten's star (M3.5 V), and Teegarden's star (M7.0 V). This selection was complemented with other line selections from the literature plus the TiO γ and ϵ bands. The SteParSyn code was only slightly modified to incorporate the instrumental profile of the CARMENES instrument as a source of spectral broadening, following Nagel (2019). For the computation of the synthetic grid, a collection of BT-Settl model atmospheres (Allard et al., 2012) alongside the radiative transfer code `turbospectrum` (Plez, 2012) were employed. Additional synthetic grids (i.e. MARCS, PHOENIX-ACES) were used to check the dependence of the Bayesian approach on the choice of model atmospheres. Furthermore, prior probability distributions in T_{eff} and $\log g$, based on the comprehensive, multi-band photometric data available for the sample (Cifuentes et al., 2020), were imposed in order to avoid any degeneracy in the parameter space, particularly between $\log g$ and [Fe/H]. This approach allowed to compute the stellar atmospheric parameters (T_{eff}, $\log g$, and [Fe/H]) for all M dwarfs in the CARMENES GTO sample that are no later than M7.0 V due to the scarcity of useful Ti I and Fe I lines and the insensitivity of the TiO bands to T_{eff}. To test the derived parameters, a strong emphasis was put on the M dwarfs with interferometrically measured diameters as well as on the FGK+M and M+M wide binary systems included in the sample. The derived M-dwarf metallicity distribution was also compared to the metallicity distribution of FGK-type stars in the solar neighbourhood and studied in tems of the Galactic populations (i.e. the thick disc, the thick disc-thin disc transition, the thin disc, and the young disc).

- Finally, Chapter 5 recapitulates the main conclusions of the PhD thesis and outlines the future work.
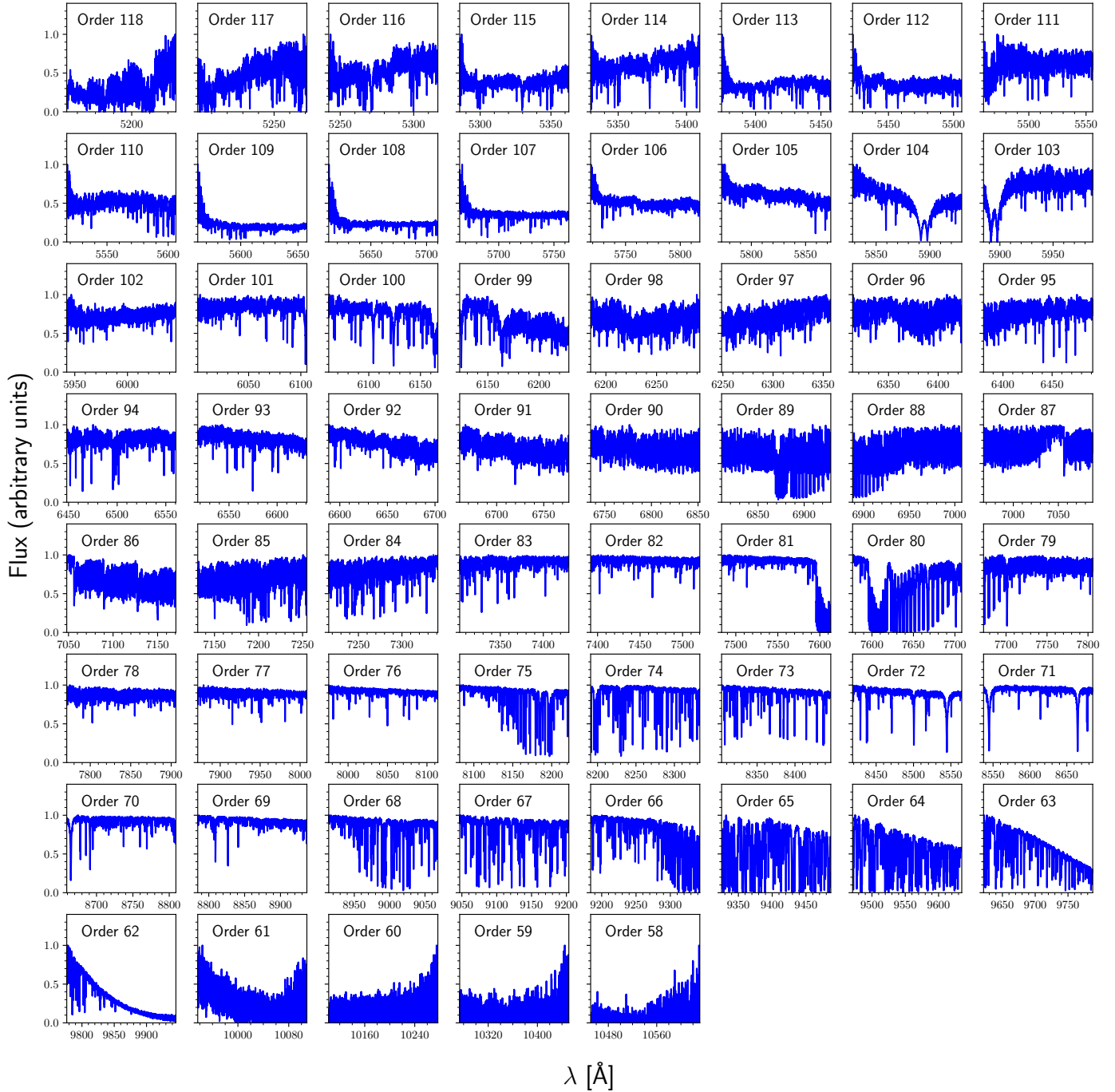
FIGURE 1.8. Order-by-order spectrum of the M1.0 V star GX And (J00183+440) obtained with CARMENES (VIS channel) on 30th September 2019, 04:56:16 UTC with an exposure time of 250 s.
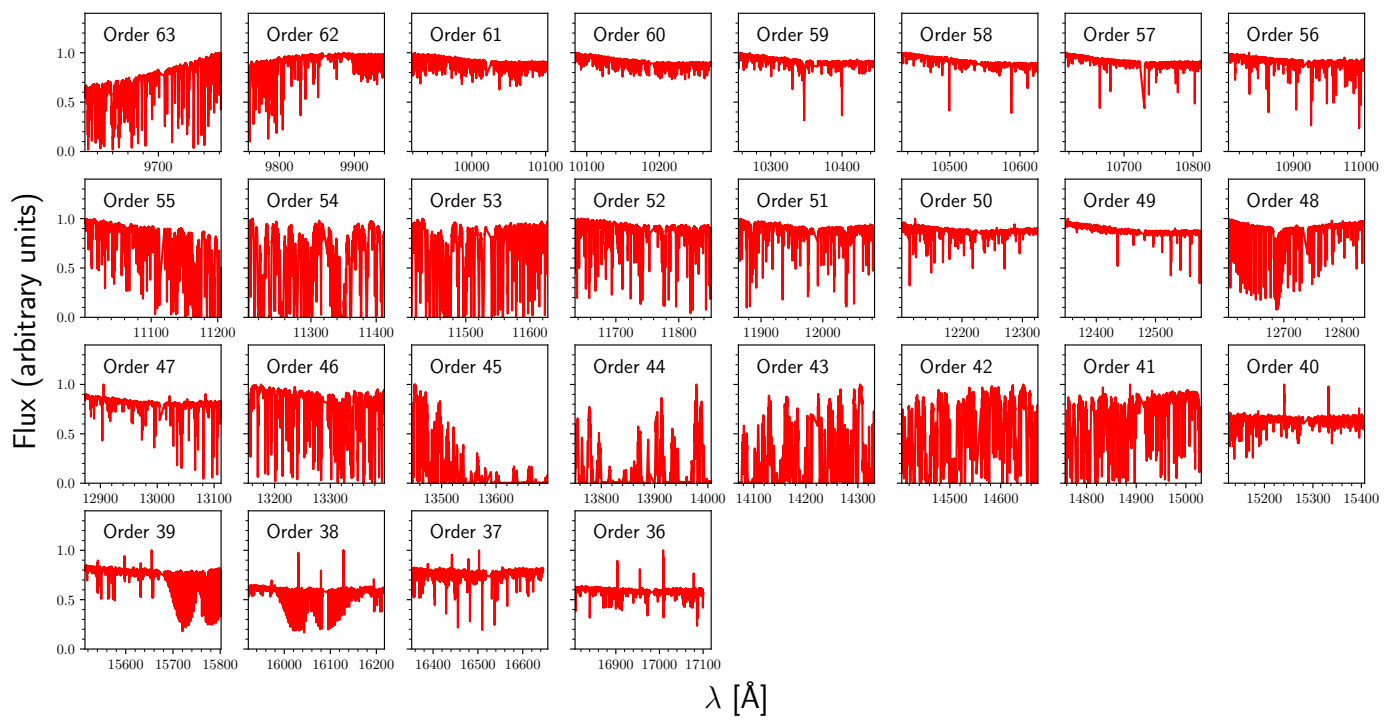
FIGURE 1.9. Same as Fig. 1.8 but for the NIR channel.

2 STEPAR: an automatic code to infer stellar atmospheric parameters

This chapter corresponds to the article that describes the performance of the code STEPAR. The article was accepted for publication on the 14th of July 2019 in the journal *Astronomy & Astrophysics* with the title **STEPAR: an automatic code to infer stellar atmospheric parameters**, Tabernero, H. M., Marfil, E., Montes, D., J. I. González Hernández (2019), A&A, 628, A131, DOI:10.1051/0004-6361/201935465.

H. M. Tabernero[1,2], E. Marfil[3], D. Montes[3], and J. I. González Hernández[4,5]

[1] Centro de Astrobiología (CSIC-INTA), Carretera de Ajalvir km 4, Torrejón de Ardoz, 28850 Madrid, Spain

[2] Instituto de Astrofísica e Ciências do Espaço, Universidade do Porto, CAUP, Rua das Estrelas, 4150-762 Porto, Portugal
e-mail: hugo.tabernero@astro.up.pt

[3] Departamento de Física de la Tierra y Astrofísica & IPARCOS-UCM (Instituto de Física de Partículas y del Cosmos de la UCM), Facultad de Ciencias Físicas, Universidad Complutense de Madrid, 28040 Madrid, Spain

[4] Instituto de Astrofísica de Canarias (IAC), 38025 La Laguna, Tenerife, Spain

[5] Universidad de La Laguna (ULL), Departamento de Astrofísica, 38206 La Laguna, Tenerife, Spain

ABSTRACT

Context. STEPAR is an automatic code written in Python 3.X designed to compute the stellar atmospheric parameters $T_{\rm eff}$, $\log g$, [Fe/H], and ξ of FGK-type stars by means of the equivalent width (EW) method. This code has already been extensively tested in different spectroscopic studies of FGK-type stars with several spectrographs and against thousands of *Gaia*-ESO Survey UVES U580 spectra of late-type, low-mass stars as one of its 13 pipelines.

Aims. We describe the code that we tested against a library of well characterised *Gaia* benchmark stars. We also release the code to the community and provide the link for download.

Methods. We carried out the required EW determination of Fe I and Fe II spectral lines using the automatic tool TAME. STEPAR implements a grid of MARCS model atmospheres and the MOOG radiative transfer code to compute stellar atmospheric parameters by means of a Downhill Simplex minimisation algorithm.

Results. We show the results of the benchmark star test and also discuss the limitations of the EW method, and hence the code. In addition, we find a small internal scatter for the benchmark stars

of 9 ± 32 K in T_{eff}, 0.00 ± 0.07 dex in $\log g$, and 0.00 ± 0.03 dex in [Fe/H]. Finally, we advise against using STEPAR on double-lined spectroscopic binaries or spectra with $R < 30\,000$, $\text{S/N} < 20$ or $v \sin i > 15$ km s^{-1}, and on stars later than K4 or earlier than F6.

Key words. techniques: spectroscopic – methods: data analysis – stars: fundamental parameters

2.1 Introduction

The characterisation of stellar spectra is a matter of utmost importance to several fields in modern astrophysics. It provides for the study and better understanding of the different constituents of our galaxy in terms of both individual and large-scale properties of target objects.

For this reason, stellar spectroscopy is a powerful tool that is being widely used in observational surveys, such as the APO Galactic Evolution Experiment (APOGEE, Dawson et al., 2013), the GALactic Archeology with HERMES (GALAH, De Silva et al., 2015), the LAMOST Experiment for Galactic Understanding and Exploration (LEGUE, Deng et al., 2012), the RAdial Velocity Experiment (RAVE, Kunder et al., 2017), the Sloan Extension for Galactic Understanding and Exploration (SEGUE, Lee et al., 2008), the *Gaia*-ESO Survey (GES, Gilmore et al., 2012), and the WHT Enhanced Area Velocity Explorer WEAVE (WEAVE, Dalton et al., 2018).

These large surveys have been specially designed to yield full sets of stellar parameters for as many stars as possible by means of automated methods that ensure the homogeneity of the results. These parameters include the effective temperature, T_{eff}; the surface gravity, $\log g$; the metallicity, [M/H]; and the micro-turbulent velocity, ξ.

In this regard, late-type, low-mass stars of FGK spectral types remain some of the most interesting targets on account of their ubiquity. Furthermore, the optical spectra of these stars have many iron features that are very sensitive to the stellar atmospheric parameters.

The computation of the stellar atmospheric parameters of FGK stars under spectroscopic scrutiny is often carried out by means of two different methods: spectral synthesis and equivalent width (EW). The former uses theoretical synthetic spectra in order to find the best match to a target observed spectrum, whereas the latter uses the strength of several spectral lines to find the set of stellar atmospheric parameteres that best reproduces the measured EWs. Recent thorough reviews of these techniques can be found in Allende Prieto (2016), Nissen & Gustafsson (2018), Jofré et al. (2019), and Blanco-Cuaresma (2019).

There are many implementations of these two methods that are publicly available to the community. Among the spectral synthesis implementations are the APOGEE pipeline (ASPCAP, García Pérez et al., 2016), and Spectroscopy Made Easy (SME, Piskunov & Valenti, 2017; Valenti & Piskunov, 1996), whereas the EW method is implemented in tools such as FAMA (Magrini et al., 2013), GALA (Mucciarelli et al., 2013), BACCHUS (Masseron et al., 2016), and SPECIES (Soto & Jenkins, 2018). Remarkably, there are also general-purpose toolkits such as the integrated Spectroscopic framework (iSpec, see Blanco-Cuaresma et al., 2014a) and FASMA (Andreasen et al., 2017; Tsantaki et al., 2018) that can compute the stellar atmospheric parameters of any given star using both methods.

In general, spectral synthesis methods are based on a χ^2 minimisation algorithm, in turn based on a pre-computed grid of atmospheric models (see Valenti & Piskunov, 1996; García Pérez et al., 2016; Tsantaki et al., 2018). The theoretical spectra, which may sometimes be split up into spectral regions of interest (see e.g. Tsantaki et al., 2014), are finally compared with the observations to find the atmospheric model that best fits the data. This approach can also be found in González Hernández et al. (2004) and Allende Prieto et al. (2006).

On the other hand, the EW method employs the standard technique based on the iron ionisation and excitation balance, taking advantage of the high sensitivity of the strength (i.e. the EW) of Fe I

and Fe II lines to the variation of the stellar atmospheric parameters. This approach rests on the curves of growth that link, by means of the Saha and Boltzmann equations, the observed EW to the column density of the chemical species that causes the line in the stellar spectrum. Further details on these two equations can be found in Hubeny & Mihalas (2014), among others. This method has already been applied to several studies found in the literature (see e.g. Ghezzi et al., 2010; Santos et al., 2004; Sousa et al., 2008).

The required EW determination of the Fe lines can be carried out either automatically or manually. There are some automatic tools designed for this task, such as ARES (Sousa et al., 2007), DAOSPEC (Stetson & Pancino, 2008), and TAME (Kang & Lee, 2012). All these tools accept some input parameters that can be fine-tuned depending on the quality of the target spectrum under analysis (e.g. the position of the stellar pseudo-continuum, the list of spectral lines to be measured, the parameters that constrain the detection of spectral lines according to the spectral resolution). In this regard, we note that any given line list is generally assembled from the analysis of a template star (usually the Sun, e.g. Santos et al. 2004; Sousa et al. 2008). However, in some cases the template star may be different, for example a cool K-type star (Tsantaki et al., 2013), or a giant star (Hekker & Meléndez, 2007). The selected lines must be as unblended as possible to avoid the contamination of neighbouring lines that could potentially affect the EW measurements.

In this work we present a full description of the automatic code STEPAR, written in Python 3.X, which is based on the EW method. This code has already been applied to the careful study of FGK-type stars (González Hernández et al., 2012; Tabernero et al., 2012, 2017; Tabernero, 2014; Jofré et al., 2017; Montes et al., 2018) and has also been extensively used to automatically analyse hundreds of *Gaia*-ESO UVES spectra since it is one of the 13 pipelines that characterise the UVES U580 spectra of late-type, low-mass stars (see Smiljanic et al., 2014; Lanzafame et al., 2015).

A concise description of the complete method is found in Sect. 2.2. Detailed explanations of the STEPAR internal workflow are given in Sect. 2.3. In Sect. 2.4 we discuss our results and compare them to those obtained in previous works, and to evolutionary tracks. Finally, in Sect. 2.5 we present the limitations of the EW method, and hence STEPAR.

2.2 The STEPAR code

2.2.1 STEPAR ingredients

The basic ingredients that STEPAR needs to derive the stellar atmospheric parameters T_{eff}, $\log g$, [Fe/H], and ξ are the following (see Sect. 2.2.2 for full explanation):

(i) A grid of stellar atmospheric models: MARCS model atmospheres (Gustafsson et al., 2008);

(ii) A code to solve the radiative transfer problem under the assumption of local thermodynamic equilibrium (LTE): the MOOG code (Sneden 1973);

(iii) A list of Fe I and Fe II spectral lines along with their atomic parameters;

(iv) A programme to measure the required EWs for later use: TAME (Kang & Lee, 2012);

(v) An optimisation algorithm: the Downhill Simplex method (Press et al., 2002).
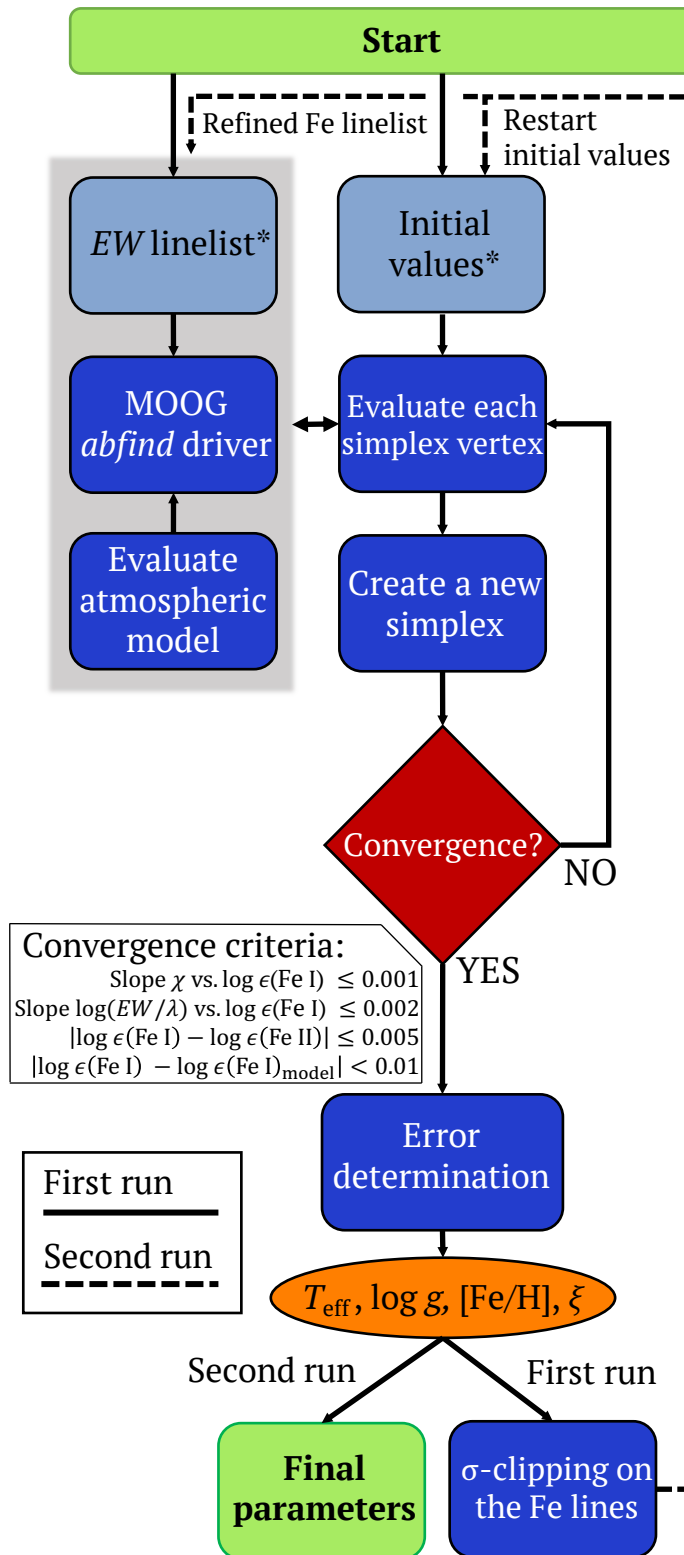
FIGURE 2.1. STEPAR workflow diagram. For any given star under analysis, the code performs two simplex runs. During the second simplex run, the initial values, which are initially set to the solar canonical values, are reset to the values obtained during the first run. Likewise, the EW line list is refined according to the σ clipping procedure on the Fe I lines. After the second run, the code halts execution and yields the final solution for the star. See Sect. 2.2.2 for explanation.

2.2.2 STEPAR workflow

The stellar atmospheric parameters of FGK-type stars, namely T_{eff}, $\log g$, ξ, and [Fe/H], can be derived in an automated fashion with STEPAR[1]. Its workflow is shown in Fig. 2.1. In the standard STEPAR version presented here, we employed the 2017 version of the MOOG code (via the `abfind` driver, see Sneden 1973) and a grid of plane-parallel and spherical MARCS model atmospheres (Gustafsson et al., 2008), although other model grids can be used alongside STEPAR (see Tabernero et al., 2012, 2017; Montes et al., 2018). For lower gravities ($\log g < 3.5$) we used the spherical grid, whereas we employed the non-spherical grid for greater gravities ($\log g \geq 3.5$). Although MOOG treats the MARCS spherical atmospheric models as if they were plane-parallel, Heiter & Eriksson (2006) proved that this potential inconsistency is negligible. However, since the MARCS grid is finite, STEPAR includes an interpolation subroutine, based on the Python Scipy library, which draws on the prior knowledge of the desired model and its neighbouring grid models to interpolate between them (Barber et al., 1996).

STEPAR needs a MOOG-compliant EW file as input, which can be provided by the user in the proper format using an automatic measurement tool. This MOOG-input file must contain the following atomic data for each line considered in the analysis:

(i) Central wavelength of the line, in Å;

(ii) A number that indicates the atomic number and ionisation stage of the chemical species that causes the line (26.0 and 26.1 in the case of Fe I and Fe II lines, respectively);

(iii) The excitation potential, χ, in eV;

(iv) The oscillator strength, $\log gf$;

(v) The EW of the line in mÅ.

To perform our analysis we opted for the automatic code TAME[2] (Kang & Lee, 2012), which can be run in either an automated or manual mode. Its manual mode has an interface that allows some user control over the EW measurements to check problematic spectra when needed. We followed the approach of Kang & Lee (2012) to adjust the `rejt` parameter of TAME according to the S/N of each spectrum. The other TAME parameters we employed were:

(i) `smoother` = 4, the recommended parameter for smoothing the derivatives used for line identification;

(ii) `space` = 3, the wavelength interval (in Å) from each side of the central line to perform the EW computation;

(iii) `lineresol` = 0.1, the minimum distance (in Å) between two lines for TAME to resolve them;

(iv) `miniline` = 2, the minimum EW that will be printed in the output.

Further details on the TAME parameters can be found in Kang & Lee (2012). In addition, we only considered measured lines with 10 mÅ < EW < 120 mÅ to avoid problems with line profiles of very intense lines and tentatively bad EW measurements of extremely weak lines. For benchmark stars that have two high signal-to-noise ratio (S/N) spectra available, we applied an additional filter on the Fe I, II lines and rejected the ones that might have a differential equivalent width beyond three

---

[1] STEPAR is available at `https://github.com/hmtabernero/StePar` under the two-clause BSD license.

[2] TAME can be downloaded from `http://astro.snu.ac.kr/~wskang/tame/`

times the standard deviation of the EW differences between the corresponding Fe I, II lines measured on each of those two spectra.

As damping prescription, we used the Anstee-Bercklem-O'Mara (ABO, see Barklem et al., 1998) data (if available), through option 1 of MOOG. The atmospheric parameters can then be inferred from previously assembled Fe I-Fe II linelists.

The minimisation procedure of STEPAR is the Downhill Simplex algorithm (Press et al., 2002), which tries to minimise a quadratic form composed of the excitation and ionisation equilibrium conditions to find the best parameters of the target star. This minimisation algorithm can reach convergence in very few iterations, and it is so fast that it is the optimisation method of choice, for instance, for the ASPCAP pipeline in APOGEE (Dawson et al., 2013). Since it does not use derivatives, they have to be estimated numerically, as in the Levenberg-Marquardt method. If we let $\log \epsilon(\text{Fe I})$, and $\log \epsilon(\text{Fe II})$ stand for the Fe abundance returned by the Fe I and Fe II lines, respectively, and $\log (\text{EW}/\lambda)$ be their reduced equivalent width, STEPAR iterates until the slopes of χ versus $\log \epsilon(\text{Fe I})$ and $\log (\text{EW}/\lambda)$ versus $\log \epsilon(\text{Fe I})$ are virtually zero (i.e. excitation equilibrium, and imposing ionization equilibrium) so that $\log \epsilon(\text{Fe I}) = \log \epsilon(\text{Fe II})$. Throughout this procedure, we checked that the [Fe/H] obtained from the iron lines is always compatible with the metallicity of the input atmospheric model. The actual convergence criteria of STEPAR, as shown in Fig. 2.1, are the following:

  (i) Slope ξ vs. $\log \epsilon(\text{Fe I}) \leq 0.001$;

 (ii) Slope $\log (\text{EW}/\lambda)$ vs. $\log \epsilon(\text{Fe I}) \leq 0.002$;

(iii) $|\log \epsilon(\text{Fe I}) - \log \epsilon(\text{Fe II})| \leq 0.005$;

(iv) $|\log \epsilon(\text{Fe I}) - \log \epsilon(\text{Fe I})_{\text{model}}| < 0.01$.

For each target spectrum, STEPAR performs two simplex runs, which in turn individually entail a full parameter determination using the Downhill Simplex optimisation method. The first run deals with the EWs file as initially measured by TAME. Next, the best model that is found in this first run by the optimisation routine is evaluated. STEPAR then performs a 3σ clipping procedure on the Fe I abundance values obtained from the Fe I lines so that we can remove the outliers, if any, due to "wrong" EW measurements that could potentially invalidate the analysis. The second run is finally launched on a new input EW file that does not contain the rejected lines. An example of this 3σ clipping procedure is shown in Fig. 2.2. As to execution time, STEPAR takes between 2 and 5 min per star to perform this whole procedure, depending on its actual position in the FGK parameter space.

To feed this minimisation process, the canonical solar values are used as initial input values ($T_{\text{eff}} = 5777$ K, $\log g = 4.44$ dex, $\xi = 1$ km s^{-1}). However, STEPAR is able to reach a solution even if the problem star is different from the Sun (e.g. a metal-poor giant). In other words, the final solution for any given star is independent of the initial set of parameters employed.

Finally, the uncertainties in the stellar parameters are determined as follows:

  (i) For the micro-turbulence, we slightly change the value of ξ until the slope of $\log (\text{Fe I})$ vs. $\log (\text{EW}/\lambda)$ varies within its own error, divided by the square root of the number of Fe I lines.

 (ii) The effective temperature is varied until the slope of $\log \epsilon(\text{Fe I})$ vs. χ increases to the error on the slope, divided by the square root of the number of Fe I lines. By increasing ξ on its error, we recompute the effective temperature. These two sources of error are added in quadrature.

(iii) The surface gravity is then varied until the Fe II abundance increases by a quantity equal to the standard deviation divided by the square root of the number of Fe II lines. All the previous errors in ξ and T_{eff} are taken into account by varying these quantities separately, thus recomputing the gravity. These differences are later added in quadrature.
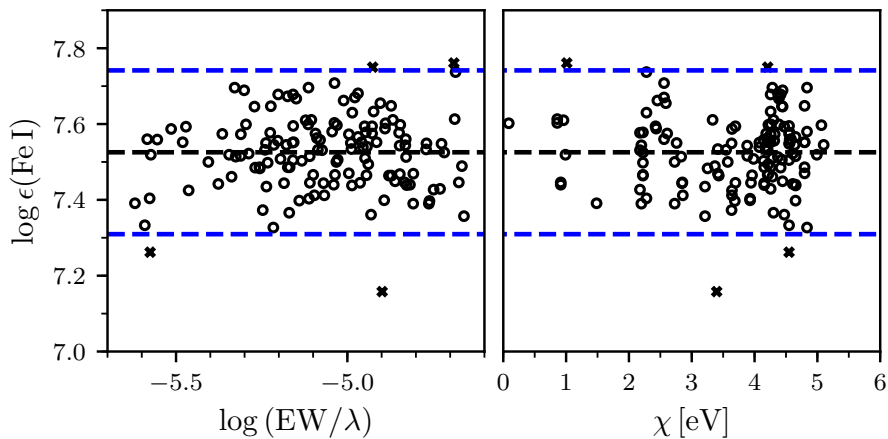
FIGURE 2.2. STEPAR inner 3σ clipping of the Fe I lines on the NARVAL spectrum of the Sun. $\log \epsilon(\text{Fe I})$ stands for the Fe abundance returned by the Fe lines, while $\log(\text{EW}/\lambda)$ represents their reduced EWs. Black crosses depict the rejected Fe I lines. The dashed black lines represent a linear fit to the points, whereas the dashed blue lines are located at the 3σ level.

(iv) Finally, to determine the error in the Fe abundance the stellar atmospheric parameters are varied in their respective uncertainties, which enables the combination of all the Fe I, II variations due to the stellar parameters uncertainties and the standard deviation of the Fe I, II abundances in quadrature.

2.3   Testing the code

2.3.1   Selection of Fe I, II line lists

The EW method requires a significantly large selection of reliable Fe I and Fe II lines. In principle, reliable lines are meant to be clean spectral lines that are not strongly affected by line blending of neighbouring lines or conspicuous spectral features. All the same, the available atomic data of these clean lines may not be precise enough for a trustworthy analysis. The main problem stems from the tabulated values of the transition probability per unit time of the spectral lines, $\log gf$. Some authors avoid this problem by calibrating this value for each line (see e.g. Santos et al., 2004; Sousa et al., 2008; Neves et al., 2009), normally by means of an inverse solar analysis where they vary the $\log gf$ value for a given line until they recover the corresponding solar abundance value. These are called the astrophysical $\log gf$s.

The *Gaia*-ESO line list (Heiter et al., 2015b) was originally extracted from a variety of sources with the aim of finding the best atomic parameters available. It contains around 560 Fe I, II features whose parameters were mostly taken from the Vienna Atomic Line Database (VALD[3], Ryabchikova et al., 2015). The prime goal was to compile a trustworthy selection of lines to compute high-precision stellar parameters.

However, given the diversity of stars across the Milky Way (metal-poor dwarfs and giants, solar-type stars, metal-rich giants, etc.) in the *Gaia*-ESO Survey, it soon became apparent that one line list may fall short for the analysis of any given star. Hence, the analysis of any stellar sample under STEPAR is set to rely on four template stars from which four different lists of Fe I, II lines are assembled: the Sun, HD 22879, ξ Hya, and Arcturus. The corresponding line lists of Fe I and Fe II

---

[3] http://www.astro.uu.se/~vald

TABLE 2.1. Line list template stars and their reference stellar atmospheric parameters from Heiter et al. (2015a), with updated values from Jofré et al. (2018).

Star	List	T_{eff} [K]	$\log g$ [dex]	[Fe/H] [dex]
Sun	MRD	5777 ± 1	4.44 ± 0.01	0.03 ± 0.01
HD 22879	MPD	5868 ± 89	4.27 ± 0.03	−0.86 ± 0.05
ξ Hya	MRG	5044 ± 40	2.87 ± 0.02	0.16 ± 0.20
Arcturus	MPG	4286 ± 35	1.60 ± 0.20	−0.52 ± 0.08

can be found in Table A.3 and Table A.4, respectively. These four template stars, which fully cover the FGK parameter space (as explained below) help us classify any star prior to the analysis with StePar.

This division of the parameter space meets the following criteria. In terms of metallicity, we distinguish between metal-rich stars, [Fe/H] ≥ −0.30, and metal-poor stars, −0.30 > [Fe/H] ≥ −1.50. In terms of surface gravity, we make a distinction between the giant regime, $\log g < 4.00$, and the dwarf regime, $\log g \geq 4.00$. These partitions mean that the global parameter space is divided into four different regions: metal-rich dwarfs (MRD), metal-poor dwarfs (MPD), metal-rich giants (MRG), and metal-poor giants (MPG). Because of their scarcity, we decided to set aside the extremely metal-poor stars with [Fe/H] < −1.50. The general scheme of this division (MRD, MPD, MRG, MPG) is shown in Table 2.1.

As already mentioned, the analysis of any given star is done blindly, that is, its stellar parameters are not known beforehand. Hence, it is not known a priori which line list corresponds to any given star. In order to overcome this issue, we measured the lines from all four line lists and did a first-pass with StePar so we could finally assign a line list to each star depending on the parameters obtained. This preliminary step allowed us to run StePar with the corresponding line list to get the final solution for the star.

2.3.2   *Gaia* benchmark test

Every spectroscopic study requires a reference point to assess the validity of the obtained results. Even though the Sun is widely used in the literature as a common reference, the use of one single star as a central point of reference provides no evidence for how a given method works in different regions of the parameter space.

In this regard, the *Gaia* benchmark stars were originally meant as calibrators to test the different approaches to the analysis. The availability of specific information for these stars was the key to determining their stellar atmospheric parameters independently from spectroscopy (Heiter et al., 2015a). In this sense, the *Gaia* benchmark stars represent a cornerstone when it comes to weighing the impact of the general limitations (e.g. wavelength coverage, line lists employed, resolution) inherent to any spectroscopic method that aims at the computation of such parameters.

Ideally, with a common background, any set of tools using the same data should converge to the same atmospheric parameters. However, given that every method takes into account a different set of spectral lines inevitably leads to slightly different stellar parameters. Although, in general, these differences are mostly dependent on the radiative transfer code, the stellar atmospheric models, the specific method, and the input data, among the GES nodes this dependence mostly comes down to the input data (measurement of EWs, S/N of the spectra, the local continuum normalisation, etc.) and the method that each node takes into consideration.

These stars, 23 in total, were taken from the stellar library[4] described in Blanco-Cuaresma et al. (2014a), which covers the optical region 4800–6800 Å. The stars span a wide range in the parameter

---

[4]The spectra of these stars can be downloaded from `https://www.blancocuaresma.com/s/benchmarkstars`

TABLE 2.2. Number of Fe I and Fe II in each of the four line lists used in this work.

Element	MRD	MPD	MRG	MPG
Fe I	146	127	113	115
Fe II	12	13	11	6
#stars	8	4	7	4

Notes. The wavelength coverage of all four lists is 4800–6800 Å, in line with that of the spectra under analysis. We also display the number of stars in each category.

space (Heiter et al., 2015a; Jofré et al., 2015b), which allowed us to test the reliability of the results given by STEPAR (see Table A.1). The internal consistency of the code was tested by deriving stellar atmospheric parameters from one or two high S/N spectra of the same star (see Table A.2).
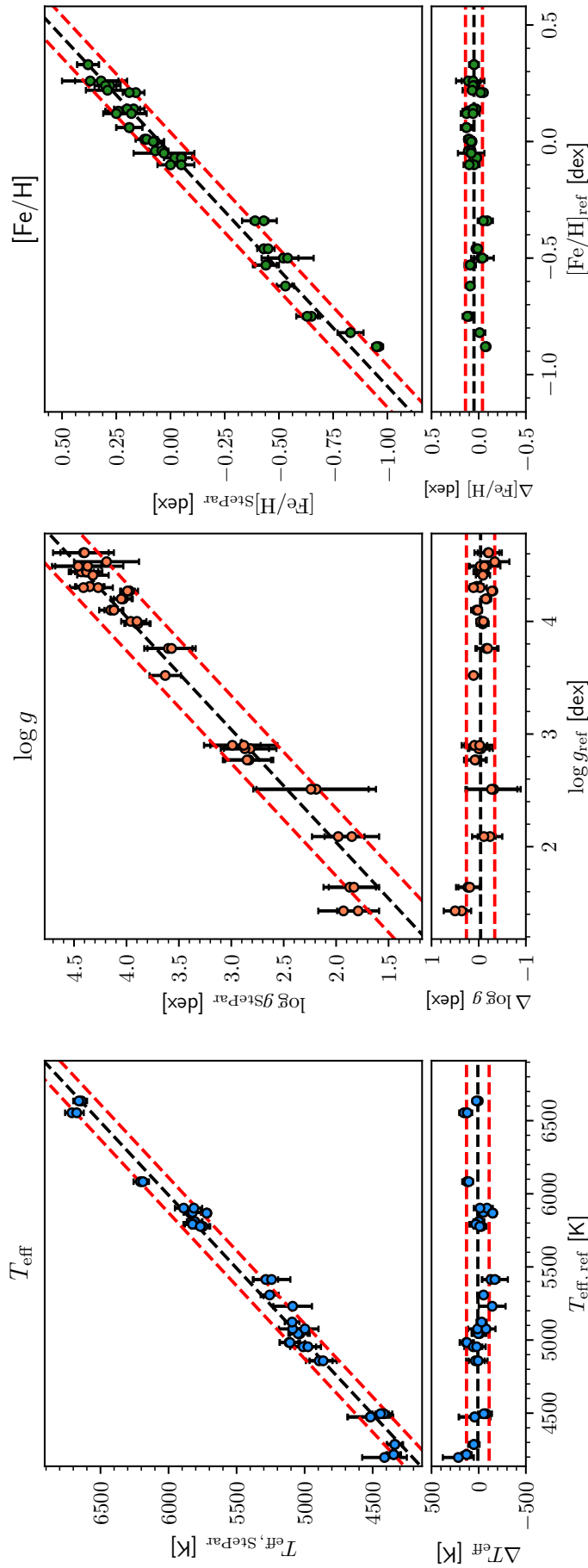
FIGURE 2.3. STEPAR results for the *Gaia* benchmark stars plotted against the literature values taken from Heiter et al. (2015a), with updated values from Jofré et al. (2018). *Upper panels*: one-to-one correspondence, whereas *bottom panels*: absolute differences. Using the values in Table 2.3, the dashed black lines in the upper panels correspond to a one-to-one relationship, shifted following the average differences in each parameter, whereas in the bottom panels they are centred on the average differences. The dashed red lines in all panels correspond to a margin of 120 K, 0.30 dex, and 0.09 dex in T_{eff}, $\log g$, and [Fe/H], respectively, according to the σ values found in the differences in each parameter.

2.4 Discussion

Although different spectra of the same object should theoretically result in exactly the same stellar atmospheric parameters, we note slight deviations in our analysis. The mean differences for the benchmark stars are 9 ± 32 K in T_{eff}, 0.00 ± 0.07 dex in $\log g$, and 0.00 ± 0.03 dex in [Fe/H].

These internal differences are mostly due to the quality of the individual spectra. The average uncertainties for the benchmark stars are 75 K in T_{eff}, 0.21 dex in $\log g$, and 0.06 dex in [Fe/H]. Furthermore, the average uncertainties are greater than the scatter that arises from the analysis of different spectra of the same object, as expected. Other sources of uncertainty might arise from systematic effects inherent to any methodology.

We compared the values of the stellar parameters for each spectrum to the reference values, as shown in Fig. 2.3. We found the following differences, all of which might be systematic: $\Delta T_{\text{eff}} = 9 \pm 89$ K, $\Delta \log g = 0.04 \pm 0.18$ dex, and Δ[Fe/H] $= 0.05 \pm 0.06$ dex. At first glance, there are no notable differences at the 1-2σ level. Additionally, in Fig. 2.4 we plot the line iron abundance retrieved by STEPAR for the final solution of the four reference stars.

However, since systematic trends may still remain hidden, we performed 10000 Monte Carlo simulations on our data (as in Tabernero et al., 2018) in the hope of assessing possible sources of tentatively systematic offsets. We took each atmospheric parameter (T_{eff}, $\log g$, and [Fe/H]) to check any possible correlations by means of the Pearson and Spearman correlation coefficients, which are a measure of the correlation between any two given variables. Specifically, the Pearson coefficient is a classical correlation indicator, whereas the Spearman coefficient is a more robust non-parametric estimator of the statistical dependence of any two given variables (for more details, see e.g. Press et al., 2002). In Table 2.3 we clearly show that no systematic trends are present above the 2σ level (i.e. within 95 % confidence interval). These results are shown in Figs. 2.3 and A.1. Interestingly enough, even if the offsets in effective temperature and surface gravity are noticeable, the offset in the iron abundance is negligible (see Fig. 2.3). This is probably due to the fact that STEPAR produces self-consistent stellar parameters. For example, a deviation on the effective temperature can be compensated by the other parameters.

TABLE 2.3. Summary of the Monte Carlo simulations performed using the stellar atmospheric parameters calculated in Sect. 2.3.

Parameter	Difference	r_{p}	r_{S}
T_{eff} [K]	9 ± 120	-0.12 ± 0.10	-0.15 ± 0.10
$\log g$ [dex]	-0.04 ± 0.30	-0.33 ± 0.16	-0.26 ± 0.14
[Fe/H] [dex]	0.05 ± 0.09	0.25 ± 0.10	0.16 ± 0.11

Notes. Here we present the average difference on each parameter, along with the values of the Pearson (r_{p}) and the Spearman (r_{S}) correlation coefficients.

TABLE 2.4. Same information as shown in Table 2.3, but organised on a per-line list basis, i.e. MRD, MPD, MRG, and MPG lists.

List	Difference		
	T_{eff} [K]	$\log g$ [dex]	[Fe/H] [dex]
MRD	14 ± 105	0.05 ± 0.19	0.06 ± 0.07
MPD	-88 ± 96	0.16 ± 0.18	0.03 ± 0.06
MRG	44 ± 122	0.05 ± 0.36	0.08 ± 0.08
MPG	28 ± 92	0.15 ± 0.31	0.05 ± 0.09
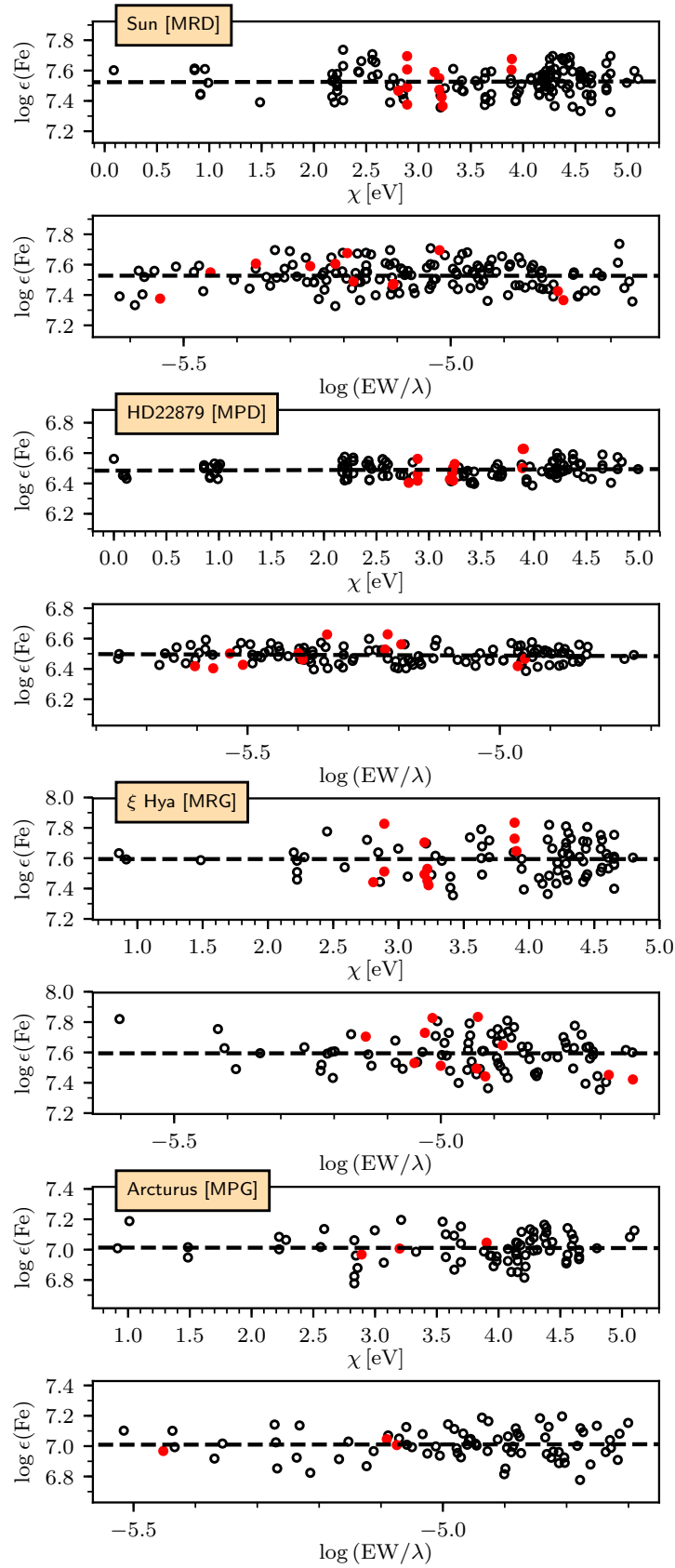
Fɪɢᴜʀᴇ 2.4. *From top to bottom*: line iron abundance retrieved by SᴛᴇPᴀʀ for the final solution of the four reference stars: the Sun (NARVAL), HD 22879 (NARVAL), ξ Hya (ESPaDOns), and Arcturus (UVES). $\log \epsilon(\mathrm{Fe})$ stands for the Fe abundance returned by the Fe lines, while $\log(\mathrm{EW}/\lambda)$ is their reduced EWs. Unfilled black dots represent Fe ɪ lines, whereas red dots are Fe ɪɪ lines. The dashed black lines represent the least-squares fit to the data points.
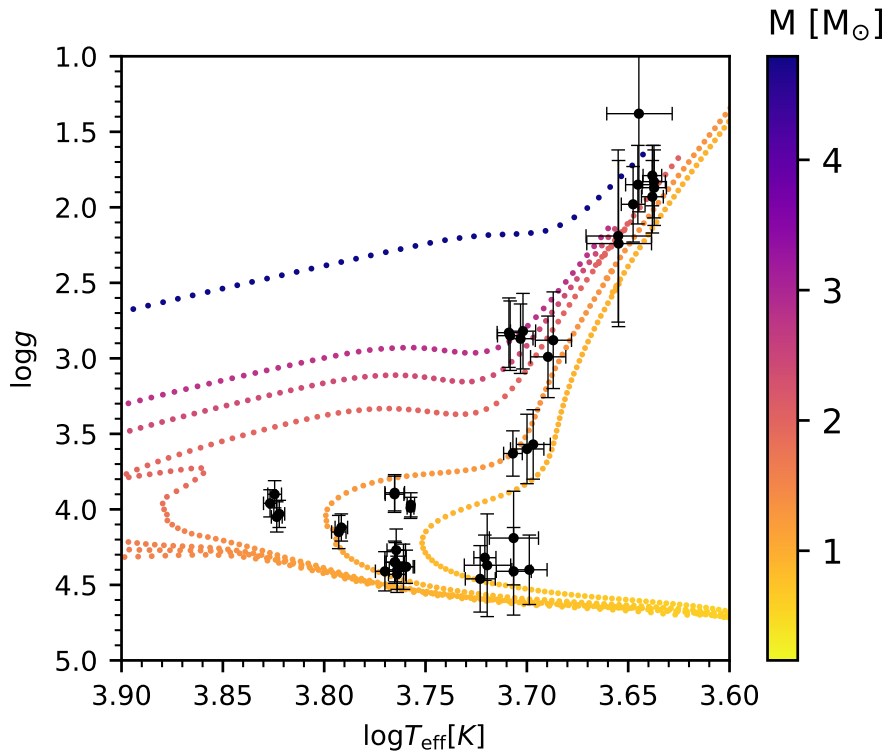
FIGURE 2.5. Kiel diagram (log g vs. log T_{eff}) for all the spectra alongside the YaPSI isochrones at 0.1, 0.4, 0.6, 1, 4, and 13 Ga (for $Z = 0.016$, see Spada et al., 2017).

Finally, we assessed the performance of SтePaꜰ in different regions of the parameter space. In Fig. 2.5 we plot a Kiel diagram (i.e. log g vs. log T_{eff}) including the latest Yale-Potsdam Stellar Isochrones (YaPSI, Spada et al., 2017). In light of this figure, we do not find any major inconsistencies with the parameter space encompassed by the isochrones in general terms. However, we note that our method does not reproduce the gravity of K stars, as they should have higher values. The former result is not entirely unexpected (Tabernero et al., 2012), and might be due to an ionisation imbalance problem (Tsantaki et al., 2019). We still find higher effective temperatures for the F-type dwarfs, although they deviate less than in previous works (i.e. Tabernero et al., 2017; Montes et al., 2018). Finally, in Table 2.4 we show how SтePaꜰ performs equally well in the four regions of the FGK parameter space defined in this work, i.e. MRD, MPD, MRG, and MPG, although the MRD and MPD line lists produce slightly larger errors than the rest. Interestingly enough, the errors on surface gravity are larger in the giant regime than in the dwarf regime. For the metallicity we find a similar scatter in the four regions. Despite these differences, we find a good agreement with the reference values.

2.5 Conclusions

In this work, we have presented a robust code, SтePaꜰ, which will be useful to the community when deriving the stellar atmospheric parameters of FGK-type stars under the EW method. This code has already been tested during the last few years against the vast quantities of *Gaia*-ESO high-resolution spectra. We have also tested SтePaꜰ against a library of *Gaia* benchmark stars. Although we find some differences with the reference parameters, they are not significant.

Finally, we want to address some general limitations of the EW method that should be taken into consideration when using SтePaꜰ. First, the data must be of high enough quality to be analysed.

Since low S/N may translate into poor EW measurements, this means that we highly recommend placing a cut at S/N < 20. In addition, we note the importance of placing a lower limit in spectral resolution at $R = 30000$ to prevent undesired line blending and suboptimal placement of the continuum level (Freeman & Bland-Hawthorn, 2002). Second, STEPAR cannot derive stellar atmospheric parameters of fast-rotating stars. Although the EWs are not in fact altered by rotation, the line profiles are affected by rotational broadening and may no longer fit a Gaussian profile properly. In this sense, blending of neighbouring lines to the one of interest can also make it nearly impossible to get a reliable EW estimate for a given line. In these cases, we advise against using STEPAR on any star with a rotational velocity higher than $15 \, \mathrm{km \, s^{-1}}$. In addition, double-lined spectroscopic binaries should also be removed from any sample to avoid obtaining unreliable parameters. Finally, we do not recommend deriving stellar parameters with STEPAR for stars earlier than F6 and later than K4.

3 Stellar atmospheric parameters of FGK-type stars with CARMENES

This chapter corresponds to the analysis of the FGK-type stars in the CARMENES stellar library using the EW method implemented in the S𝚃𝚎P𝙰𝚛 code. The paper was accepted for publication on the 28th of December 2019 in the journal *Monthly Notices of the Royal Astronomical Society* with the title *Stellar atmospheric parameters of FGK-type stars from high-resolution optical and near-infrared CARMENES spectra* Marfil, E., Tabernero, H. M., Montes, D., Caballero, J. A. Soto, M. G., González Hernández, J. I., Kaminski, A., Nagel, E. Jeffers, S. V., Reiners, A. Ribas, I. Quirrenbach, A., Amado, P. J, 2020, MNRAS, 492, 4, pp. 5470–5507,

E. Marfil[1], H. M. Tabernero[2,3], D. Montes[1], J. A. Caballero[2], M. G. Soto[4],
J. I. González Hernández[5,6], A. Kaminski[7], E. Nagel[8], S. V. Jeffers[9], A. Reiners[9], I. Ribas[10,11],
A. Quirrenbach[7], and P. J. Amado[12]

[1]Facultad de Ciencias Físicas, Departamento de Física de la Tierra y Astrofísica & IPARCOS-UCM (Instituto de Física de Partículas y del Cosmos de la UCM), Universidad Complutense de Madrid, 28040 Madrid, Spain
e-mail: `emigom01@ucm.es`
[2]Centro de Astrobiología (CSIC-INTA), ESAC, Camino Bajo del Castillo s/n, 28691, Villanueva de la Cañada, Madrid, Spain
[3]Instituto de Astrofísica e Ciências do Espaço, Universidade do Porto, CAUP, Rua das Estrelas, 4150-762 Porto, Portugal
[4]School of Physics and Astronomy, Queen Mary, University of London, 327 Mile End Rd. London, United Kingdom
[5]Departamento de Astrofísica, Universidad de La Laguna, E-38206 La Laguna, Tenerife, Spain
[6]Instituto de Astrofísica de Canarias, vía Láctea s/n, 38205 La Laguna, Tenerife, Spain
[7]Landessternwarte, Zentrum für Astronomie der Universität Heidelberg, Königstuhl 12, 69117 Heidelberg, Germany
[8]Hamburger Sternwarte, Gojenbergsweg 112, 21029 Hamburg, Germany
[9]Institut für Astrophysik, Georg-August-Universität-Göttingen, Friedrich-Hund-Platz 1, D-37077 Göttingen, Germany
[10]Institut de Ciències de l'Espai (CSIC), Campus UAB, C/ de Can Magrans s/n, 08193 Cerdanyola del Vallès, Spain
[11]Institut d'Estudis Espacials de Catalunya (IEEC), C/ Gran Capità 2-4, 08034 Barcelona, Spain
[12]Instituto de Astrofísica de Andalucía (IAA-CSIC), Glorieta de la Astronomía s/n, 18008 Granada, Spain

ABSTRACT

With the purpose of assessing classic spectroscopic methods on high-resolution and high signal-to-noise ratio spectra in the near-infrared wavelength region, we selected a sample of 65 F-, G-, and K-type stars observed with CARMENES, the new, ultra-stable, double-channel spectrograph at the 3.5 m Calar Alto telescope. We computed their stellar atmospheric parameters ($T_{\rm eff}$, $\log g$, ξ, and [Fe/H]) by means of the STEPAR code, a Python implementation of the equivalent width method that employs the 2017 version of the MOOG code and a grid of MARCS model atmospheres. We compiled four Fe I and Fe II line lists suited to metal-rich dwarfs, metal-poor dwarfs, metal-rich giants, and metal-poor giants that cover the wavelength range from 5300 to 17100 Å, thus substantially increasing the number of identified Fe I and Fe II lines up to 653 and 23, respectively. We examined the impact of the near-infrared Fe I and Fe II lines upon our parameter determinations after an exhaustive literature search, placing special emphasis on the 14 *Gaia* benchmark stars contained in our sample. Even though our parameter determinations remain in good agreement with the literature values, the increase in the number of Fe I and Fe II lines when the near-infrared region is taken into account reveals a deeper $T_{\rm eff}$ scale that might stem from a higher sensitivity of the near-infrared lines to $T_{\rm eff}$.

Key words. line: identification – techniques: spectroscopic – stars: fundamental parameters – stars: solar-type – infrared: stars

3.1 Introduction

The homogeneous, automated computation of stellar atmospheric parameters from stellar spectra, i.e. effective temperature $T_{\rm eff}$, surface gravity $\log g$, stellar metallicity [M/H], and micro-turbulent velocity ξ, plays a crucial role in many astrophysical contexts. First, it leads to the analysis of the fundamental properties of individual objects as well as of large stellar samples (Valenti & Fischer, 2005; Adibekyan et al., 2014). In this regard, large stellar spectroscopic surveys such as RAVE (Steinmetz et al., 2006), APOGEE (Allende Prieto et al., 2008), the *Gaia*-ESO Survey (Gilmore et al., 2012), and GALAH (De Silva et al., 2015) have laid the foundations for our current understanding of the structure and evolution of the Milky Way. Secondly, exoplanetary studies also rely on stellar parameter determinations not only to enable the determination of both planetary radii and masses (e.g. Mann et al., 2019; Schweitzer et al., 2019) but also to characterise the habitable zones around planet-harbouring stars (Kasting et al., 1993; Kopparapu et al., 2013). Furthermore, correlations between the stellar metallicity and planet occurrence rates are now well established and shed light on planet formation mechanisms (Adibekyan et al., 2014; Delgado Mena et al., 2018; Montes et al., 2018).

The equivalent width (EW) method (see e.g. Sousa et al., 2008; Tabernero et al., 2012; Mucciarelli et al., 2013; Tsantaki et al., 2013; Bensby et al., 2014; Andreasen et al., 2016) is, along with the spectral synthesis method (see e.g. Valenti & Fischer, 2005; Piskunov & Valenti, 2017), one of the most widely used spectroscopic techniques for determining stellar atmospheric parameters. A full account of the key caveats of these two methods can be found in Jofré et al. (2019) and Blanco-Cuaresma (2019). The advent of high-resolution near-infrared (NIR) spectrographs such as CARMENES (Quirrenbach et al., 2018), SPIRou (Artigau et al., 2014), GIANO (Origlia et al., 2014; Oliva et al., 2018), CRIRES+ (Hatzes, 2017), IRD (Kotani et al., 2014), HPF (Wright et al., 2018), and NIRPS (Wildi et al., 2017) allows us to revisit these techniques, originally applied in the optical, in order to assess the impact of the NIR wavelength range on stellar parameter computations. In this context, new observations of FGK-type stars carried out with CARMENES[1], the double-channel spectrograph at the 3.5 m Calar Alto telescope open up a unique opportunity to test the reliability

---

[1] http://carmenes.caha.es

of such techniques on high-resolution and high signal-to-noise (S/N) ratio spectra in the optical and near-infrared windows.

In this work, we compute the spectroscopic parameters of 65 FGK-type stars selected from a CARMENES stellar library by means of the EW method, which relies on the strength (i.e the EW measurements) of Fe I and Fe II absorption lines to derive the stellar atmospheric parameters T_{eff}, $\log g$, [Fe/H], and ξ assuming local thermodynamic equilibrium. To do so, we followed the approach of Sousa et al. (2007) to automatically measure the EW of the iron lines, and the StePar code (Tabernero et al., 2019) to automatically compute the stellar atmospheric parameters imposing excitation and ionisation equilibrium conditions on the Fe I and Fe II lines.

The wavelength coverage provided by CARMENES, from 5200 Å up to 17100 Å, allowed us to substantially increase the number of Fe I and Fe II lines subject to analysis with the EW method with respect to previous studies restricted to the optical window (Meléndez & Barbuy, 2009; Jofré et al., 2014). Furthermore, the high spectral resolution of CARMENES, which is $R = 94600$ in the VIS channel and $R = 80400$ in the NIR channel (Quirrenbach et al., 2018), significantly improves both the line identification process and the EW measurements. Despite the availability of iron line lists optimised for the NIR region in the literature, the impact on stellar parameter determinations of FGK-type stars is still unknown, mostly due to the fact that such line lists have not as yet been systematically applied to significantly large samples covering a wide portion of the stellar parameter space. For instance, Andreasen et al. (2016) compiled a line list of Fe I and Fe II lines in the region 10000–25000 Å, but only tested it against the spectra of the Sun and the F8 IV star HD 20010.

Several other spectral libraries of high-resolution spectra in the near-infrared have been developed over the past few years. For example, Lebzelter et al. (2012) presented the CRIRES-POP spectral library, which provides high-resolution ($R \sim 100\,000$) spectra for 25 stars between B and M spectral types at 1–5 μm. Furthermore, Nicholls et al. (2017) described the data reduction process and presented the first CRIRES-POP spectral atlas of the K giant 10 Leo. Although the resolution of the spectra in this library is comparable to that of CARMENES, the number of available spectra is significantly lower than the size of the library analysed in this work, and does not satisfactorily cover the parameter space of FGK-type stars. Another example is the IGRINS spectral library (Park et al., 2018), which contains spectra of 84 stars between O and M spectral types in the H (1.49–1.80 μm) and K (1.96–2.46 μm) bands with a resolution of $R = 45\,000$, which is almost half of that provided by CARMENES in the NIR channel. Finally, large surveys such as APOGEE (Zamora et al., 2015; Majewski et al., 2017) have obtained intermediate-resolution ($R \sim 22\,500$) spectra for hundreds of thousands of stars, but with a narrow wavelength coverage in the H band (1.5–1.7 μm).

The analysis performed in this work is structured as follows. In Section 3.2, we describe the selection of the sample. In Section 3.3, we outline the main steps of our analysis, including the line selection process and the workflow of the StePar code. In Sections 3.4 and 3.5, we discuss the results and highlight the conclusions, respectively.

3.2 Sample

We observed an extensive sample of dwarf, giant, and supergiant stars and brown dwarfs with spectral types from O4 to late L as part of the first open time proposal that used CARMENES. While further details on this stellar library will be provided in forthcoming publications (Caballero et al. in prep.), we start here its scientific exploitation.

From the stellar library we selected 65 stars with spectral types later than F5 and earlier than K4, and projected equatorial rotational velocities $v \sin i < 15\,\text{km}\,\text{s}^{-1}$ (see Table B.1). The restriction in spectral type stems from the general limitations of the EW method and hence, StePar, as explained in Tabernero et al. (2019), while stars with high rotational velocities have line profiles that cannot be properly fitted by a Gaussian shape, leading to less reliable EW measurements. None of the observed
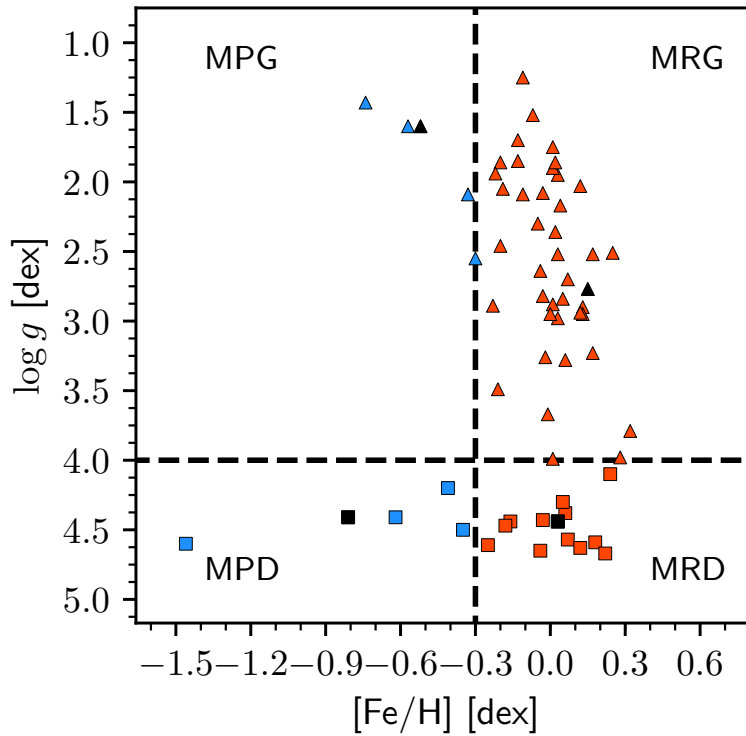
FIGURE 3.1. Division of the parameter space in the sample according to the stellar atmospheric parameters found in the literature. Vertical and horizontal dashed black lines represent the boundaries at [Fe/H] = −0.3 dex and log g = 4.0 dex, respectively, for metal-rich dwarfs (MRDs, orange squares), metal-poor dwarfs (MPDs, blue squares), metal-rich giants (MRGs, orange triangles), and metal-poor giants (MPGs, blue triangles). The stars taken as a reference for each of these regions are shown in black.

65 FGK-type stars had a known visual (physical) or optical (non-physical) companion at less than 5 arcsec. However, we excluded from this analysis one of the giants found in the library, c Gem, with spectral type K4.5 III (Keenan & McNeil, 1989), as it appeared as an SB2 binary system after cross-correlating its spectrum with the atlas spectrum of Arcturus, as explained in Sect. 3.3.1.

Our target list contains 14 *Gaia* benchmark stars (Jofré et al., 2014, 2018; Heiter et al., 2015a), including the Sun. The spectrum of the Sun was obtained through the observation of the asteroid 1 Ceres due to the allocation of Calar Alto Director's discretionary time. According to their original purpose, the fact that the fundamental parameters of these stars have been computed independently from spectroscopy makes them suitable as a reference to assess any method aimed at the automated analysis of cool stars.

Table B.1 displays the star names, Henry-Draper numbers, equatorial coordinates from 2MASS (Skrutskie et al., 2006), parallaxes from the *Gaia* Data Release 2 (Gaia Collaboration et al., 2018) if available, and the *Hipparcos* mission (van Leeuwen, 2007), along with the spectral types, the values of T_{eff}, log g, ξ, [Fe/H], and the stellar projected rotational velocities, $v \sin i$, found in the literature for the selected sample. For the *Gaia* benchmark stars, we adopted the parameters from Jofré et al. (2014) and Heiter et al. (2015a), with updated values from Jofré et al. (2018). For the remaining stars, we tabulate the stellar parameters from the most recent references found in the PASTEL catalogue (Soubiran et al., 2016).

Following Tabernero et al. (2019), we divided the parameter space into four different regions in terms of log g and [M/H], using [Fe/H] as a proxy of stellar metallicity, in order to simplify our search for iron lines in the CARMENES spectra, as explained in Sect. 3.3.2. We thus made a distinction between the dwarf regime, log g ≥ 4.00, and the giant regime, log g < 4.00, and between metal-rich
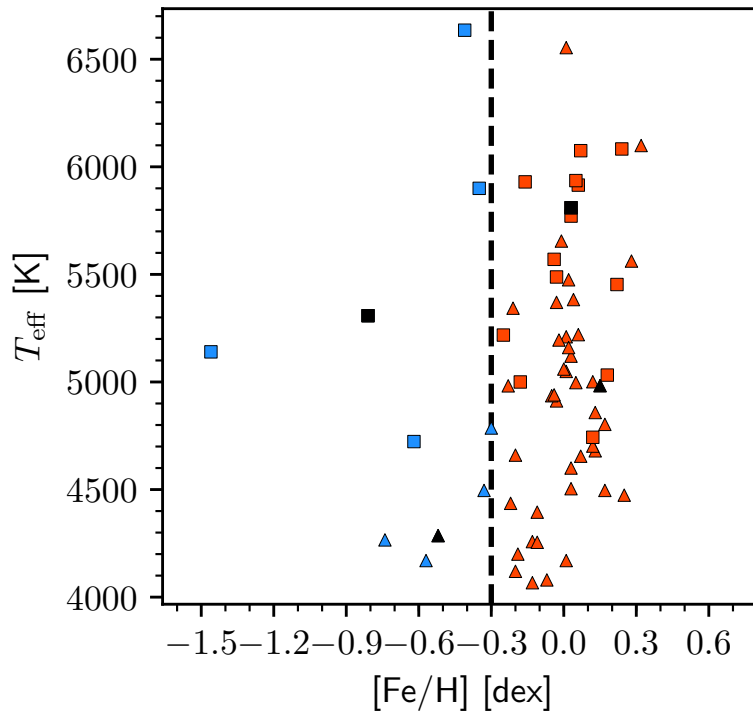
FIGURE 3.2. Same as Fig. 3.1, but for literature values of T_{eff} versus [Fe/H] in the sample. Only the boundary at [Fe/H] = −0.3 dex is shown.

stars, [Fe/H] > −0.30, and metal-poor stars, [Fe/H] ≤ −0.30. We dubbed the four resulting line lists metal-rich dwarfs (MRDs), metal-poor dwarfs (MPDs), metal-rich giants (MRGs), and metal-poor giants (MPGs). We selected the following *Gaia* benchmark stars, all of which were observed with CARMENES, as a reference for the assembly of the corresponding Fe I and Fe II line lists: 18 Sco for the MRD, μ Cas for the MPD, ϵ Vir for the MRG, and Arcturus for the MPG. We show this division of the parameter space in Figs. 3.1 and 3.2.

3.3 Analysis

3.3.1 Data processing

The 65 pairs of VIS and NIR spectra were taken in service mode between 2016 March and 2016 June with the two CARMENES channels operating simultaneously. In general, exposure times were manually adjusted to reach an S/N between 100 and 300 in the *J* band. The observations were carried out without the simultaneous wavelength calibration of the Fabry-Pérot etalons since there was no particular interest in precise radial velocity determinations (i.e. better than ~ 20 m s^{-1}) for these stars.

The spectra were taken in 'target + sky' mode, i.e. the stars were observed in fibre A and the sky in fibre B. Both fibres are identical but fibre B is located at 88 arcsec to the east. Star and sky spectra are available through the Calar Alto archive. In our work, we did not subtract the corresponding sky spectrum to each star spectrum, as this is an ongoing analysis (Nagel et al. in prep.).

The raw spectra were reduced with the CARACAL pipeline (Zechmeister et al., 2014; Caballero et al., 2016b), which is based on the IDL REDUCE package (Piskunov & Valenti, 2002).

CARACAL generates one fully reduced, wavelength-calibrated, one-dimensional spectrum of the individual spectral orders. Fig. 3.3 displays the CARACAL S/N of the four reference spectra as a function of the diffraction order *m*. We estimated the global S/N of the spectra with the integrated Spectroscopic framework (iSpec, see Blanco-Cuaresma et al., 2014b) in terms of the median of the flux values divided by their corresponding flux errors. The global S/N of the selected spectra can also be found in Table B.2.

Next, we employed a wavelength grid to merge the spectral orders of both channels into one single spectrum. The wavelength grid, which is evenly spaced on a logarithmic scale, mirrors the natural wavelength spacing of the CARMENES spectrographs across the orders. In Fig. 3.4, we show the normalised, merged spectra of the four stars taken as a reference in this work.

Since the CARMENES instrument operates in vacuum, we performed a vacuum-to-air wavelength conversion of the order-merged, channel-merged, CARMENES spectra to provide the wavelengths of the Fe I and Fe II lines on an air scale, following the International Astronomical Union standard (Morton, 2000):

$$\lambda_{\text{air}} = \frac{\lambda_{\text{vacuum}}}{n}, \tag{3.1}$$

where *n* is the refraction index, which is given by the following expression:

$$n = 1 + 8.34254 \times 10^{-5} + \frac{2.406147 \times 10^{-2}}{130 - s^2} + \frac{1.5998 \times 10^{-4}}{38.9 - s^2}, \tag{3.2}$$

where $s = 10^4/\lambda_{\text{vacuum}}$, with λ_{vacuum} in Å.

After the vacuum-to-air wavelength conversion, we accounted for the barycentric velocity of the observatory at the time of observations. We then computed the radial velocities with iSpec by means of the cross-correlation function between the observed CARMENES spectra and a template spectrum provided by iSpec in the following way. In the dwarf regime, we set as the template a solar spectrum based on data from the NARVAL (Aurière, 2003) and HARPS (Mayor et al., 2003) instruments (see Blanco-Cuaresma et al., 2014b) covering the overlap region with CARMENES, i.e. the 5200–10480 Å range. Likewise, in the giant regime we set as the template spectrum an atlas of Arcturus covering the 5200–9260 Å range (Hinkle et al., 2000). Both template spectra were corrected from telluric absorption features, which makes them suitable for cross correlation. This allowed us to correct the spectra from the corresponding Doppler shift. In Fig. 3.5, we compare the radial velocities thus computed against the literature values. Four stars exhibit a difference in radial velocity greater than 1 km s^{-1} compared to literature values. These are all single-lined (SB1) spectroscopic binaries: μ Cas (Worek & Beardsley, 1977), α CMi (Girardi et al., 2000), α UMa (Spencer Jones & Furner, 1937), and ζ Her (Scarfe et al., 1983). The radial velocities of our sample can also be found in Table B.2. The average difference in the computed radial velocities of the sample with respect to the literature values is 0.09 ± 0.64 km s^{-1}.

3.3.2 Fe I and Fe II line selections

We requested four line lists from the Vienna Atomic Line Database (VALD3, Piskunov et al., 1995; Kupka et al., 2000, 1999; Ryabchikova et al., 2015), corresponding each to one of our four reference spectra. We used the option `Extract stellar` available at the VALD3 website[2], with a wavelength range from 5300 to 17100 Å, a minimum line depth of 5 per cent with respect to the continuum flux, and the corresponding input stellar parameters found in Table B.1. We excluded the wavelength range 5200–5300 Å from this search because of the low S/N of the CARMENES spectra in this region.

---

[2]http://vald.astro.uu.se
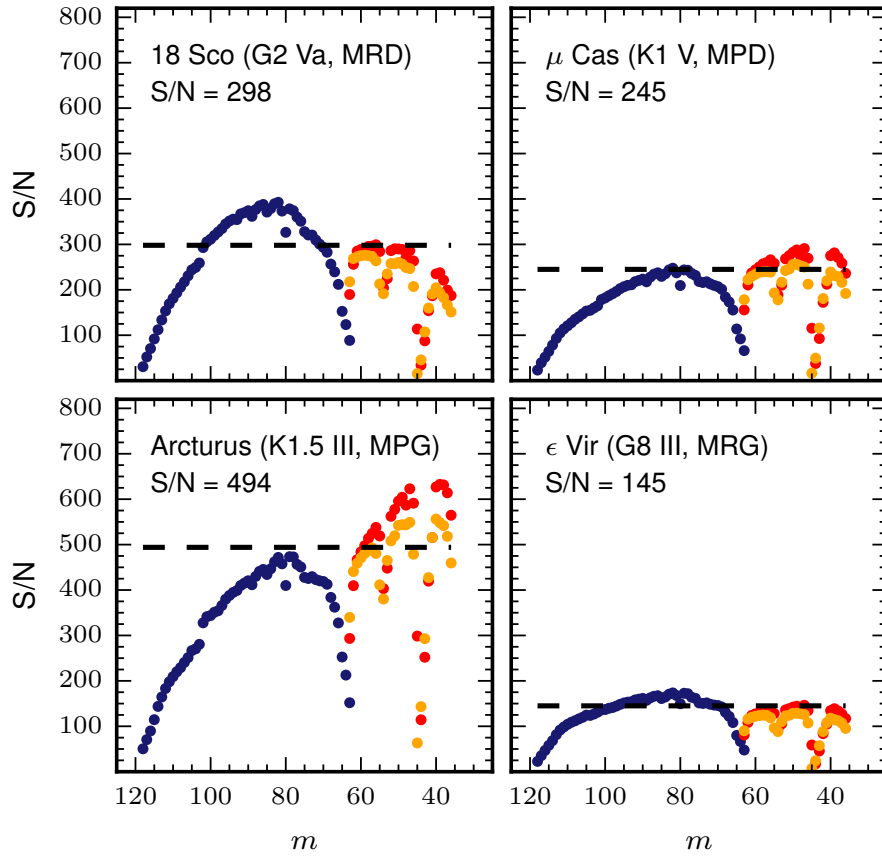
FIGURE 3.3. CARACAL S/N of the CARMENES spectra of the reference stars (18 Sco, μ Cas, ϵ Vir, and Arcturus) as a function of the spectral order m. The blue circles are the orders in the VIS channel, while the orange and red circles are the two HgCdTe array detectors of the NIR channel. The dashed black lines mark the global S/N estimation given by iSpec.

TABLE 3.1. Number of Fe I and Fe II lines reported in this work, Sousa et al. (2008, Sou08), Andreasen et al. (2016, And16), and Tabernero et al. (2019, Tab19) from 5300 to 17100 Å.

Reference	Line list/region	#lines	
		Fe I	Fe II
This work	MRD	386	16
This work	MPD	295	9
This work	MRG	306	13
This work	MPG	379	4
This work	CARMENES VIS channel	437	21
This work	CARMENES NIR channel	216	2
This work	Globally	653	23
Tab19	MRD	112	8
Tab19	MPD	82	8
Tab19	MRG	72	7
Tab19	MPG	95	5
Tab19	Globally	175	14
Sou08	...	172	19
And16	...	272	12
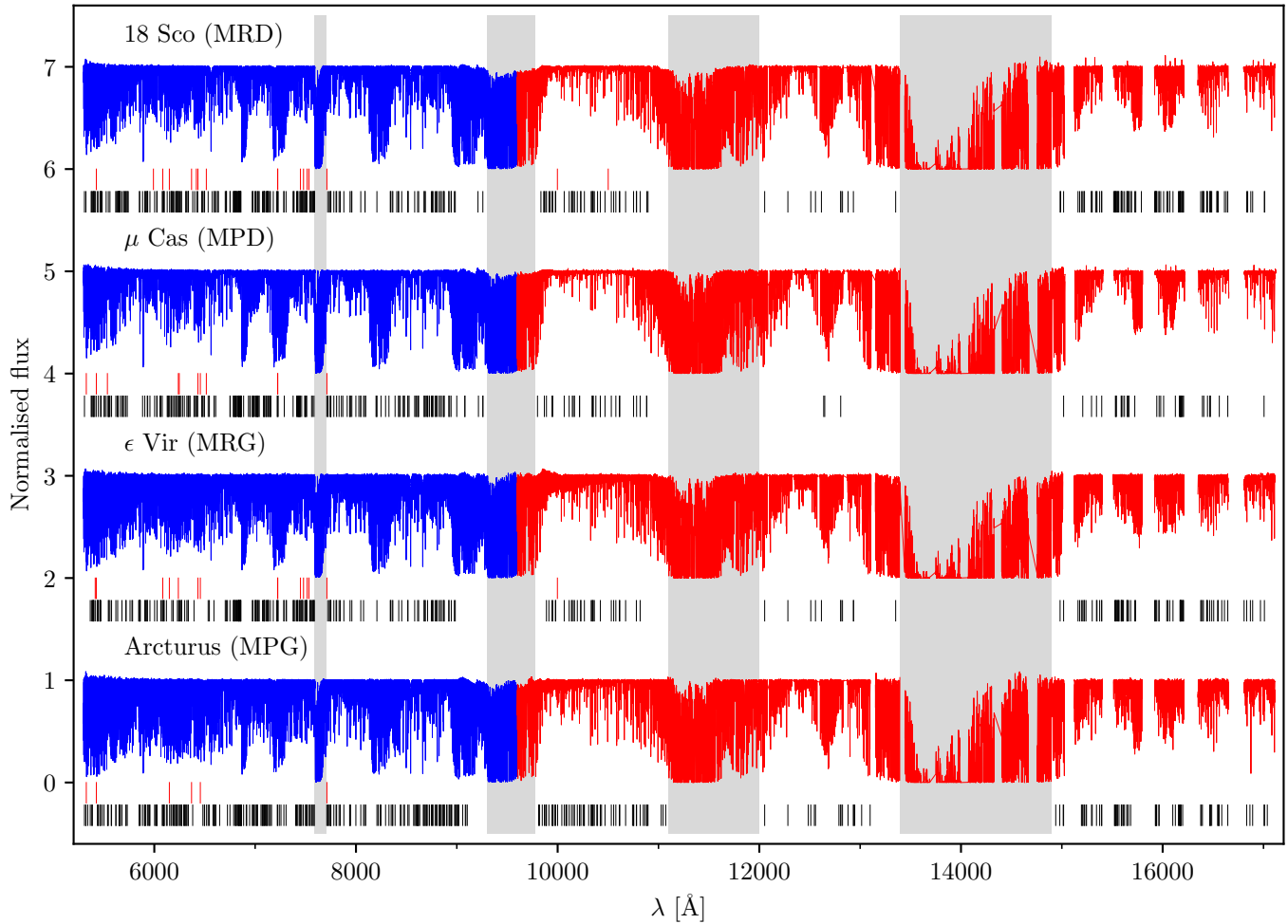
FIGURE 3.4. Distribution of the selected Fe I and Fe II absorption lines in the reference spectra. The Fe I and Fe II lines are shown as black and pink vertical lines, respectively, below the spectra. The VIS and NIR channels of the CARMENES instrument are shown in blue and red, respectively. The grey shaded areas show the regions severely affected by telluric absorption.

Because of its user-friendly interface, we used iSpec to select the Fe I and Fe II spectral lines by visually projecting the VALD3 line list files on to the corresponding processed reference spectra. We rejected Fe I and Fe II lines that showed spectral blending with close atomic and molecular lines. Since telluric lines are ubiquitous in the near-infrared and at the red end of the optical (see e.g. Reiners et al., 2018), we computed a synthetic transmission spectrum via the telluric-correction tool `molecfit` (Kausch et al., 2015; Smette et al., 2015), which makes use of the line-by-line radiative transfer model (LBLRTM, Clough et al., 2005) and the HITRAN molecular line database (Gordon et al., 2017), to model the Earth's atmospheric transmission spectrum. This allowed us to prevent wrong line identification throughout the visual inspection of the reference spectra. Further details on the telluric correction of the CARMENES spectra can be found in Passegger et al. (2019). A full description of the correction will appear in a forthcoming publication of the CARMENES series (Nagel et al. in prep.).

To expedite our analysis, we also looked for Fe I and Fe II line compilations found in the literature that overlap with the wavelength range covered by CARMENES. Since the careful analysis of the optical wavelength range up to ~6860 Å has already led to several line lists published in previous works that were specifically compiled to yield the best possible set of stellar atmospheric parameters for FGK-type stars (see e.g. Sousa et al., 2008; Jofré et al., 2014; Tabernero et al., 2019), we refrained
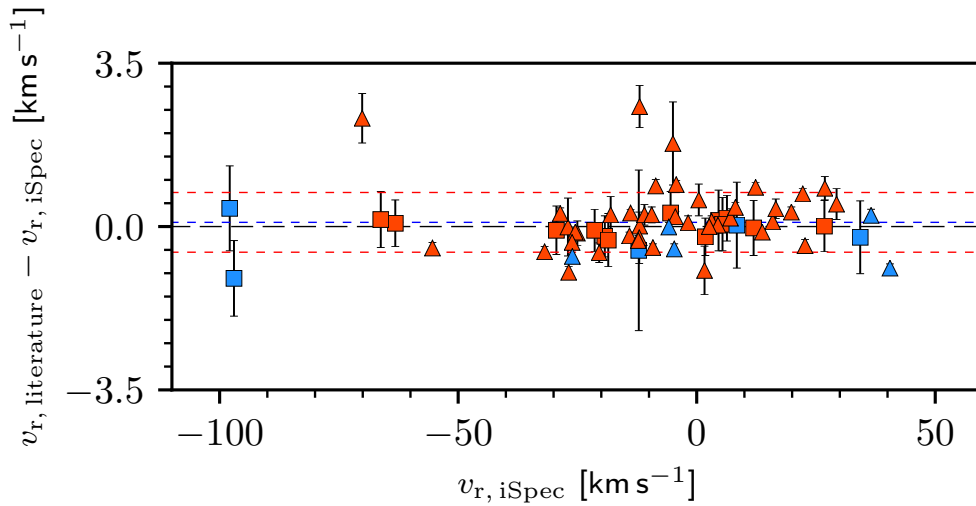
FIGURE 3.5. Comparison between the radial velocities v_r of the sample obtained with iSpec and the literature values. Symbols are the same as in Fig. 3.1. The dotted blue and red lines are the average difference and the corresponding 1σ dispersion, respectively.

from further refining the line selection in this window and adopted the iron lines given in Sousa et al. (2008). As to the near-infrared region, we checked our iron line selections from 10000 to 17100 Å against the ones tabulated in Andreasen et al. (2016). Despite our careful search for Fe II in the NIR region, we only found one Fe II line at $\lambda = 10501.503$ Å. Finally, iron lines found in the region 6800–10000 Å were not compared with the literature due to the lack of line compilations in this spectral window. In Table 3.1 we show a summary of the number of iron lines listed in this work on a global and per-line list basis, i.e. MRD, MPD, MRG, and MPG, in comparison with those tabulated in Sousa et al. (2008) and Andreasen et al. (2016) in the wavelength region covered by CARMENES.

Since we assembled the line lists considering four specific reference spectra, we removed the Fe I and Fe II line identifications that fall into any of the CARMENES inter- and intra-order gaps[3] as a consequence of the corresponding Doppler shift corrections in the remaining spectra of the sample.

In Fig. 3.4, we show the distribution of the selected Fe I and Fe II lines in the reference spectra. In addition, in Fig. B.1 we give a close-up view of the spectrum of the reference, solar-type star 18 Sco along with the line selections. We give the central wavelength in air, λ_{air}, the excitation potential, χ, and the oscillator strength, $\log gf$, of the selected Fe I and Fe II lines in Tables B.4 and B.5, respectively.

3.3.3 EW measurements

We computed the EWs by fitting Gaussian profiles to the absorption lines[4], as shown in Fig 3.6. First, we selected a region approximately 6 Å wide centred at the selected absorption line, l, and performed a continuum normalisation on the spectra following Sousa et al. (2007). Specifically, we fitted a third-degree polynomial to the data, selecting only the points that lie within `rejt` times the polynomial, where `rejt` $= 1 - 1/(S/N)$, and S/N is the signal-to-noise ratio of the region. We then identified the absorption lines present in the spectra by finding the points where the first derivative of the data was zero, and the second derivative was positive. Finally, we fitted Gaussian profiles to the lines detected, and integrated the profile corresponding to the selected line l to obtain the EW.

---

[3]http://carmenes.caha.es/ext/instrument/
[4]The code is available at: https://github.com/msotov/EWComputation.
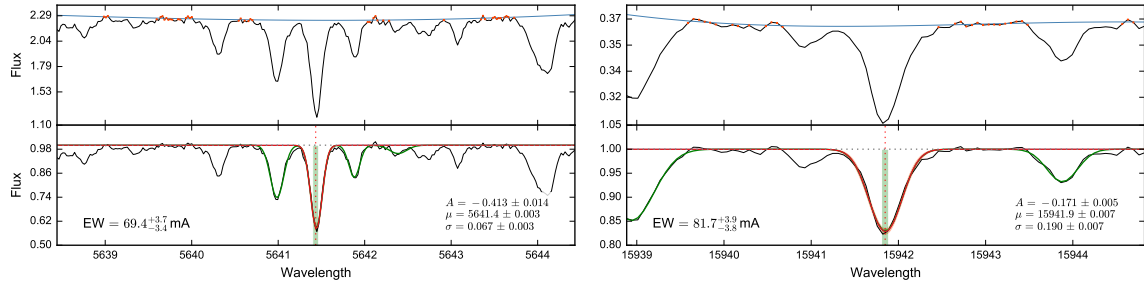
FIGURE 3.6. EW measurements of two Fe I lines in the spectrum of 18 Sco, at 5641.434 Å (left) and 12824.859 Å (right). The upper panels illustrate the continuum determination, where the points used for the final polynomial fit are highlighted in red. The bottom panels show the full fit performed for all detected lines, shown in green, and the Gaussian fit of the selected line, shown in red, parametrised by the central intensity in normalised units, A, the central wavelength in Å, μ, and the Gaussian dispersion, σ. The shaded red area depicts the 1σ confidence intervals of the Gaussian fit, and the green square, the EW estimation, as explained in the text.

The uncertainty in the EW was estimated by changing the Gaussian parameter estimates within 1σ of their uncertainty for a total of 1000 iterations, and looking at the EW distribution.

As in Tabernero et al. (2019), we only considered lines with $10\,\text{mÅ} < \text{EW} < 120\,\text{mÅ}$ for all stars in the sample to avoid problems with line profiles of very intense lines and potentially bad EW measurements of extremely weak lines.

3.3.4   STEPAR

The STEPAR code[5] is a Python implementation of the EW method specifically designed for the automated and simultaneous computation of the stellar atmospheric parameters of FGK-type stars, namely T_{eff}, $\log g$, [Fe/H], and ξ. STEPAR is one of the 13 pipelines in the *Gaia*-ESO Survey used in the analysis of UVES U580 spectra of late-type, low-mass stars. A full description of its workflow and performance can be found in Tabernero et al. (2019). STEPAR is an iterative code that derives the stellar parameters and their associated uncertainties by imposing both excitation and ionisation equilibrium conditions on a set of Fe I and Fe II lines, using the 2017 version of the MOOG[6] code (Sneden, 1973) and a grid of plane-parallel and spherical MARCS[7] model atmospheres (Gustafsson et al., 2008).

For any given MOOG-compliant EW input file comprised of a significant number of Fe I and Fe II lines, STEPAR follows a Downhill Simplex minimisation algorithm (Press et al., 2002) across the parameter space in order to find the stellar atmospheric parameters that best reproduce the observed EWs. The code takes $T_{\text{eff}} = 5777$ K, $\log g = 4.44$ dex, and $\xi = 1.0$ km s^{-1} as the initial input values.

If we let $\epsilon(\text{Fe})$ represent the iron abundance retrieved from any given Fe line and χ be the excitation potential of the line, STEPAR iterates until the slopes of χ versus $\log \epsilon(\text{Fe\,I})$ and $\log (\text{EW}/\lambda)$ versus $\log \epsilon(\text{Fe\,I})$ are zero, i.e. the iron atoms are in excitation equilibrium. It also imposes ionisation equilibrium so that $\log \epsilon(\text{Fe\,I}) = \log \epsilon(\text{Fe\,II})$. Throughout this iterative process, the code verifies that the average [Fe/H] in the MOOG output is always compatible with the iron abundance of the input atmospheric model. Next, STEPAR performs an individual σ clipping on the Fe I and Fe II lines to remove the ones that imply an iron abundance, $\log \epsilon(\text{Fe})$, that exceeds the 3σ limit with respect to the median abundance of all lines. After this step, STEPAR restarts the minimisation algorithm with the remaining Fe I and Fe II lines, taking as initial input values the parameters computed in the first

---

[5]STEPAR is available at: https://github.com/hmtabernero/StePar.
[6]https://www.as.utexas.edu/~chris/moog.html
[7]http://marcs.astro.uu.se

run. SтеРаr computes the uncertainties in the stellar atmospheric parameters following the sequence: $\delta\xi$, δT_{eff}, $\delta \log g$, and δ[Fe/H]. This computation relies on the retrieved Fe I and Fe II abundances and the uncertainties in the slopes that define the equilibria conditions. The code also propagates the uncertainties following the previous sequence. For example, the uncertainty in [Fe/H] is a quadrature between the standard deviation of the Fe I and Fe II abundances and the propagated uncertainties in the remaining stellar parameters. Further details on the computation of the uncertainties can be found in Tabernero et al. (2019).

3.4   Results and discussion

In Table B.2 we give the stellar atmospheric parameters of the sample computed with SтеРаr. These were obtained after matching the corresponding Fe I and Fe II line lists to the stars according to their reference parameters reported in Table B.1.

We also performed the analysis of the sample with the EW method taking into account only the Fe I and Fe II lines found in the optical region covered by the VIS channel of the CARMENES instrument. The parameters thus obtained can be found in Table B.3. Unfortunately, we could not attempt to analyse the NIR in the same manner because of the scarcity of Fe II lines above 9600 Å.

In Fig. 3.7, we display a Kiel diagram, i.e. $\log g$ versus $\log T_{\text{eff}}$, of our sample as computed with SтеРаr, along with the Yale-Potsdam Stellar Isochrones (YaPSI, Spada et al., 2017) at solar metallicity, namely $Z = 0.016$. Overall, we found no disparity between our derived values and the region of the parameter space covered by the isochrones. As pointed out by Tabernero et al. (2019), SтеРаr returns slightly higher effective temperatures for F-type dwarfs. Five luminous, G-type, giant stars (β Dra, F Hya, ϵ Leo, 37 LMi, and ζ Mon) are located at an anomalous position in the Kiel diagram. According to Luck (2014), these stars are thought to be the evolved counterparts of early F- to B-type main-sequence stars that have reached the He-burning evolutionary stage.

In the cool regime, i.e. K-type stars, where stellar spectra become increasingly more crowded, the continuum placement is more uncertain, and the iron lines are subject to blending with other spectral features. On the other hand, sufficiently strong iron lines become increasingly scarce towards early F-type stars. This has a strong impact on the computed errors in the stellar atmospheric parameters, in particular the effective temperature, and the line-to-line scatter in [Fe/H], as shown in Fig. 3.8 and 3.9, respectively.
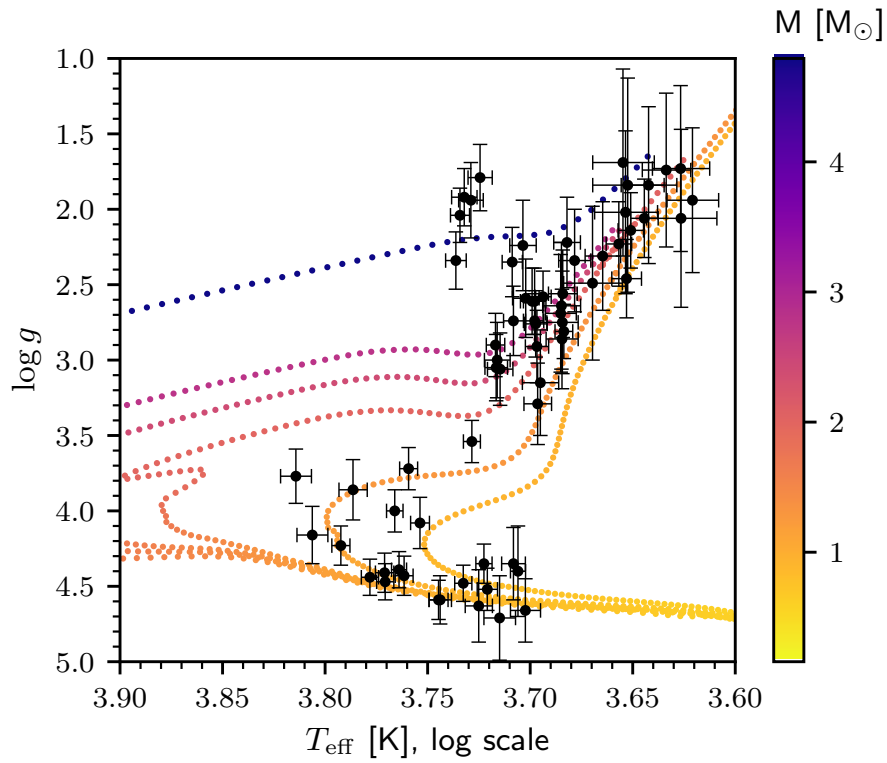
FIGURE 3.7. Kiel diagram (log g versus log $T_{\rm eff}$) of the sample along with the YaPSI isochrones at 0.1, 0.4, 0.6, 1, 4, and 13 Ga (for Z=0.016, see Spada et al. 2017).
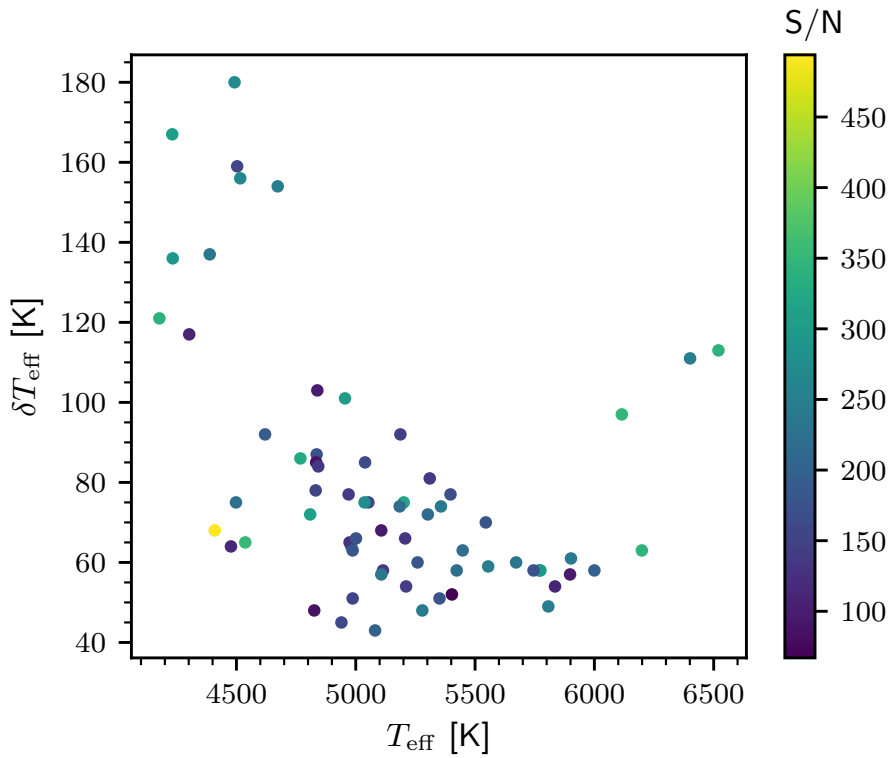
FIGURE 3.8. Uncertainties in $T_{\rm eff}$, $\delta T_{\rm eff}$, versus $T_{\rm eff}$ for our sample, as computed with STEPAR.
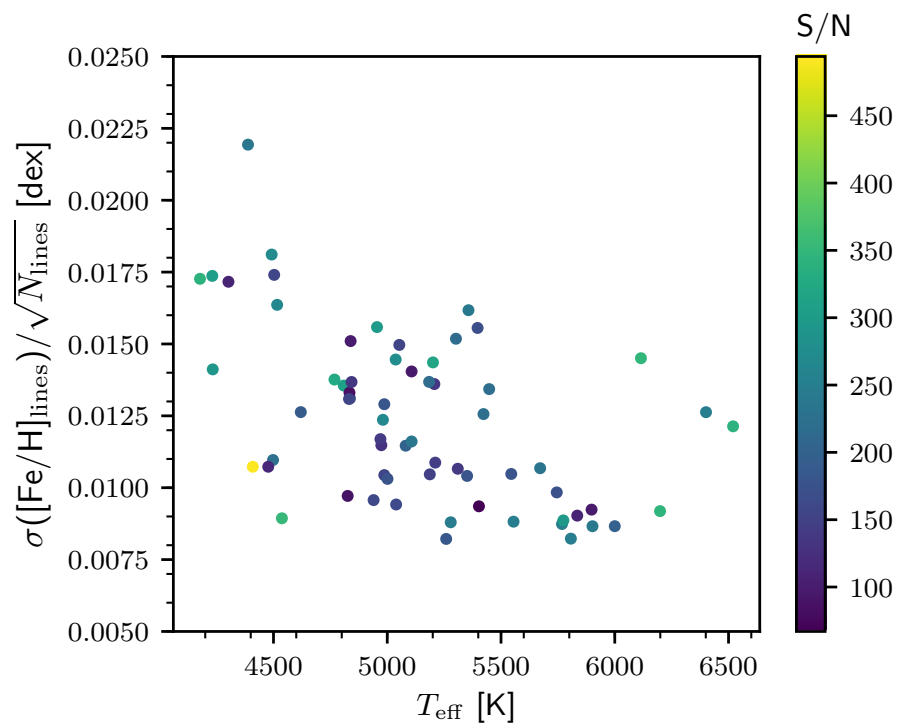
FIGURE 3.9. Line-to-line scatter in [Fe/H] versus $T_{\rm eff}$ and S/N in the sample.
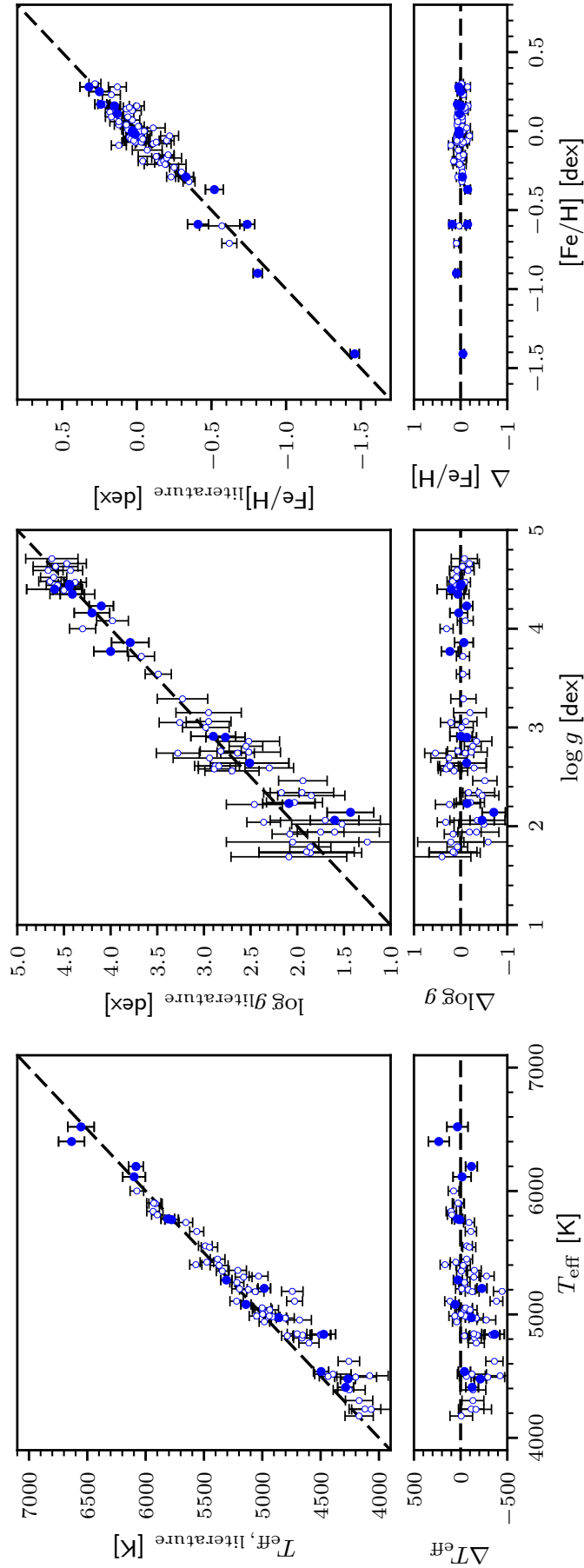
FIGURE 3.10. Comparison between the stellar atmospheric parameters obtained with STEPAR including the VIS and NIR channels of CARMENES and the literature values. The blue filled circles are the *Gaia* benchmark stars in our sample. The remaining stars in the sample are shown with the blue open circles. The dashed black lines indicate the one-to-one relationship. From left to right: T_{eff}, $\log g$, and [Fe/H].
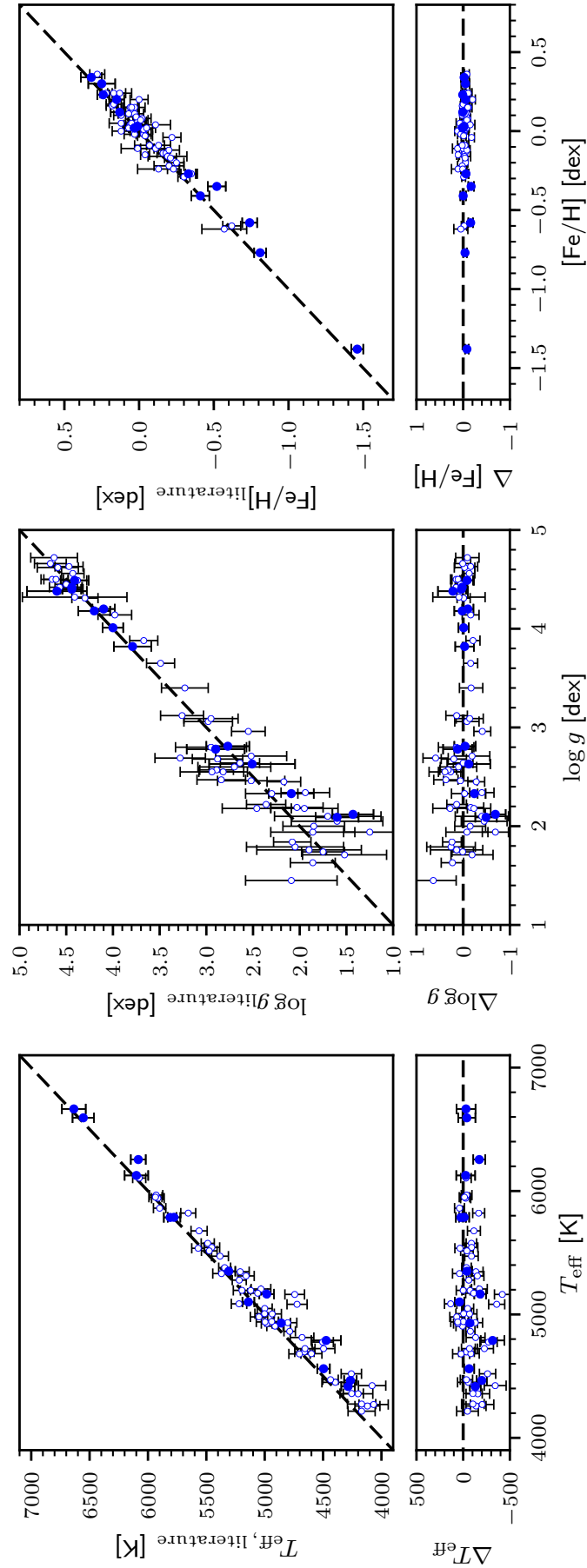
FIGURE 3.11. Same as Fig. 3.10 but restricting the analysis to the Fe I and Fe II lines found in the optical wavelength region covered by the VIS channel of CARMENES.

TABLE 3.2. Summary of the Monte Carlo simulations carried out on the $T_{\rm eff}$, log g, and [Fe/H] values of the sample as computed with STEPAR. We show the average difference on each parameter and the values of the Pearson ($r_{\rm p}$) and Spearman ($r_{\rm s}$) correlation coefficients.

Parameter	Difference	$r_{\rm p}$	$r_{\rm s}$
VIS and NIR channels			
$T_{\rm eff}$ [K]	-100 ± 166	0.40 ± 0.07	0.41 ± 0.07
log g [dex]	-0.03 ± 0.38	0.10 ± 0.10	0.07 ± 0.11
[Fe/H] [dex]	0.00 ± 0.11	-0.09 ± 0.06	-0.12 ± 0.07
VIS channel only			
$T_{\rm eff}$ [K]	-92 ± 135	0.21 ± 0.08	0.21 ± 0.09
log g [dex]	-0.01 ± 0.38	-0.01 ± 0.10	0.00 ± 0.10
[Fe/H] [dex]	-0.04 ± 0.10	-0.01 ± 0.08	-0.07 ± 0.09

In Figs. 3.10 and 3.11, we compare the stellar atmospheric parameters computed with STEPAR with values from the literature (McWilliam, 1990; Heiter & Luck, 2003; Allende Prieto et al., 2004; Valenti & Fischer, 2005; Hekker & Meléndez, 2007; Liu et al., 2007; Sousa et al., 2008; Takeda et al., 2008; Lyubimkov et al., 2010; Wu et al., 2011; Thygesen et al., 2012; Santos et al., 2013; Jofré et al., 2014, 2015a; Luck, 2014; Morel et al., 2014; da Silva et al., 2015; Jofré et al., 2018), taking into account the VIS and NIR channels simultaneously, and only the VIS channel, respectively. To explore possible sources of potential systematic trends or offsets, we followed the Monte Carlo method implemented in Tabernero et al. (2018). We generated 10 000 synthetic samples based on our derived stellar atmospheric parameters. We computed all data points in each of these artificial samples by means of a normal distribution centred at the original measurements, and took the uncertainties in each parameter as the width of the distribution. The summary of the Monte Carlo simulations can be found in Table 3.2. We computed the Pearson and Spearman correlation coefficients, which quantify the degree of correlation between any two given variables. We found a significant correlation in the differences between our own $T_{\rm eff}$ values and the literature versus the literature values. However, no such correlation was found in the derived log g and [Fe/H] values.

At first glance, it seems that our temperature scale has an intrinsic systematic error with respect to the literature values. The offset appears to be linked to the fact that we now include the NIR channel, given that the correlation diminishes when we restrict the analysis to the iron lines found in the VIS channel. Although the STEPAR code could be thought to be the underlying reason for this correlation, we are not comparing the same temperature scale. In other words, we now take into account iron absorption lines in a wavelength region that is different from most studies found in the literature. In addition, this offset is more noticeable for the coolest stars. The former result could arise from the fact that the NIR lines are more sensitive to the effective temperature than the optical lines, at least for the cool stars. In other words, although the inclusion of the NIR in the analysis does not bring extreme differences of the derived stellar parameters with respect to the analysis using the optical range, it seems to reveal a deeper $T_{\rm eff}$ scale as suggested by the meaningful correlation found in Table 3.2 as well as Figs. 3.10 and 3.11.

In Fig. 3.12, we show the values of log g derived with STEPAR against those obtained adopting the distances from *Gaia* DR2 (Gaia Collaboration et al., 2018), if available, and the *Hipparcos* mission (van Leeuwen, 2007). We computed the latter log g values by means of the PARAM web interface[8] (da Silva et al., 2006; Rodrigues et al., 2014, 2017), which employs a Bayesian approach to derive the stellar parameters, including stellar age, mass, and radius. The log g values obtained with PARAM can be found in Tables B.2 and B.3. Following the Monte Carlo method described above, we found a systematic offset of 0.15 ± 0.38 dex. The Pearson and Spearman correlation coefficients, which are

---

[8] http://stev.oapd.inaf.it/cgi-bin/param
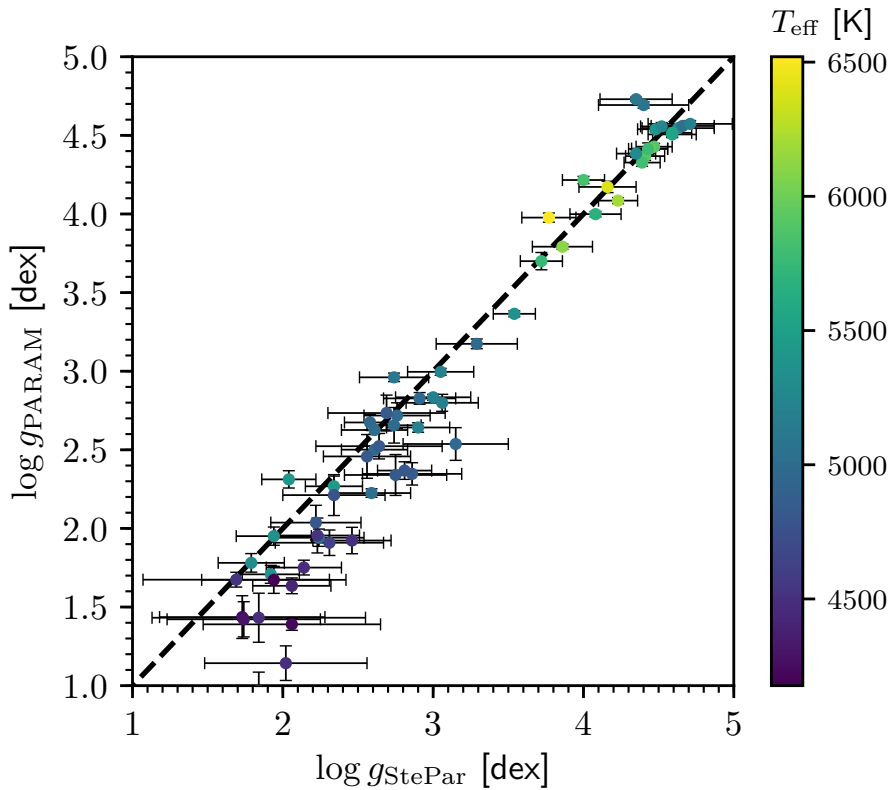
FIGURE 3.12. Surface gravities, log g, derived for the sample with STEPAR versus those obtained with the code PARAM, adopting the distances from *Gaia* DR2.

$r_{\rm p} = -0.302 \pm 0.093$ and $r_{\rm s} = 0.259 \pm 0.104$, respectively, reveal a correlation of around 9 per cent, which is slightly lower than previous works (see e.g. Tabernero et al., 2017).

Regarding the micro-turbulent velocity, Fig. 3.13 shows the values of ξ obtained with STEPAR against the literature. Our derived values for ξ are compatible with the literature values to a large extent. However, six stars (i.e. β Dra, F Hya, ζ Mon, σ Oph, θ Her, and HD 77912), with computed ξ values larger than 3 km s^{-1}, show larger deviations with respect to the literature, which can be as large as 1.6 km s^{-1}, as in the case of the star ζ Mon. In addition, we retrieved a significantly lower ξ value for the star υ Boo compared to the literature. Although ξ and [Fe/H] are thought to be partially degenerate (Valenti & Fischer, 2005), we fail to identify the impact that such high or low ξ values have on [Fe/H] for these stars in our analysis. For example, a difference of 1.6 km s^{-1} in ξ for the star ζ Mon leads to a difference of only 0.07 dex in [Fe/H] between the literature and the analysis with STEPAR, and both computed and literature values are compatible within error bars.

A closer look at the comparison between our parameter determinations and the *Gaia* benchmark star parameters from Heiter et al. (2015a), with updated values from Jofré et al. (2018), can be found in Fig. 3.14. We find good agreement between our derived values and the fundamental $T_{\rm eff}$ and log g, i.e. derived from the fundamental relations $L = 4\pi R^2 \sigma T_{\rm eff}^4$ and $g = GM/R^2$, respectively, by means of specific information that is available for these stars, such as the parallax, the angular diameter, and the bolometric flux. Nonetheless, we note four outliers in $T_{\rm eff}$ ($\Delta T_{\rm eff} > 200$ K) and two in log g (Δ log $g > 0.25$ dex). Among the outliers in log g are Arcturus and 7 Psc. According to Heiter et al. (2015a), the log g value of Arcturus remains uncertain, with literature values ranging from 1.4 up to 2.0 dex, while both the $T_{\rm eff}$ and log g values for the star 7 Psc are, in fact, not recommended for use as reference values. Among the outliers in $T_{\rm eff}$ are the stars HD 49933, μ Leo, ϵ Vir, and 7 Psc. As stated by Heiter et al. (2015a), the fundamental $T_{\rm eff}$ value for the stars ϵ Vir and μ Leo is significantly
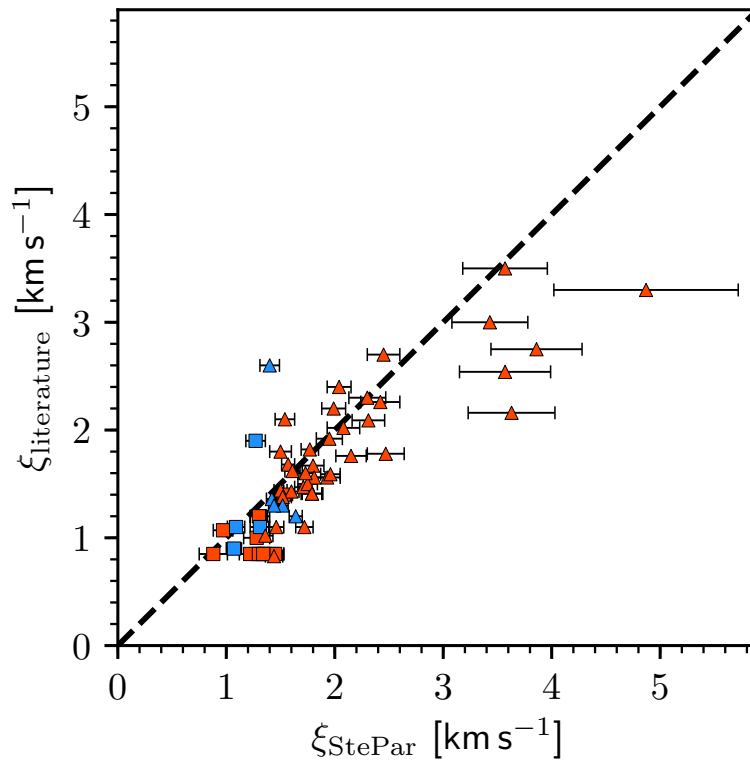
FIGURE 3.13. Micro-turbulent velocity derived for the sample with STEPAR, ξ_{StePar}, versus literature values. Symbols are the same as in Fig. 3.1.
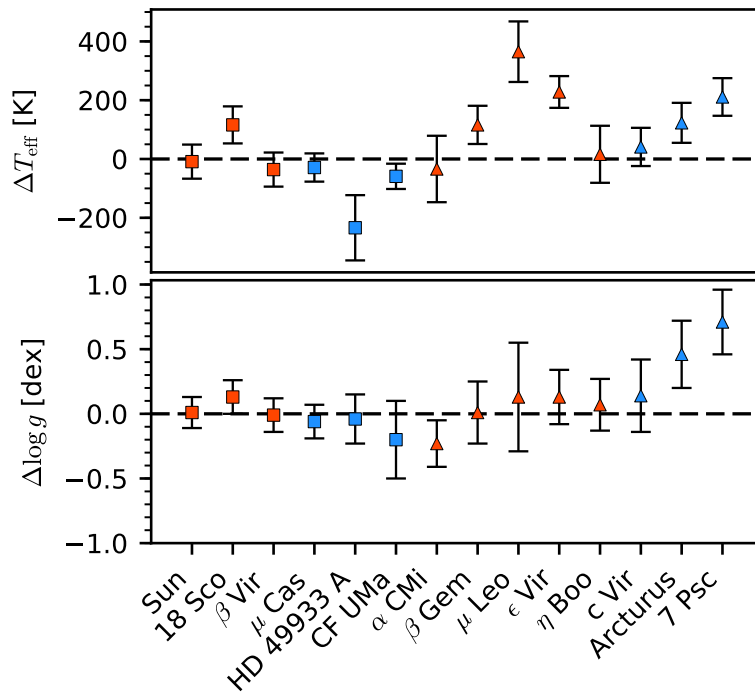
FIGURE 3.14. Differences in T_{eff} and $\log g$ between this work and Heiter et al. (2015a), with updated values from Jofré et al. (2018), for the *Gaia* benchmark stars in our sample. Symbols are the same as in Fig. 3.1.

lower (∼ 3 per cent) than the value derived in spectroscopic studies. Lastly, at the hot regime, the typical spectroscopic T_{eff} values computed for the star HD 49933 are generally larger.

Lastly, in Fig. 3.15, we show the final Fe I and Fe II abundances versus the excitation potential and the reduced EW of the lines, for the four reference CARMENES spectra (18 Sco, μ Cas, ϵ Vir, and Arcturus).

3.5   Conclusions

In this work, we have expanded previous optical Fe I and Fe II line lists into the wavelength range covered by CARMENES, i.e. from 5300 to 17100 Å. The line lists are suited for FGK-type stars and relate to MRDs, MPDs, MRGs, and MPGs. For the first time, we provide Fe I and Fe II lines in the wavelength region between 6800 Å and 10000 Å. Altogether, these new line lists contain 653 Fe I and 23 Fe II lines, of which 351 and eight are new additions to the line lists compiled in Tabernero et al. (2019), respectively. This implies more than doubling the number of Fe I and Fe II lines useful for abundance and radial-velocity analyses. The availability of these Fe I and Fe II line lists is also an asset for other new high-resolution near-infrared spectrographs such as SPIRou, GIANO, CRIRES+, IRD, HPF, and NIRPS that also provide wavelength coverage in the near-infrared wavelength region.

We have reported that the star c Gem (HD 62285) is a new SB2 system, as shown by the cross-correlation with an atlas spectrum of Arcturus.

In addition, we have computed an homogenised set of stellar atmospheric parameters for a sample of 65 FGK-type stars observed with CARMENES by means of the EW method. We made a comprehensive comparison of our T_{eff}, log g, and [Fe/H] values with those of virtually all relevant determinations of stellar atmospheric parameters of FGK-type stars. Our parameter determinations are in good agreement with the literature values in general, particularly with the region of the parameter space covered by the YaPSI isochrones (Spada et al., 2017) and the *Gaia* benchmark stars (Jofré et al., 2014, 2018; Heiter et al., 2015a). The scarcity of Fe II lines in the NIR wavelength range covered by CARMENES prevented us from performing the stellar parameter determinations using this spectral region alone. However, when using both VIS and NIR CARMENES channel data, we found a broader T_{eff} scale that seems to be linked to a higher sensitivity to effective temperature of the iron lines found in the NIR region.

The line selections provided in this work will be useful for the spectroscopic analysis of any FGK-type star simultaneously observed in the optical and near-infrared wavelength regions. Finally, in a forthcoming publication we plan to expand optical line lists of additional chemical species into the NIR covered by CARMENES and thus assess the impact of the near-infrared wavelength region upon chemical abundance computations for FGK-type stars.

FIGURE 3.15. *From top to bottom:* line iron abundance retrieved by STEPAR for the final solution of the four reference stars: 18 Sco, μ Cas, ϵ Vir, and Arcturus. $\log \epsilon(\text{Fe})$ stands for the Fe abundance returned by the Fe lines, while $\log(\text{EW}/\lambda)$ is their reduced EWs. The open black dots represent Fe I lines, whereas the pink dots are Fe II lines. The dashed black lines represent the least-squares fit to the data points.

4 Stellar atmospheric parameters of target M dwarfs with spectral synthesis

This chapter corresponds to the analysis of the CARMENES GTO sample of M dwarfs. The paper was accepted for publication on the 7th of October 2021 in the journal *Astronomy & Astrophysics* under the title **The CARMENES search for exoplanets around M dwarfs. Stellar atmospheric parameters of target stars with SteParSyn**, Marfil, E., Tabernero, H. M., Montes, D. et al. (2021), A&A, 656, A162,

The CARMENES search for exoplanets around M dwarfs.
Stellar atmospheric parameters of target stars with SteParSyn

E. Marfil[1,2], H. M. Tabernero[3,4], D. Montes[1], J. A. Caballero[2], F. J. Lázaro[1],
J. I. González Hernández[5,6], E. Nagel[7,8], V. M. Passegger[7,9], A. Schweitzer[7], I. Ribas[10,11],
A. Reiners[12], A. Quirrenbach[13], P. J. Amado[14], C. Cifuentes[2], M. Cortés-Contreras[2], S. Dreizler[12],
C. Duque-Arribas[1], D. Galadí-Enríquez[15], Th. Henning[16], S. V. Jeffers[17,12], A. Kaminski[13],
M. Kürster[16], M. Lafarga[10,11,18], Á. López-Gallifa[1], J. C. Morales[10,11], Y. Shan[12], and
M. Zechmeister[12]

[1] Departamento de Física de la Tierra y Astrofísica & IPARCOS-UCM (Instituto de Física de Partículas y del Cosmos de la UCM), Facultad de Ciencias Físicas, Universidad Complutense de Madrid, 28040 Madrid, Spain
e-mail: emigom01@ucm.es

[2] Centro de Astrobiología (CSIC-INTA), ESAC, Camino Bajo del Castillo s/n, 28691 Villanueva de la Cañada, Madrid, Spain

[3] Centro de Astrobiología (CSIC-INTA), Carretera a Ajalvir km 4, 28850 Torrejón de Ardoz, Madrid, Spain

[4] Instituto de Astrofísica e Ciências do Espaço, Universidade do Porto, CAUP, Rua das Estrelas, 4150-762 Porto, Portugal

[5] Instituto de Astrofísica de Canarias, c/ vía Láctea s/n, 38205 La Laguna, Tenerife, Spain

[6] Universidad de La Laguna, Departamento de Astrofísica, 38206 La Laguna, Tenerife, Spain

[7] Hamburger Sternwarte, Gojenbergsweg 112, 21029 Hamburg, Germany

[8] Thüringer Landessternwarte Tautenburg, Sternwarte 5, 07778 Tautenburg, Germany

[9] Homer L. Dodge Department of Physics and Astronomy, University of Oklahoma, 440 West Brooks Street, Norman, OK-73019 Oklahoma, United States of America

[10] Institut de Ciències de l'Espai (CSIC), Campus UAB, c/ de Can Magrans s/n, 08193 Cerdanyola del Vallès, Spain

[11] Institut d'Estudis Espacials de Catalunya (IEEC), c/ Gran Capità 2-4, 08034 Barcelona, Spain

[12] Institut für Astrophysik, Georg-August-Universität-Göttingen, Friedrich-Hund-Platz 1, 37077 Göttingen, Germany

[13] Landessternwarte, Zentrum für Astronomie der Universität Heidelberg, Königstuhl 12, 69117 Heidelberg, Germany

[14] Instituto de Astrofísica de Andalucía (IAA-CSIC), Glorieta de la Astronomía s/n, 18008 Granada, Spain

[15] Observatorio de Calar Alto, Sierra de los Filabres, 04550 Gérgal, Almería, Spain

[16] Max-Planck-Institut für Astronomie, Königstuhl 17, 69117 Heidelberg, Germany

[17] Max-Planck-Institut für Sonnensystemforschung, Justus-von-Liebig-Weg 3, 37077 Göttingen, Germany

[18] Department of Physics, University of Warwick, Gibbet Hill Road, Coventry CV4 7AL, United Kingdom

ABSTRACT

We determined effective temperatures, surface gravities, and metallicities for a sample of 343 M dwarfs observed with CARMENES, the double-channel, high-resolution spectrograph installed at the 3.5 m telescope at Calar Alto Observatory. We employed SteParSyn, a Bayesian spectral synthesis implementation particularly designed to infer the stellar atmospheric parameters of late-type stars following a Markov chain Monte Carlo approach. We made use of the BT-Settl model atmospheres and the radiative transfer code Turbospectrum to compute a grid of synthetic spectra around 75 magnetically insensitive Fe I and Ti I lines plus the TiO γ and ϵ bands. To avoid any potential degeneracy in the parameter space, we imposed Bayesian priors on $T_{\rm eff}$ and $\log g$ based on the comprehensive, multi-band photometric data available for the sample. We find that this methodology is suitable down to M7.0 V, where refractory metals such as Ti are expected to condense in the stellar photospheres. The derived $T_{\rm eff}$, $\log g$, and [Fe/H] range from 3000 to 4200 K, 4.5 to 5.3 dex, and -0.7 to 0.2 dex, respectively. Although our $T_{\rm eff}$ scale is in good agreement with the literature, we report large discrepancies in the [Fe/H] scales, which might arise from the different methodologies and sets of lines considered. However, our [Fe/H] is in agreement with the metallicity distribution of FGK-type stars in the solar neighbourhood and correlates well with the kinematic membership of the targets in the Galactic populations. Lastly, excellent agreement in $T_{\rm eff}$ is found for M dwarfs with interferometric angular diameter measurements as well as in the [Fe/H] between the components in the wide physical FGK+M and M+M systems included in our sample.

Key words. techniques: spectroscopic – stars: fundamental parameters – stars: late-type – stars: low-mass

4.1	Introduction

   M dwarfs are cool and faint stars that comprise about two-thirds of the stellar population in the solar neighbourhood (Henry et al., 2018; Reylé et al., 2021). With main-sequence lifespans longer than the age of the universe (Laughlin et al., 1997), these stars are not only an excellent record of the structure and evolution of the Milky Way (Bochanski et al., 2007), but have also become prime targets for exoplanet surveys owing to their low mass, low temperature, and ubiquity (Bonfils et al., 2013; Dressing & Charbonneau, 2013; Reiners et al., 2018); this combination favours detections of Earth-mass planets inside their habitable zone where liquid water can be sustained (Scalo et al., 2007).

   Installed at the 3.5 m telescope at the Calar Alto Observatory, the CARMENES instrument (Quirrenbach et al., 2020) is, along with SPIRou (Donati et al., 2020), NIRPS (Wildi et al., 2017), HPF (Mahadevan et al., 2012), IRD (Kotani et al., 2018), MAROON-X (Seifahrt et al., 2020), NEID (Schwab et al., 2016), and GIARPS (Claudi et al., 2018), a new-generation spectrograph designed to detect Earth-mass planets around M dwarfs by means of the radial velocity technique (Reiners et al., 2018). It consists of optical (hereafter VIS) and near-infrared (NIR) channels that cover the

5200–9600 Å and 9600–17100 Å wavelength regions with spectral resolutions of $R = 94\,600$ and $R = 80\,400$, respectively. As of mid-2020, the CARMENES exoplanet survey had collected more than 18 500 VIS and 18 000 NIR spectra for a sample of 365 M dwarfs (Quirrenbach et al., 2020) obtained as part of its 750-night guaranteed time observations (GTO) programme. In addition to detecting and characterising the orbits of exoplanets (e.g. Trifonov et al., 2018, 2020; Luque et al., 2019; Zechmeister et al., 2019) and their atmospheres (Nortmann et al., 2018; Alonso-Floriano et al., 2019; Yan et al., 2019), the survey represents a unique opportunity to gain insights into the nature of M dwarfs (namely, their photospheric parameters, chemical compositions, magnetic fields, and chromospheric activity levels) in a statistically relevant way (Fuhrmeister et al., 2018, 2020; Passegger et al., 2018, 2019; Hintz et al., 2019, 2020; Schöfer et al., 2019; Schweitzer et al., 2019; Shulyak et al., 2019; Abia et al., 2020; Shan et al., 2021).

In the context of exoplanet research, a thorough account of the general properties of host stars directly affects the determination of the position of the habitable zone (Selsis et al., 2007; Kopparapu et al., 2013), the radius and mass of detected exoplanets, and their composition (Maldonado et al., 2020; Ishikawa et al., 2020). In addition, planet formation theories attempt to explain the observed occurrence rate of exoplanets (Johnson et al., 2010; Howard et al., 2012; Buchhave et al., 2012; Sabotta et al., 2021) and selection effects (Winn & Fabrycky, 2015) in terms of the stellar parameters.

However, the computation of the photospheric parameters for M dwarfs from stellar spectra, namely the effective temperature, $T_{\rm eff}$, surface gravity, $\log g$, and stellar metallicity, [Fe/H], is an arduous challenge. The low photospheric temperatures give rise to pervasive molecular bands that severely distort the stellar continuum (Kirkpatrick et al., 1991; Tinney & Reid, 1998; Reiners et al., 2018). This alone rules out classical techniques commonly adopted in the analysis of solar-type spectra, such as the equivalent width (EW) method (Marfil et al., 2020). Stellar convection in M dwarfs also calls into question some of the physical assumptions behind the model atmospheres of late-type stars, such as local thermodynamic equilibrium (LTE) and one-dimensional (1D) geometry for radiative transfer, which often represents a limitation to the interpretation at the resolution achieved by modern spectrographs (Bergemann et al., 2017; Olander et al., 2021). Furthermore, M dwarfs may exhibit strong magnetic fields that not only drive stellar activity (Delfosse et al., 1998; Donati et al., 2008) but may also distort magnetically sensitive lines via the Zeeman effect (Landi Degl'Innocenti & Landolfi, 2004; Passegger et al., 2019). It is, therefore, difficult to choose a set of lines to disentangle the impact of the magnetic field and the photospheric parameters on the stellar spectra (Shulyak et al., 2019). To make matters worse, telluric absorption is ubiquitous in the NIR (Reiners et al., 2018; Nagel, 2019), where the spectral energy distribution of M dwarfs peaks (Cifuentes et al., 2020).

Despite the above, several methods have proved fruitful for inferring $T_{\rm eff}$, $\log g$, and [Fe/H] in M dwarfs, including spectral synthesis (e.g. Passegger et al., 2018, 2019; Rajpurohit et al., 2018b; Souto et al., 2020; Hejazi et al., 2020), pseudo EWs (e.g. Mann et al., 2013a, 2014; Neves et al., 2014; Maldonado et al., 2015, 2020), and spectral indices (e.g. Rojas-Ayala et al., 2012; Khata et al., 2020), all of which can be further investigated following a machine-learning approach (e.g. Sarro et al., 2018; Antoniadis-Karnavas et al., 2020; Passegger et al., 2020; Li et al., 2021). In general terms, spectral synthesis relies on a minimisation algorithm to find the synthetic spectrum that best matches the observed spectrum (Valenti & Fischer, 2005; Brewer et al., 2016), while pseudo EWs and spectral index approaches draw on the sensitivity of certain features to $T_{\rm eff}$ and [Fe/H], as well as on calibrations with wide physical binaries harbouring an FGK-type primary with known metallicity (Casagrande et al., 2008; Neves et al., 2012; Montes et al., 2018, and references therein). Further studies have focused on ensuring consistency between these two approaches (Veyette et al., 2017).

Semi-empirically calibrated methods have been widely adopted in the literature. For example, based on observations in the photometric Y band (9470–11210 Å) with NIRSPEC on Keck II, Veyette et al. (2017) used a method to derive $T_{\rm eff}$, [Fe/H], and [Ti/H] that rests on the approach described by Mann et al. (2013b) and a calibration sample of M dwarfs in common proper motion FGK+M

binaries from Mann et al. (2013a). The method relies on the measured FeH index in the Wing-Ford band and on the EWs of seven Fe I and ten Ti I lines found in the Y-band. More recently, Maldonado et al. (2020) derived T_{eff}, $\log g$, and [Fe/H] for a sample of 204 stars with spectral types from K7.0 V to M4.0 V with HARPS and HARPS-N data assuming the photometric M_K-[Fe/H] relationship from Neves et al. (2012) and the T_{eff} scale from Mann et al. (2013b).

M-dwarf studies based on spectral synthesis differ from one to another in terms of the synthetic grid employed, the spectral resolution of the data, and the features selected for comparison across different wavelength regions. For instance, Passegger et al. (2018) derived T_{eff}, $\log g$, and [Fe/H] for 300 M dwarfs, 235 of which were observed with CARMENES. They adopted a χ^2 minimisation procedure based on the PHOENIX-ACES library of synthetic spectra (Husser et al., 2013) and several spectral features in the VIS wavelength region covered by CARMENES, namely the TiO γ band and several K I, Fe I, Ti I, and Mg I lines. To avoid unreliable values of $\log g$ and [Fe/H] for some stars in the sample caused by degeneracies in the parameter space, they constrained $\log g$ by using the evolutionary models of Baraffe et al. (1998). Passegger et al. (2019) expanded the analysis into the NIR wavelength region covered by CARMENES. For the first time, they directly compared the stellar parameters of 282 M dwarfs determined from simultaneous observations in the VIS and NIR wavelength regions. Despite some discrepancies, Passegger et al. (2019) conclude that it is best to consider both regions simultaneously to maximise the amount of spectral information and, thus, minimise the effects of imperfect modelling in M dwarfs. Furthermore, Passegger et al. (2019) lessened the impact of the Zeeman line broadening caused by the stellar magnetic field in the parameter computations in the NIR by selecting lines with low effective Landé factors. Adapting the method described in Rajpurohit et al. (2012, 2018b), Rajpurohit et al. (2018a) computed T_{eff}, $\log g$, and [Fe/H] for 292 M dwarfs from the individual CARMENES spectra published by Reiners et al. (2018), using a grid of BT-Settl models (Allard et al., 2012), while keeping $\log g$ free throughout the minimisation process. Hejazi et al. (2020) also employed BT-Settl models to derive the T_{eff}, $\log g$, metallicity [M/H], and α element to iron abundance ratio, [α/Fe], of 1544 M dwarfs in the solar neighbourhood from low- and medium-resolution spectra collected at the Michigan-Darmouth-MIT, Lick, Kitt Peak National, and Cerro-Tololo Inter-American observatories. Souto et al. (2020) computed T_{eff}, $\log g$ and [Fe/H] for 21 M dwarfs from mid-resolution ($R \approx 22\,500$) APOGEE H-band spectra (Wilson et al., 2010), a grid of MARCS models (Gustafsson et al., 2008) and the turbospectrum code (Plez, 2012) through the bacchus wrapper (Masseron et al., 2016), and find excellent agreement in [Fe/H] between components in the wide physical binaries included in their sample. More recently, Sarmento et al. (2021) derived T_{eff}, $\log g$, [M/H], and v_{mic} for a sample of 313 M dwarfs from APOGEE H-band spectra by means of a χ^2 minimisation against a synthetic grid generated with turbospectrum, ispec (Blanco-Cuaresma et al., 2014b), and MARCS model atmospheres, and find good agreement with the parameters obtained with the APOGEE Stellar Parameter and Chemical Abundances Pipeline (García Pérez et al., 2016).

In this work we derived the stellar atmospheric parameters (T_{eff}, $\log g$, and [Fe/H]) for a sample of 343 M dwarfs observed with CARMENES (i.e. 5200–17100 Å at $R \sim 90\,000$) by means of the STEPARSYN code (Tabernero et al., 2021b), a Bayesian implementation of the spectral synthesis technique. This approach relied on the comparison of a synthetic grid against 75 magnetically insensitive Ti I and Fe I absorption lines along with the TiO γ and ϵ bands. For the computation of the synthetic grid, we employed the turbospectrum code (Plez, 2012) along with the BT-Settl model atmospheres (Allard et al., 2012). In contrast to other works that disregard stellar activity (Rajpurohit et al., 2018b; Sarmento et al., 2021), our methodology allowed us to expand the analysis to M dwarfs that are strongly active, fast-rotating, or late-type (down to M7.0 V), as a result of the careful selection of Ti I and Fe I lines according to their low sensitivity to chromospheric activity and the stellar magnetic field. In addition, the selected Ti I and Fe I lines are mostly free from non-LTE effects, which seem to affect lines of other elements widely used in other works (Passegger et al., 2018, 2019; Rajpurohit et al., 2018b), such as K I (Olander et al., 2021).
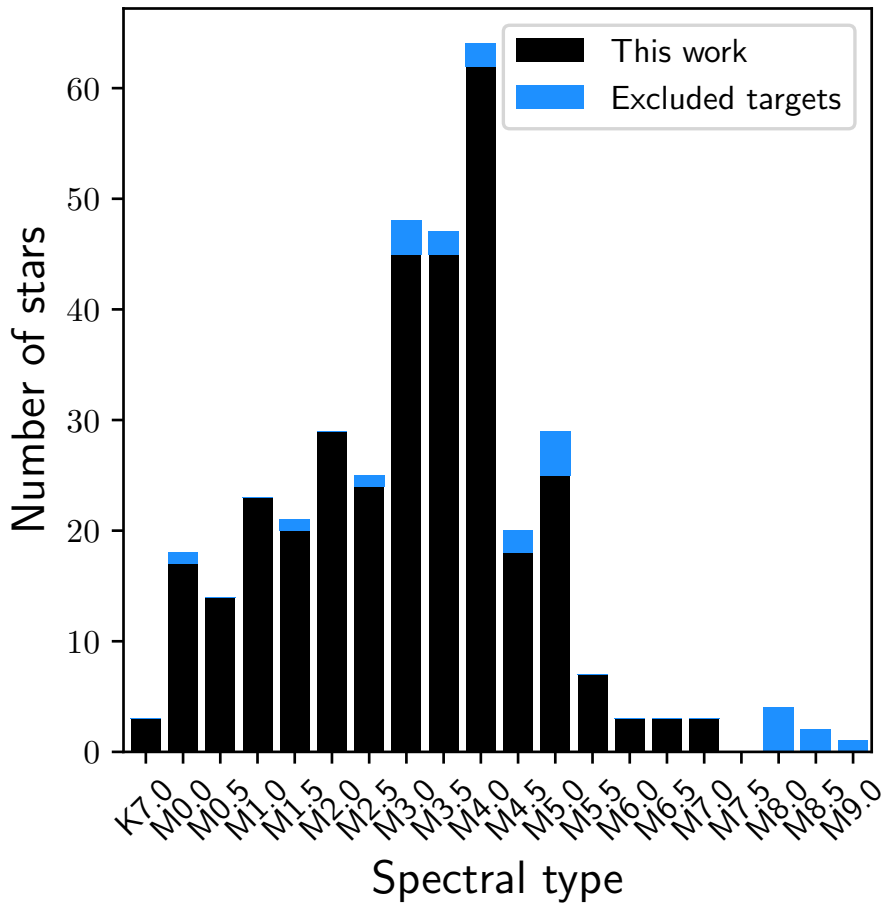
FIGURE 4.1. Histogram of the M-dwarf sample analysed in this work (black) and the excluded CARMENES GTO targets (blue).

This study is structured as follows. In Sect. 4.2 we describe the CARMENES GTO sample. We explain the derivation of the stellar atmospheric parameters in Sect. 4.3. Finally, we discuss the results and highlight the main conclusions in Sects. 4.4 and 4.5, respectively.

4.2   Sample

Until mid-2020, the CARMENES M-dwarf radial velocity survey comprised 365 targets that cover the full M sequence from M0.0 V to M9.0 V (Quirrenbach et al., 2020). The sample also includes three K7 dwarfs. Spectra for all stars were collected as part of the GTO programme of the instrument consortium from January 2016 to March 2021, equivalent to more than 5 000 hours of observing time.

A histogram of the M-dwarf sample analysed in this work is shown in Fig. 4.1, while all targets excluded from further analysis are listed in Table 4.1. Among these targets are one eclipsing binary (CM Dra, Morales et al., 2009), ten double-line spectroscopic (SB2) binaries (Baroch et al., 2018, 2021), and two triple-line spectroscopic triple systems (Baroch et al., 2021), for which no reliable parameter determinations could be made. We also discarded three targets because of conspicuous artefacts over multiple orders of their CARMENES spectra. Lastly, after performing the spectral processing presented in Sect. 4.3.1, seven M dwarfs with spectral types M8.0 V or later were excluded due to limitations in our method. Altogether, our final sample includes 343 CARMENES GTO stars.
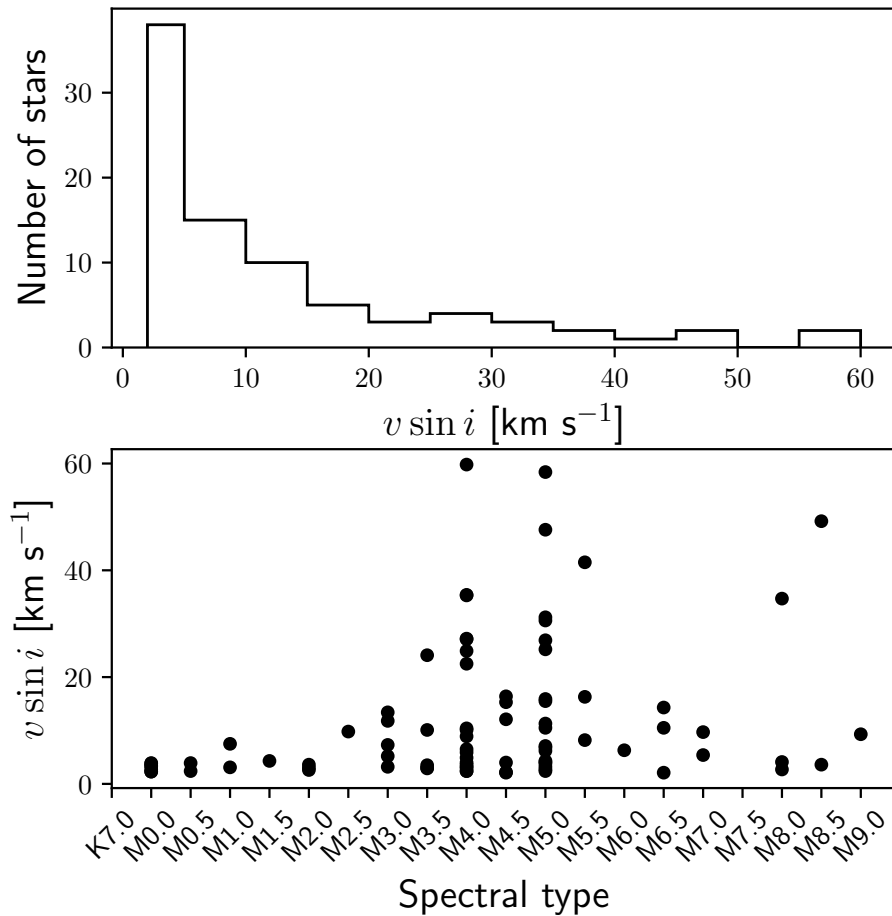
FIGURE 4.2. Distribution of the projected rotational velocities larger than $2\,\mathrm{km\,s^{-1}}$ in the sample.

Table C.1 displays the CARMENES identifiers, common names, spectral types from the CARMENES Cool dwarf Information and daTa Archive (Carmencita, Alonso-Floriano et al., 2015; Caballero et al., 2016a), radial velocities (v_r), projected rotational velocities ($v \sin i$) adopted from Reiners et al. (2018) if available or computed following the same method otherwise, signal-to-noise ratios (S/N) over the entire spectra, and activity flags for the sample. Active stars are identified with an activity flag 1 if the pseudo-EW of the Hα line satisfies pEW$'$(Hα) < -0.3 Å, following Schöfer et al. (2019). For most targets, radial velocities were adopted from Lafarga et al. (2020), who used cross-correlation with weighted binary masks. For targets that were not in Lafarga et al. (2020), we adopted the radial velocities provided by the CARMENES standard radial-velocity pipeline serval[1] (Zechmeister et al., 2018, 2020), based on least-squares fitting using high-S/N templates.

The distribution of $v \sin i$ in the sample is shown in Fig. 4.2. Most targets in our sample (268 stars) do not exhibit significant rotation, that is, $v \sin i < 2\,\mathrm{km\,s^{-1}}$, while targets with $v \sin i$ values higher than this upper limit (74 stars) are typically mid-type M dwarfs (M4.0–5.0 V).

4.3   Analysis

In the following we describe the processing of the CARMENES observations, the selection of the spectral features to be compared with the synthetic spectra, the computation of the synthetic

---

[1]www.github.com/mzechmeister/serval
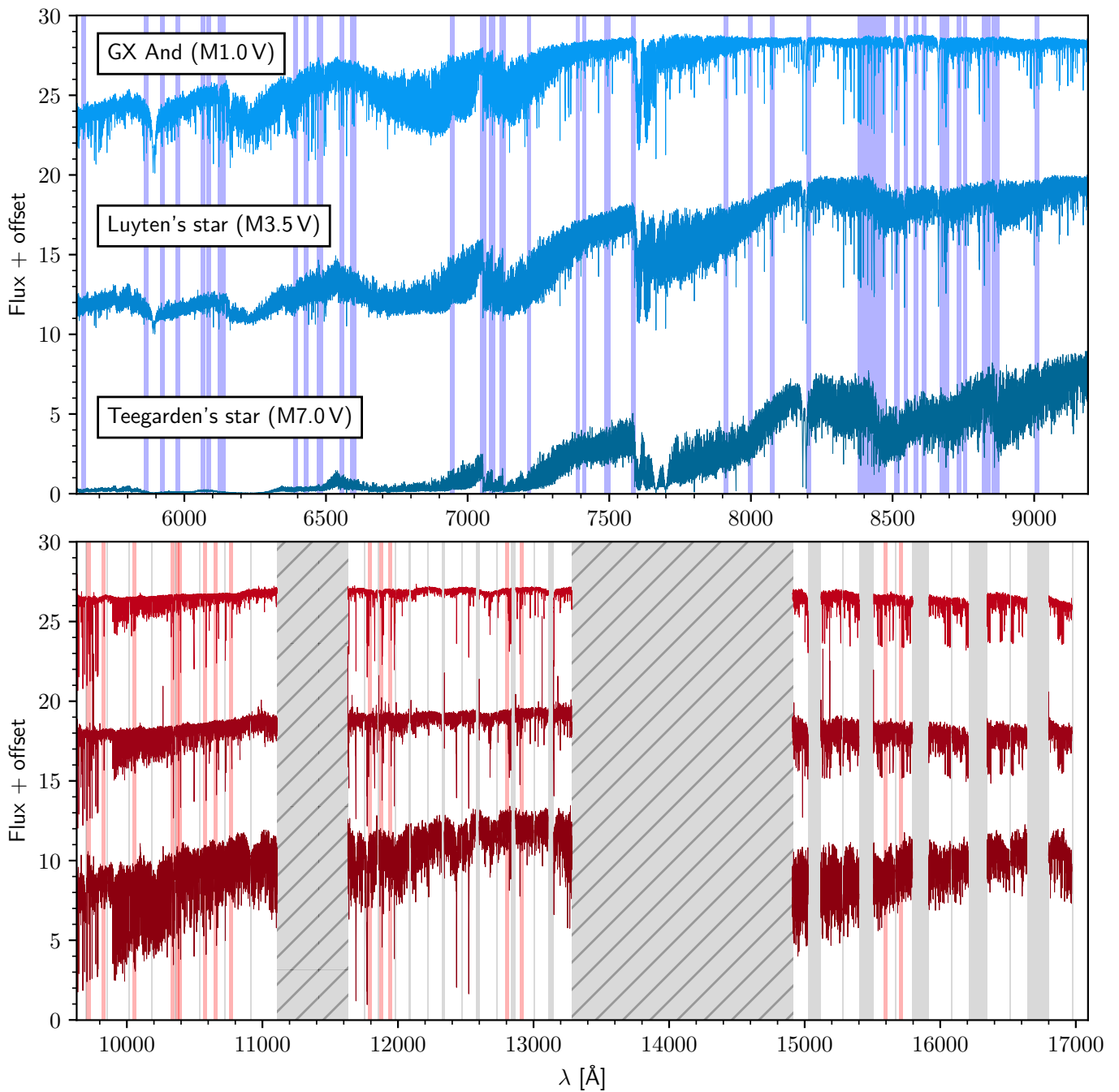
FIGURE 4.3. CARMENES template spectra of GX And (M1.0 V, J00183+440), Luyten's star (M3.5 V, J07274+052), and Teegarden's star (M7.0 V, J02530+168) in the VIS channel (*top panel*) and the NIR channel (*bottom panel*). Blue and red shaded regions denote the ranges synthesised in this work. The two wide spectral gaps in the NIR channel shown as hatched rectangles correspond to regions severely affected by telluric absorption (Reiners et al., 2018). Inter- and intra-order gaps in the NIR channel are also shown, as grey shaded regions.

TABLE 4.1. GTO M dwarfs excluded from the analysis.

Karmn	Name	Reason
J00162+198W	EZ Psc AB	(1)
J01056+284	GJ 1029 AB	(1)
J02486+621	2MASS J02483695+6211228	(3)
J02573+765	G 245-61	(3)
J04198+425	LSR J0419+4233	(4)
J04219+213	K2-155	(3)
J05394+406	LSR J0539+4038	(4)
J05532+242	Ross 59 AB	(1)
J07001−190	2MASS J07000682−1901235 AB	(1)
J08536−034	LP 666-009	(4)
J10182−204	NLTT 23956 AB	(1)
J10354+694	LP 037-179 AB	(1)
J14155+046	GJ 1182 AB	(1)
J15412+759	UU UMi AB	(1)
J15474−108	LP 743-031 ABC	(2)
J16343+571	CM Dra Aab	(5)
J18356+329	LSR J1835+3259	(4)
J19169+051S	V1298 Aql	(4)
J19255+096	LSPM J1925+0938	(4)
J20198+229	LP 395-008 AB	(1)
J20556−140N	GJ 810 Aab	(1)
J23064−050	2MUCD 12171 (Trappist-1)	(4)
J23585+076	Wolf 1051 ABC	(2)

Notes. (1) Double-line spectroscopic (SB2) binary (Baroch et al., 2018, 2021). (2) Triple-line spectroscopic triple systems (Baroch et al., 2021). (3) Conspicuous artifacts in the CARMENES template spectra. (4) Spectral type M8.0 V or later. (5) Eclipsing binary (Morales et al., 2009).

grid by means of the BT-Settl models and `turbospectrum`, and the analysis of the sample with the STEPARSYN code.

4.3.1 Spectral processing

All M dwarfs under analysis have been observed with CARMENES at several epochs since January 2016 (Reiners et al., 2018; Quirrenbach et al., 2020). The spectra were reduced following the standard CARMENES data flow. They were processed and calibrated in wavelength with the `caracal` pipeline (Caballero et al., 2016b). The wavelength calibration relies on a combination of hollow cathode lamps and two temperature- and pressure-stabilised Fabry-Pérot units that ensure median uncertainties of about 1 m s^{-1} in the VIS channel (Trifonov et al., 2018; Zechmeister et al., 2018). As an additional step in the data flow, individual spectra were corrected for telluric absorption before the co-addition into template spectra as a way to increase the S/N. The modelling of the telluric spectra was done with the software package `molecfit`[2] (Smette et al., 2015; Kausch et al., 2015), which incorporates the line-by-line radiative transfer code LBLRTM (Clough et al., 2005) and the HITRAN molecular line list (Rothman et al., 2009). Further details on the removal of the telluric features can be found in Nagel (2019). The radial velocity pipeline `serval` (Zechmeister et al., 2018) co-adds all individual spectra and provides one high-S/N template spectrum per star and

---

[2]http://www.eso.org/sci/software/pipelines/skytools/molecfit
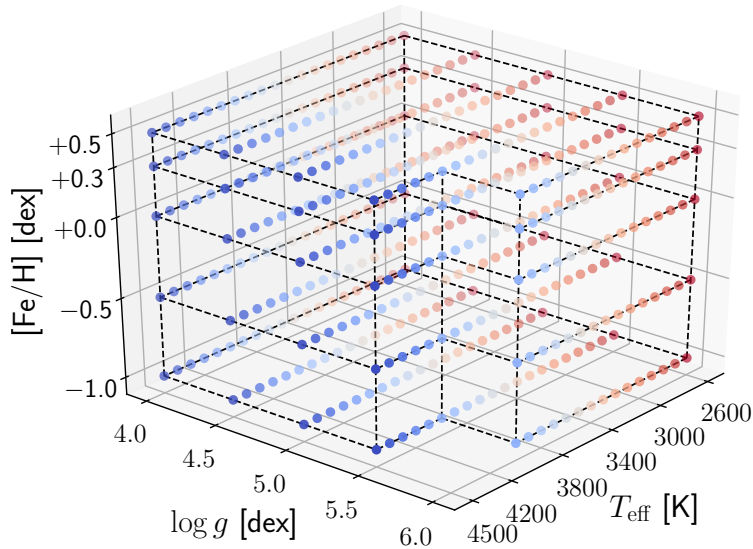
FIGURE 4.4. Coverage of our synthetic grid in T_{eff}, $\log g$, and [Fe/H].

TABLE 4.2. Reference stars for the selection of Fe I and Ti I lines.

Reference star	SpT	T_{eff} [K]
GX And	M1.0 V	~3700
Luyten's star	M3.5 V	~3400
Teegarden's star	M7.0 V	~2900

instrument channel. We transformed the wavelengths onto an air scale following the International Astronomical Union standard (Morton, 2000) and corrected the spectra for the Doppler shift using the corresponding radial velocities of the targets.

4.3.2 Selection of spectral features and line masks

The selection of Fe I and Ti I lines employed in this work was the result of a careful inspection of the template spectra of three representative early-, mid-, and late-type M dwarfs, namely GX And, Luyten's star, and Teegarden's star (see Table 4.2). These M dwarfs show no significant rotation or activity, except for Teegarden's star, which shows relatively little activity for its spectral type (Zechmeister et al., 2019). This choice of reference stars mirrors that of Reiners et al. (2018) for their spectral atlas.

For this purpose, we first requested several line lists from the Vienna Atomic Line Database[3] (VALD3; Ryabchikova et al., 2015) via the `extract all` option, across the VIS and NIR wavelength regions covered by CARMENES. Following the prescriptions of Passegger et al. (2019), we excluded all Fe I and Ti I lines in the NIR channel ($\lambda > 9600\,\text{Å}$) with large Landé factors (i.e. $g_{\text{eff}} > 1.5$) to alleviate the impact of the stellar magnetic field on the line profiles. The visual inspection was complemented by a literature search to include some of the Fe I and Ti I line selections of Tabernero et al. (2018) and Passegger et al. (2019). The final list of Fe I and Ti I lines along with the synthesised wavelength ranges can be found in Table C.2. The ranges are wide enough (i.e. a few Å) to circumvent potential problems posed by convolution at the edges. We also included the TiO

---

[3] http://vald.astro.uu.se

TABLE 4.3. List of TiO bands and wavelength ranges synthesised.

TiO band	Range		Band head
	$\lambda_{\min}$ [Å]	$\lambda_{\max}$ [Å]	λ_{head} [Å]
	7049.69	7058.85	~7054
γ-bands	7082.49	7092.31	~7087
	7120.30	7129.69	~7125
ϵ-bands	8436.60	8446.51	~8440
	8854.87	8864.58	~8859

γ and ϵ bands for the present analysis (see Table 4.3) given their high sensitivity to T_{eff} (Rajpurohit et al., 2014; Passegger et al., 2016). In Fig. 4.3 we show the template spectra of the three reference stars along with the selected wavelength ranges (see also Figs. 4.6 and 4.7). In contrast to the some of the lines used in other works, such as K I (Passegger et al., 2018, 2019; Rajpurohit et al., 2018b), non-LTE effects are negligible for Fe I and Ti I lines (Olander et al., 2021).

We followed Tabernero et al. (2021b) to define the wavelength regions around the observed Fe I and Ti I line profiles in the template spectra to be compared with the synthetic grid (i.e. the line masks). We first performed a preliminary Gaussian fit to the Ti I and Fe I lines by means of the Levenberg-Marquardt algorithm through the Python `scipy` package (Virtanen et al., 2020). Next, we adjusted the line profiles assuming an initial width of 3σ around their centre, avoiding adjacent spectral features. For targets with $v \sin i > 4 \text{ km s}^{-1}$ where the Gaussian approximation may no longer accurately reproduce the line profiles, we also broadened these line regions to account for rotation, following the expression (Tabernero et al., 2021b):

$$\Delta\lambda = 2\lambda_{\text{line}}\frac{v\sin i}{c}, \tag{4.1}$$

where $\Delta\lambda$ is the broadening, λ_{line} is the central wavelength of the line, and c is the speed of light.

For active stars (as indicated by the Hα flag), we specifically excluded some Fe I and Ti I lines that appear to be particularly sensitive to the chromospheric activity and the stellar magnetic field. These lines are marked as magnetically sensitive in Table C.2 and will be discussed in a future publication (López-Gallifa et al., in prep.; for more details, see Montes et al., 2020). This additional consideration is particularly relevant for M dwarfs showing magnetic fields that can be as high as several kilogauss, such as EV Lac and YZ CMi (Shulyak et al., 2019). Overall, the line exclusion affected a total of 91 active stars in our sample, and proved crucial in reaching convergence and, thus, avoiding getting unreliable parameters with STEPARSYN.

4.3.3   Synthetic grid

After the line selection step, we computed a coarse grid of synthetic spectra based on a set of BT-Settl model atmospheres (Allard et al., 2012) and the 1D LTE spectrum synthesis code `turbospectrum` (Alvarez & Plez, 1998; Plez, 2012). The grid is representative of the M-dwarf regime and ranges from 2600 K to 4500 K and 4.0 dex to 6.0 dex, when available (i.e. 5.5 dex instead for models with $T_{\text{eff}} > 4000$ K) in steps of 100 K and 0.5 dex in T_{eff} and $\log g$, respectively (see Fig. 4.4). We set the metallicity, [Fe/H], to the following values: -1.0, -0.5, 0.0, $+0.3$, and $+0.5$ dex. For all models, we adopted the same micro-turbulence velocities as in the PHOENIX-ACES library of synthetic spectra[4] (Husser et al., 2013). We assumed the solar abundances as reported by Asplund et al. (2009) and scaled the abundances of the α elements (O, Ne, Mg, Si, S, Ar,

---

[4]http://phoenix.astro.physik.uni-goettingen.de/

Ca, and Ti) following the discussion of Gustafsson et al. (2008) for the standard grid of MARCS models, so that $[\alpha/\text{Fe}] = -0.4[\text{Fe/H}]$ for $-1.0 \leq [\text{Fe/H}] \leq 0.0$, and $[\alpha/\text{Fe}] = 0.0$ (i.e. no enhancement) for $[\text{Fe/H}] \geq 0.0$. The synthetic grid was finally stored in a binary file by means of the Python module `pickle` (Van Rossum, 2020).

The atomic data were gathered via automatic email requests to the VALD3 database using the `extract all` option for all the ranges listed in Tables 4.3 and C.2. The required molecular data were compiled from several sources and included H_2O (Barber et al., 2006), FeH (Dulick et al., 2003), MgH (Kurucz, 2014), CO (Goorvitch, 1994), SiH (Kurucz, 2014), OH (Kurucz, 2014), VO (McKemmish et al., 2016), CaH, ZrO, and TiO (B. Plez priv. comm., see Heiter et al., 2021). To reduce computation times, we only considered the most relevant transitions in each molecular line list by applying the following Boltzmann cut (Gray, 2008):

$$\log(gf \cdot \lambda_i) - \chi_i \cdot \theta > \max_i[\log(gf \cdot \lambda_i) - \chi_i \cdot \theta] - 5, \tag{4.2}$$

where λ_i denotes the wavelength in Å of the transition i, $\log gf$ is the oscillator strength, χ_i is the excitation potential in eV, and $\theta = 5040\,\text{K}/T$, with $T = 3000\,\text{K}$.

As discussed in Tabernero et al. (2021b), the STEPARSYN code allows the synthetic grid to be sequentially convolved on the fly (i.e. prior to the comparison with the observed spectra) to account for both the stellar rotation and the instrumental profile as the main sources of spectral broadening. As for rotation, we assumed the rotational profile with a limb darkening coefficient of 0.6 from Gray (2008), and adopted the projected rotational velocities from Table C.1. Finally, to account for the instrumental profile, we convolved the spectra with a Voigt profile, assuming the corresponding median averaged Gaussian and Lorentzian components for the CARMENES VIS and NIR channels (Nagel, 2019).

4.3.4   STEPARSYN

STEPARSYN is a Bayesian code written in Python 3 designed to map the probability distributions of the stellar atmospheric parameters (T_{eff}, $\log g$, [Fe/H], and $v \sin i$) from a given observed spectrum following an Markov chain Monte Carlo approach (Tabernero et al., 2021b). It has already been employed in many astrophysical contexts, including the study of stars in open clusters (Lohr et al., 2018; Alonso-Santiago et al., 2019), stars in galaxies of the Local Group (Tabernero et al., 2018), and exoplanet host stars (Borsa et al., 2021; Demangeon et al., 2021).

In broad terms, the STEPARSYN code compares the observed spectrum with a grid of synthetic spectra computed around particular features. Prior decomposition of the synthetic grid following a principal component analysis (Francis & Wills, 1999) helps to assess any given point of the parameter space in a computationally inexpensive way. STEPARSYN finally returns the marginalised posterior distributions in the stellar atmospheric parameters, as shown in Fig. 4.5 for a representative case (the M1.0 V star HD 233153), along with the best synthetic fits for the atomic lines and molecular bands, as shown in Figs. 4.6 and 4.7, respectively, for the same star (see Figs. C.1 to C.9 for the reference stars GX And, Luyten's star, and Teegarden's star). The corner plot showing the marginalised posterior distribution obtained with STEPARSYN was made with the Python `pygtc` package (Bocquet & Carter, 2016). Further details about STEPARSYN can be found in Tabernero et al. (2021b).

To avoid degeneracies in the parameter space, particularly between $\log g$ and [Fe/H], we assumed Gaussian prior probability distributions in T_{eff} and $\log g$ centred according to the T_{eff}, stellar mass, and radius reported by Cifuentes et al. (2020) for each target when available[5], or otherwise the averaged parameters as listed in Table 6 in Cifuentes et al. (2020), with standard deviations of 200 K and 0.2 dex, respectively. T_{eff} and $\log g$ prior distributions for our sample are included in Table C.3.

---
[5]https://github.com/ccifuentesr/CARMENES-V
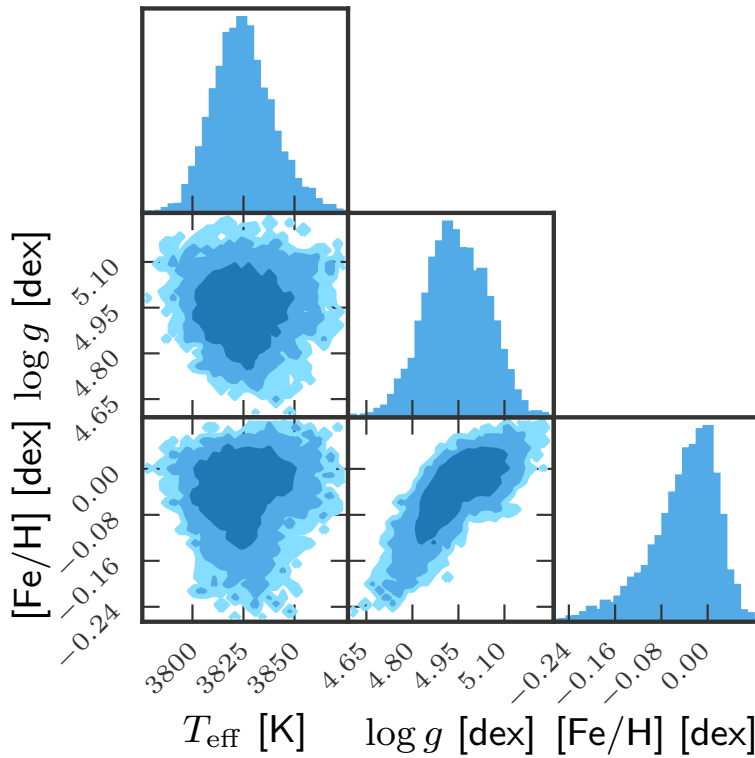
FIGURE 4.5. Marginalised posterior distributions in T_{eff}, $\log g$, and [Fe/H] for the M1.0 V star HD 233153 (J05415+534). The colour shades denote the 1σ, 2σ, and 3σ levels. The retrieved parameters are $T_{\text{eff}} = 3825 \pm 14$ K, $\log g = 4.94 \pm 0.10$ dex, and [Fe/H] $= -0.04 \pm 0.06$ dex.

These T_{eff} were derived from a thorough multi-band photometric analysis carried out with the Virtual Observatory Spectral energy distribution Analyser (`vosa`, Bayo et al., 2008), whereas the stellar radii and masses were obtained from the Stefan-Boltzmann law and the mass-radius relation derived by Schweitzer et al. (2019), respectively.

In Fig. 4.8 we show a Kiel diagram (i.e. $\log g$ versus T_{eff}) of the prior T_{eff} and $\log g$ values that we adopted for our sample. Some stars show low $\log g$ values, which can be explained with stellar age. These stars were already identified as young stars by Schweitzer et al. (2019) on account of their membership in young stellar kinematic groups (Cortés-Contreras et al. in prep.). Among these are the Local Association, β Pictoris Moving Group, the IC 2391 Supercluster, and Castor Moving Group, with estimated ages of 10-150 Ma (Bell et al., 2015), 18.5 Ma (Miret-Roig et al., 2020), 50 Ma (Barrado y Navascués et al., 2004), and 440 Ma (Mamajek et al., 2013), respectively. On the contrary, a few additional targets exhibit a high $\log g$, probably due to their behaviour akin to subdwarfs, following the discussion by Schweitzer et al. (2019). All these outliers in $\log g$ are listed in Table 4.4.
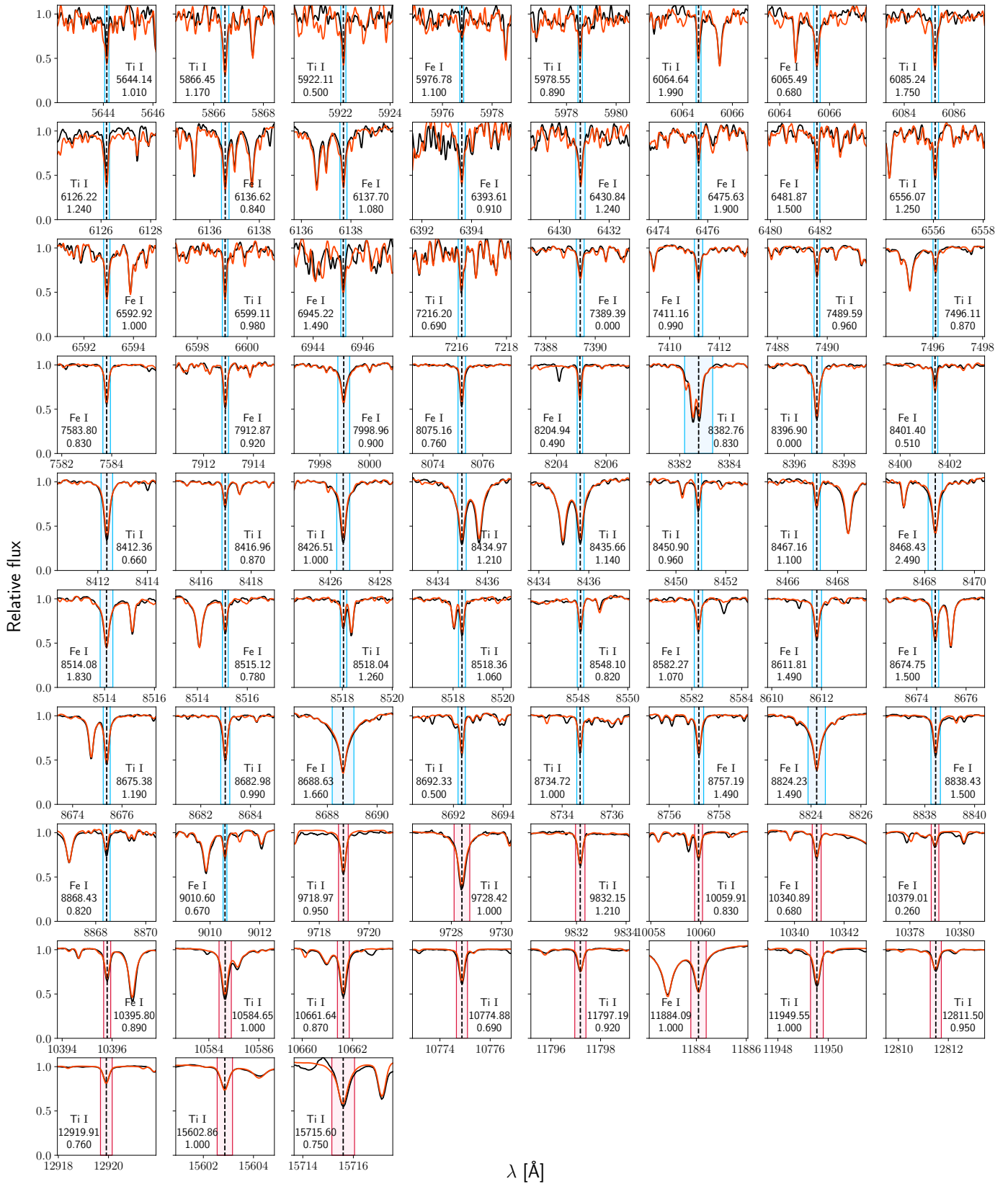
FIGURE 4.6. Atomic line fits for the M1.0 V star HD 233153 (J05415+534). The solid black and orange lines are the observed and synthetic spectra, respectively. The blue and pink shaded areas are the regions of comparison between the observed and the synthetic spectra (i.e. line masks) for features in the VIS and NIR channels of CARMENES, respectively. The vertical dashed black lines mark the central wavelengths. The species, the central wavelength, and the effective Landé factor, g_{eff}, of the lines are indicated inside each box.
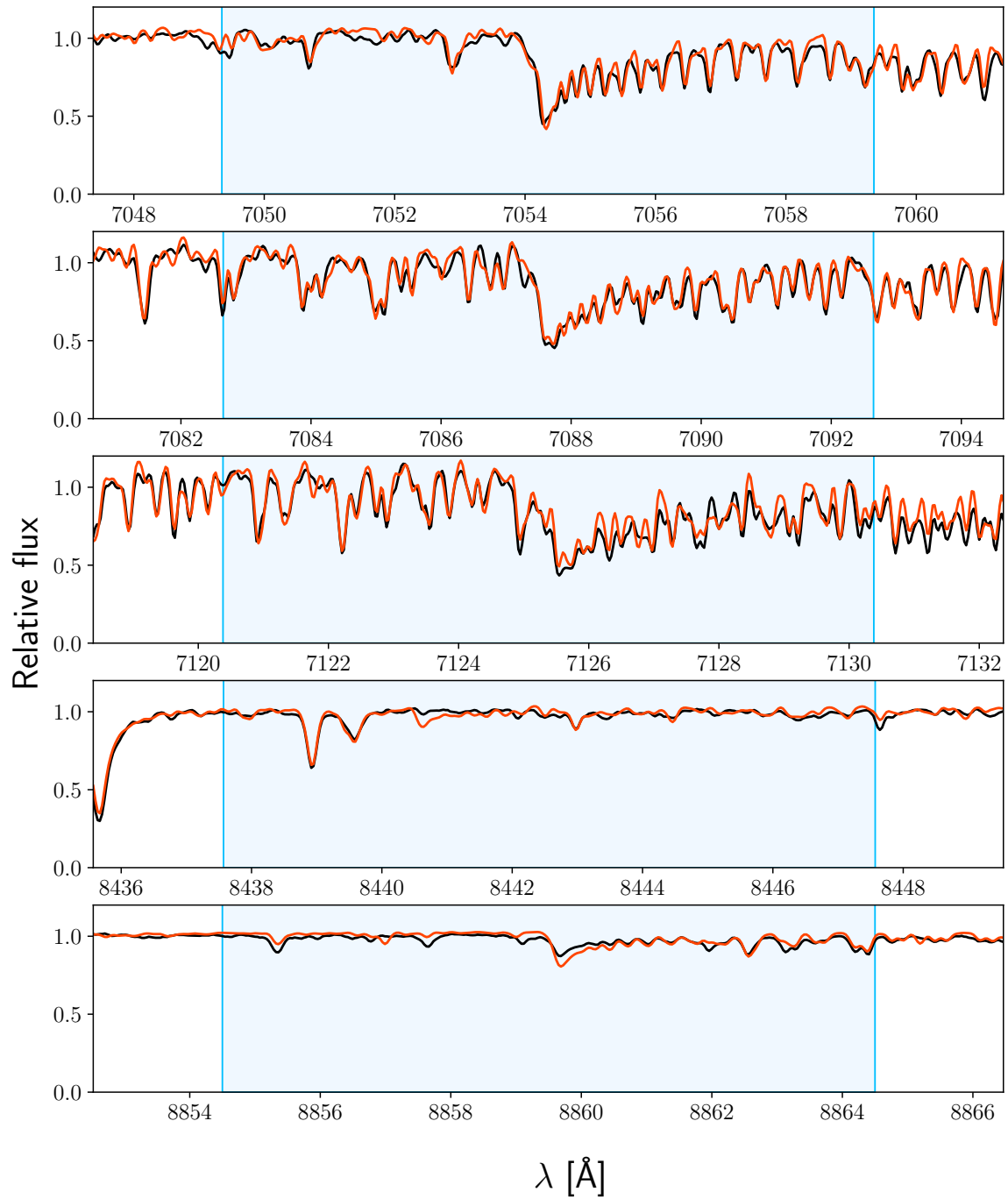
FIGURE 4.7. Same as Fig. 4.6, but for the TiO γ and ϵ bands.
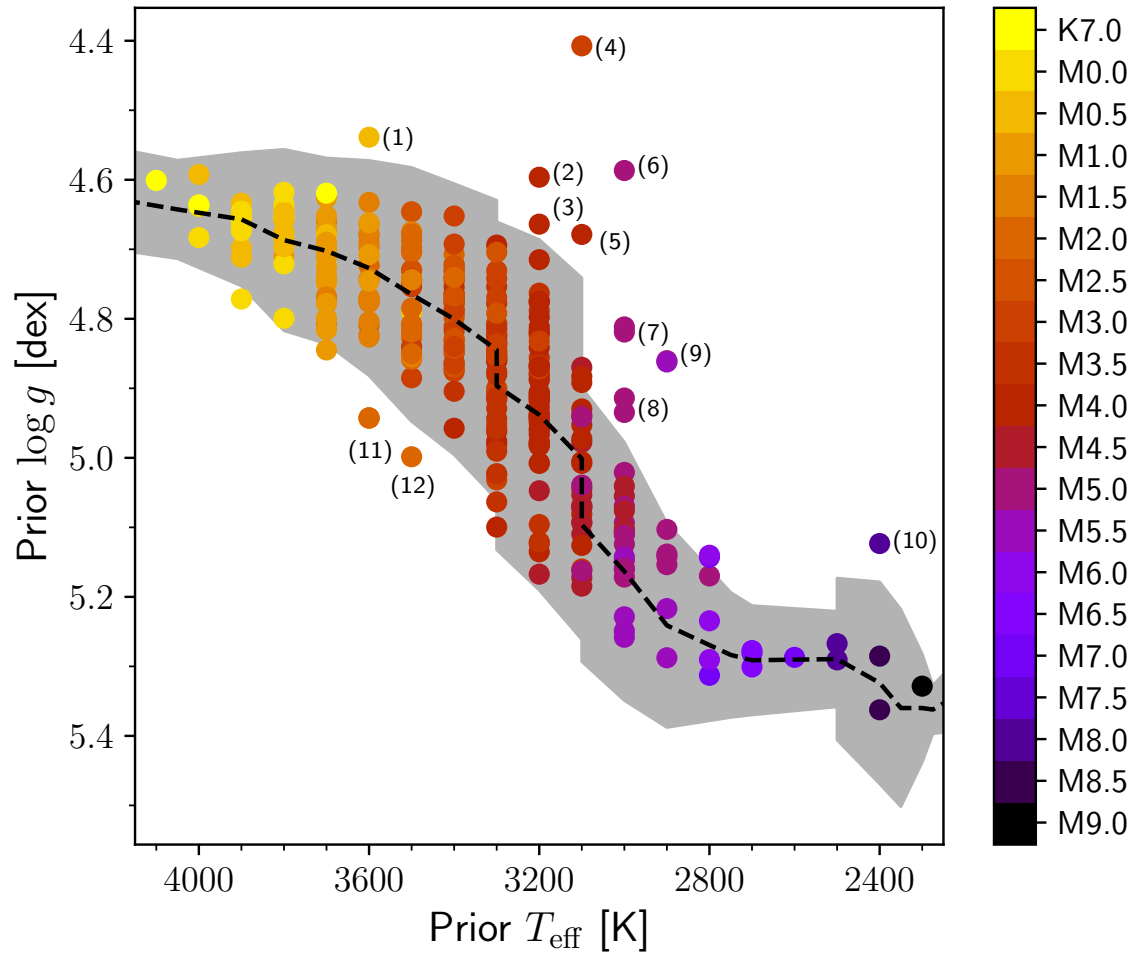
FIGURE 4.8. Central prior $T_{\rm eff}$ and $\log g$ values for the sample following Cifuentes et al. (2020). The spectral types are colour-coded. The dashed black line is the average $T_{\rm eff}$ and $\log g$ for K7 V to M9.0 V objects, with the corresponding uncertainties shaded in grey. The 15 outliers discussed in Sect. 4.3.4 are labelled and listed in Table 4.4. Two and three stars are superimposed under labels (7) and (11), respectively.

TABLE 4.4. List of outliers in log g.

Name	Karmn	SpT	Prior log g [dex]	Label [a]	Remarks
Barta 161 12	J01352−072	M4.0 V	4.60	(2)	Member of β Pictoris Moving Group
RX J0447.2+2038	J04472+206	M5.0 V	4.82	(7)	Member of IC 2391 Supercluster
1RXS J050156.7+010845	J05019+011	M4.0 V	4.66	(3)	Member of β Pictoris Moving Group
RX J0506.2+0439	J05062+046	M4.0 V	4.68	(5)	Member of β Pictoris Moving Group
2MASS J05082729−2101444	J05084−210	M5.0 V	4.59	(6)	Member of Local Association
LP 205-044	J06318+414	M5.0 V	4.81	(7)	Member of Local Association
1RXS J114728.8+664405	J11474+667	M5.0 V	4.91	(8)	Member of Castor Moving Group
K2-33	J16102−193	M3.0 V	4.41	(4)	Member of Local Association
1RXS J173353.5+165515	J17338+169	M5.5 V	4.86	(9)	Member of Local Association
LSPM J1925+0938	J19255+096	M8.0 V	5.12	(10)	Spectral type M8.0 V (see Table 4.2)
AU Mic	J20451−313	M1.0 V	4.54	(1)	Member of β Pictoris Moving Group
Ross 695	J12248−182	M2.0 V	5.00	(12)	Behaviour akin to a subdwarf
GJ 625	J16254+543	M1.5 V	4.94	(11)	Behaviour akin to a subdwarf
Ross 730	J19070+208	M2.0 V	4.94	(11)	Behaviour akin to a subdwarf
HD 349726	J19072+208	M2.0 V	4.94	(11)	Behaviour akin to a subdwarf

Notes. Membership in young stellar kinematic groups following Cortés-Contreras et al. in prep. [a]Label column refers to Fig. 4.8. Two and three stars are superimposed under labels (7) and (11), respectively.

4.4   Results and discussion

The stellar atmospheric parameters of the sample computed with STEPARSYN (T_{eff}, log g, [Fe/H]) are given in Table C.3. Since some M-dwarf studies do not consider alpha enhancement in the computation of synthetic spectra (see e.g. Passegger et al., 2018), we corrected our [Fe/H] scale into [Fe/H]$_{\text{corr}}$ in order to compare our results more directly with that of the literature. We did this through a linear interpolation scheme via the `scipy` package between the mass fraction of elements heavier than helium (Z) and the corresponding [Fe/H] value in alpha-enhanced and alpha-solar (i.e. no alpha enhancement) models, respectively, as shown in Fig. 4.9. The correspondence between Z and [Fe/H] was adopted from the MARCS atmosphere models with standard and alpha-poor compositions[6]. The interpolation scheme retrieves the [Fe/H]$_{\text{corr}}$ value that corresponds to a given Z defined by the original [Fe/H] scale.

We note the limitations of our methodology with respect to the analysis of M dwarfs with spectral types M8.0 V or later due to the scarcity of useful Fe I and Ti I lines and the poor sensitivity of the TiO molecular bands to T_{eff} as a result of dust formation in the stellar photospheres (Tsuji et al., 1996; Allard et al., 2001). Furthermore, the version of the BT-Settl models used in this work does not allow for the formation of enough dust in very late M dwarfs (Allard et al., 2012). However, we note that this limit in spectral type is similar to other studies based on spectral synthesis in M dwarfs (Rajpurohit et al., 2018b; Schweitzer et al., 2019).

We compared our results against some recent M-dwarf studies, including Passegger et al. (2019, Fig. 4.10), Rojas-Ayala et al. (2012, Fig. C.10), Gaidos & Mann (2014, Fig. C.11), Maldonado et al. (2015, Fig. C.12), Mann et al. (2015, Fig. C.13), Passegger et al. (2018, Fig. C.14), Rajpurohit et al. (2018b, Fig. C.15), Schweitzer et al. (2019, Fig. C.16), Maldonado et al. (2020, Fig. C.17), and Passegger et al. (2020, Fig. C.18). The approaches to the computation of stellar parameters in the M-dwarf regime are manifold and generally dependent on the covered wavelength region $\Delta\lambda$, the spectral resolution R, and the S/N of the spectra. For instance, T_{eff} can be derived from the H$_2$O-K2 index (Rojas-Ayala et al., 2012), the pseudo-EW of spectral features (Maldonado et al., 2015, 2020), and spectral fitting to a variety of synthetic grids, including PHOENIX-ACES (Passegger et al., 2018; Schweitzer et al., 2019), PHOENIX-SESAM (Passegger et al., 2019), and grids based on BT-Settl models (Gaidos & Mann, 2014; Mann et al., 2015; Rajpurohit et al., 2018b). As for log g, in some studies it is left as a free parameter in the fitting procedure (Rajpurohit et al., 2018b), while in others log g is kept fixed instead based on evolutionary models to break the observed degeneracy in the M-dwarf parameter space (Rojas-Ayala et al., 2012; Passegger et al., 2018, 2019). In other cases, log g is derived indirectly from the stellar masses and radii obtained from different approaches, primarily semi-empirical calibrations (Gaidos & Mann, 2014; Mann et al., 2015; Maldonado et al., 2015, 2020; Schweitzer et al., 2019). Lastly, stellar metallicity is usually derived from semi-empirically calibrated relations established between the spectral features of M dwarfs that are companions of FGK-type stars with known metallicities (Terrien et al., 2012; Mann et al., 2013a, 2014, 2015; Newton et al., 2014; Neves et al., 2014; Maldonado et al., 2015, 2020), and the use of weights in the spectral fitting for spectral features that appear to be more sensitive to metallicity variations (Passegger et al., 2016, 2018, 2019).

To explore possible sources of systematic trends or offsets, we followed the same Monte Carlo method as in Tabernero et al. (2018). We generated 10 000 artificial samples based on the stellar atmospheric parameters derived with STEPARSYN by assuming a normal distribution centred at the original measurements, and widths equal to the uncertainties in the parameters. The summary of these Monte Carlo simulations can be found in Table 4.5. We computed the Pearson (r_{p}) and the Spearman (r_{s}) correlation coefficients, which quantify the degree of correlation between any two given variables. Our temperature scale appears to have an intrinsic systematic offset relative to the

---

[6]https://marcs.astro.uu.se/
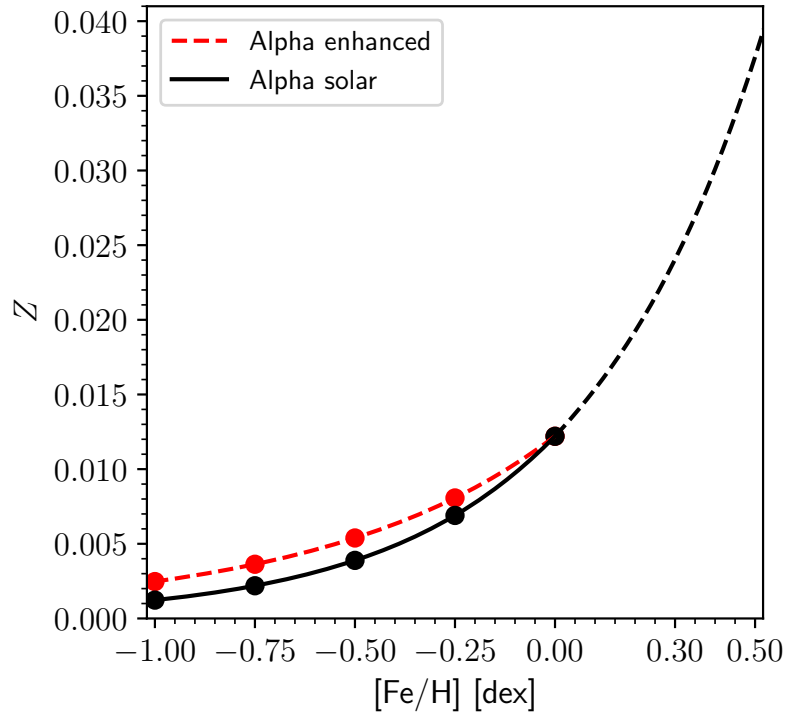
FIGURE 4.9.   Interpolation scheme between Z and [Fe/H] in alpha-enhanced (red) and alpha-solar (black) models.

literature values in the range from 4 K to 85 K. The offset is smallest for Gaidos & Mann (2014) and largest for Mann et al. (2015). In other words, all literature sources report on average slightly lower effective temperatures. However, we note that the offsets are compatible with zero in all instances but Mann et al. (2015). Regarding $\log g$, our values appear to be higher (between 0.02 and 0.17 dex on average with respect to the literature), except for Rajpurohit et al. (2018b), although even in that case the discrepancies are compatible with zero. As to metallicity, our [Fe/H] scale seems to agree best with the results by Rojas-Ayala et al. (2012), Mann et al. (2015), and Maldonado et al. (2015, 2020). In contrast, larger discrepancies in metallicity can be seen when comparing our results with Passegger et al. (2018, 2019), and Schweitzer et al. (2019). Among the plausible explanations are the use of different synthetic models, minimisation algorithms, and sets of lines in their analyses, especially K I lines, which have been shown to be affected by non-LTE effects that can translate into metallicity corrections of the order of 0.2 dex (Olander et al., 2021).
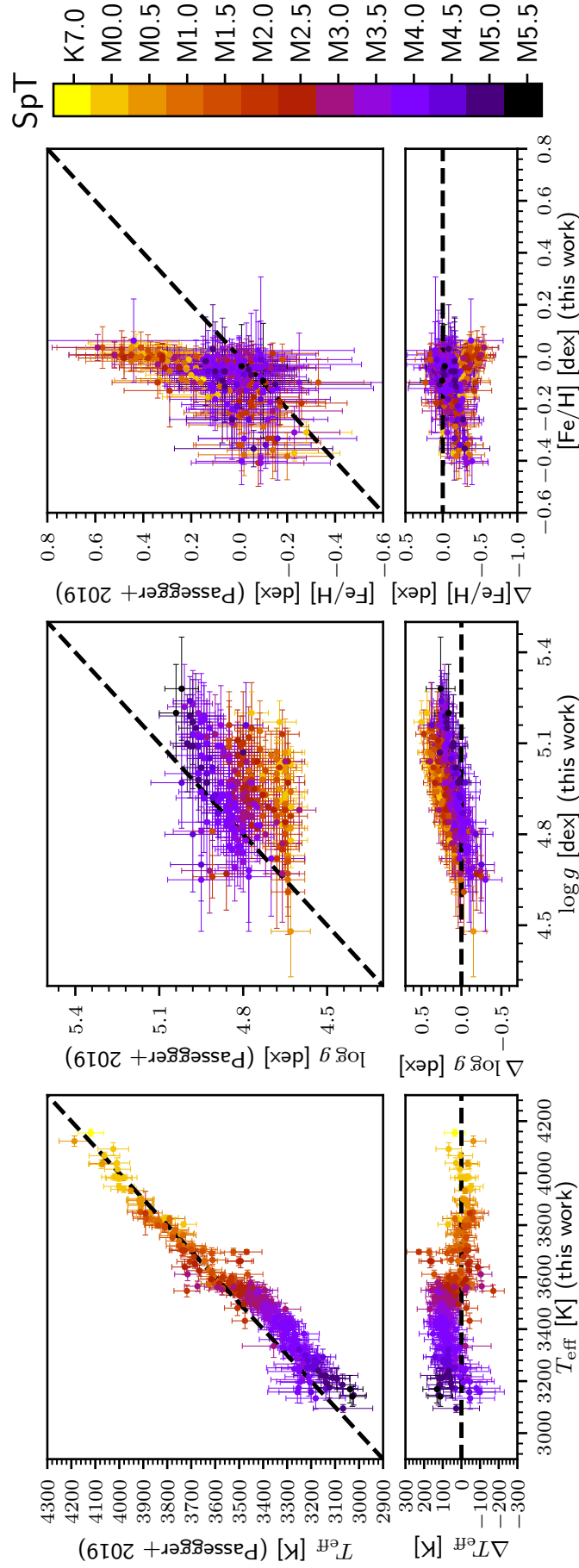
FIGURE 4.10. Comparison between this work and the VIS+NIR analysis done by Passegger et al. (2019). Spectral types are colour-coded. The dashed black lines indicate the 1:1 relationship.
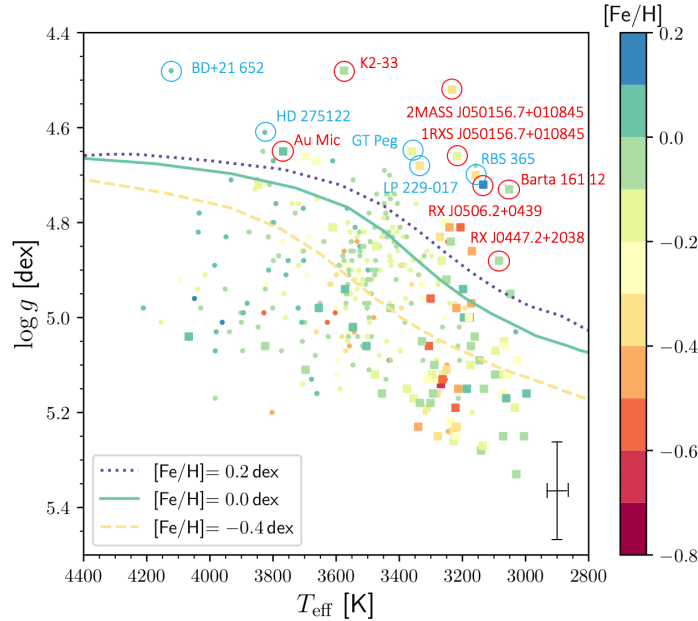
FIGURE 4.11. Kiel diagram of the sample showing the parameters computed with STEPARSYN. Squares depict Hα-active stars. The metallicity [Fe/H]$_{corr}$ is colour-coded. Lines correspond to 5-Ga PARSEC isochrones with [Fe/H] = −0.4, 0.0, and 0.2 dex (Bressan et al., 2012). Typical uncertainties in log g and T_{eff} are shown in the bottom-right corner. Outliers in log g are marked with red and blue circles (see Sect. 4.4 for details).

Regarding the comparison between our results and the prior distributions, we find that the spectroscopic T_{eff} values are higher by 136 ± 88 K, which is in agreement with the findings of Cifuentes et al. (2020) when comparing their estimations using photometry and vosa to spectroscopic studies, namely Passegger et al. (2019) and Rajpurohit et al. (2018b). This difference is in turn more noticeable towards the mid-type and late M dwarfs, probably due to missing opacity sources. Regarding log g, it also seems to be higher by 0.08 ± 0.14 dex with respect to the prior values.

Similarly to Fig. 4.8, Fig. 4.11 is a Kiel diagram of our sample showing the results obtained with STEPARSYN along with theoretical isochrones from the PAdova and TRieste Stellar Evolution Code (PARSEC, Bressan et al., 2012). Since M dwarfs evolve very slowly once they reach the main sequence (Burrows et al., 1997), we selected a set of isochrones with an age of 5 Ga and different compositions, namely [Fe/H] = −0.4, 0.0, and 0.2 dex. Active and inactive stars in Fig 4.11 are shown with different symbols. First, we note that the fraction of active stars increases towards the late M-dwarf regime, as discussed by Tal-Or et al. (2018) and Reiners et al. (2018). While some stars fall inside the region encompassed by the isochrones, we note that most of them deviate towards higher values of log g. However, the trend established by the isochrones is preserved in the retrieved log g values throughtout the diagram. Aditionally, conspicuous outliers have been labelled and marked with red and blue circles. Red circles denote seven of the ten targets identified as young according to Table 4.4, whereas blue circles indicate other stars that also correspond to higher log g values. We note that most of them are active stars, with the exception of the early M dwarfs BD+21 652 and HD 275122.

In light of such a large dispersion in log g, we performed an additional run by fixing log g to the prior values. The results of this run ($T_{eff, fixed}$, [Fe/H]$_{fixed}$, and [Fe/H]$_{corr, fixed}$) can also be found in Table C.3. In Fig. 4.12 we show the differences in T_{eff} and [Fe/H] between these two runs. The impact of fixing log g on T_{eff} is well below 100 K for most targets, whereas the impact on [Fe/H] is between 0.1 and 0.2 dex in most cases. In general terms, the larger the difference in log g between the runs, the larger the change in [Fe/H], as expected.

To check our metallicity scale, in Fig. 4.13 we compare the M-dwarf metallicity distribution
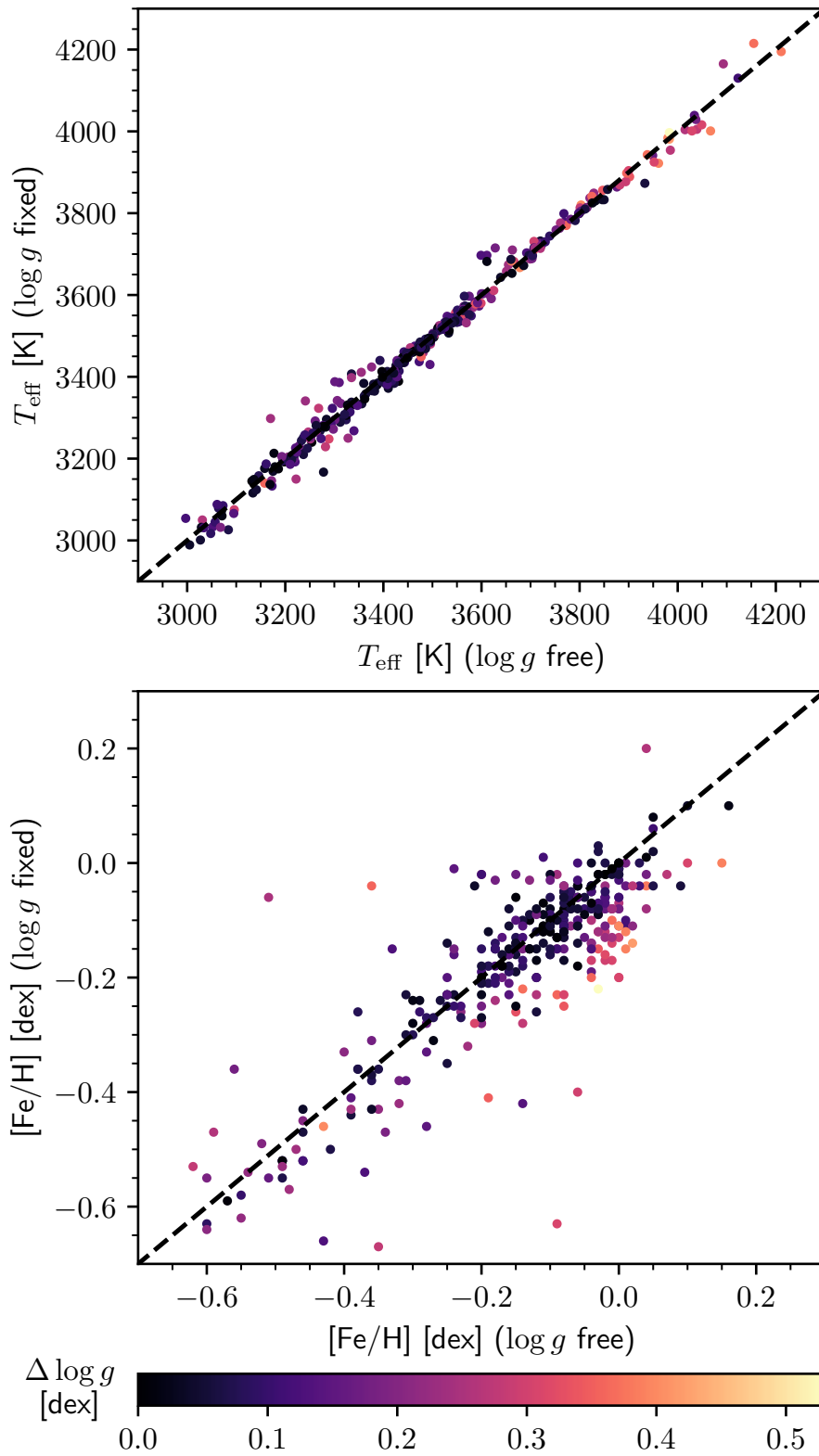
FIGURE 4.12. Comparison of T_{eff} (*top panel*) and [Fe/H] (*bottom panel*) between the runs with free and fixed $\log g$. The quantity $\Delta \log g$ is calculated as $\log g$ (prior) $- \log g$ (free).
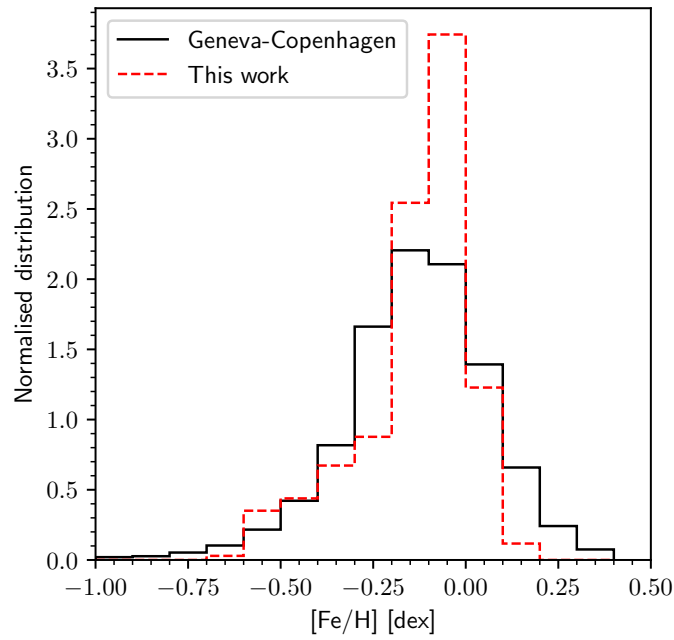
FIGURE 4.13. Metallicity distribution in this work and in the Geneva-Copenhagen survey (Nordström et al., 2004).
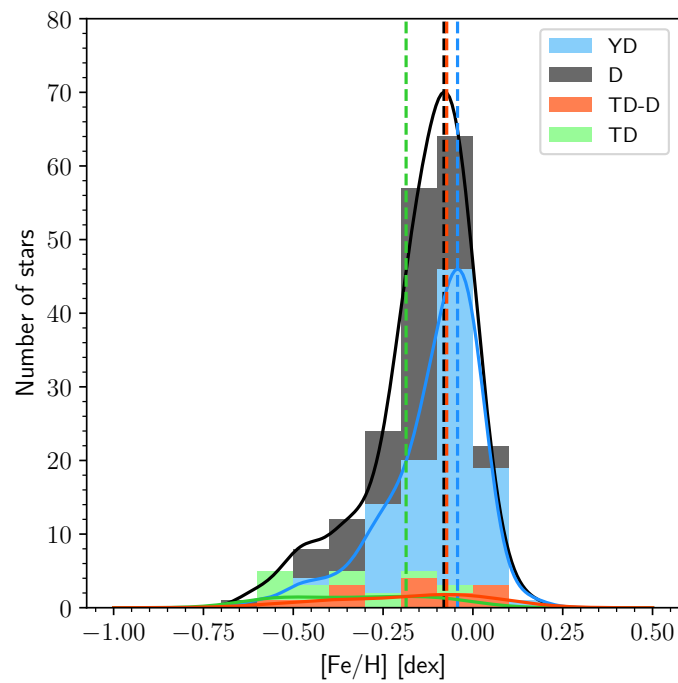
FIGURE 4.14. M-dwarf metallicity distributions separated by the kinematic membership of the targets in the thick disc (TD), the thick disc-thin disc transition (TD-D), the thin disc (D), and the young disc (YD), following Cortés-Contreras et al. in prep. The vertical dashed lines indicate the peak of the distributions.

presented in this work to that from the Geneva-Copenhagen survey (Nordström et al., 2004), which comprises around 14 000 F- and G-type dwarfs in the solar neighbourhood, and is volume-complete to a distance of ~40 pc. We note that the two distributions are very similar in the low-metallicity regime, whereas high-metallicity stars appear to be marginally underrepresented. There appears to be an excess of M dwarfs with solar metallicity and we retrieve no metallicity higher than 0.25 dex. The scarcity of high-metallicity values is also noticeable when comparing our determinations with the literature, as shown in Figs. C.10 (Rojas-Ayala et al., 2012), C.11 (Gaidos & Mann, 2014), and C.13 (Mann et al., 2015).

We also investigated the M-dwarf metallicity distribution in terms of the kinematic membership of the stars in the Galactic populations, namely the thick disc (TD), the thick disc-thin disc transition (TD-D), the thin disc (D), and the young disc (YD) (Montes et al., 2001, Cortés-Contreras et al. in prep.), as shown in Fig. 4.14. It can be seen that the mean metallicity of M dwarfs belonging to the TD is lower than that of those belonging to the D, in accordance with the results presented by Bensby et al. (2003, 2005).

4.4.1   M dwarfs with interferometric angular measurements

In Table 4.6 we compile the 18 M dwarfs in our sample with interferometrically measured radii from Boyajian et al. (2012b) and von Braun et al. (2014), which may be used along with other information (e.g. trigonometric parallax, bolometric flux, isochrone fitting, and mass-luminosity relations) to derive T_{eff} and $\log g$ independently from spectroscopy. For this reason, this set of stars is particularly helpful as a benchmark test for any method aimed at determining stellar atmospheric parameters (Casagrande et al., 2008; Mann et al., 2015; Birky et al., 2020).

Fig. 4.15 shows the comparison in T_{eff} and $\log g$ for these M dwarfs between Boyajian et al. (2012b), von Braun et al. (2014), and this work. The $\log g$ value was computed from the stellar mass and radius using the standard definition (i.e. $g = GM/R^2$, where G is the gravitational constant). In general, we find good agreement, with systematic offsets of 72 ± 67 K in T_{eff}, and 0.10 ± 0.09 dex in $\log g$. However, we note two outliers in T_{eff}, namely Il Aqr and HD 173740, which show a difference around 300 K between the interferometric and the spectroscopic approaches. Interestingly enough, HD 173740 also belongs to a wide binary system together with HD 173739, as discussed in Sect. 4.4.3. Although they exhibit similar chemical compositions and differ by only one spectral subtype, the T_{eff} derived from interferometry appears to be irreconcilable between the two components. In contrast, we derived very similar T_{eff} with STEPARSYN for both components. However, accounting for this difference is beyond the scope of this paper.
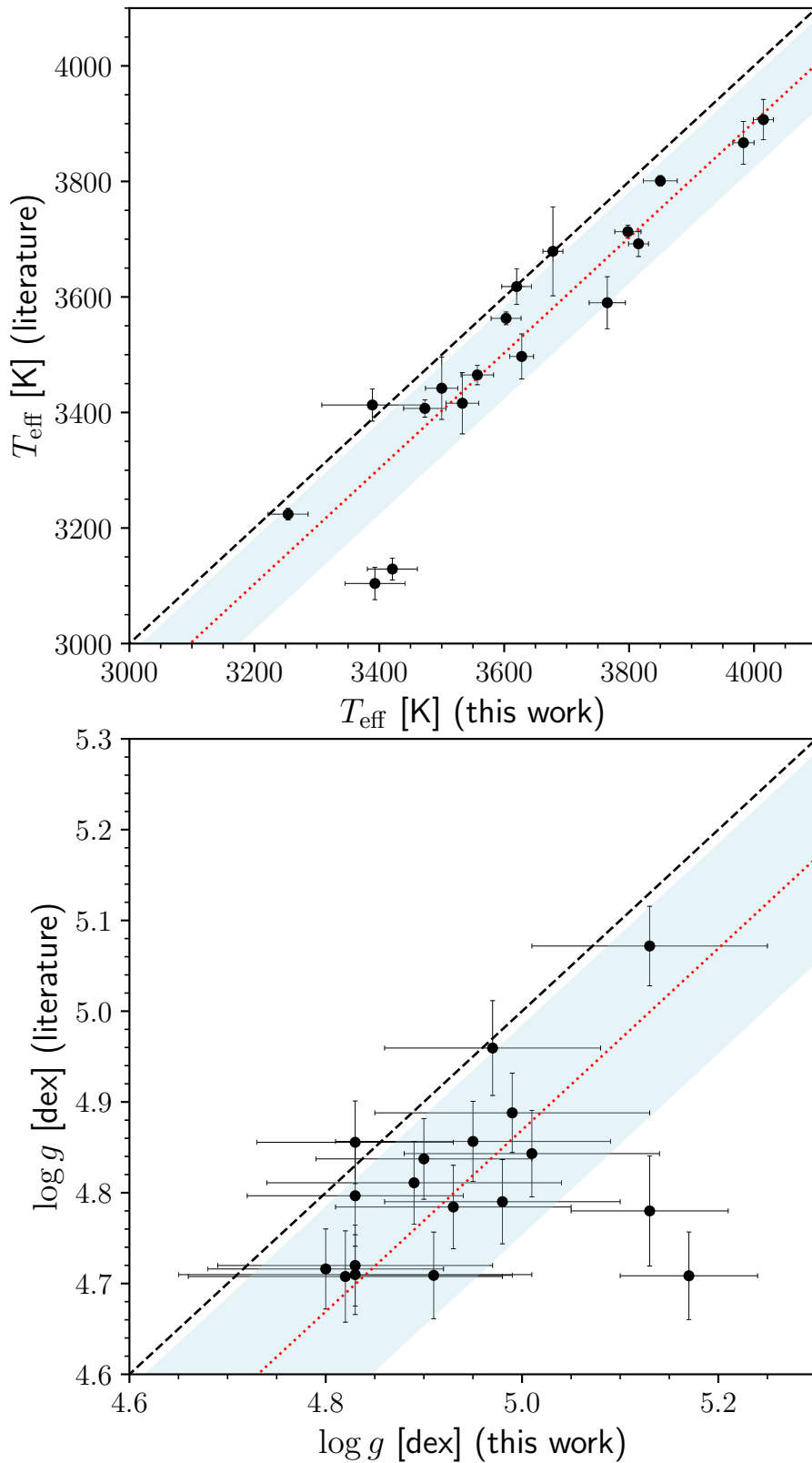
FIGURE 4.15. Comparison in $T_{\rm eff}$ (*upper panel*) and $\log g$ (*bottom panel*) for M dwarfs with interferometric angular measurements (see Table 4.6). The dashed black lines indicate the 1:1 relationship, whereas the dotted red lines show the 1:1 relationship, shifted following the average differences in each parameter. The blue shaded region denotes the 1σ level.

TABLE 4.5. Summary of the Monte Carlo simulations on $T_{\rm eff}$, $\log g$, and [Fe/H] between different comparison samples.

Sample	Size	Parameter	Difference	$r_{\rm p} \pm \sigma_{\rm p}$	$r_{\rm s} \pm \sigma_{\rm s}$
Rajpurohit et al. (2018b)	292	$T_{\rm eff}$	64 ± 95 K	0.807 ± 0.016	0.824 ± 0.013
		$\log g$	-0.23 ± 0.30 dex	0.069 ± 0.054	0.051 ± 0.054
		[Fe/H]	-0.25 ± 0.28 dex	0.079 ± 0.054	0.084 ± 0.053
Schweitzer et al. (2019)	287	$T_{\rm eff}$	25 ± 53 K	0.937 ± 0.006	0.940 ± 0.005
		$\log g$	0.03 ± 0.20 dex	0.253 ± 0.040	0.288 ± 0.039
		[Fe/H]	-0.19 ± 0.17 dex	0.397 ± 0.018	0.467 ± 0.013
Passegger et al. (2019)	282	$T_{\rm eff}$	48 ± 61 K	0.931 ± 0.007	0.930 ± 0.006
		$\log g$	0.13 ± 0.14 dex	0.223 ± 0.041	0.259 ± 0.042
		[Fe/H]	-0.20 ± 0.15 dex	0.275 ± 0.051	0.288 ± 0.049
Passegger et al. (2018)	235	$T_{\rm eff}$	29 ± 44 K	0.932 ± 0.008	0.945 ± 0.005
		$\log g$	0.02 ± 0.15 dex	0.182 ± 0.045	0.241 ± 0.045
		[Fe/H]	-0.10 ± 0.12 dex	0.288 ± 0.051	0.350 ± 0.048
Maldonado et al. (2020)	102	$T_{\rm eff}$	29 ± 80 K	0.883 ± 0.014	0.877 ± 0.015
		$\log g$	0.08 ± 0.15 dex	0.249 ± 0.071	0.285 ± 0.072
		[Fe/H]	-0.06 ± 0.15 dex	0.312 ± 0.063	0.364 ± 0.065
Mann et al. (2015)	86	$T_{\rm eff}$	85 ± 63 K	0.928 ± 0.011	0.924 ± 0.011
		$\log g$	0.11 ± 0.13 dex	0.355 ± 0.063	0.427 ± 0.060
		[Fe/H]	-0.13 ± 0.13 dex	0.611 ± 0.057	0.648 ± 0.046
Gaidos & Mann (2014)	63	$T_{\rm eff}$	4 ± 76 K	0.850 ± 0.030	0.860 ± 0.023
		$\log g$	0.09 ± 0.15 dex	0.088 ± 0.084	0.156 ± 0.083
		[Fe/H]	-0.12 ± 0.11 dex	0.643 ± 0.064	0.665 ± 0.051
Passegger et al. (2020)	50	$T_{\rm eff}$	23 ± 107 K	0.917 ± 0.017	0.911 ± 0.015
		$\log g$	0.17 ± 0.16 dex	0.341 ± 0.088	0.398 ± 0.098
		[Fe/H]	-0.32 ± 0.12 dex	0.264 ± 0.122	0.245 ± 0.138
Rojas-Ayala et al. (2012)	40	$T_{\rm eff}$	41 ± 124 K	0.915 ± 0.019	0.886 ± 0.021
		$\log g$ [a]	$\dots$	$\dots$	$\dots$
		[Fe/H]	-0.15 ± 0.13 dex	0.513 ± 0.103	0.533 ± 0.099
Maldonado et al. (2015)	21	$T_{\rm eff}$	39 ± 42 K	0.884 ± 0.040	0.883 ± 0.037
		$\log g$	0.12 ± 0.13 dex	0.213 ± 0.169	0.210 ± 0.171
		[Fe/H]	-0.07 ± 0.14 dex	0.576 ± 0.116	0.581 ± 0.100

Notes. We give the average difference on each parameter and the Pearson ($r_{\rm p}$) and the Spearman ($r_{\rm s}$) correlation coefficients (see Sect. 4.4 for details). [a]Rojas-Ayala et al. (2012) fixed $\log g$ to 5.0 dex.

TABLE 4.6. M dwarfs with interferometric angular diameter measurements in common with the CARMENES GTO survey.

Name	Karmn	SpT	R [$R_\odot$]	$T_{\rm eff}$ [K]	$L_{\rm bol}$ [$10^{-4} L_\odot$]	M [$M_\odot$]	Ref. [a]	$T_{\rm eff}$ [b] [K]	$\log g$ [b] [dex]	$[\rm Fe/H]_{\rm corr}$ [b] [dex]
HD 79210	J09143+526	M0.0 V	0.5773 ± 0.0131	3907 ± 35	697 ± 21	0.622	B12	4015 ± 16	4.91 ± 0.08	−0.12 ± 0.05
HD 79211	J09144+526	M0.0 V	0.5673 ± 0.0137	3867 ± 37	647 ± 19	0.600	B12	3983 ± 17	5.17 ± 0.07	−0.03 ± 0.04
GX And	J00183+440	M1.0 V	0.3874 ± 0.0023	3563 ± 11	217.3 ± 2.1	0.423	B12	3603 ± 24	4.99 ± 0.14	−0.52 ± 0.11
BD+44 2051 A	J11054+435	M1.0 V	0.3982 ± 0.0091	3497 ± 39	212.9 ± 2.6	0.403	B12	3628 ± 19	5.01 ± 0.13	−0.56 ± 0.09
BD+25 3173	J16581+257	M1.0 V	0.5387 ± 0.0157	3590 ± 45	432 ± 13	0.54	v14	3782 ± 17	4.87 ± 0.09	−0.05 ± 0.05
HD 199305	J20533+621	M1.0 V	0.5472 ± 0.0067	3692 ± 22	499.0 ± 6.2	0.573	B12	3815 ± 16	4.83 ± 0.14	−0.10 ± 0.08
HD 36395	J05314−036	M1.5 V	0.5735 ± 0.0044	3801 ± 9	616.3 ± 8.8	0.615	B12	3850 ± 27	4.71 ± 0.18	0.05 ± 0.08
Lalande 21185	J11033+359	M1.5 V	0.3921 ± 0.0037	3465 ± 17	198.9 ± 1.2	0.403	B12	3557 ± 26	4.95 ± 0.14	−0.49 ± 0.10
HD 119850	J13457+148	M1.5 V	0.4840 ± 0.0084	3618 ± 31	360 ± 5	0.520	B12	3620 ± 24	4.93 ± 0.12	−0.34 ± 0.07
HD 216899	J22565+165	M1.5 V	0.5477 ± 0.0048	3713 ± 11	511.2 ± 7.4	0.569	B12	3798 ± 21	4.80 ± 0.12	0.03 ± 0.06
HD 285968	J04429+189	M2.0 V	0.4525 ± 0.0221	3679 ± 77	337 ± 18	0.45	v14	3678 ± 16	5.13 ± 0.08	0.00 ± 0.03
Ross 905	J11421+267	M2.5 V	0.4546 ± 0.0182	3416 ± 53	252.5 ± 1.2	0.472	B12	3533 ± 26	4.83 ± 0.11	−0.12 ± 0.10
HO Lib	J15194−077	M3.0 V	0.2990 ± 0.0100	3442 ± 54	113 ± 8	0.297	B12	3500 ± 26	4.97 ± 0.11	−0.08 ± 0.07
BD+68 946	J17364+683	M3.0 V	0.4183 ± 0.0070	3413 ± 28	212.8 ± 2.3	0.413	B12	3389 ± 81	4.89 ± 0.15	−0.06 ± 0.13
HD 173739	J18427+526N	M3.0 V	0.3561 ± 0.0039	3407 ± 15	153.1 ± 1.8	0.318	B12	3473 ± 34	4.90 ± 0.11	−0.31 ± 0.12
Barnard's star	J17578+046	M3.5 V	0.1867 ± 0.0012	3224 ± 10	33.8 ± 0.2	0.150	B12	3254 ± 32	5.13 ± 0.12	−0.57 ± 0.10
HD 173740	J18427+596S	M3.5 V	0.3232 ± 0.0061	3104 ± 28	87.1 ± 1.2	0.235	B12	3393 ± 48	4.98 ± 0.12	−0.38 ± 0.18
IL Aqr	J22532−142	M4.0 V	0.3761 ± 0.0059	3129 ± 19	122 ± 2	0.37	v14	3421 ± 40	4.83 ± 0.10	−0.06 ± 0.10

Notes. [a] Stellar radii, effective temperatures, luminosities, and stellar masses from Boyajian et al. (2012b, B12) and von Braun et al. (2014, v14). The estimates of the stellar mass from these works conservatively assume 10 % and 5 % uncertainties, respectively. [b] This work.

4.4.2   M dwarfs in FGK+M systems

The study of multi-star systems serves as a benchmark test for [Fe/H] given that all components are thought to be formed from the same molecular cloud, be coeval, and have roughly similar chemical compositions (Desidera et al., 2006; Önehag et al., 2012; Souto et al., 2020; Ishikawa et al., 2020). In Table 4.7 we compile all M dwarfs in our sample that are bound in wide physical binaries with an FGK-type primary (Montes et al., 2018). For the FGK-type primaries, we adopted the metallicities from Montes et al. (2018), who employed the STEPAR code (Tabernero et al., 2019) as the preferred implementation of the EW method. For the fast-rotating F7 V star θ Boo A ($v \sin i = 30.4 \text{ km s}^{-1}$, Luck, 2017), we adopted the metallicity from Tabernero et al. (2021b).

In Fig. 4.16 we show the comparison in [Fe/H] between the components in these FGK+M systems. We find good agreement between our [Fe/H] determinations for the M-dwarf secondaries, with an internal scatter of -0.01 ± 0.19 dex, which is similar to what is found in other works (Souto et al., 2020; Antoniadis-Karnavas et al., 2020). The largest discrepancy in metallicity between components is found for ρ Cnc B. If we assume a homogeneous chemical composition in FGK+M systems, this star also exhibits a C/O ratio that is larger than expected for an M dwarf, since C/O = 1.12 for the primary star (Delgado Mena et al., 2010). We note that the pseudo-continuum level is very sensitive to C/O and alterations in C/O can explain a large fraction of the variation in the strength of the atomic metal lines in M-dwarf spectra (Veyette et al., 2016; Souto et al., 2020). However, disentangling the effect of C/O on [Fe/H] computations is beyond the scope of this paper.

4.4.3   M dwarfs in M+M systems

Similarly to FGK+M systems, wide physical M+M binaries can also prove useful as a benchmark test for [Fe/H]. In this case, both components are analysed with the same methodology, i.e. spectral synthesis. In Table 4.9 we list the astrometric parameters (parallax π, proper motion μ, and radial velocity v_r) along with the stellar atmospheric parameters (T_{eff}, $\log g$, and [Fe/H]) of the 32 M dwarfs in our sample bound in M+M systems. These include two SB2 systems (EZ Psc and GJ 810) and the M8.0 V star V1298 Aql, for which no reliable parameter determinations could be made (see Table 4.1). Parallaxes and proper motions were compiled from the *Gaia* DR2 and EDR3 releases (Gaia Collaboration et al., 2018, 2021).

In Fig. 4.16 we compare the metallicity computed in this work for both components, in the same way as for the FGK+M wide binaries. The mean difference in [Fe/H] between components is 0.10 ± 0.08 dex, which is in agreement with other works (0.06 ± 0.07 dex, Antoniadis-Karnavas et al., 2020). However, we note that the differences become larger (i.e. up to ~0.2 dex) in cases where the components differ by more than one spectral type.
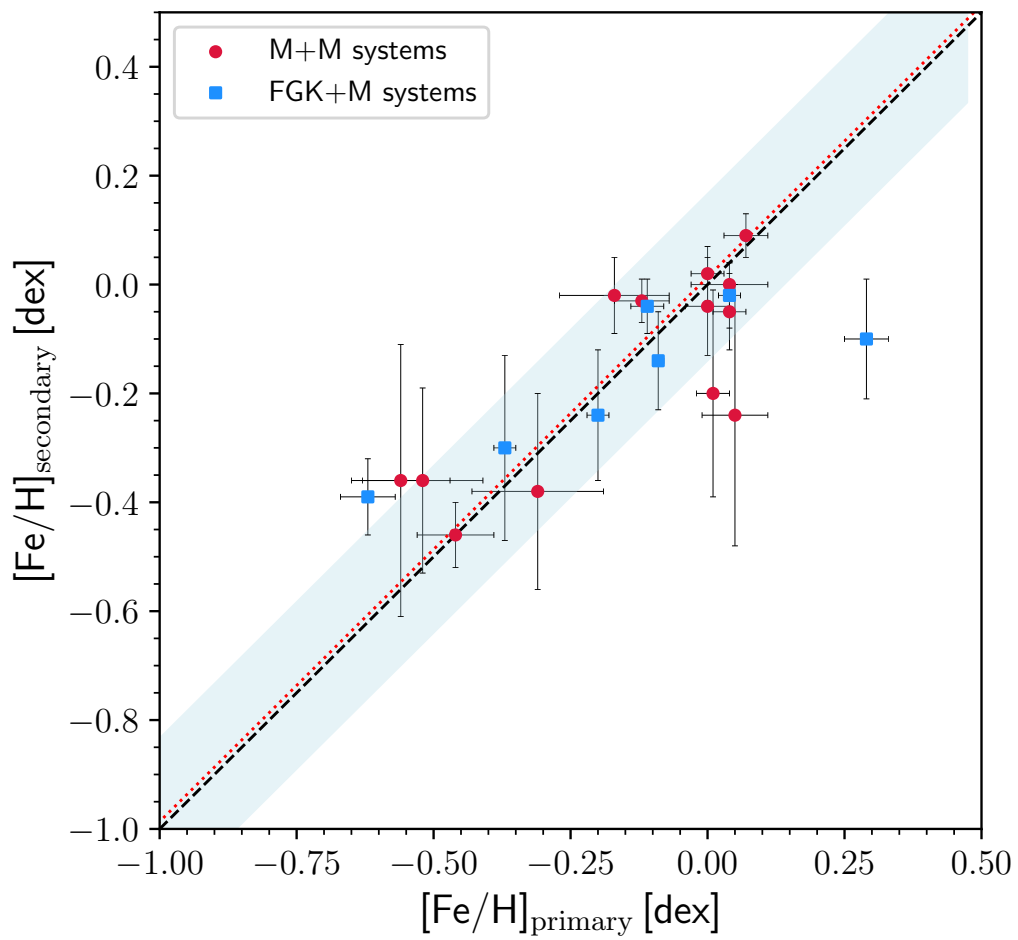
FIGURE 4.16. Same as Fig. 4.15, but for the comparison in [Fe/H] between the components in FGK+M (blue) and M+M (red) systems (see Tables 4.7 and 4.9).

TABLE 4.7. M dwarfs in wide physical binaries with FGK-type primaries in common with the CARMENES GTO survey.

Primary			Secondary					
Name	SpT	[Fe/H] [dex]	Name	Karmn	SpT	T_{eff} [K]	$\log g$ [dex]	[Fe/H]$_{corr}$ [dex]
V538 Aur	K1 V	0.04 ± 0.02	HD 233153	J05415+534	M1.0 V	3825 ± 14	4.94 ± 0.10	-0.02 ± 0.06
V869 Mon	K0/2 V	-0.11 ± 0.03	GJ 282 C	J07361−031	M1.0 V	3825 ± 12	5.06 ± 0.08	-0.04 ± 0.06
HD 15436	K5 V	-0.62 ± 0.05	HD 154363 B	J17052−050	M1.5 V	3587 ± 14	4.89 ± 0.10	-0.39 ± 0.07
θ Boo A	F7 V	-0.09 ± 0.01	θ Boo B	J14251+518	M2.5 V	3551 ± 22	4.90 ± 0.10	-0.14 ± 0.06
HD 16160	K3 V	-0.20 ± 0.02	BX Cet	J02362+068	M4.0 V	3335 ± 45	4.91 ± 0.10	-0.24 ± 0.12
o^{02} Eri A	K0.5 V	-0.37 ± 0.02	o^{02} Eri C	J04153−076	M4.5 V	3179 ± 61	5.00 ± 0.18	-0.30 ± 0.17
ρ Cnc	G8 V	0.29 ± 0.04	ρ Cnc B	J08526+283	M4.5 V	3321 ± 37	4.87 ± 0.08	-0.10 ± 0.11

Notes. Metallicities of the FGK-type primary stars from Montes et al. (2018), except for θ Boo A, which is from Tabernero et al. (2021b). Stellar atmospheric parameters of the M-dwarf secondaries (T_{eff}, $\log g$, and [Fe/H]) as computed in this work.

TABLE 4.8. Parameters derived for the reference stars with different synthetic grids.

Reference star	Grid	T_{eff} [K]	$\log g$ [dex]	[Fe/H]$_{\text{corr}}$ [dex]
GX And	BT-Settl	3603 ± 24	4.99 ± 0.14	-0.52 ± 0.11
	MARCS	3675 ± 30	4.90 ± 0.10	-0.45 ± 0.08
	PHOENIX-ACES	3664 ± 37	4.84 ± 0.12	-0.54 ± 0.13
Luyten's star	BT-Settl	3380 ± 43	4.96 ± 0.11	-0.11 ± 0.11
	MARCS	3429 ± 38	4.88 ± 0.10	-0.08 ± 0.09
	PHOENIX-ACES	3412 ± 50	4.81 ± 0.14	-0.19 ± 0.12
Teegarden's star	BT-Settl	3034 ± 45	5.19 ± 0.20	-0.11 ± 0.28
	MARCS	3072 ± 51	5.08 ± 0.16	-0.13 ± 0.24
	PHOENIX-ACES	3081 ± 57	5.10 ± 0.17	-0.24 ± 0.25

4.4.4   Choice of model atmospheres

Recent studies have shown that different parameter determination methods can lead to significant variations in the results for the same stars (Blanco-Cuaresma, 2019; Passegger et al., 2021). These differences can be attributed to a number of factors, including the choice of model atmospheres, atomic and molecular data, and radiative transfer code. For this reason, we performed a test on the reference stars (i.e. GX And, Luyten's star, and Teegarden's star) with the aim of evaluating the impact of different sets of models on our parameter computations with STEPARSYN.

We first computed a synthetic grid based on MARCS models by following the same procedure as described in Sect. 4.3.3. We set the MARCS grid from 2500 K to 3900 K, 4.0 dex to 5.5 dex, and -1.0 dex to $+1.0$ dex, in steps of 100 K, 0.5 dex, and 0.25 dex in T_{eff}, $\log g$, and [Fe/H], respectively. Similarly, we adopted the PHOENIX-ACES grid used by Passegger et al. (2021), which ranges from 2700 K to 4500 K, 4.2 dex to 5.5 dex, and -1.0 to $+0.8$ dex, in steps of 100 K, 0.1 dex, and 0.1 dex in T_{eff}, $\log g$, and [Fe/H], respectively. While the MARCS grid is based on atmosphere models with standard composition and, thus, follows the same scaled [α/Fe] pattern as the BT-Settl grid, the PHOENIX-ACES grid has [α/Fe] = 0 since models with [α/Fe] $\neq$ 0 are only available for T_{eff} > 3500 K (Husser et al., 2013; Passegger et al., 2018). Therefore, metallicities derived with the PHOENIX-ACES grid do not need to be corrected with the interpolation scheme described in Sect. 4.4.

In Table 4.8 we list the parameters obtained for the reference stars and the considered grids (BT-Settl, MARCS, and PHOENIX-ACES). The derived $\log g$ and [Fe/H] values agree within uncertainties for all models, while the average differences in T_{eff}, $\log g$, and [Fe/H] between models are around 32 K, 0.11 dex, and 0.06 dex, respectively. In addition, the derived T_{eff} values appear to be slightly higher when using the MARCS and PHOENIX-ACES models. In contrast, $\log g$ values are slightly lower. The differences in these results might arise from the synthetic gap (Passegger et al., 2020), that is, the fact that synthetic spectra do not perfectly match the observed spectra as a result of the underlying chemo-physical assumptions (e.g. different equations of state). However, a more detailed study is required to further explore the origin of these small discrepancies.

4.5   Summary and conclusions

We have computed the stellar atmospheric parameters (T_{eff}, $\log g$, [Fe/H], and [Fe/H]$_{\text{corr}}$) of 342 M dwarfs observed with CARMENES with the STEPARSYN code as a Bayesian implementation of the spectral synthesis technique, along with a grid of BT-Settl models, and the radiative transfer

code `turbospectrum`. We excluded one eclipsing binary, ten SB2 binaries, two triple-line spectroscopic triple systems, and three targets with low-quality spectra to prevent unreliable parameter determinations. To avoid any potential degeneracy in the M-dwarf parameter space, we imposed prior probability distributions in T_{eff} and $\log g$ based on the comprehensive, multi-band photometric data available for the sample (Cifuentes et al., 2020). Our method is suited for the M sequence from M0.0 V to M7.0 V, but not beyond, due to the scarcity of Ti ɪ and Fe ɪ lines at M8.0 V and later spectral types, as well as the insensitivity of TiO bands to T_{eff} as a result of dust formation (Tsuji et al., 1996; Allard et al., 2001).

We selected 75 Fe ɪ and Ti ɪ lines in the VIS and NIR wavelength regions covered by CARMENES. Following the prescriptions of Passegger et al. (2019), NIR lines with low Landé factors (i.e. $g_{\mathrm{eff}} < 1.5$) were selected to minimise the impact of the stellar magnetic field on parameter computations. Even so, some Fe ɪ and Ti ɪ lines appear to be highly sensitive to chromospheric activity and the stellar magnetic field and were excluded in the analysis of the active stars in our sample based on the Hα flag. Such lines will be discussed in a future publication (López-Gallifa et al. in prep.).

We also compared our derived parameters with some recent M-dwarf studies in the literature (Rojas-Ayala et al., 2012; Maldonado et al., 2015, 2020; Mann et al., 2015; Rajpurohit et al., 2018b; Schweitzer et al., 2019; Passegger et al., 2018, 2019, 2020), finding similar T_{eff} but disparate metallicity scales. The metallicity determinations that correlate best with the literature are the [Fe/H]$_{\mathrm{corr}}$ values since they are corrected from the α enhancement of the synthetic grid. The best agreement in metallicity is found when comparing with Mann et al. (2015), Gaidos & Mann (2014), and Rojas-Ayala et al. (2012). The M-dwarf metallicity distribution for our sample is also in agreement with both the Geneva-Copenhagen survey of FG-type stars in the solar neighbourhood (Nordström et al., 2004) and the kinematic membership of the targets in the Galactic populations (Cortés-Contretas et al. in prep.). Regarding $\log g$, we find larger values than the ones reported in the literature, although fixing $\log g$ to the prior values does not have a strong impact on either the derived T_{eff} or the [Fe/H] scales. As a benchmark test, we placed special emphasis on the M dwarfs with interferometrically measured radii (Boyajian et al., 2012b; von Braun et al., 2014), wide physical FGK+M binaries (Montes et al., 2018), and M+M systems. Despite systematic offsets that are inherent to any methodology, we find that our parameter determinations are fairly consistent with the literature values in all these cases.

TABLE 4.9. Astrometric and stellar atmospheric parameters of the M dwarfs bound in M+M systems in the CARMENES GTO sample.

Karmn	Name	SpT	π [mas]	$\mu_\alpha \cos\delta$ [mas a⁻¹]	μ_δ [mas a⁻¹]	v_r [km s⁻¹]	T_{eff} [K]	$\log g$ [dex]	[Fe/H]$_{corr}$ [dex]
J00162+198E	LP 404−062	M4.0 V	65.05 ± 0.04	708.14 ± 0.05	−748.88 ± 0.04	−1.62 ± 0.02	3329 ± 30	4.93 ± 0.07	−0.11 ± 0.09
J00162+198W	EZ Psc AB [a]	M4.0 V	65.11 ± 0.04	714.64 ± 0.05	−761.97 ± 0.04	−0.50 ± 0.04	...	...	...
J00183+440	GX And	M1.0 V	280.71 ± 0.02	2891.52 ± 0.02	411.83 ± 0.01	+11.48 ± 0.02	3603 ± 24	4.99 ± 0.14	−0.52 ± 0.11
J00184+440	GQ And	M3.5 V	280.69 ± 0.03	2862.80 ± 0.02	336.43 ± 0.02	+10.68 ± 0.03	3318 ± 53	5.20 ± 0.11	−0.36 ± 0.17
J01026+623	BD+61 195	M1.5 V	101.42 ± 0.02	731.09 ± 0.01	90.53 ± 0.02	−6.30 ± 0.02	3791 ± 19	4.76 ± 0.11	0.05 ± 0.06
J01033+623	V388 Cas	M5.0 V	101.37 ± 0.05	730.40 ± 0.04	85.97 ± 0.05	−6.52 ± 0.08	3057 ± 49	5.12 ± 0.18	−0.24 ± 0.24
J02489−145W	PM J02489−1432W	M2.0 V	26.57 ± 0.03	164.07 ± 0.03	46.55 ± 0.03	+32.27 ± 0.06	3655 ± 25	4.98 ± 0.10	0.04 ± 0.05
J02489−145E	PM J02489−1432E	M2.5 V	26.54 ± 0.02	174.43 ± 0.03	45.47 ± 0.03	+32.40 ± 0.06	3572 ± 27	4.94 ± 0.12	0.00 ± 0.04
J05365+113	V2689 Ori	M0.0 V	87.53 ± 0.02	−2.82 ± 0.03	−56.35 ± 0.02	+21.51 ± 0.02	4067 ± 14	5.04 ± 0.07	0.01 ± 0.03
J05366+112	PM J05366+1117	M4.0 V	87.35 ± 0.03	−3.32 ± 0.04	−60.84 ± 0.03	+21.53 ± 0.02	3355 ± 23	5.17 ± 0.16	−0.20 ± 0.10
J09143+526	HD 79210	M0.0 V	157.89 ± 0.02	−1545.79 ± 0.02	−569.05 ± 0.02	+10.69 ± 0.02	4015 ± 16	4.91 ± 0.08	−0.12 ± 0.05
J09144+526	HD 79211	M0.0 V	157.88 ± 0.02	−1573.04 ± 0.02	−659.91 ± 0.02	+11.90 ± 0.02	3983 ± 12	5.17 ± 0.07	−0.03 ± 0.04
J09425+700	GJ 360	M2.0 V	84.33 ± 0.02	−671.78 ± 0.02	−271.16 ± 0.02	+6.70 ± 0.02	3547 ± 23	5.02 ± 0.12	0.00 ± 0.03
J09428+700	GJ 362	M3.0 V	84.30 ± 0.02	−670.96 ± 0.02	−265.46 ± 0.02	+6.35 ± 0.03	3504 ± 30	5.06 ± 0.12	0.02 ± 0.05
J11054+435	BD+44 2051 A	M1.0 V	203.89 ± 0.03	−4406.47 ± 0.03	938.53 ± 0.03	+68.58 ± 0.02	3628 ± 19	5.01 ± 0.13	−0.56 ± 0.09
J11055+435	WX UMa	M5.5 V	203.83 ± 0.05	−4339.85 ± 0.05	960.70 ± 0.04	+69.16 ± 0.02	3278 ± 86	5.25 ± 0.20	−0.36 ± 0.25
J11110+304E	HD 97101 A	K7.0 V	84.18 ± 0.03	591.60 ± 0.02	−197.12 ± 0.03	−16.00 ± 0.03	4211 ± 13	4.98 ± 0.07	0.04 ± 0.03
J11110+304W	HD 97101 B	M2.0 V	84.16 ± 0.02	604.91 ± 0.02	−206.05 ± 0.02	−15.69 ± 0.02	3730 ± 20	4.78 ± 0.13	−0.05 ± 0.07
J14257+236W	BD+24 2733 A	M0.0 V	61.24 ± 0.02	792.55 ± 0.01	−1116.41 ± 0.02	+8.88 ± 0.02	3985 ± 13	4.89 ± 0.08	0.07 ± 0.04
J14257+236E	BD+24 2733 B	M0.5 V	61.20 ± 0.02	793.44 ± 0.01	−1118.91 ± 0.02	+7.96 ± 0.02	3933 ± 12	4.71 ± 0.11	0.09 ± 0.04
J16167+672S	HD 147379	M0.0 V	92.88 ± 0.01	−497.92 ± 0.02	84.05 ± 0.02	−19.36 ± 0.02	4034 ± 17	4.78 ± 0.09	0.00 ± 0.04
J16167+672N	EW Dra	M3.0 V	92.90 ± 0.02	−483.01 ± 0.02	89.05 ± 0.02	−18.78 ± 0.03	3569 ± 32	4.97 ± 0.11	−0.02 ± 0.06
J16554−083N	GJ 643	M3.5 V	153.88 ± 0.05	−817.58 ± 0.05	−898.60 ± 0.04	+15.50 ± 0.03	3397 ± 33	5.07 ± 0.12	−0.17 ± 0.10
J16555−083	vB 8	M7.0 V	153.97 ± 0.06	−813.04 ± 0.06	−870.61 ± 0.04	+14.41 ± 0.03	3005 ± 21	5.25 ± 0.18	−0.04 ± 0.09
J18427+596N	HD 173739	M3.0 V	283.84 ± 0.02	−1311.68 ± 0.03	1792.33 ± 0.03	−0.75 ± 0.08	3473 ± 34	4.90 ± 0.11	−0.31 ± 0.12
J18427+596S	HD 173740	M3.5 V	283.84 ± 0.03	−1400.26 ± 0.04	1862.53 ± 0.03	+1.02 ± 0.08	3393 ± 48	4.98 ± 0.12	−0.38 ± 0.18
J19070+208	Ross 730	M2.0 V	113.25 ± 0.03	−478.27 ± 0.02	−349.09 ± 0.03	+32.06 ± 0.02	3543 ± 21	5.03 ± 0.12	−0.46 ± 0.07
J19072+208	HD 349726	M2.0 V	113.22 ± 0.02	−480.75 ± 0.02	−332.50 ± 0.02	+31.83 ± 0.02	3558 ± 19	5.06 ± 0.10	−0.46 ± 0.06

TABLE 4.9. *continued*

Karmn	Name	SpT	π [mas]	$\mu_\alpha \cos\delta$ [mas a^{-1}]	μ_δ [mas a^{-1}]	v_r [km s^{-1}]	$T_{\rm eff}$ [K]	$\log g$ [dex]	[Fe/H]$_{\rm corr}$ [dex]
J19169+051N	V1428 Aql	M2.5 V	169.06 ± 0.02	−579.08 ± 0.03	−1332.87 ± 0.02	+35.61 ± 0.03	3575 ± 25	4.88 ± 0.12	−0.08 ± 0.08
J19169+051S	V1298 Aql[b]	M8.0 V	168.95 ± 0.07	−598.76 ± 0.07	−1366.06 ± 0.07	+35.73 ± 0.03	...	...	...
J20556−140N	GJ 810 Aab[a]	M4.0 V	84.86 ± 0.47	1416.62 ± 0.44	−472.38 ± 0.33	−142.10 ± 0.02	...	...	...
J20556−140S	GJ 810 B	M5.0 V	80.20 ± 0.04	1420.76 ± 0.04	−472.27 ± 0.03	−142.04 ± 0.02	3193 ± 23	4.98 ± 0.10	−0.36 ± 0.11

Parallaxes (π) and proper motions ($\mu_\alpha \cos\delta$, μ_δ) from *Gaia* DR2 and DR3 (Gaia Collaboration et al., 2018, 2021). Radial velocities (v_r) from Lafarga et al. (2020), except for J00162+198W and J20556–140N, which are from Baroch et al. (2018), and J02489–145E, J02489–145W, J11110+304E, and J18427+596S, which were computed with serval (Zechmeister et al., 2018, 2020). [a]Double-line spectroscopic (SB2) binary (Baroch et al., 2018). [b]Spectral type M8.0 V or later.

5 Conclusions and future work

5.1 Conclusions

The objective of this PhD thesis has been the spectroscopic analysis of FGKM-type stars observed with CARMENES, the high-resolution, double-channel spectrograph installed at the 3.5 m telescope at Calar Alto Observatory (Spain) using both open-time and CARMENES GTO data. The analysis relied on the equivalent width method and spectral synthesis as widely used techniques to determine stellar atmospheric parameters (i.e. effective temperature, T_{eff}, surface gravity, $\log g$, and stellar metallicity, [Fe/H]).

The main conclusions of this PhD thesis drawn from each analysis can be summarised as follows:

- The performance of the STEPAR code (Chapter 2, Tabernero et al. 2019). In this chapter, the STEPAR code was presented, in particular its workflow and main ingredients (i.e. choice of radiative transfer code, model atmospheres, and optimisation algorithm), along with its limitations in the analysis of FGK-type spectra. The conclusions drawn from Chapter 2 include the following:

  - STEPAR, which has been made publicly available to the community[1], has proved to be a robust Python code that can provide the stellar atmospheric parameters (T_{eff}, $\log g$, and [Fe/H]) of FGK-type stars from its spectrum in a matter of 2 to 5 minutes depending on the actual position of the star in the parameter space.

  - The code was put to the test by analysing a set of *Gaia* benchmark stars (see Jofré et al., 2014, 2018), which were originally intended to calibrate and evaluate any methodology based on stellar spectra. Although some differences were found regarding the reference parameters, the code performs reasonably well in light of its internal consistency (i.e. its capability to retrieve similar parameters for the same star from spectra obtained with different spectrographs), and the comparison with theoretical isochrones (YaPSI, Spada et al., 2017).

  - Nonetheless, two shortcomings of the STEPAR code were identified during the analysis. The code seems to systematically underestimate the surface gravity of K-type stars, probably as a consequence of an ionisation imbalance in the Fe I and Fe II lines (see Tsantaki et al., 2019). Furthermore, the retrieved T_{eff} for F-type dwarfs is higher than expected for this type of stars.

  - The code also suffers from the general limitations of the EW method, meaning that it is not recommended to use STEPAR to derive parameters for stars earlier than F6 or later than K4, fast rotators (i.e. $v \sin i > 15\,\mathrm{km\,s^{-1}}$), double-lined spectroscopic binaries, or spectra with resolutions lower than 30 000 and/or S/N below 20.

- The analysis of the FGK-type stars from the CARMENES stellar library with the STEPAR code (Chapter 3, Marfil et al. 2020). In this chapter, a detailed analysis with the STEPAR code was presented for a sample of 65 FGK-type stars observed with CARMENES. The conclusions corresponding to Chapter 3 are the following:

---

[1] `https://github.com/hmtabernero/StePar`

- A homogeneous determination of the stellar atmospheric parameters (T_{eff}, $\log g$, [Fe/H], and ξ) was provided for 65 FGK-type stars (including the Sun) selected from the CAR-MENES stellar library. The analysis relied on the STEPAR code (Tabernero et al., 2019) as a robust implementation of the EW method.

- In general terms, good agreement was found in all parameters with respect to the literature values, which included a comprehensive list of virtually all relevant determinations of stellar atmospheric determinations in FGK-type stars.

- The inclusion of the near-infrared wavelength region covered by CARMENES resulted in several line lists that more than double the number of Fe I and Fe II lines employed in classical studies restricted to the optical wavelength region (e.g. Sousa et al., 2008). Altogether, 653 Fe I lines and Fe II lines were selected in the 5300–17100 Å range and were arranged into four different line lists that are best suited for the analysis of different kinds of FGK-type stars, including metal-rich dwarfs, metal-poor dwarfs, metal-rich giants, and metal-poor giants. These line lists have already proved useful in spectroscopic studies based on observations with near-infrared spectrographs that are similar to CARMENES (e.g. GIARPS, see Baratella et al., 2020). Others studies have also benefited from these line selections in the near-infrared (e.g. Matsunaga et al., 2021).

- Despite the increase in the global number of Fe I and Fe II lines found, the scarcity of Fe II lines in the NIR region prevented a full parameter determination relying on this spectral window alone. However, the analysis in the VIS+NIR wavelength region covered by CARMENES revealed a deeper T_{eff} scale that might stem from the higher sensitivity of the near-infrared Fe I and Fe II lines to T_{eff}.

- The analysis of the CARMENES GTO M dwarfs with the STEPARSYN code (Chapter 4, Marfil et al. 2021. In this chapter, 343 M dwarfs observed with CARMENES in the context of its GTO programme were analysed with the STEPARSYN code, a Bayesian implementation of spectral synthesis. The conclusions drawn from Chapter 4 are as follows:

  - A homogeneous determination of the stellar atmospheric parameters (T_{eff}, $\log g$, and [Fe/H]) was provided for a sample of 343 M dwarfs observed in the context of the CAR-MENES GTO programme. The analysis relied on the STEPARSYN code[2] (Tabernero et al., 2021b) as a Bayesian implementation of spectral synthesis.

  - The methodology adopted for the analysis has been demonstrated to be well suited for the M sequence from M0.0 V to M7.0 V, but not beyond, due to the scarcity of Ti I and Fe I lines at M8.0 V and later spectral types, and the insensitivity of TiO bands to T_{eff} as a result of dust formation (Tsuji et al., 1996; Allard et al., 2001).

  - A total of 75 Fe I and Ti I lines were carefully selected in terms of their low sensitivity to the stellar magnetic field (i.e. low effective Landé factors g_{eff}), following the prescriptions by Passegger et al. (2019). This approach is necessary to avoid any negative impact of the stellar magnetic field and activity phenomena on parameter computations.

  - The exclusion of certain Fe I and Ti I lines that appear to be particularly sensitive to the stellar activity and magnetic field (Montes et al. 2020, López-Gallifa et al. in prep.) has revealed as crucial for accurate parameter determinations in M dwarfs that exhibit particularly strong magnetic fields (i.e. up to several kG), such as EV Lac and YZ CMi (Shulyak et al., 2019). In other words, including such lines in the analysis of very active M dwarfs may translate into unreliable parameter determinations with STEPARSYN.

  - The analysis corroborated the apparent mismatch between the effective temperature scales inferred from photometry and spectroscopy, which was already noted by Cifuentes

---

[2]https://github.com/hmtabernero/SteParSyn

et al. (2020) when comparing their T_{eff} estimations from comprehensive, multi-band photometry with the works by Rajpurohit et al. (2018a) and Passegger et al. (2019).

- The results obtained with SteParSyn for the subsample of 18 M dwarfs with interferometrically measured radii (Boyajian et al., 2012b; von Braun et al., 2014) exhibit systematic offsets in T_{eff} and $\log g$ that are inherent to any methodology. It must be noted, however, that some unexpected discrepancies were found. For example, the stars HD 173739 and HD 173740, which are bound in a M+M wide binary system and, therefore, are expected to share very similar compositions, have interferometrically measured radii that lead to a difference of ~300 K between components, which cannot be attributed to a mismatch in spectral type or composition. In contrast, the analysis with SteParSyn revealed a similar T_{eff} for both components.

- The derived metallicity distribution for the M-dwarf sample follows a similar pattern to those found in other spectroscopic surveys of FGK-type stars in the solar neighbourhood, such as the Geneva-Copenhagen survey (Nordström et al., 2004). A close inspection of the metallicity distribution in the Geneva-Copenhagen survey reveals that our metallicity distribution is very similar at the low-metallicity regime, whereas high-metallicity targets appear to be marginally underrepresented.

- The M-dwarf metallicity distributions based on the kinematic membership of the targets in the Galactic populations (i.e. thick disc, thick-thin disc transition, thin disc, and young disc) are in agreement with the results presented by Bensby et al. (2003, 2005).

- Overall, excellent agreement in metallicity was found between the components in the 7 FGK+M and 16 M+M wide binaries included in our sample. Nonetheless, the 55 Cnc system stands as a notable exception and seems to point towards the impact of the relative abundance of carbon to oxygen (C/O) on metallicity determinations.

On the whole, the PhD thesis has explored the performance of the EW method and spectral synthesis in deriving accurate stellar atmospheric parameters (T_{eff}, $\log g$, and [Fe/H]) from high-resolution, high-S/N, FGKM-type spectra in the optical and near-infrared wavelength regions. Thus, the dissertation represents a step forward so far as it can help to pave the way for present and future high-resolution spectrographs with coverage in these two wavelength regions, such as GIARPS. It is important to note that the general limitations in spectral type of the EW method and, hence, StePar, has prompted the use of alternative methods for the analysis of M-dwarf spectra, such as the spectral synthesis technique implemented in the SteParSyn code. Despite the need for prior probability distributions in T_{eff} and $\log g$ to mitigate degeneracies in the parameter space, the Bayesian approach, along with a careful selection of the spectral features (i.e. magnetically insensitive Ti I and Fe I lines plus the γ and ϵ TiO bands), has made it possible to expand the analysis towards very active and fast-rotating M dwarfs. Only very cool M dwarfs (i.e. M8.0 V and beyond) had to be excluded due to limitations in the methodology. Even though the analysis has revealed great discrepancies in [Fe/H] with other spectroscopic studies in the M-dwarf domain (e.g. Passegger et al., 2018, 2019), good agreement in [Fe/H] was found when comparing the results obtained for the M dwarfs in FGK+M and M+M systems, as well as in T_{eff} for M dwarfs with interferometrically measured radii.

5.2 Future work

The ionisation and excitation balance of Fe I and Fe II lines was the foundation for the analysis of the FGK-type stars from the CARMENES stellar library presented in Chapter 3. This approach draws on the fact that Fe is by far the most common element present in both ionisation stages in FGK-type spectra, closely followed by titanium (Ti), scandium (Sc), and chromium (Cr). In this context, recent studies (Tsantaki et al., 2019) suggest that the ionisation equilibrium of titanium can

provide more precise and accurate log g estimates than iron. However, other authors (Baratella et al., 2020), after expanding on this approach, note that the excitation potential of the Ti lines (0–2 eV) is much narrower than that of Fe lines (0–5 eV), so a combination of Fe and Ti is needed. Naturally, these works would largely benefit from the wavelength coverage of CARMENES as far as it would open up the near-infrared wavelengths to search for additional Ti lines and, thus, to presumably allow to impose equilibria conditions on this element alone.

In the same manner, access to near-infrared wavelengths may help expand line lists aimed at stellar abundance studies (see Table 2 in Neves et al., 2009). Since the final abundance is usually the average value of the abundances given by all lines detected in a given star and element (Adibekyan et al., 2012), including more lines can help to reduce the line-to-line scatter.

Although spectral synthesis was introduced in Chapter 4 regarding the analysis of M dwarfs, the application of this technique on the FGK-type stars from the CARMENES stellar library can also help overcome some of the limitations of the EW method, such as those caused by stellar rotation (i.e. $v \sin i > 15 \, \mathrm{km \, s^{-1}}$) or by restrictions in spectral types (i.e. earlier than F6 or later than K4). Naturally, the next step would be to compare both methods to one another using the same Fe I and Fe II line selections in the optical and near-infrared windows and to analyse potential differences in the derived parameters (Tabernero et al., 2021b).

As discussed in Chapter 4, very late-type M dwarfs (i.e. spectral type M8.0 V or later) had to be excluded from the analysis due to limitations in the methodology that stem from the scarcity of useful Fe I and Ti I lines and the insensitivity of TiO γ and ϵ bands to T_{eff} caused by dust formation. Dust formation is a key factor in modelling not only the emergent flux of very late M dwarfs (Tsuji et al., 1996), but also cooler objects, including L-, T-, and Y-type brown dwarfs (Phillips et al., 2020) and even hot exoplanets (e.g. ultra-hot Jupiters, Fortney, 2018; Parmentier et al., 2018). For this purpose, several atmosphere models are available in the literature in an attempt to cater for such a diversity of astrophysical contexts. They mostly differ in the input physics that drives dust formation (chemical equilibrium conditions, advective mixing, and dust settling, among others) and its effects on the photospheric emergent flux (e.g. treatment of opacities and irradiation). Some of the most popular collections of atmosphere models and synthetic spectra, including the AMES models (AMES-cond and AMES-dusty Allard et al., 2001), the BT-Settl models (Allard et al., 2012), and the NextGen models (Hauschildt et al., 1999), among others, can be directly accessed from the Spanish Virtual Observatory (SVO) webpage[3]. A further step in the analysis would be to quantify the impact of all these synthetic models on parameter computations with STEPARSYN.

A critical factor that has proved to be highly significant in performing accurate parameter computations for the M-dwarf sample has been the stellar activity and the magnetic field, which are often neglected in parameter determination studies found in the literature (e.g. Rajpurohit et al., 2018a; Sarmento et al., 2021). Although the analysis was carried out following the prescriptions by Passegger et al. (2019) in terms of Landé g_{eff} factors of the lines to minimise Zeeman broadening, it does not completely rule out the impact of the stellar activity and the magnetic field on parameter computations and, thus, a more detailed study is needed to quantify such effects.

Although many efforts have been made to quantify the differences on atmospheric parameters and abundances from FGK-type spectra that are caused by the different methodologies (i.e. choice of radiative transfer code, model atmospheres, sets of lines, or the accuracy of line data; for further details, see Blanco-Cuaresma, 2019; Jofré et al., 2019), there is a distinct lack of similar studies in the M-dwarf domain focused on quantifying the inherent differences between methodologies (Passegger et al., 2021). The still-existing discrepancies between methodologies in the M-dwarf domain (e.g. pseudo-EWs, spectral synthesis, spectral indices, and their machine- and deep-learning implementations) are sometimes hard to reconcile, especially regarding metallicity. A dedicated study is still much needed to further explore this issue, which may have its roots in the instrinsic differences

---

[3]http://svo2.cab.inta-csic.es/theory/newov2/index.php

between atmospheric models and radiative transfer codes, the choice of continuum-normalisation approaches, the minimisation algorithms, and the completeness and accuracy of the line data required, among other factors.

Accurate parameter determinations are also a crucial step towards reliable abundance studies. Even though steady progress is currently being made in abundance studies in M dwarfs, including elements such as Rb, Sr, Zr (Abia et al., 2020), and V (Shan et al., 2021), there are still open questions, especially regarding the impact of the C/O ratio in metallicity determinations. It is important to note that exoplanet bulk composition is dictated by stellar compositions, as suggested by observations in our own solar system and also by theoretical considerations. Thus, stellar elemental abundances, primarily that of Fe, Si, and Mg (Tabernero et al. in prep.), play a central role in lessening degeneracy in exoplanet interior structure models and in constraining mantle composition (Dorn et al., 2015).

List of publications

Published in refereed journals

— Included in this thesis:

1. STEPAR*: an automatic code to infer stellar atmospheric parameters*, Tabernero, H. M., **Marfil, E.**, Montes, D., and González Hernández, J. I., 2019, A&A, 628, A131

   DOI:10.1051/0004-6361/201935465

2. *Stellar atmospheric parameters of FGK-type stars from high-resolution optical and near-infrared CARMENES spectra*, **Marfil, E.**, Tabernero, H. M., Montes, D., et al. 2020, MNRAS, 492, 4 pp. 5470–5507

   DOI:10.1093/mnras/staa058

3. *The CARMENES search for exoplanets around M dwarfs. Stellar atmospheric parameters of target stars with* STEPARSYN, **Marfil, E.**, Tabernero, H. M., Montes, D., et al. 2021, A&A, 656, A162

   DOI:10.1051/0004-6361/202141980

— Additional publications:

1. *Calibrating the metallicity of M dwarfs in wide physical binaries with F-, G-, and K-primaries - I: High-resolution spectroscopy with HERMES: stellar parameters, abundances, and kinematics*, Montes, D. (including **Marfil, E.**) et al. 2018, MNRAS, 479, 1, pp. 1332–1382

   DOI:10.1093/mnras/sty1295

2. *The CARMENES search for exoplanets around M dwarfs. HD147379 b: A nearby Neptune in the temperate zone of an early-M dwarf*, Reiners, A. et al. (including **Marfil, E.**) 2018, A&A, 609, L5

   DOI:10.1051/0004-6361/201732165

3. *The CARMENES search for exoplanets around M dwarfs . First visual-channel radial-velocity measurements and orbital parameter updates of seven M-dwarf planetary systems*, Trifonov, T. et al. (including **Marfil, E.**) 2018, A&A, 609, A117

   DOI:10.1051/0004-6361/201731442

4. *The CARMENES search for exoplanets around M dwarfs. High-resolution optical and near-infrared spectroscopy of 324 survey stars*, Reiners, A. et al. (including **Marfil, E.**) 2018, A&A, 612, A49

   DOI:10.1051/0004-6361/201732054

5. *The CARMENES search for exoplanets around M dwarfs. Different roads to radii and masses of the target stars*, Schweitzer, A. et al. (including **Marfil, E.**) 2019, A&A, 625, A68

   DOI:10.1051/0004-6361/201834965

6. *The CARMENES search for exoplanets around M dwarfs. Two temperate Earth-mass planet candidates around Teegarden's Star*, Zechmeister, M. et al. (including **Marfil, E.**) 2019, A&A, 627, A49

   DOI:10.1051/0004-6361/201935460

7. *A giant exoplanet orbiting a very-low-mass star challenges planet formation models*, Morales, J. C. et al. (including **Marfil, E.**) 2019, Science, 365, 6460, pp. 1441–1445

   DOI:10.1126/science.aax3198

8. *The Gaia-ESO Survey: Calibrating the lithium-age relation with open clusters and associations. I. Cluster age range and initial membership selections.*, Gutiérrez Albarrán, M. L. et al. (including **Marfil, E.**) 2020, A&A, 643, A71

   DOI:10.1051/0004-6361/202037620

9. *The CARMENES search for exoplanets around M dwarfs. A deep learning approach to determine fundamental parameters of target stars*, Passegger, V. M. et al. (including **Marfil, E.**) 2020, A&A, 642, A22

   DOI:10.1051/0004-6361/202038787

10. *The CARMENES search for exoplanets around M dwarfs. Rubidium abundances in nearby cool stars*, Abia, C. et al. (including **Marfil, E.**) 2020, A&A, 642, A227

    DOI:10.1051/0004-6361/202039032

11. *The nature of VX Sagitarii: Is it TŻO, a RSG or a high-mass AGB star?*, Tabernero, H. M., Dorda, R., Negueruela, I., and **Marfil, E.**, 2021, A&A, 646, A98

    DOI:10.1051/0004-6361/202039236

12. *The CARMENES search for exoplanets around M dwarfs. Not-so-fine hyperfine-split vanadium lines in cool star spectra*, Shan, Y. et al. (including **Marfil, E.**), A&A, 654, A118

    DOI:10.1051/0004-6361/202141530

13. SteParSyn*: A Bayesian code to infer stellar atmospheric parameters using spectral synthesis*, Tabernero, H. M., **Marfil, E.**, Montes, D., González Hernández, J. I., and Caballero, J. A., A&A, in press

    DOI:10.1051/0004-6361/202141763

14. *Metallicities in M dwarfs: Investigating different determination techniques*, Passegger, V. M. et al. (including **Marfil, E.**), A&A, in press

    DOI:10.1051/0004-6361/202141920

15. *Photometric calibrations of M dwarf metallicity with Markov chain Monte Carlo and Bayesian inference*, Duque-Arribas, C., Montes, D., Tabernero, H. M., **Marfil, E.**, and Caballero, J. A., A&A, submitted

Conference proceedings

1. *Deriving spectroscopic stellar parameters of cool stars from visible and near-infrared CARMENES spectra*, **Marfil, E.** et al. in the XXIX Canary Islands Winter School of Astrophysics held between 13 and 17 November 2017 at La Laguna, Tenerife, Spain

   http://research.iac.es/winterschool/2017

2. *Deriving spectroscopic stellar parameters of cool stars from visible and near-infrared CAR-MENES spectra*, Montes, D., **Marfil, E.** et al. in the European Week of Astronomy and Space Science 2017 held between 26 and 30 June 2017 at Prague, Czech Republic

   https://eas.unige.ch/EWASS2017/

3. *Stellar atmospheric parameters of FGK-type stars from high-resolution optical and near-infrared CARMENES spectra*, **Marfil, E.** et al. Highlights on Spanish Astrophysics X, Proceedings of the XIII Scientific Meeting of the Spanish Astronomical Society held on July 16-20, 2018, in Salamanca, Spain

   https://www.sea-astronomia.es/reunion-cientifica-2018

4. *Spectral synthesis of CARMENES M-type stars: stellar atmospheric parameters*, Lázaro, F. J. et al. (including **Marfil, E.**) Highlights on Spanish Astrophysics X, Proceedings of the XIII Scientific Meeting of the Spanish Astronomical Society held on July 16-20, 2018, in Salamanca, Spain

   https://www.sea-astronomia.es/reunion-cientifica-2018

5. *Spectral synthesis of CARMENES M-type stars: stellar atmospheric parameters*, **Marfil, E.** et al. in the 20th Cambridge Workshop on Cool Stars, Stellar Systems and the Sun, held 29 July – 3 August, 2018 in Boston, MA, USA

   DOI:10.5281/zenodo.1451488

6. *Calibrating the metallicity of M dwarfs in wide physical binaries with F-, G-, and K- primaries: spectral indices and photometry of the M dwarfs secondaries*, Montes et al. (including **Marfil, E.**) in the 20th Cambridge Workshop on Cool Stars, Stellar Systems and the Sun, held from 29 July to 3 August 2018 in Boston, MA, USA

   DOI:10.5281/zenodo.1473032

7. *CARMENES: high-resolution spectra and precise radial velocities in the red and infrared*, Quirrenbach, A. et al. (including **Marfil, E.**), Proceedings of the SPIE, Volume 10702, id. 107020W 18 pp. August 2018

   DOI:10.1117/12.2313689

8. *Stellar atmospheric parameters from CARMENES near-infrared and optical spectroscopy*, Marfil, E. (invited speaker) in the Sino-German workshop on Exoplanets held in Hamburg, Germany, on July 15-17 2019

9. *Stellar atmospheric parameters of FGKM-type stars from high-resolution optical and near-infrared CARMENES spectra*, **Marfil E.** (oral contribution) in the Gaia RIA meeting "Expanding Gaia Legacy: The Role of Spanish Ground-Based Facilities. A celebration of the research career of Jordi Torra" held in Barcelona, Spain, on February 17-19 2020

   https://riastronomia.es/expanding-the-gaia-legacy-the-role-of-spanish-ground-based-facilities/

10. *Stellar atmospheric parameters of FGK-type stars (EW method) and M-type stars (spectral synthesis) from high-resolution optical and near-infrared CARMENES spectra*, **Marfil, E.** et al., Contributions to the XIV.0 Scientific Meeting (virtual) of the Spanish Astronomical Society, held 13-15 July 2020, id.156

    https://www.sea-astronomia.es/reunion-cientifica-2020

11. STEPAR/STEPARSYN*: two automatic codes to infer stellar atmospheric parameters*, Tabernero, H. M., **Marfil, E.**, Montes, D., and González Hernández, J. I., Contributions to the XIV.0 Scientific Meeting (virtual) of the Spanish Astronomical Society, held 13-15 July 2020, id.190

    https://www.sea-astronomia.es/reunion-cientifica-2020

12. *The Gaia-ESO Survey: Calibrating the lithium-age relation with open clusters and associations*, Gutiérrez Albarrán, M. L. et al. (including **Marfil, E.**) Contributions to the XIV.0 Scientific Meeting (virtual) of the Spanish Astronomical Society, held 13-15 July 2020, id.145

    https://www.sea-astronomia.es/reunion-cientifica-2020

13. *Identifying activity-sensitive spectral lines in the CARMENES VIS and NIR spectral range of M dwarfs*, Montes, D. et al. (including **Marfil, E.**), Contributions to the XIV.0 Scientific Meeting (virtual) of the Spanish Astronomical Society, held 13-15 July 2020, id.168

    https://www.sea-astronomia.es/reunion-cientifica-2020

14. *The CARMENES M-dwarf planet survey*, Quirrenbach, A. et al. (including **Marfil, E.**), Proceedings of the SPIE, Volume 11447, id. 114473C December 2020

    DOI:10.1117/12.2561380

15. *Stellar atmospheric parameters of CARMENES GTO M dwarfs with spectral synthesis and STEPARSYN*, **Marfil, E.** et al. in the 20th (and a half) Cambridge Workshop on Cool Stars, Stellar Systems and the Sun, held virtually from 2 – 4 March 2021 by the Smithsonian Astrophysical Observatory in Cambridge, MA, USA

    DOI:10.5281/zenodo.4559144

16. *A tale of two stellar characterisation codes:* STEPAR *and* STEPARSYN, Tabernero, H. M. et al. (including **Marfil, E.**) in the 20th (and a half) Cambridge Workshop on Cool Stars, Stellar Systems and the Sun, held virtually from 2 – 4 March 2021 by the Smithsonian Astrophysical Observatory in Cambridge, MA, USA

    DOI:10.5281/zenodo.4565089

17. *The metallicity of M dwarfs: photometric calibrations with Markov chain Monte Carlo and Bayesian inference*, Duque-Arribas, C. (including **Marfil, E.**) in the 20th (and a half) Cambridge Workshop on Cool Stars, Stellar Systems and the Sun, held virtually from 2 – 4 March 2021 by the Smithsonian Astrophysical Observatory in Cambridge, MA, USA

    DOI:10.5281/zenodo.4562444

18. *Activity-sensitive spectral lines of M dwarfs in the CARMENES visible and near-infrared spectral range: impact on radial velocity determinations and stellar parameter determinations*, López-Gallifa, Á. et al. (including **Marfil, E.**) in the 20th (and a half) Cambridge Workshop on Cool Stars, Stellar Systems and the Sun, held virtually from 2 – 4 March 2021 by the Smithsonian Astrophysical Observatory in Cambridge, MA, USA

    DOI:10.5281/zenodo.456419

19. *On the nature of VX Sagitarii: is it the first galactic super-AGB star found?*, Tabernero, H. M. et al. (including **Marfil, E.**) in the 20th (and a half) Cambridge Workshop on Cool Stars, Stellar Systems and the Sun, held virtually from 2 – 4 March 2021 by the Smithsonian Astrophysical Observatory in Cambridge, MA, USA

    10.5281/zenodo.4566086

20. *A deep learning approach to photospheric parameters of CARMENES target stars*, Passegger, V. M. et al. (including **Marfil, E.**) in the 20th (and a half) Cambridge Workshop on Cool Stars, Stellar Systems and the Sun, held virtually from 2 –4 March 2021 by the Smithsonian Astrophysical Observatory in Cambridge, MA, USA

    DOI:10.5281/zenodo.4716785

21. *The lines are not fine: measuring vanadium abundances in M dwarfs from hyperfine-split lines*, Shan, Y. et al. (including **Marfil, E.**) in the 20th (and a half) Cambridge Workshop on Cool Stars, Stellar Systems and the Sun, held virtually from 2 – 4 March 2021 by the Smithsonian Astrophysical Observatory in Cambridge, MA, USA

DOI:10.5281/zenodo.4565083

Acronyms

4MOST	4-meter Multi-Object Spectroscopic Telescope
APOGEE	Apache Point Observatory Galactic Evolution Experiment
ARES	Automatic Routine for Line Equivalent widths in stellar Spectra
ASPCAP	APOGEE Stellar Parameter and Chemical Abundance Pipeline
BACCHUS	Brussels Automatic Code for Characterizing High accUracy Spectra
CARACAL	CARMENES Reduction and CALibration software
Carmencita	CARMENES Cool dwarf Information and daTa Archive
CARMENES	Calar Alto high-Resolution search for M dwarfs with Exoearths with Near-infrared and optical Échelle Spectrographs
CRIRES	CRyogenic high-resolution InfraRed Échelle Spectrograph
DAOSPEC	Dominion Astronomical Observatory SPECtrum analysis code
ESPaDOnS	Échelle SpectroPolarimetric Device for the Observation of Stars
ESPRESSO	Échelle SPectrograph for Rocky Exoplanet and Stable Spectroscopic Observations
FAMA	Fast Automatic MOOG Analysis
FASMA	Fast Analysis of Spectra Made Automatically
GALAH	GALactic Archeology with HERMES
GES	Gaia-ESO Survey
GIARPS	GIANO + HARPS
HARPS	High Accuracy Radial velocity Planet Searcher
HORuS	High Optical Resolution Spectrograph
HPF	Habitable zone Planet Finder
IRD	InfraRed Doppler instrument
LAMOST	Large Sky Area Multi-Object fibre Spectroscopic Telescope
LEGUE	LAMOST Experiment for Galactic Understanding and Exploration
MPD	Metal-poor dwarf
MPG	Metal-poor giant
MRD	Metal-rich dwarf
MRG	Metal-rich giant
NIRPS	Near Infra Red Planet Searcher
POP	Paranal Observatory Project
SEGUE	Sloan Extension for Galactic Understanding and Exploration
SERVAL	SpEctrum Radial Velocity AnaLyser
SME	Spectroscopy Made Easy
SPECIES	Spectroscopic Parameters and atmosphEric chemIstriEs of Stars
SpiROU	SPectropolarimètre InfraROuge
TAME	Tool for Automatic Measurement of Equivalent width
TESS	Transiting Exoplanet Survey Satellite
UVES	Ultraviolet and Visual Échelle Spectrograph
VALD	Vienna Atomic Line Database
WEAVE	WHT Enhanced Area Velocity Explorer
YaPSI	Yale–Potsdam Stellar Isochrones

Symbols

Symbol	Description	Unit
T_{eff}	effective temperature	K
$\log g$	surface gravity	dex
ξ	microturbulent velocity	km s^{-1}
[Fe/H]	metallicity	dex
χ	excitation potential	eV
$\log gf$	oscillator strength	dex
EW	equivalent width	mÅ
λ	wavelength	Å
$v \sin i$	projected rotational velocity	km s^{-1}
v_{r}	radial velocity	km s^{-1}
S/N	signal-to-noise ratio	—

A Appendix of Chapter 2

This appendix contains the figure and tables referenced in Chapter 2.

- Figure A.1 shows the performance of STEPAR against different spectrographs (NARVAL, HARPS, UVES, and ESPaDOnS).

- Table A.1 lists the stellar atmospheric parameters of the *Gaia* benchmark stars taken from Heiter et al. (2015a), with updated values from Jofré et al. (2018).

- Table A.2 compiles the results obtained with STEPAR for the sample.

- Table A.3 gathers the Fe I line lists for metal-rich dwarfs (MRD), metal-poor dwarfs (MPD), metal-rich giants (MRG), and metal-poor giants (MPG).

- Table A.4 is the same as A.3, but for Fe II lines.
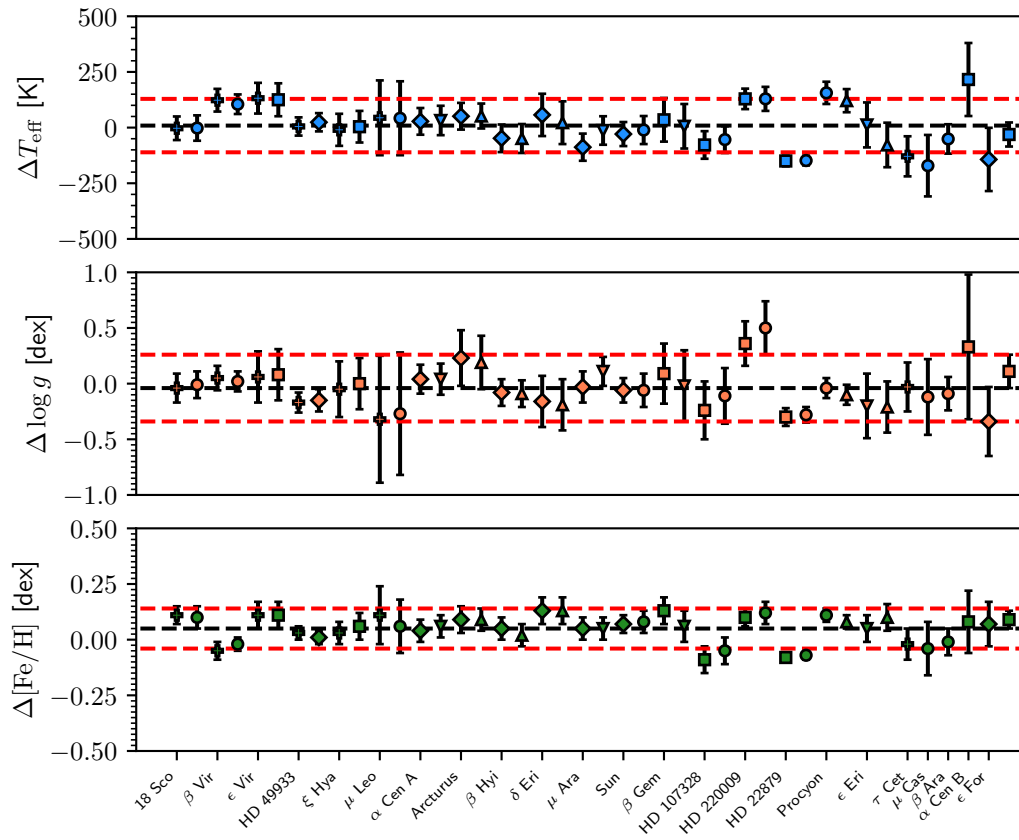
FIGURE A.1. STEPAR differences with respect to the reference values (Heiter et al., 2015a), where each symbol denotes a different spectrograph: NARVAL (circles); HARPS.GBOG (squares); HARPS.Archive (diamonds); UVES.POP (upward triangles); UVES (downward triangles); ESPaDOnS (crosses).

TABLE A.1. Reference stellar atmospheric parameters of the *Gaia* benchmark stars taken from Heiter et al. (2015a), with updated values from Jofré et al. (2018).

Star	Spectral type	T_{eff} [K]	$\log g$ [dex]	[Fe/H] [dex]
Metal-rich dwarfs (MRD)
Procyon	F5IV-V	6554 ± 84	4.00 ± 0.02	0.01 ± 0.08
β Vir	F9V	6083 ± 41	4.10 ± 0.02	0.24 ± 0.07
μ Ara	G3IV-V	5902 ± 66	4.30 ± 0.03	0.35 ± 0.13
18 Sco	G2Va	5810 ± 80	4.44 ± 0.03	0.03 ± 0.03
α Cen A	G2V	5792 ± 16	4.31 ± 0.01	0.26 ± 0.08
Sun	G2V	5771 ± 1	4.44 ± 0.00	0.03 ± 0.05
α Cen B	K1V	5231 ± 20	4.53 ± 0.03	0.22 ± 0.10
ϵ Eri	K2Vk:	5076 ± 30	4.61 ± 0.03	−0.09 ± 0.06
Metal-poor dwarfs (MPD)
HD 49933	F2V	6635 ± 91	4.20 ± 0.03	−0.41 ± 0.08
HD 22879	F9V	5868 ± 89	4.27 ± 0.04	−0.86 ± 0.05
τ Cet	G8.5V	5414 ± 21	4.49 ± 0.02	−0.49 ± 0.03
μ Cas	G5Vb	5308 ± 29	4.41 ± 0.06	−0.81 ± 0.03
Metal-rich giants (MRG)
β Hyi	G0V	5873 ± 45	3.98 ± 0.02	−0.04 ± 0.06
ξ Hya	G7III	5044 ± 40	2.87 ± 0.02	0.16 ± 0.20
ϵ Vir	G8III	4983 ± 61	2.77 ± 0.02	0.15 ± 0.16
δ Eri	K1III-IV	4954 ± 30	3.76 ± 0.02	0.06 ± 0.05
β Gem	K0IIIb	4858 ± 60	2.90 ± 0.08	0.13 ± 0.16
μ Leo	K2III	4474 ± 60	2.51 ± 0.11	0.25 ± 0.15
β Ara	K3Ib-II	4197 ± 50	1.05 ± 0.15	−0.05 ± 0.39
Metal-poor dwarfs (MPG)
ϵ For	K2V*	5123 ± 78	3.52 ± 0.08	−0.60 ± 0.10
HD 107328	K0IIIb	4496 ± 59	2.09 ± 0.13	−0.33 ± 0.16
Arcturus	K1.5III	4286 ± 35	1.60 ± 0.20	−0.52 ± 0.08
HD 220009	K2III	4217 ± 60	1.43 ± 0.12	−0.74 ± 0.13

TABLE A.2. STEPAR results.

Star	Spectral type	Source	S/N	T_{eff} [K]	ΔT_{eff} [K]	$\log g$ [dex]	$\Delta \log g$ [dex]	ξ_{micro} [km s^{-1}]	$\Delta \xi_{\text{micro}}$ [km s^{-1}]	[Fe/H] [dex]	Δ[Fe/H] [dex]
					Metal-rich dwarfs (MRD)						
Procyon	F5IV-V	NARVAL	765	6710	50	3.96	0.09	1.70	0.06	0.07	0.03
Procyon	F5IV-V	UVES.POP	1016	6675	52	3.90	0.09	1.63	0.06	0.04	0.03
β Vir	F9V	ESPaDOnS	635	6206	51	4.15	0.11	1.43	0.07	0.16	0.04
β Vir	F9V	NARVAL	400	6188	44	4.12	0.09	1.33	0.05	0.19	0.03
μ Ara	G3IV-V	HARPS.Archive	252	5814	61	4.27	0.14	0.95	0.09	0.38	0.05
μ Ara	G3IV-V	UVES	309	5889	64	4.41	0.13	1.03	0.10	0.38	0.05
18 Sco	G2Va	ESPaDOnS	383	5807	53	4.40	0.13	0.69	0.11	0.12	0.04
18 Sco	G2Va	NARVAL	380	5808	57	4.43	0.12	0.74	0.11	0.11	0.05
α Cen A	G2V	HARPS.Archive	496	5820	60	4.35	0.13	0.96	0.09	0.28	0.05
α Cen A	G2V	UVES	316	5824	66	4.35	0.14	0.86	0.11	0.30	0.05
Sun	G2V	HARPS.Archive	549	5748	54	4.38	0.11	0.62	0.12	0.07	0.04
Sun	G2V	NARVAL	828	5766	63	4.38	0.15	0.70	0.12	0.08	0.05
α Cen B	K1V	HARPS	469	5088	142	4.19	0.31	0.50	0.30	0.29	0.10
ϵ Eri	K2Vk:	UVES	220	5088	101	4.41	0.29	0.78	0.21	−0.05	0.06
ϵ Eri	K2Vk:	UVES.POP	1653	4998	100	4.40	0.23	0.41	0.28	0.00	0.06
					Metal-poor dwarfs (MPD)						
HD 49933	F2V	HARPS.Archive	319	6659	41	4.05	0.10	1.54	0.05	−0.45	0.03
HD 49933	F2V	ESPaDOnS	1169	6640	41	4.03	0.09	1.56	0.05	−0.43	0.03
HD 22879	F9V	HARPS.GBOG	322	5718	24	3.97	0.08	1.04	0.03	−0.96	0.02
HD 22879	F9V	NARVAL	297	5720	22	3.99	0.07	1.02	0.03	−0.95	0.02
τ Cet	G8.5V	ESPaDOnS	1238	5285	90	4.46	0.22	0.43	0.21	−0.52	0.07
τ Cet	G8.5V	NARVAL	357	5243	138	4.37	0.34	0.50	0.35	−0.54	0.12
μ Cas	G5Vb	NARVAL	269	5257	66	4.32	0.15	0.42	0.24	−0.83	0.06
					Metal-rich giants (MRG)						
β Hyi	G0V	HARPS.Archive	428	5825	62	3.90	0.12	0.84	0.08	−0.02	0.05
β Hyi	G0V	UVES.POP	676	5824	65	3.89	0.12	0.92	0.07	−0.05	0.05
ξ Hya	G7III	HARPS.GBOG	391	5048	71	2.87	0.23	1.17	0.07	0.20	0.06
ξ Hya	G7III	ESPaDOnS	526	5034	72	2.82	0.25	1.20	0.07	0.17	0.05
ϵ Vir	G8III	ESPaDOnS	435	5115	69	2.83	0.23	1.33	0.07	0.24	0.06
ϵ Vir	G8III	HARPS.GBOG	392	5108	74	2.85	0.23	1.33	0.07	0.24	0.06
δ Eri	K1III-IV	HARPS.Archive	525	5011	95	3.60	0.23	0.77	0.13	0.19	0.06
δ Eri	K1III-IV	UVES.POP	548	4976	96	3.57	0.23	0.72	0.14	0.19	0.06
β Gem	K0IIIb	HARPS.GBOG	370	4893	98	2.99	0.27	1.07	0.09	0.25	0.06
β Gem	K0IIIb	UVES	163	4864	100	2.88	0.32	1.14	0.10	0.18	0.07
μ Leo	K2III	ESPaDOnS	779	4518	168	2.19	0.57	1.25	0.12	0.37	0.13
μ Leo	K2III	NARVAL	402	4516	166	2.24	0.55	1.34	0.13	0.32	0.12
β Ara	K3Ib-II	HARPS.GBOG	414	4413	164	1.38	0.65	2.20	0.18	0.03	0.14
					Metal-poor giants (MPG)						
ϵ For	K2V*	HARPS.GBOG	334	5092	54	3.63	0.15	0.70	0.10	−0.53	0.04
HD 107328	K0IIIb	HARPS.GBOG	459	4418	62	1.85	0.26	1.71	0.07	−0.43	0.06
HD 107328	K0IIIb	NARVAL	375	4442	60	1.98	0.25	1.68	0.06	−0.39	0.06
Arcturus	K1.5III	HARPS.Archive	475	4337	60	1.87	0.25	1.64	0.07	−0.44	0.06
Arcturus	K1.5III	UVES.POP	1208	4338	56	1.83	0.24	1.59	0.06	−0.44	0.05
HD 220009	K2III	HARPS.GBOG	347	4346	46	1.79	0.20	1.42	0.05	−0.65	0.04
HD 220009	K2III	NARVAL	376	4346	54	1.93	0.24	1.45	0.06	−0.63	0.05

TABLE A.3. Merged Fe I line lists.

λ_{air} [Å]	χ_1 [eV]	$\log gf$	List			
			MRD	MPD	MRG	MPG
4808.148	3.25	−2.690	•		•	
4809.938	3.57	−2.620	•			•
4869.463	3.55	−2.420	•		•	•
4875.877	3.33	−1.900	•	•		
4877.604	3.00	−3.050			•	•
4882.143	3.42	−1.480		•	•	
4892.859	4.22	−1.290	•	•	•	•
4903.310	2.88	−0.903			•	
4905.133	3.93	−1.730	•			
4907.732	3.43	−1.700	•	•		
4917.230	4.19	−1.080		•		
4924.770	2.28	−2.216	•	•		
4939.687	0.86	−3.336	•	•		•
4946.387	3.37	−1.110	•	•	•	•
4950.105	3.42	−1.490	•	•		
4961.913	3.63	−2.190	•			
4962.572	4.18	−1.182	•	•	•	
4966.088	3.33	−0.792	•	•		
4969.917	4.22	−0.710		•		
4985.253	3.93	−0.447		•		
4986.223	4.22	−1.290		•		
4992.785	4.26	−2.350			•	
4993.680	4.21	−1.370	•			
4994.130	0.92	−3.058	•	•	•	•
5002.792	3.40	−1.460	•	•	•	•
5012.695	4.28	−1.690	•		•	
5014.942	3.94	−0.183		•	•	•
5022.235	3.98	−0.370		•	•	
5023.186	4.28	−1.500			•	
5029.618	3.42	−1.950	•			
5031.914	4.37	−1.570				•
5044.211	2.85	−2.038	•	•	•	
5048.436	3.96	−1.005			•	
5049.820	2.28	−1.348		•	•	
5054.642	3.64	−1.921	•			•
5060.078	0.00	−5.431		•	•	
5067.150	4.22	−0.970	•	•		
5068.766	2.94	−1.041			•	
5074.748	4.22	−0.230		•	•	
5079.223	2.20	−2.068		•		
5079.740	0.99	−3.221		•		
5083.338	0.96	−2.939		•	•	
5088.153	4.15	−1.680				•
5090.773	4.26	−0.440	•	•		
5104.438	4.28	−1.590			•	
5107.447	0.99	−3.089		•		

TABLE A.3. *continued*

λ_{air} [Å]	χ_1 [eV]	$\log gf$	MRD	MPD	MRG	MPG
5109.652	4.30	−0.980			•	
5127.359	0.92	−3.306		•		
5133.688	4.18	0.360		•	•	
5141.739	2.42	−1.978			•	•
5143.723	2.20	−3.690			•	
5150.839	0.99	−3.008		•	•	
5151.911	1.01	−3.322	•	•		
5159.058	4.28	−0.820		•		
5162.273	4.18	0.020		•		
5197.936	4.30	−1.540	•		•	
5198.711	2.22	−2.135	•	•	•	
5213.806	3.94	−2.760			•	
5215.180	3.27	−0.861			•	
5216.274	1.61	−2.082			•	
5217.389	3.21	−1.074	•	•	•	•
5225.526	0.11	−4.789		•		
5228.376	4.22	−1.190		•		
5229.845	3.28	−0.967		•		
5242.491	3.63	−0.967	•	•	•	•
5243.776	4.26	−1.050	•	•	•	•
5247.050	0.09	−4.949	•	•		
5250.209	0.12	−4.933		•		
5250.646	2.20	−2.180		•		
5253.462	3.28	−1.579		•	•	
5285.127	4.44	−1.660	•		•	•
5288.525	3.70	−1.493	•			•
5293.959	4.14	−1.770			•	•
5294.547	3.64	−2.760	•		•	
5295.312	4.42	−1.590	•		•	•
5307.361	1.61	−2.912	•	•		•
5321.108	4.44	−1.089				•
5322.041	2.28	−2.802	•			•
5339.929	3.27	−0.635				•
5364.871	4.45	0.228			•	•
5373.709	4.47	−0.710	•	•		
5379.574	3.70	−1.514	•	•	•	•
5386.333	4.15	−1.670	•		•	•
5389.479	4.42	−0.410		•	•	
5397.618	3.63	−2.528			•	
5398.279	4.45	−0.630	•	•	•	
5400.501	4.37	−0.160	•	•		
5401.266	4.32	−1.820	•		•	
5409.133	4.37	−1.200	•	•		
5417.033	4.42	−1.580	•		•	
5424.068	4.32	0.520		•		
5436.295	4.39	−1.440	•		•	•

TABLE A.3. *continued*

λ_{air} [Å]	χ_1 [eV]	$\log gf$	MRD	MPD	MRG	MPG
5436.588	2.28	−2.964			•	
5441.339	4.31	−1.630	•		•	•
5445.042	4.39	−0.020		•	•	•
5460.873	3.07	−3.426			•	•
5461.550	4.45	−1.800	•		•	
5463.275	4.44	0.070			•	•
5464.280	4.14	−1.402			•	
5466.396	4.37	−0.630	•	•		•
5470.093	4.45	−1.710	•		•	
5472.709	4.21	−1.495	•			
5473.900	4.15	−0.720	•	•		
5483.099	4.15	−1.392	•			•
5501.465	0.96	−3.046		•		
5506.779	0.99	−2.795		•		
5522.446	4.21	−1.450	•	•		
5536.580	2.83	−3.710				•
5539.280	3.64	−2.560				•
5543.147	3.70	−1.470		•		
5543.936	4.22	−1.040	•	•	•	•
5546.506	4.37	−1.210		•		
5549.949	3.70	−2.810			•	
5554.894	4.55	−0.270		•		
5560.212	4.44	−1.090	•	•	•	
5572.842	3.40	−0.289				•
5576.089	3.43	−0.900		•	•	•
5618.632	4.21	−1.255	•	•	•	•
5619.595	4.39	−1.600	•			•
5633.946	4.99	−0.230		•		
5635.822	4.26	−1.790	•			
5636.696	3.64	−2.510	•		•	
5638.262	4.22	−0.720	•	•		
5641.434	4.26	−1.080	•	•		
5649.987	5.10	−0.820	•			•
5651.469	4.47	−1.900	•			
5652.318	4.26	−1.850	•			
5653.865	4.39	−1.540	•			•
5655.176	5.06	−0.600	•			•
5661.345	4.28	−1.756	•			•
5662.516	4.18	−0.447	•	•		•
5679.023	4.65	−0.820	•	•	•	•
5691.497	4.30	−1.450		•		
5696.089	4.55	−1.720	•			
5701.544	2.56	−2.193	•	•		
5705.464	4.30	−1.355	•			
5717.833	4.28	−0.990	•	•	•	•
5720.886	4.55	−1.631	•		•	•

TABLE A.3. *continued*

λ_{air} [Å]	χ_{l} [eV]	$\log gf$	MRD	MPD	MRG	MPG
5731.762	4.26	−1.200	•	•		•
5732.296	4.99	−1.460	•			
5741.848	4.26	−1.672	•			
5759.262	4.65	−2.216			•	
5778.453	2.59	−3.430			•	
5784.658	3.40	−2.547			•	
5844.918	4.15	−3.054			•	
5849.683	3.70	−2.890				•
5852.219	4.55	−1.230	•		•	
5853.148	1.49	−5.180			•	•
5855.076	4.61	−1.478	•		•	
5856.088	4.29	−1.327			•	
5858.778	4.22	−2.160			•	
5861.109	4.28	−2.304			•	•
5883.816	3.96	−1.260	•	•		•
5902.473	4.59	−1.710				•
5905.671	4.65	−0.690	•	•	•	•
5909.972	3.21	−2.587	•		•	•
5916.247	2.45	−2.994	•		•	•
5927.789	4.65	−0.990	•		•	
5929.676	4.55	−1.310	•		•	
5930.180	4.65	−0.230	•	•	•	
5934.654	3.93	−1.070	•	•		•
5940.991	4.18	−2.050				•
5952.718	3.98	−1.340				•
5956.694	0.86	−4.599	•	•	•	•
6003.011	3.88	−1.100	•	•	•	•
6012.210	2.22	−4.038				•
6019.365	3.57	−3.310				•
6024.057	4.55	−0.120	•	•		•
6027.051	4.08	−1.089	•	•	•	•
6056.005	4.73	−0.320		•		
6065.482	2.61	−1.529		•	•	
6079.008	4.65	−1.020	•	•	•	•
6082.710	2.22	−3.576	•		•	•
6093.643	4.61	−1.400	•		•	•
6094.373	4.65	−1.840				•
6096.664	3.98	−1.830	•			•
6098.244	4.56	−1.859	•		•	•
6120.246	0.92	−5.970			•	•
6127.906	4.14	−1.399	•	•		•
6136.615	2.45	−1.402		•		
6136.994	2.20	−2.950		•		
6137.691	2.59	−1.402		•		
6151.617	2.18	−3.295	•	•		•
6165.360	4.14	−1.473	•	•		•

Table A.3. *continued*

λ_{air} [Å]	χ_{l} [eV]	$\log gf$	List			
			MRD	MPD	MRG	MPG
6170.506	4.80	−0.440	●	●		
6173.334	2.22	−2.880	●	●	●	●
6180.203	2.73	−2.591	●			
6187.989	3.94	−1.620	●		●	●
6191.557	2.43	−1.416		●		
6199.506	2.56	−4.430				●
6200.312	2.61	−2.433	●	●		●
6213.429	2.22	−2.481	●	●		●
6219.280	2.20	−2.432	●	●		●
6220.780	3.88	−2.058				●
6226.734	3.88	−2.120	●			
6229.226	2.85	−2.805	●		●	●
6230.722	2.56	−1.281	●	●		
6240.646	2.22	−3.230	●	●	●	●
6246.318	3.60	−0.771	●	●	●	
6252.555	2.40	−1.699	●	●	●	●
6265.132	2.18	−2.550	●	●	●	●
6270.223	2.86	−2.470	●		●	●
6271.278	3.33	−2.703			●	●
6280.617	0.86	−4.390		●		
6290.543	2.59	−4.330				●
6297.793	2.22	−2.737		●		●
6301.500	3.65	−0.720		●	●	●
6311.499	2.83	−3.141	●			●
6315.811	4.08	−1.630	●			●
6322.685	2.59	−2.430	●	●	●	●
6335.330	2.20	−2.177	●	●	●	●
6336.823	3.69	−0.852	●	●	●	●
6338.876	4.80	−0.960	●			
6344.148	2.43	−2.919		●		
6355.028	2.85	−2.340		●		
6380.743	4.19	−1.375	●			●
6393.600	2.43	−1.452		●	●	
6400.317	0.92	−4.318	●	●		
6411.648	3.65	−0.596		●		
6421.350	2.28	−2.012	●	●		
6430.845	2.18	−2.005	●	●		
6469.192	4.84	−0.730	●	●		
6475.624	2.56	−2.941	●	●		
6481.870	2.28	−2.981	●	●		●
6494.980	2.40	−1.268		●		
6495.741	4.84	−0.840	●			
6496.466	4.80	−0.530	●	●		●
6498.938	0.96	−4.687	●			●
6518.366	2.83	−2.438				●
6533.928	4.56	−1.360	●	●	●	●

TABLE A.3. *continued*

λ_{air} [Å]	χ_{l} [eV]	$\log gf$	MRD	MPD	MRG	MPG
6546.238	2.76	−1.536		●	●	●
6574.227	0.99	−5.004	●			
6581.209	1.49	−4.679				●
6591.313	4.59	−2.081			●	●
6592.912	2.73	−1.473	●	●		●
6593.869	2.43	−2.420	●	●		●
6597.559	4.80	−0.970	●			●
6608.025	2.28	−3.930	●			●
6609.110	2.56	−2.691	●	●		●
6627.544	4.55	−1.590	●			
6633.412	4.84	−1.390	●			
6633.749	4.56	−0.799	●			
6648.080	1.01	−5.918				●
6703.566	2.76	−3.060	●		●	
6710.318	1.49	−4.764	●			
6713.743	4.80	−1.500	●		●	
6716.236	4.58	−1.836	●			
6725.356	4.10	−2.100			●	●
6750.151	2.42	−2.618	●	●	●	●
6752.707	4.64	−1.204	●			

TABLE A.4. Merged Fe II line lists.

λ_{air} [Å]	χ_1 [eV]	$\log gf$	List			
			MRD	MPD	MRG	MPG
4993.350	2.81	−3.684	•	•	•	
5197.568	3.23	−2.220	•	•	•	
5234.623	3.22	−2.180	•	•	•	•
5256.932	2.89	−4.182	•		•	
5264.802	3.23	−3.130		•		
5284.103	2.89	−3.195		•		
5325.552	3.22	−3.160		•		•
5414.070	3.22	−3.580			•	
5425.248	3.20	−3.220	•	•	•	•
5534.838	3.25	−2.865		•		
5991.371	3.15	−3.647	•			
6084.102	3.20	−3.881	•		•	
6149.246	3.89	−2.841	•		•	•
6238.386	3.89	−2.600		•	•	
6247.557	3.89	−2.435		•		
6369.459	2.89	−4.110	•			•
6416.919	3.89	−2.877	•			
6432.676	2.89	−3.570	•	•	•	
6456.380	3.90	−2.185		•	•	•
6516.077	2.89	−3.310	•	•		

B Appendix of Chapter 3

This appendix contains the figure and tables referenced in Chapter 3.

- Table B.1 lists the literature values of the stellar atmospheric parameters for the selected sample from the CARMENES stellar library.

- Tables B.2 and B.3 compile the stellar atmospheric parameters computed with STEPAR in the whole VIS + NIR region and VIS region only, respectively.

- Tables B.4 and B.5 list the Fe I and Fe II lines along with their parameters, respectively, for metal-rich dwarfs (MRD), metal-poor dwarfs (MPD), metal-rich giants (MRG), and metal-poor giants (MPG).

- Figure B.1 shows the CARMENES spectrum of the reference, metal-rich dwarf 18 Sco, along with the Fe I and Fe II lines indicated in red and green, respectively.

TABLE B.1. Reference stellar parameters of the selected CARMENES sample.

Name	HD	α (J2000)	δ (J2000)	π [mas]	Ref.[a]	SpT[b]	v_r [km s^{-1}]	Ref.[c]	$v \sin i$ [km s^{-1}]	Ref.[d]	T_{eff} [K]	log g [dex]	ξ [km s^{-1}]	[Fe/H] [dex]	Ref.[e]
Metal-rich dwarfs (MRD)															
Sun[f]	...	...	...	... ± ...	...	G2 V	0.00	...	1.6	Pav12	5771 ± 1	4.44 ± 0.00	1.20 ± 0.18	+0.03 ± 0.05	Jof18
HD 3765	3765	00 40 49.29	+40 11 13.3	55.7562 ± 0.1002	G	K2 V	−63.11	Sou13	9.2	Mar10	5032 ± 44	4.59 ± 0.06	0.85 ± ...	+0.18 ± 0.03	Val05
HD 100167	100167	11 31 53.92	+41 26 21.5	28.4793 ± 0.1513	G	F8 V	−29.49	Nid02	5.0	McC14	5915 ± 44	4.38 ± 0.06	0.85 ± ...	+0.06 ± 0.03	Val05
61 UMa[f]	101501	11 41 03.01	+34 12 06.4	104.3904 ± 0.1287	G	G8 V	−5.18	Nid02	3.3	Mar10	5488 ± 44	4.43 ± 0.06	0.85 ± ...	−0.03 ± 0.03	Val05
β Vir[f]	102870	11 50 41.73	+01 45 52.8	89.9258 ± 0.5195	G	F9 V	+4.71	Nid02	3.4	Mar10	6083 ± 41	4.10 ± 0.02	1.40 ± 0.09	+0.24 ± 0.07	Jof18
β CVn	109358	12 33 44.54	+41 21 27.0	116.1298 ± 0.6776	G	G0 V	+6.52	Nid02	3.2	Mar10	5930 ± 44	4.44 ± 0.06	0.85 ± ...	−0.16 ± 0.03	Val05
β Com	114710	13 11 52.38	+27 52 41.1	108.8951 ± 0.3487	G	F9.5 V	+5.46	Nid02	4.7	Mar10	6075 ± 44	4.57 ± 0.06	0.85 ± ...	+0.07 ± 0.03	Val05
ξ Boo	131156	14 51 23.28	+19 06 03.4	148.5195 ± 0.2436	G	G7 Ve+	+1.59	Kar04	3.3	Mar10	5570 ± 44	4.65 ± 0.06	0.85 ± ...	−0.04 ± 0.03	Val05
λ Ser	141004	15 46 26.61	+07 21 10.9	84.6121 ± 0.2559	G	G0IV–V	−66.07	Nid02	3.2	Mar10	5936 ± 44	4.30 ± 0.06	0.85 ± ...	+0.05 ± 0.03	Val05
18 Sco[f]	146233	16 15 37.26	−08 22 09.6	70.7675 ± 0.1119	G	G2 Va	+11.90	Gaia	2.1	San16	5810 ± 80	4.44 ± 0.03	1.20 ± 0.20	+0.03 ± 0.03	Jof18
HD 166620	166620	18 09 37.45	+38 27 28.8	90.1264 ± 0.0200	G	K2 V	−19.47	Sou13	4.8	Mar10	5000 ± 44	4.47 ± 0.06	0.85 ± ...	−0.18 ± 0.03	Val05
HD 182488	182488	19 23 34.01	+33 13 19.1	64.0623 ± 0.0218	G	G9 V	−21.47	Sou13	0.6	Fek97	5453 ± 44	4.67 ± 0.06	0.85 ± ...	+0.22 ± 0.03	Val05
σ Dra	185144	19 32 21.53	+69 39 41.3	173.2405 ± 0.2070	G	G9 V	+26.78	Nid02	6.8	Mar10	5218 ± 96	4.61 ± 0.05	1.07 ± ...	−0.25 ± 0.02	All04
HD 219134	219134	23 13 16.92	+57 10 05.9	153.0808 ± 0.0895	G	K3 V	−18.83	Nid02	6.9	Mar10	4743 ± 86	4.63 ± 0.04	1.00 ± ...	+0.12 ± 0.02	All04
Metal-poor dwarfs (MPD)															
η Cas	4614	00 49 06.22	+57 48 54.5	171.2861 ± 0.5815	G	F9 V+	+8.44	Nid02	3.2	Mar10	5900 ± 50	4.50 ± 0.05	0.90 ± 0.05	−0.35 ± 0.04	Hei03
μ Cas[f]	6582	01 08 15.97	+54 55 14.8	132.38 ± 0.82	H	K1 V	−98.10	Pou04	4.2	Mar10	5308 ± 29	4.41 ± 0.06	1.10 ± 0.29	−0.81 ± 0.03	Jof18
HD 49933[f]	49933	06 50 49.83	−00 32 27.0	33.4441 ± 0.0891	G	F3 V	−12.65	Gaia	5.0	Tak05	6635 ± 91	4.20 ± 0.03	1.90 ± 0.35	−0.41 ± 0.08	Jof18
CF UMa[f]	103095	11 52 58.80	+37 43 06.0	108.9551 ± 0.0490	G	G8 Vp	−97.49	Hay18	9.3	Mar10	5140 ± 55	4.60 ± 0.03	1.10 ± 0.57	−1.46 ± 0.39	Jof18
HD 154363	154363	17 03 07.86	+14 05 31.0	95.5499 ± 0.0651	G	K4 V	+34.22	Mon18	1.9	Mar10	4723 ± 89	4.41 ± 0.24	... ± ...	−0.62 ± 0.04	Sou08
Metal-rich giants (MRG)															
ι Gem	58207	07 25 43.59	+27 47 52.9	24.8793 ± 0.3562	G	G9 IIIb	+7.26	Mas08	0.0	Mas08	4912 ± 56	2.82 ± 0.28	1.47 ± 0.09	−0.03 ± 0.10	Sil15
α CMi[f]	61421	07 39 18.05	+05 13 29.8	284.56 ± 1.26	H	F5 IV–V	−4.10	Mal10	5.4	Mar10	6554 ± 84	4.00 ± 0.02	1.80 ± 0.11	−0.01 ± 0.08	Jof18
κ Gem	62345	07 44 26.84	+24 23 52.6	23.6199 ± 0.3954	G	G8 IIIa	+20.15	Sou08	3.3	Mas08	5120 ± 28	2.98 ± 0.16	1.56 ± 0.04	+0.03 ± 0.05	Sil15
β Gem[f]	62509	07 45 18.91	+28 01 34.0	96.54 ± 0.27	H	K0IIIb	+3.23	Jof15	2.3	Jof15	4858 ± 60	2.90 ± 0.08	1.10 ± 0.21	+0.13 ± 0.16	Jof18
ζ Mon	67594	08 08 35.65	−02 59 01.5	4.7723 ± 0.3259	G	G2 Iab/b	+31.20	Gaia	6.7	Med02	5210 ± 100	1.75 ± 0.07	3.3 ± 0.5	+0.01 ± 0.12	Lyu10
β Cnc	69267	08 16 30.90	+09 11 08.0	11.0443 ± 0.6561	G	K4 III	+22.94	Fam05	6.9	Mas08	4200 ± ...	2.05 ± ...	2.30 ± ...	−0.19 ± ...	Hek07
F Hya	74395	08 43 40.37	−07 14 01.2	1.8273 ± 0.2985	G	G0/2 Ib	+27.68	Gaia	7.5	Med02	5370 ± 100	2.08 ± 0.06	3.5 ± 0.5	−0.03 ± 0.13	Lyu10
ζ Hya	76294	08 55 23.62	+05 56 44.1	20.7182 ± 0.3925	G	G9II–III	+22.30	Gon06	2.5	Mas08	5049 ± 55	2.88 ± 0.30	1.67 ± 0.08	+0.01 ± 0.11	Sil15
HD 77912	77912	09 06 31.77	+38 27 08.0	5.0045 ± 0.1977	G	G7 II	+16.04	Gaia	1.5	Med02	5001 ± ...	2.03 ± ...	2.16 ± ...	+0.12 ± ...	Luc14
α Hya	81797	09 27 35.24	−08 39 30.8	18.09 ± 0.18	H	K3 IIIa	−4.27	Jof15	4.0	Jof15	4395 ± 37	2.09 ± 0.11	1.76 ± 0.12	−0.11 ± 0.05	Jof15
DK UMa	82210	09 34 28.88	+69 49 49.0	30.9269 ± 0.1621	G	G5III–IV	−27.07	Gaia	5.5	Med00	5343 ± 33	3.49 ± 0.08	... ± ...	−0.21 ± 0.07	Wu11
10 LMi	82635	09 34 13.38	+36 23 51.3	18.1458 ± 0.2345	G	G8.5 III	−11.94	Mas08	6.5	Mas08	5195 ± 40	3.26 ± 0.26	1.56 ± 0.06	−0.02 ± 0.07	Sil15
ε Leo	84441	09 45 51.08	+23 46 27.3	11.1759 ± 0.9166	G	G1 II	+4.48	Sou08	8.1	Mas08	5383 ± ...	2.17 ± ...	2.09 ± ...	+0.04 ± ...	Luc14
μ Leo[f]	85503	09 52 45.85	+26 00 24.8	30.6493 ± 0.4219	G	K2 III	+13.63	Fam05	4.5	Mas08	4474 ± 60	2.51 ± 0.11	2.1 ± ...	+0.25 ± 0.15	Jof18
β LMi	90537	10 27 53.02	+36 42 25.9	21.19 ± 0.50	H	G9 IIIb	+8.52	Gaia	7.1	Mas08	5060 ± ...	2.95 ± ...	2.1 ± ...	0.00 ± 0.10	McW90
37 LMi	92125	10 38 43.21	+31 58 34.6	5.2136 ± 0.4108	G	G3 Ib–II	−7.71	Gaia	9.5	Lyu12	5475 ± 50	2.36 ± 0.04	2.7 ± 0.5	+0.02 ± 0.11	Lyu10
α UMa	95689	11 03 43.64	+61 45 03.4	26.54 ± 0.48	H	G8III+	−9.40	Gon06	2.7	Gra18	4660 ± ...	2.46 ± ...	2.2 ± ...	−0.20 ± 0.07	McW90
ψ UMa	96833	11 09 39.79	+44 29 54.4	21.0443 ± 0.5249	G	K1 III	−3.39	Fam05	5.5	Mas08	4600 ± 22	1.95 ± 0.08	... ± ...	+0.03 ± 0.08	Thy12
ν UMa	98262	11 18 28.74	+33 05 39.3	14.2521 ± 0.5672	G	K3 III	−9.63	Fam05	2.7	Fam05	4120 ± ...	1.86 ± ...	2.4 ± ...	−0.20 ± 0.12	McW90
56 UMa	98839	11 22 49.58	+43 28 57.7	5.8742 ± 0.1937	G	G8 IIIa	+1.01	Pou04	4.0	Leb06	4936 ± 25	2.30 ± 0.08	1.78 ± 0.10	−0.05 ± 0.04	Tak08

TABLE B.1. *continued*

Name	HD	α (J2000)	δ (J2000)	Ref.[a]	π [mas]	SpT[b]	v_r [km s⁻¹]	Ref.[c]	$v \sin i$ [km s⁻¹]	Ref.[d]	T_{eff} [K]	log g [dex]	ξ [km s⁻¹]	[Fe/H] [dex]	Ref.[e]
ε Vir[f]	113226	13 02 10.59	+10 57 32.9	G	30.5624 ± 0.4379	G8 III	−14.29	Jof15	1.4	Jof15	4983 ± 61	2.77 ± 0.02	1.10 ± 0.25	+0.15 ± 0.16	Jof18
η Boo[f]	121370	13 54 41.06	+18 23 51.4	H	87.75 ± 1.24	G0 IV	+0.70	Jof15	12.3	Jof15	6099 ± 28	3.79 ± 0.02	1.92 ± 0.03	+0.32 ± 0.08	Jof15
ρ Boo	127665	14 31 49.77	+30 22 16.9	G	21.9348 ± 0.3952	K3 III	−13.57	Mas08	5.0	Mas08	4258 ± 65	1.85 ± 0.36	1.59 ± 0.12	−0.13 ± 0.12	Sil15
β UMi	131873	14 50 42.35	+74 09 19.9	H	24.91 ± 0.12	K4 III	+16.96	Fam05	1.6	Gon99	4067 ± 13	1.70 ± 0.11	... ± ...	−0.13 ± 0.05	Wu11
δ Boo	135722	15 15 30.15	+33 18 53.7	G	26.7797 ± 0.3806	G8 IV	−12.29	Sou08	3.6	Mas08	4982 ± 28	2.89 ± 0.19	1.44 ± 0.04	−0.23 ± 0.06	Sil15
ι Dra	137759	15 24 55.78	+58 57 57.7	G	31.5727 ± 0.2959	K2 III	−12.31	Gaia	1.9	Jof15	4504 ± 16	2.52 ± 0.07	1.41 ± 0.07	+0.03 ± 0.04	Jof15
α Ser	140573	15 44 16.05	+06 25 32.4	G	39.3696 ± 0.8514	K2 IIIb	+2.63	Fam05	4.3	Mas08	4496 ± ...	2.52 ± ...	1.5 ± 0.2	+0.17 ± ...	Liu07
κ CrB	142091	15 51 13.94	+35 39 26.4	G	33.2328 ± 0.1083	K0 III–IV	−23.16	Jof15	1.4	Jof15	4803 ± 25	3.23 ± 0.04	0.83 ± 0.06	+0.17 ± 0.05	Jof15
ε CrB	143107	15 57 35.23	+26 52 40.0	G	14.2898 ± 0.2149	K2 III	−32.42	Fam05	2.4	Fam05	4436 ± 56	1.94 ± 0.15	1.68 ± 0.06	−0.22 ± 0.03	San13
ε Oph	146791	16 18 19.28	−04 41 32.7	G	30.2620 ± 0.7915	G9.5 IIIb	−9.18	Mas08	3.6	Mas08	4940 ± 55	2.64 ± 0.06	1.43 ± 0.06	−0.04 ± 0.10	Mor14
ζ Her	150680	16 41 17.28	+31 36 09.3	H	93.32 ± 0.47	G1 IV	−67.80	Gon06	3.1	Mar10	5655 ± 148	3.67 ± 0.12	1.38 ± ...	−0.01 ± 0.02	All04
κ Oph	153210	16 57 40.07	+09 22 29.9	G	36.8142 ± 0.4578	K2 III	−55.85	Mas08	4.7	Mas08	4655 ± ...	2.70 ± ...	1.82 ± ...	+0.07 ± ...	Hek07
π Her	156283	17 15 02.85	+36 48 32.9	G	9.1810 ± 0.4201	K3 II	−25.57	Fam05	1.3	Leb06	4170 ± ...	1.90 ± ...	2.26 ± ...	+0.01 ± ...	Hek07
σ Oph	157999	17 26 30.87	+04 08 25.2	G	3.8431 ± 0.2836	K2 III	−27.81	Fam05	4.2	Leb06	4080 ± ...	1.52 ± ...	2.54 ± ...	−0.07 ± ...	Hek07
β Dra	159181	17 30 25.97	+52 18 05.1	G	8.1882 ± 0.5562	G2 Ib–IIa	−21.00	Sou08	10.7	Leb06	5160 ± 150	1.86 ± 0.04	3.0 ± 0.5	+0.02 ± 0.10	Lyu10
β Oph	161096	17 43 28.35	+04 34 02.2	G	40.0945 ± 0.6752	K2 III	−12.53	Fam05	5.4	Mas08	4680 ± ...	2.95 ± ...	2.02 ± ...	+0.13 ± ...	Hek07
μ Her	161797	17 46 27.52	+27 43 14.2	G	119.1128 ± 0.4848	G5 IV	−17.69	Mon18	1.7	Jof15	5562 ± 35	3.98 ± 0.05	1.02 ± 0.07	+0.28 ± 0.05	Jof15
ξ Dra	163588	17 53 31.73	+56 52 21.6	G	29.8654 ± 0.3051	K2 III	−26.46	Mas08	2.3	Mas08	4702 ± 76	2.94 ± 0.33	1.41 ± 0.21	+0.12 ± 0.14	Sil15
θ Her	163770	17 56 15.17	+37 15 01.9	G	2.7547 ± 0.2684	K1 II+	−28.32	Fam05	3.4	Gra86	4255 ± ...	1.25 ± ...	2.75 ± ...	−0.11 ± ...	Hek07
ξ Her	163993	17 57 45.88	+29 14 52.3	G	25.2599 ± 0.3303	G8 III	−1.72	Fam05	2.8	Mas08	5220 ± 51	3.28 ± 0.26	1.62 ± 0.08	+0.06 ± 0.09	Sil15
ν Oph	163917	17 59 01.60	−09 46 24.9	G	23.0524 ± 0.4626	K1 III	+13.19	Jof15	2.8	Jof15	4997 ± 56	2.84 ± 0.09	1.60 ± 0.05	+0.05 ± 0.07	Jof15
Metal-poor giants (MPG)															
c Vir[f]	107328	12 20 20.99	+03 18 45.3	G	9.7577 ± 0.2536	K0 IIIb	+36.66	Gaia	1.9	Mas08	4496 ± 59	2.09 ± 0.13	1.20 ± 0.26	−0.33 ± 0.16	Jof18
υ Boo	120477	13 49 28.67	+15 47 52.3	G	14.2758 ± 0.3494	K5.5 III	−5.85	Fam05	5.1	Mas08	4170 ± ...	1.60 ± ...	2.60 ± ...	−0.57 ± ...	Hek07
Arcturus[f]	124897	14 15 39.68	+19 10 55.8	H	88.83 ± 0.54	K1.5 III	−5.19	Mas08	4.2	Mas08	4286 ± 35	1.60 ± 0.20	1.30 ± 0.12	−0.52 ± 0.08	Jof18
γ Lib	138905	15 35 31.57	−14 47 22.2	G	21.0823 ± 0.4010	G8.5 III	−26.71	Jof15	1.6	Jof15	4786 ± 13	2.55 ± 0.04	1.36 ± 0.05	−0.30 ± 0.03	Jof15
7 Psc[f]	220009	23 20 20.58	+05 22 52.8	G	9.5042 ± 0.1880	K1 IV	+40.46	Gaia	1.0	Med00	4266 ± 60	1.43 ± 0.12	1.30 ± 0.14	−0.74 ± 0.13	Jof14

[a] References for parallax, π: G: *Gaia* DR2 (Gaia Collaboration et al., 2018); H: *Hipparcos* (van Leeuwen, 2007).

[b] Reference for spectral type, SpT: Caballero et al. (in prep.).

[c] References for v_r: Fam05: Famaey et al. (2005); Gaia: Gaia Collaboration et al. (2018); Gon06: Gontcharov (2006); Hay18: Hayes et al. (2018); Kar04: Karataş et al. (2004); Jof15: Jofré et al. (2015a); Mal10: Maldonado et al. (2010); Mas08: Massarotti et al. (2008); Mon18: Montes et al. (2018); Nid02: Nidever et al. (2002); Pou04: Pourbaix et al. (2004); Sou13: Soubiran et al. (2013).

[d] References for $v \sin i$: San16: dos Santos et al (2016); Jof15: Jofré et al. (2015a); Gra86: Gray & Toner (1986); Gra18: Gray (2018); Leb06: Lèbre et al. (2006); Lyu12: Lyubimkov et al. (2012); Mar10: Martínez-Arnáiz et al. (2010); Mas08: Massarotti et al. (2008); McC14: McCarthy & Wilhelm (2014); Med02: De Medeiros et al. (2002); Pav12: Pavlenko et al. (2012); Tak05: Takeda et al. (2005).

[e] References for T_{eff}, log g, ξ, and [Fe/H]: All04: Allende Prieto et al. (2004); Hei03: Heiter & Luck (2003); Hek07: Hekker & Meléndez (2007); Jof14: Jofré et al. (2014); Jof15: Jofré et al. (2015a); Jof18: Jofré et al. (2018); Liu07: Liu et al. (2007); Luc14: Luck (2014); Lyu10: Lyubimkov et al. (2010); McW90: McWilliam (1990); Mor14: Morel et al. (2014); San13: Santos et al. (2013); Sil15: De Silva et al. (2015); Sou08: Sousa et al. (2008); Tak08: Takeda et al. (2008); Thy12: Thygesen et al. (2012); Val05: Valenti & Fischer (2005); Wu11: Wu et al. (2011).

[f] *Gaia* benchmark star (Jofré et al., 2014, 2018; Heiter et al., 2015a).

TABLE B.2. Stellar atmospheric parameters of the selected sample under STEPAR and $\log g$ values obtained with PARAM assuming parallaxes from *Gaia* DR2 and the *Hipparcos* mission.

Name	v_r [km s^{-1}]	S/N	T_{eff} [K]	$\log g$ [dex]	$\log g_{\text{PARAM}}$ [dex]	ξ [km s^{-1}]	[Fe/H] [dex]
			Metal-rich dwarfs (MRD)				
Sun	0.00 ± 0.00	249	5768 ± 58	4.45 ± 0.12	$... \pm ...$	1.31 ± 0.09	-0.01 ± 0.04
HD 3765	-63.18 ± 0.50	138	5310 ± 81	4.63 ± 0.24	4.55 ± 0.02	1.43 ± 0.10	$+0.12 \pm 0.03$
HD 100167	-29.41 ± 0.52	98	5898 ± 57	4.47 ± 0.12	4.43 ± 0.02	1.27 ± 0.09	$+0.01 \pm 0.04$
61 UMa	-5.47 ± 0.46	248	5555 ± 59	4.59 ± 0.13	4.52 ± 0.02	1.36 ± 0.10	-0.07 ± 0.03
β Vir	$+4.58 \pm 0.65$	345	6199 ± 63	4.23 ± 0.13	4.09 ± 0.02	1.53 ± 0.08	$+0.17 \pm 0.04$
β CVn	$+6.34 \pm 0.49$	241	5902 ± 61	4.41 ± 0.13	4.37 ± 0.03	1.22 ± 0.10	-0.20 ± 0.04
β Com	$+5.41 \pm 0.57$	198	6000 ± 58	4.44 ± 0.12	4.42 ± 0.01	1.30 ± 0.08	$+0.04 \pm 0.04$
ξ Boo	$+1.81 \pm 0.40$	67	5403 ± 52	4.48 ± 0.12	4.54 ± 0.02	1.45 ± 0.08	-0.19 ± 0.03
λ Ser	-66.22 ± 0.60	109	5835 ± 54	4.00 ± 0.14	4.22 ± 0.02	1.34 ± 0.07	-0.04 ± 0.04
18 Sco	$+11.93 \pm 0.59$	298	5774 ± 58	4.43 ± 0.13	4.41 ± 0.04	1.30 ± 0.08	0.00 ± 0.04
HD 166620	-19.26 ± 0.44	163	5039 ± 85	4.66 ± 0.21	4.56 ± 0.02	0.88 ± 0.13	-0.19 ± 0.03
HD 182488	-21.39 ± 0.45	178	5545 ± 70	4.59 ± 0.16	4.51 ± 0.02	1.34 ± 0.10	$+0.17 \pm 0.04$
σ Dra	$+26.77 \pm 0.55$	183	5259 ± 60	4.52 ± 0.14	4.56 ± 0.02	0.97 ± 0.09	-0.23 ± 0.03
HD 219134	-18.54 ± 0.57	149	5187 ± 92	4.71 ± 0.28	4.57 ± 0.02	1.28 ± 0.12	$+0.04 \pm 0.03$
			Metal-poor dwarfs (MPD)				
η Cas	$+8.41 \pm 0.92$	246	5807 ± 49	4.39 ± 0.12	4.33 ± 0.02	1.07 ± 0.07	-0.32 ± 0.04
μ Cas	-96.99 ± 0.81	245	5279 ± 48	4.35 ± 0.13	4.39 ± 0.03	1.09 ± 0.08	-0.90 ± 0.03
HD 49933	-12.14 ± 1.72	248	6401 ± 111	4.16 ± 0.19	4.17 ± 0.04	1.27 ± 0.09	-0.59 ± 0.07
CF UMa	-97.88 ± 0.91	201	5081 ± 43	4.40 ± 0.30	4.69 ± 0.02	1.31 ± 0.09	-1.41 ± 0.03
HD 154363	$+34.27 \pm 0.78$	96	5107 ± 68	4.35 ± 0.24	4.73 ± 0.01	1.07 ± 0.14	-0.71 ± 0.05
			Metal-rich giants (MRG)				
ι Gem	$+7.08 \pm 0.20$	268	4981 ± 64	2.76 ± 0.22	2.72 ± 0.08	1.71 ± 0.08	-0.01 ± 0.04
α CMi	-4.98 ± 0.89	341	6520 ± 113	3.77 ± 0.18	3.98 ± 0.03	1.50 ± 0.10	-0.02 ± 0.06
κ Gem	$+19.84 \pm 0.11$	318	5201 ± 75	3.00 ± 0.25	2.83 ± 0.02	1.93 ± 0.12	$+0.07 \pm 0.05$
β Gem	$+3.12 \pm 0.12$	130	4974 ± 65	2.91 ± 0.24	2.83 ± 0.04	1.46 ± 0.07	$+0.11 \pm 0.04$
ζ Mon	$+29.32 \pm 0.33$	239	5357 ± 74	1.94 ± 0.25	1.95 ± 0.06	4.87 ± 0.85	-0.06 ± 0.06
β Cnc	$+22.24 \pm 0.11$	270	4492 ± 180	1.84 ± 0.71	1.43 ± 0.16	2.30 ± 0.17	-0.21 ± 0.14
F Hya	$+26.86 \pm 0.25$	169	5397 ± 77	1.92 ± 0.19	1.71 ± 0.06	3.57 ± 0.39	-0.04 ± 0.06
ζ Hya	$+22.71 \pm 0.13$	182	4987 ± 63	2.61 ± 0.22	2.50 ± 0.02	1.80 ± 0.10	-0.02 ± 0.05
HD 77912	$+15.94 \pm 0.11$	153	5053 ± 75	2.24 ± 0.30	1.94 ± 0.06	3.63 ± 0.40	-0.09 ± 0.05
α Hya	-4.48 ± 0.11	267	4516 ± 156	1.69 ± 0.62	1.67 ± 0.05	2.15 ± 0.14	-0.08 ± 0.12
DK UMa	-26.99 ± 0.62	180	5351 ± 51	3.54 ± 0.14	3.37 ± 0.02	1.35 ± 0.07	-0.15 ± 0.04
10 LMi	-11.95 ± 0.11	134	5207 ± 66	3.05 ± 0.22	3.00 ± 0.02	1.81 ± 0.10	0.00 ± 0.05
ϵ Leo	$+4.45 \pm 0.17$	219	5448 ± 63	2.34 ± 0.19	2.27 ± 0.07	2.31 ± 0.15	-0.05 ± 0.05
μ Leo	$+13.75 \pm 0.08$	100	4839 ± 103	2.64 ± 0.42	2.52 ± 0.08	1.85 ± 0.12	$+0.25 \pm 0.07$
β LMi	$+8.11 \pm 0.10$	217	5184 ± 74	3.06 ± 0.24	2.80 ± 0.05	1.54 ± 0.09	$+0.16 \pm 0.05$
37 LMi	-8.58 ± 0.14	221	5423 ± 58	2.04 ± 0.18	2.31 ± 0.06	2.45 ± 0.15	-0.02 ± 0.04
α UMa	-11.97 ± 0.45	312	4809 ± 72	2.22 ± 0.30	2.04 ± 0.11	1.99 ± 0.11	-0.06 ± 0.05
ψ UMa	-4.26 ± 0.09	324	4768 ± 86	2.34 ± 0.34	2.21 ± 0.13	1.77 ± 0.10	$+0.01 \pm 0.06$
ν UMa	-9.18 ± 0.08	293	4233 ± 136	1.73 ± 0.55	1.44 ± 0.14	2.04 ± 0.11	-0.17 ± 0.10
56 UMa	$+0.44 \pm 0.34$	276	5037 ± 75	2.59 ± 0.26	2.23 ± 0.03	2.47 ± 0.17	0.00 ± 0.05
ϵ Vir	-14.09 ± 0.08	145	5211 ± 54	2.90 ± 0.21	2.64 ± 0.03	1.72 ± 0.08	$+0.16 \pm 0.04$
η Boo	$+1.64 \pm 0.52$	348	6115 ± 97	3.86 ± 0.20	3.79 ± 0.02	1.95 ± 0.12	$+0.28 \pm 0.06$

TABLE B.2. *continued*

Name	v_r [km s^{-1}]	S/N	T_{eff} [K]	$\log g$ [dex]	$\log g_{PARAM}$ [dex]	ξ [km s^{-1}]	[Fe/H] [dex]
ρ Boo	-13.86 ± 0.07	190	4620 ± 92	2.31 ± 0.36	1.91 ± 0.08	1.96 ± 0.09	-0.07 ± 0.07
β UMi	$+16.58 \pm 0.21$	304	4231 ± 167	2.06 ± 0.59	1.39 ± 0.04	2.13 ± 0.15	-0.16 ± 0.12
δ Boo	-12.05 ± 0.55	162	4940 ± 45	2.58 ± 0.17	2.67 ± 0.05	1.50 ± 0.06	-0.29 ± 0.03
ι Dra	-10.96 ± 0.22	175	4836 ± 87	2.86 ± 0.33	2.35 ± 0.07	1.79 ± 0.09	$+0.13 \pm 0.06$
α Ser	$+2.63 \pm 0.09$	84	4834 ± 85	2.75 ± 0.34	2.34 ± 0.13	1.75 ± 0.09	$+0.23 \pm 0.06$
κ CrB	-25.02 ± 0.26	142	4970 ± 77	3.29 ± 0.27	3.17 ± 0.03	1.44 ± 0.08	$+0.09 \pm 0.04$
ϵ CrB	-31.88 ± 0.11	224	4498 ± 75	2.46 ± 0.26	1.92 ± 0.08	1.57 ± 0.06	-0.03 ± 0.06
ϵ Oph	-9.43 ± 0.17	155	4987 ± 51	2.74 ± 0.18	2.66 ± 0.11	1.60 ± 0.07	-0.05 ± 0.04
ζ Her	-70.12 ± 0.53	173	5745 ± 58	3.72 ± 0.14	3.70 ± 0.06	1.52 ± 0.08	$+0.03 \pm 0.04$
κ Oph	-55.39 ± 0.12	155	4832 ± 78	2.56 ± 0.29	2.46 ± 0.14	1.77 ± 0.08	$+0.14 \pm 0.05$
π Her	-25.45 ± 0.11	109	4302 ± 117	1.74 ± 0.51	1.42 ± 0.11	2.42 ± 0.18	-0.07 ± 0.09
σ Oph	-26.83 ± 0.12	157	4503 ± 159	2.02 ± 0.54	1.14 ± 0.11	3.57 ± 0.42	-0.12 ± 0.10
β Dra	-20.44 ± 0.21	217	5302 ± 72	1.79 ± 0.22	1.78 ± 0.06	3.43 ± 0.35	-0.06 ± 0.06
β Oph	-12.23 ± 0.11	301	4955 ± 101	3.15 ± 0.35	2.54 ± 0.10	2.08 ± 0.15	$+0.28 \pm 0.06$
μ Her	-18.03 ± 0.39	233	5672 ± 60	4.08 ± 0.17	3.99 ± 0.02	1.36 ± 0.07	$+0.30 \pm 0.04$
ξ Dra	-26.12 ± 0.07	136	4843 ± 84	2.69 ± 0.39	2.73 ± 0.11	1.79 ± 0.10	$+0.06 \pm 0.06$
θ Her	-28.60 ± 0.12	237	4388 ± 137	1.84 ± 0.52	0.97 ± 0.12	3.86 ± 0.42	$+0.02 \pm 0.08$
ξ Her	-1.72 ± 0.15	237	5107 ± 57	2.74 ± 0.23	2.96 ± 0.03	1.61 ± 0.07	$+0.09 \pm 0.04$
ν Oph	$+12.35 \pm 0.11$	176	5001 ± 66	2.61 ± 0.22	2.63 ± 0.03	1.73 ± 0.07	$+0.15 \pm 0.04$
Metal-poor giants (MPG)							
c Vir	$+36.55 \pm 0.13$	353	4537 ± 65	2.23 ± 0.28	1.96 ± 0.11	1.64 ± 0.06	-0.29 ± 0.05
υ Boo	-5.84 ± 0.10	342	4177 ± 121	1.94 ± 0.48	1.67 ± 0.09	1.40 ± 0.09	-0.60 ± 0.15
α Boo	-4.71 ± 0.11	494	4409 ± 68	2.06 ± 0.26	1.64 ± 0.05	1.52 ± 0.05	-0.37 ± 0.06
γ Lib	-26.07 ± 0.14	88	4826 ± 48	2.81 ± 0.18	2.37 ± 0.06	1.42 ± 0.05	-0.26 ± 0.03
7 Psc	$+40.51 \pm 0.09$	117	4477 ± 64	2.14 ± 0.25	1.75 ± 0.05	1.44 ± 0.05	-0.59 ± 0.05

TABLE B.3. Stellar atmospheric parameters of the selected sample under STEPAR restricted to the optical and log *g* values obtained with PARAM assuming parallaxes from *Gaia* DR2 and the *Hipparcos* mission.

Name	v_r [km s^{-1}]	S/N	T_eff [K]	log *g* [dex]	log g_PARAM [dex]	ξ [km s^{-1}]	[Fe/H] [dex]
Metal-rich dwarfs (MRD)
Sun	0.00 ± 0.00	249	5787 ± 54	4.42 ± 0.11	... ± ...	0.98 ± 0.08	+0.02 ± 0.03
HD 3765	−63.18 ± 0.50	138	5206 ± 84	4.62 ± 0.22	4.55 ± 0.02	1.17 ± 0.12	+0.16 ± 0.04
HD 100167	−29.41 ± 0.52	98	5942 ± 54	4.49 ± 0.10	4.43 ± 0.02	1.04 ± 0.09	+0.04 ± 0.04
61 UMa	−5.47 ± 0.46	248	5576 ± 56	4.56 ± 0.12	4.52 ± 0.02	1.07 ± 0.09	−0.01 ± 0.03
β Vir	+4.58 ± 0.65	345	6255 ± 64	4.20 ± 0.12	4.09 ± 0.02	1.45 ± 0.08	+0.23 ± 0.04
β CVn	+6.34 ± 0.49	241	5967 ± 57	4.40 ± 0.12	4.37 ± 0.03	0.96 ± 0.09	−0.14 ± 0.04
β Com	+5.41 ± 0.57	198	6105 ± 56	4.42 ± 0.11	4.42 ± 0.01	1.18 ± 0.07	+0.02 ± 0.04
ξ Boo	+1.81 ± 0.40	67	5536 ± 55	4.50 ± 0.12	4.54 ± 0.02	1.25 ± 0.09	−0.15 ± 0.03
λ Ser	−66.22 ± 0.60	109	5950 ± 56	4.31 ± 0.14	4.22 ± 0.02	1.22 ± 0.08	+0.05 ± 0.04
18 Sco	+11.93 ± 0.59	298	5786 ± 54	4.40 ± 0.10	4.41 ± 0.04	0.99 ± 0.09	+0.02 ± 0.04
HD 166620	−19.26 ± 0.44	163	5048 ± 64	4.63 ± 0.15	4.56 ± 0.02	0.80 ± 0.18	−0.14 ± 0.02
HD 182488	−21.39 ± 0.45	178	5543 ± 67	4.66 ± 0.17	4.51 ± 0.02	1.12 ± 0.10	+0.24 ± 0.04
σ Dra	+26.77 ± 0.55	183	5278 ± 60	4.50 ± 0.13	4.56 ± 0.02	0.79 ± 0.11	−0.20 ± 0.05
HD 219134	−18.54 ± 0.57	149	5162 ± 84	4.72 ± 0.25	4.57 ± 0.02	1.08 ± 0.13	+0.10 ± 0.05
Metal-poor dwarfs (MPD)
η Cas	+8.41 ± 0.92	246	5861 ± 53	4.45 ± 0.12	4.33 ± 0.02	0.89 ± 0.09	−0.27 ± 0.04
μ Cas	−96.99 ± 0.81	245	5350 ± 56	4.49 ± 0.15	4.39 ± 0.03	0.87 ± 0.22	−0.77 ± 0.04
HD 49933	−12.14 ± 1.72	248	6665 ± 102	4.18 ± 0.17	4.17 ± 0.04	1.32 ± 0.09	−0.41 ± 0.06
CF UMa	−97.88 ± 0.91	201	5101 ± 51	4.38 ± 0.32	4.69 ± 0.02	1.27 ± 0.10	−1.38 ± 0.04
HD 154363	+34.27 ± 0.78	96	5082 ± 86	4.32 ± 0.56	4.73 ± 0.01	1.12 ± 0.13	−0.60 ± 0.06
Metal-rich giants (MRG)
ι Gem	+7.08 ± 0.20	268	4905 ± 70	2.55 ± 0.26	2.72 ± 0.08	1.57 ± 0.08	−0.02 ± 0.05
α CMi	−4.98 ± 0.89	341	6593 ± 92	4.01 ± 0.11	3.98 ± 0.03	1.52 ± 0.08	+0.03 ± 0.05
κ Gem	+19.84 ± 0.11	318	5194 ± 88	3.06 ± 0.26	2.83 ± 0.02	1.74 ± 0.12	+0.11 ± 0.06
β Gem	+3.12 ± 0.12	130	4930 ± 79	2.78 ± 0.31	2.83 ± 0.04	1.36 ± 0.09	+0.12 ± 0.06
ζ Mon	+29.32 ± 0.33	239	5346 ± 77	1.74 ± 0.23	1.95 ± 0.06	4.56 ± 0.26	+0.06 ± 0.06
β Cnc	+22.24 ± 0.11	270	4357 ± 126	1.79 ± 0.52	1.43 ± 0.16	1.98 ± 0.14	−0.16 ± 0.13
F Hya	+26.86 ± 0.25	169	5331 ± 75	1.84 ± 0.20	1.71 ± 0.06	2.71 ± 0.20	+0.01 ± 0.06
ζ Hya	+22.71 ± 0.13	182	4980 ± 74	2.68 ± 0.27	2.50 ± 0.02	1.66 ± 0.09	+0.04 ± 0.06
HD 77912	+15.94 ± 0.11	153	5006 ± 83	2.19 ± 0.28	1.94 ± 0.06	2.55 ± 0.19	+0.00 ± 0.06
α Hya	−4.48 ± 0.11	267	4450 ± 115	1.45 ± 0.49	1.67 ± 0.05	2.00 ± 0.12	−0.11 ± 0.10
DK UMa	−26.99 ± 0.62	180	5379 ± 51	3.65 ± 0.15	3.37 ± 0.02	1.24 ± 0.07	−0.17 ± 0.04
10 LMi	−11.95 ± 0.11	134	5195 ± 74	3.12 ± 0.23	3.00 ± 0.02	1.52 ± 0.10	+0.08 ± 0.06
ε Leo	+4.45 ± 0.17	219	5472 ± 72	2.45 ± 0.18	2.27 ± 0.07	2.12 ± 0.13	+0.02 ± 0.06
μ Leo	+13.75 ± 0.08	100	4789 ± 127	2.63 ± 0.46	2.52 ± 0.08	1.56 ± 0.12	+0.30 ± 0.09
β LMi	+8.11 ± 0.10	217	5172 ± 85	3.09 ± 0.29	2.80 ± 0.05	1.37 ± 0.09	+0.20 ± 0.06
37 LMi	−8.58 ± 0.14	221	5515 ± 67	2.22 ± 0.21	2.31 ± 0.06	2.25 ± 0.13	+0.09 ± 0.05
α UMa	−11.97 ± 0.45	312	4696 ± 83	2.18 ± 0.37	2.04 ± 0.11	1.75 ± 0.10	−0.12 ± 0.07
ψ UMa	−4.26 ± 0.09	324	4682 ± 90	2.18 ± 0.36	2.21 ± 0.13	1.67 ± 0.10	−0.02 ± 0.07
ν UMa	−9.18 ± 0.08	293	4258 ± 107	1.94 ± 0.45	1.44 ± 0.14	1.81 ± 0.11	−0.22 ± 0.10
56 UMa	+0.44 ± 0.34	276	5004 ± 79	2.33 ± 0.28	2.23 ± 0.03	2.18 ± 0.15	+0.02 ± 0.06
ε Vir	−14.09 ± 0.08	145	5165 ± 63	2.81 ± 0.23	2.64 ± 0.03	1.52 ± 0.07	+0.20 ± 0.05
η Boo	+1.64 ± 0.52	348	6126 ± 101	3.82 ± 0.20	3.79 ± 0.02	1.94 ± 0.13	+0.34 ± 0.07

TABLE B.3. *continued*

Name	v_r [km s^{-1}]	S/N	T_{eff} [K]	$\log g$ [dex]	$\log g_{PARAM}$ [dex]	ξ [km s^{-1}]	[Fe/H] [dex]
ρ Boo	-13.86 ± 0.07	190	4519 ± 87	2.00 ± 0.33	1.91 ± 0.08	1.75 ± 0.09	-0.09 ± 0.08
β UMi	$+16.58 \pm 0.21$	304	4270 ± 125	2.10 ± 0.57	1.39 ± 0.04	1.71 ± 0.11	-0.24 ± 0.14
δ Boo	-12.05 ± 0.55	162	4926 ± 47	2.57 ± 0.18	2.67 ± 0.05	1.37 ± 0.05	-0.24 ± 0.04
ι Dra	-10.96 ± 0.22	175	4776 ± 92	2.71 ± 0.38	2.35 ± 0.07	1.63 ± 0.09	$+0.15 \pm 0.07$
α Ser	$+2.63 \pm 0.09$	84	4723 ± 97	2.46 ± 0.36	2.34 ± 0.13	1.50 ± 0.10	$+0.24 \pm 0.08$
κ CrB	-25.02 ± 0.26	142	4933 ± 78	3.40 ± 0.25	3.17 ± 0.03	1.30 ± 0.08	$+0.17 \pm 0.05$
ϵ CrB	-31.88 ± 0.11	224	4471 ± 66	2.34 ± 0.26	1.92 ± 0.08	1.52 ± 0.06	-0.04 ± 0.06
ϵ Oph	-9.43 ± 0.17	155	4942 ± 58	2.64 ± 0.21	2.66 ± 0.11	1.44 ± 0.06	-0.03 ± 0.05
ζ Her	-70.12 ± 0.53	173	5821 ± 64	3.88 ± 0.15	3.70 ± 0.06	1.39 ± 0.08	$+0.07 \pm 0.05$
κ Oph	-55.39 ± 0.12	155	4723 ± 86	2.60 ± 0.39	2.46 ± 0.14	1.61 ± 0.08	$+0.11 \pm 0.07$
π Her	-25.45 ± 0.11	109	4274 ± 121	1.76 ± 0.56	1.42 ± 0.11	2.07 ± 0.15	-0.11 ± 0.11
σ Oph	-26.83 ± 0.12	157	4423 ± 117	1.71 ± 0.45	1.14 ± 0.11	2.73 ± 0.24	-0.09 ± 0.10
β Dra	-20.44 ± 0.21	217	5312 ± 70	1.63 ± 0.24	1.78 ± 0.06	2.59 ± 0.18	$+0.03 \pm 0.06$
β Oph	-12.23 ± 0.11	301	4813 ± 101	2.80 ± 0.38	2.54 ± 0.10	1.82 ± 0.14	$+0.24 \pm 0.08$
μ Her	-18.03 ± 0.39	233	5677 ± 69	4.14 ± 0.18	3.99 ± 0.02	1.19 ± 0.08	$+0.36 \pm 0.05$
ξ Dra	-26.12 ± 0.07	136	4680 ± 91	2.55 ± 0.34	2.73 ± 0.11	1.52 ± 0.10	$+0.05 \pm 0.08$
θ Her	-28.60 ± 0.12	237	4359 ± 100	1.94 ± 0.28	0.97 ± 0.12	4.28 ± 0.12	$+0.04 \pm 0.10$
ξ Her	-1.72 ± 0.15	237	5086 ± 66	2.69 ± 0.27	2.96 ± 0.03	1.44 ± 0.07	$+0.15 \pm 0.05$
ν Oph	$+12.35 \pm 0.11$	176	4939 ± 75	2.47 ± 0.26	2.63 ± 0.03	1.59 ± 0.08	$+0.15 \pm 0.05$
Metal-poor giants (MPG)							
c Vir	$+36.55 \pm 0.13$	353	4560 ± 54	2.33 ± 0.24	1.96 ± 0.11	1.70 ± 0.08	-0.27 ± 0.05
υ Boo	-5.84 ± 0.10	342	4216 ± 116	2.05 ± 0.49	1.67 ± 0.09	1.45 ± 0.10	-0.62 ± 0.15
α Boo	-4.71 ± 0.11	494	4416 ± 58	2.09 ± 0.23	1.64 ± 0.05	1.48 ± 0.07	-0.35 ± 0.06
γ Lib	-26.07 ± 0.14	88	4863 ± 49	2.96 ± 0.18	2.37 ± 0.06	1.36 ± 0.06	-0.29 ± 0.04
7 Psc	$+40.51 \pm 0.09$	117	4465 ± 54	2.12 ± 0.22	1.75 ± 0.05	1.43 ± 0.05	-0.58 ± 0.05

TABLE B.4. Merged Fe I line lists.

λ_{air} [Å]	χ_I [eV]	$\log gf$	MRD	MPD	MRG	MPG	Reference [b]
5307.361	1.61	−2.912	•	•		•	Sou08
5321.108	4.44	−1.089				•	Sou08
5322.041	2.28	−2.802	•			•	Sou08
5339.929	3.27	−0.635				•	Sou08
5364.871	4.45	+0.228			•	•	Sou08
5373.709	4.47	−0.710	•	•			Sou08
5379.574	3.70	−1.514	•	•	•	•	Sou08
5386.333	4.15	−1.670	•		•	•	Sou08
5389.479	4.42	−0.410		•	•		Sou08
5397.618	3.63	−2.528			•		Sou08
5398.279	4.45	−0.630	•	•	•		Sou08
5400.501	4.37	−0.160	•	•			Sou08
5401.266	4.32	−1.820	•		•		Sou08
5409.133	4.37	−1.200	•	•			Sou08
5417.033	4.42	−1.580	•		•		Sou08
5424.068	4.32	+0.520		•			Sou08
5436.295	4.39	−1.440	•		•	•	Sou08
5436.588	2.28	−2.964			•		Sou08
5441.339	4.31	−1.630	•		•	•	Sou08
5445.042	4.39	−0.020		•	•	•	Sou08
5460.873	3.07	−3.426			•	•	Sou08
5461.550	4.45	−1.800	•		•		Sou08
5463.275	4.44	+0.070			•	•	Sou08
5464.280	4.14	−1.402			•		Sou08
5466.396	4.37	−0.630	•	•		•	Sou08
5470.093	4.45	−1.710	•		•		Sou08
5472.709	4.21	−1.495	•				Sou08
5473.900	4.15	−0.720	•	•			Sou08
5483.099	4.15	−1.392	•			•	Sou08
5501.465	0.96	−3.047		•		•	Sou08
5506.778	0.99	−2.797		•			Sou08
5522.446	4.21	−1.550	•	•			Sou08
5536.580	2.83	−3.810				•	Sou08
5539.280	3.64	−2.660				•	Sou08
5543.147	3.69	−1.570		•			Sou08
5543.935	4.22	−1.140	•	•	•	•	Sou08
5546.505	4.37	−1.310		•			Sou08
5549.949	3.69	−2.910			•		Sou08
5554.894	4.55	−0.440		•			Sou08
5560.211	4.43	−1.190	•	•	•		Sou08
5572.842	3.40	−0.275				•	Sou08
5576.089	3.43	−1.000		•	•	•	Sou08
5618.632	4.21	−1.276	•	•	•	•	Sou08
5619.595	4.39	−1.700	•			•	Sou08
5633.946	4.99	−0.270		•			Sou08
5635.822	4.26	−1.890	•				Sou08

TABLE B.4. *continued*

λ_{air} [Å]	χ_{I} [eV]	$\log gf$	Line list [a]				Reference [b]
			MRD	MPD	MRG	MPG	
5636.695	3.64	−2.610	●		●		Sou08
5638.262	4.22	−0.870	●	●			Sou08
5641.434	4.26	−1.180	●	●			Sou08
5649.987	5.10	−0.920	●			●	Sou08
5651.468	4.47	−2.000	●				Sou08
5652.317	4.26	−1.950	●				Sou08
5653.864	4.39	−1.640	●			●	Sou08
5655.176	5.06	−0.640	●			●	Sou08
5661.344	4.28	−1.736	●			●	Sou08
5662.516	4.18	−0.573	●	●		●	Sou08
5679.023	4.65	−0.920	●	●	●	●	Sou08
5691.496	4.30	−1.520		●			Sou08
5696.088	4.55	−1.720	●				Sou08
5701.543	2.56	−2.216	●	●			Sou08
5705.464	4.30	−1.355	●				Sou08
5717.832	4.28	−1.130	●	●	●	●	Sou08
5720.886	4.55	−1.950	●		●	●	Sou08
5731.761	4.26	−1.300	●	●		●	Sou08
5732.296	4.99	−1.560	●				Sou08
5741.847	4.26	−1.854	●				Sou08
5759.262	4.65	−2.070			●		Sou08
5778.453	2.59	−3.430			●		Sou08
5784.658	3.40	−2.532			●		Sou08
5844.918	4.15	−2.940			●		Sou08
5849.683	3.69	−2.990				●	Sou08
5852.218	4.55	−1.330	●		●		Sou08
5853.148	1.48	−5.280			●	●	Sou08
5855.075	4.61	−1.478	●		●		Sou08
5856.088	4.29	−1.328			●		Sou08
5858.778	4.22	−2.260			●		Sou08
5861.108	4.28	−2.450			●	●	Sou08
5883.816	3.96	−1.360	●	●		●	Sou08
5902.472	4.59	−1.810				●	Sou08
5905.671	4.65	−0.730	●	●	●	●	Sou08
5909.972	3.21	−2.587	●		●	●	Sou08
5916.247	2.45	−2.994	●		●	●	Sou08
5927.788	4.65	−1.090	●		●		Sou08
5929.676	4.55	−1.462	●		●		Sou08
5930.180	4.65	−0.230	●	●	●		Sou08
5934.654	3.93	−1.170	●	●		●	Sou08
5940.991	4.18	−2.150				●	Sou08
5952.718	3.98	−1.440				●	Sou08
5956.693	0.86	−4.605	●	●	●	●	Sou08
6003.011	3.88	−1.120	●	●	●	●	Sou08
6012.209	2.22	−4.038				●	Sou08
6019.365	3.57	−3.360				●	Sou08

TABLE B.4. *continued*

λ_{air} [Å]	χ_I [eV]	$\log gf$	Line list [a]				Reference [b]
			MRD	MPD	MRG	MPG	
6024.057	4.55	−0.120	•	•		•	Sou08
6027.051	4.08	−1.089	•	•	•	•	Sou08
6056.004	4.73	−0.460		•			Sou08
6065.481	2.61	−1.530		•	•		Sou08
6079.007	4.65	−0.729	•	•	•	•	Sou08
6082.710	2.22	−3.573	•		•	•	Sou08
6093.642	4.61	−1.500	•		•	•	Sou08
6094.372	4.65	−1.940				•	Sou08
6096.664	3.98	−1.930	•			•	Sou08
6098.243	4.56	−1.880	•		•	•	Sou08
6120.246	0.91	−5.950			•	•	Sou08
6127.906	4.14	−1.399	•	•		•	Sou08
6136.614	2.45	−1.400		•			Sou08
6136.993	2.20	−2.950		•			Sou08
6137.691	2.59	−1.403		•			Sou08
6151.617	2.18	−3.299	•	•		•	Sou08
6165.359	4.14	−1.474	•	•		•	Sou08
6170.506	4.80	−0.440	•	•			Sou08
6173.334	2.22	−2.880	•	•	•	•	Sou08
6180.202	2.73	−2.586	•				Sou08
6187.989	3.94	−1.720	•		•	•	Sou08
6191.557	2.43	−1.417		•			Sou08
6199.506	2.56	−4.430				•	Sou08
6200.312	2.61	−2.437	•	•		•	Sou08
6213.429	2.22	−2.482	•	•		•	Sou08
6219.280	2.20	−2.433	•	•		•	Sou08
6220.779	3.88	−2.460				•	Sou08
6226.734	3.88	−2.220	•				Sou08
6229.225	2.85	−2.805	•		•	•	Sou08
6230.722	2.56	−1.281	•	•			Sou08
6240.646	2.22	−3.233	•	•	•	•	Sou08
6246.318	3.60	−0.733	•	•	•		Sou08
6252.555	2.40	−1.687	•	•	•	•	Sou08
6265.132	2.18	−2.550	•	•	•	•	Sou08
6270.223	2.86	−2.464	•		•	•	Sou08
6271.278	3.33	−2.703			•	•	Sou08
6280.617	0.86	−4.387		•			Sou08
6290.543	2.59	−4.330				•	Sou08
6297.792	2.22	−2.740		•		•	Sou08
6301.499	3.65	−0.718			•	•	Sou08
6311.499	2.83	−3.141	•			•	Sou08
6315.811	4.08	−1.710	•			•	Sou08
6322.685	2.59	−2.426	•	•	•	•	Sou08
6335.329	2.20	−2.177	•	•	•	•	Sou08
6336.823	3.69	−0.856	•	•	•	•	Spou08
6338.875	4.80	−1.060	•				Sou08

TABLE B.4. *continued*

λ_{air} [Å]	χ_I [eV]	$\log gf$	MRD	MPD	MRG	MPG	Reference [b]
6344.147	2.43	−2.923		●			Sou08
6355.028	2.85	−2.350		●			Sou08
6380.743	4.19	−1.376	●			●	Sou08
6393.600	2.43	−1.432		●	●		Sou08
6400.316	0.91	−4.318	●	●			Sou08
6411.648	3.65	−0.595		●			Sou08
6421.350	2.28	−2.027	●	●			Sou08
6430.845	2.18	−2.006	●	●			Sou08
6469.192	4.83	−0.770	●	●			Sou08
6475.623	2.56	−2.942	●	●			Sou08
6481.869	2.28	−2.984	●	●		●	Sou08
6494.980	2.40	−1.273		●			Sou08
6495.741	4.83	−0.940	●				Sou08
6496.465	4.80	−0.570	●	●		●	Sou08
6498.938	0.96	−4.699	●			●	Sou08
6518.365	2.83	−2.460				●	Sou08
6533.928	4.56	−1.460	●	●	●	●	Sou08
6546.237	2.76	−1.536		●	●	●	Sou08
6574.226	0.99	−5.023	●				Sou08
6581.209	1.48	−4.679				●	Sou08
6591.312	4.59	−2.070			●	●	Sou08
6592.912	2.73	−1.473	●	●		●	Sou08
6593.869	2.43	−2.422	●	●		●	Sou08
6597.561	4.80	−1.070				●	Sou08
6608.025	2.28	−4.030	●			●	Sou08
6609.109	2.56	−2.692	●	●		●	Sou08
6627.543	4.55	−1.680	●				Sou08
6633.412	4.83	−1.490	●				Sou08
6633.748	4.56	−0.799	●				Sou08
6648.079	1.01	−5.429				●	Sou08
6703.565	2.76	−3.160	●		●		Sou08
6710.318	1.48	−4.880	●				Sou08
6713.742	4.80	−1.600	●		●		Sou08
6716.236	4.58	−1.920	●				Sou08
6725.355	4.10	−2.300			●	●	Sou08
6750.151	2.42	−2.621	●	●	●	●	Sou08
6752.707	4.64	−1.204	●	●			Sou08
6783.703	2.59	−3.980	●	●	●		This work
6786.858	4.19	−2.070	●	●	●	●	This work
6793.258	4.08	−2.326	●	●	●		This work
6793.619	4.80	−1.329	●	●	●		This work
6796.123	4.14	−2.530	●		●		This work
6801.865	1.61	−4.829				●	This work
6803.999	4.65	−1.496	●	●			This work
6804.270	4.58	−1.813	●	●			This work
6806.842	2.73	−3.210	●	●	●	●	This work

TABLE B.4. *continued*

λ_{air} [Å]	χ_I [eV]	$\log gf$	MRD	MPD	MRG	MPG	Reference [b]
6810.262	4.61	−0.986	•	•	•	•	This work
6819.588	4.10	−2.764	•		•		This work
6820.371	4.64	−1.320	•	•	•	•	This work
6828.591	4.64	−0.920	•	•	•	•	This work
6833.225	4.64	−2.080	•		•		This work
6837.005	4.59	−1.687	•	•	•	•	This work
6838.827	5.84	−0.361	•	•	•		This work
6839.829	2.56	−3.450	•	•	•	•	This work
6841.338	4.61	−0.750	•	•	•		This work
6842.685	4.64	−1.320	•	•	•	•	This work
6843.655	4.55	−0.930	•	•	•	•	This work
6850.435	5.46	−1.053	•		•		This work
6851.635	1.61	−5.320				•	This work
6854.823	4.59	−1.926	•	•			This work
6855.161	4.56	−0.742	•	•	•		This work
6855.712	4.61	−1.820	•	•	•		This work
6857.249	4.08	−2.150	•	•	•	•	This work
6858.148	4.61	−0.930	•	•	•		This work
6859.479	2.85	−4.520				•	This work
6861.937	2.42	−3.890		•			This work
6862.480	4.56	−1.570		•		•	This work
6864.311	4.56	−2.320				•	This work
6885.754	4.65	−1.380		•		•	This work
6911.511	2.42	−4.040				•	This work
6916.680	4.15	−1.450				•	This work
6933.617	2.43	−3.580		•			This work
6945.204	2.42	−2.482				•	This work
6947.488	4.58	−1.611		•			This work
6951.245	4.56	−0.908		•			This work
6971.932	3.02	−3.340	•	•	•	•	This work
6975.426	5.83	−0.215	•	•			This work
6977.428	4.59	−1.564		•		•	This work
6978.850	2.48	−2.500	•	•	•		This work
6988.523	2.40	−3.660		•		•	This work
6999.883	4.10	−1.560	•	•	•		This work
7000.614	4.14	−2.386	•		•	•	This work
7007.965	4.18	−2.060	•	•	•		This work
7011.343	4.59	−1.316		•	•	•	This work
7014.986	2.45	−4.250				•	This work
7016.055	2.42	−3.210		•			This work
7022.390	4.30	−2.290	•		•	•	This work
7022.952	4.19	−1.250		•		•	This work
7024.050	4.08	−2.208	•	•	•		This work
7024.641	4.56	−1.080		•			This work
7038.220	4.22	−1.300	•	•	•		This work
7038.769	4.26	−1.990	•	•	•		This work

TABLE B.4. *continued*

λ_{air} [Å]	χ_I [eV]	$\log gf$	MRD	MPD	MRG	MPG	Reference [b]
				Line list [a]			
7057.953	3.65	−3.380				●	This work
7069.531	2.56	−4.340				●	This work
7071.860	4.61	−1.700				●	This work
7072.791	5.90	−0.882	●				This work
7072.818	4.08	−2.840			●		This work
7083.394	4.91	−1.202	●	●	●	●	This work
7086.724	3.60	−2.356	●	●	●	●	This work
7090.383	4.23	−1.210	●	●	●		This work
7091.921	4.96	−1.298	●		●	●	This work
7095.407	4.21	−2.020	●	●	●		This work
7100.193	2.73	−3.897				●	This work
7107.459	4.19	−1.343		●			This work
7112.167	2.99	−2.998	●	●	●	●	This work
7114.548	2.69	−4.010	●	●	●	●	This work
7118.096	5.01	−1.570	●		●	●	This work
7120.021	4.56	−1.936	●				This work
7127.567	4.99	−1.046	●	●	●		This work
7130.921	4.22	−0.790	●	●	●		This work
7132.986	4.08	−1.628	●		●	●	This work
7142.517	4.96	−0.848		●		●	This work
7145.306	4.61	−1.145	●	●			This work
7151.469	2.48	−3.730	●	●	●	●	This work
7155.630	5.01	−0.725		●			This work
7162.343	5.02	−1.064				●	This work
7179.994	1.48	−4.780	●		●		This work
7212.435	4.96	−0.825	●		●		This work
7219.682	4.08	−1.690	●	●	●	●	This work
7221.202	4.56	−1.184	●	●	●		This work
7223.657	3.02	−2.225				●	This work
7228.695	2.76	−3.380	●	●	●		This work
7239.866	4.21	−1.852				●	This work
7256.134	4.96	−1.590				●	This work
7284.834	4.14	−1.750	●		●	●	This work
7285.275	4.61	−1.700	●		●		This work
7288.736	4.22	−1.035		●			This work
7306.562	4.18	−1.740	●		●	●	This work
7311.074	4.28	−0.967			●		This work
7376.480	6.00	+0.089	●	●	●		This work
7381.333	5.35	−1.087	●		●		This work
7386.333	4.91	−0.267	●		●		This work
7396.507	4.99	−1.640			●		This work
7401.683	4.19	−1.599				●	This work
7411.153	4.28	−0.299	●	●	●	●	This work
7418.666	4.14	−1.376	●	●	●	●	This work
7421.559	4.64	−1.800	●	●	●		This work
7430.538	2.59	−3.860		●			This work

TABLE B.4. *continued*

λ_{air} [Å]	χ_I [eV]	$\log gf$	MRD	MPD	MRG	MPG	Reference [b]
7430.855	4.61	−1.539		•			This work
7435.591	5.31	−0.716	•	•	•	•	This work
7440.911	4.91	−0.573		•	•		This work
7443.022	4.19	−1.820		•		•	This work
7445.748	4.26	−0.102		•			This work
7447.393	4.96	−0.846	•	•	•	•	This work
7453.997	4.19	−2.410	•			•	This work
7461.519	2.56	−3.580	•	•	•	•	This work
7463.382	5.06	−1.720	•		•		This work
7464.293	5.41	−1.066	•		•		This work
7472.750	5.35	−0.994	•				This work
7473.554	4.61	−1.870	•		•		This work
7477.506	3.88	−3.045				•	This work
7484.297	5.09	−1.700	•				This work
7491.647	4.30	−0.900	•	•	•		This work
7495.065	4.22	+0.052		•			This work
7498.530	4.14	−2.250	•	•	•	•	This work
7504.270	5.39	−1.006	•		•		This work
7506.013	5.06	−1.219	•				This work
7507.265	4.42	−1.485	•	•	•	•	This work
7511.018	4.18	+0.099	•	•	•	•	This work
7514.198	5.39	−0.874	•		•	•	This work
7531.143	4.37	−0.951				•	This work
7540.429	2.73	−3.850	•		•	•	This work
7547.896	5.10	−1.350	•		•	•	This work
7551.104	5.09	−1.630	•		•		This work
7559.719	5.06	−1.080	•	•	•		This work
7563.010	4.83	−2.047				•	This work
7568.898	4.28	−0.773	•	•	•	•	This work
7573.413	6.58	+0.302	•		•		This work
7582.121	4.96	−1.750	•		•		This work
7583.788	3.02	−1.885	•	•	•	•	This work
7586.017	4.31	−0.470	•		•	•	This work
7588.844	5.10	−1.672	•				This work
7620.513	4.73	−0.664		•			This work
7689.036	5.10	−1.370				•	This work
7710.363	4.22	−1.113		•		•	This work
7719.048	5.03	−1.153	•	•	•	•	This work
7723.207	2.28	−3.617		•		•	This work
7733.723	5.06	−1.536	•		•	•	This work
7745.513	5.09	−1.170	•	•	•	•	This work
7746.595	5.06	−1.284	•	•	•	•	This work
7748.269	2.95	−1.751		•	•	•	This work
7751.108	4.99	−0.754	•	•	•	•	This work
7780.556	4.47	+0.030	•	•	•	•	This work
7802.473	5.09	−1.335	•		•	•	This work

TABLE B.4. *continued*

λ_{air} [Å]	χ_{I} [eV]	$\log gf$	MRD	MPD	MRG	MPG	Reference [b]
7807.908	4.99	−0.542	●	●	●	●	This work
7832.195	4.43	+0.112	●	●	●	●	This work
7844.558	4.83	−1.810	●		●	●	This work
7855.399	5.06	−1.017		●			This work
7869.609	4.37	−1.880		●			This work
7879.756	5.03	−1.650	●		●	●	This work
7912.866	0.86	−4.848		●			This work
7937.139	4.31	+0.228		●		●	This work
7941.087	3.27	−2.286	●	●	●	●	This work
7945.846	4.39	+0.227		●		●	This work
7954.934	2.99	−3.675	●				This work
7959.142	5.03	−1.212	●	●	●		This work
7998.944	4.37	+0.151		●		●	This work
8028.312	4.47	−0.689		●			This work
8046.046	4.42	+0.032		●			This work
8047.617	0.86	−4.787	●	●	●	●	This work
8075.149	0.91	−5.062		●	●	●	This work
8085.171	4.45	−0.121		●		●	This work
8089.353	5.07	−1.147	●				This work
8090.325	4.58	−1.912	●				This work
8096.875	4.08	−1.776		●		●	This work
8198.920	4.43	−0.566		●			This work
8204.936	0.96	−5.058		●			This work
8207.741	4.45	−0.856	●	●	●	●	This work
8220.377	4.32	+0.275				●	This work
8239.127	2.42	−3.180				●	This work
8248.128	4.37	−0.892		●		●	This work
8293.512	3.30	−2.175		●		●	This work
8327.055	2.20	−1.525		●		●	This work
8340.502	5.07	−1.701	●		●		This work
8342.856	4.99	−1.468	●		●		This work
8349.045	0.91	−5.705				●	This work
8358.520	2.99	−3.145	●		●		This work
8360.793	4.47	−1.688				●	This work
8365.631	3.25	−2.047	●		●	●	This work
8387.771	2.18	−1.493		●		●	This work
8404.395	5.79	−0.705	●				This work
8419.271	6.18	−0.231	●				This work
8422.913	4.14	−2.002		●			This work
8424.141	4.96	−1.156	●	●	●		This work
8439.570	4.55	−0.591		●		●	This work
8447.636	0.96	−6.699				●	This work
8453.657	5.54	−1.043	●		●		This work
8468.406	2.22	−2.072		●			This work
8471.743	4.96	−1.019		●		●	This work
8481.980	4.19	−1.999		●		●	This work

Table B.4. *continued*

λ_{air} [Å]	χ_I [eV]	$\log gf$	MRD	MPD	MRG	MPG	Reference [b]
				Line list [a]			
8514.071	2.20	−2.229	●	●	●	●	This work
8515.108	3.02	−2.073	●	●	●		This work
8517.305	6.13	−0.259	●				This work
8526.669	4.91	−0.760		●		●	This work
8571.804	5.01	−1.391				●	This work
8582.257	2.99	−2.134	●	●	●	●	This work
8592.951	4.96	−1.086		●		●	This work
8598.828	4.39	−1.089		●		●	This work
8607.080	5.01	−1.557				●	This work
8611.803	2.85	−1.926	●	●	●	●	This work
8613.939	4.99	−1.246				●	This work
8616.280	4.91	−0.707		●		●	This work
8621.601	2.95	−2.321	●	●	●	●	This work
8632.413	4.10	−2.409				●	This work
8667.366	2.45	−4.939				●	This work
8674.746	2.83	−1.800	●	●	●	●	This work
8678.930	2.45	−5.418				●	This work
8679.632	4.97	−1.276	●	●	●		This work
8688.623	2.18	−1.212	●	●	●	●	This work
8698.706	2.99	−3.442				●	This work
8699.454	4.96	−0.380		●		●	This work
8710.392	4.91	−0.532		●	●		This work
8713.187	2.95	−2.467		●		●	This work
8729.143	3.41	−2.872		●		●	This work
8747.425	3.02	−3.174	●	●	●	●	This work
8757.187	2.85	−2.059	●	●	●	●	This work
8763.966	4.65	−0.146	●	●	●	●	This work
8784.440	4.96	−1.593	●	●	●	●	This work
8793.341	4.61	−0.092		●			This work
8796.484	4.96	−1.229	●		●	●	This work
8804.624	2.28	−3.234	●	●	●	●	This work
8824.219	2.20	−1.540	●	●	●	●	This work
8828.091	4.96	−2.240				●	This work
8834.016	4.22	−2.590				●	This work
8838.428	2.86	−2.050	●	●	●	●	This work
8846.740	5.01	−0.781	●	●	●	●	This work
8863.587	4.97	−1.519				●	This work
8866.931	4.55	+0.083	●	●	●	●	This work
8868.430	3.02	−2.909	●	●	●	●	This work
8876.024	5.02	−1.052	●	●	●		This work
8878.250	2.99	−3.383				●	This work
8897.899	4.91	−1.937				●	This work
8902.924	4.99	−2.106				●	This work
8920.013	5.06	−0.415	●	●	●		This work
8922.650	4.99	−1.698	●		●	●	This work
8929.075	5.09	−0.893		●		●	This work

Table B.4. *continued*

λ_{air} [Å]	χ_{I} [eV]	$\log gf$	MRD	MPD	MRG	MPG	Reference [b]
8931.776	3.05	−3.216				•	This work
8943.065	2.83	−3.346	•	•		•	This work
8945.189	5.03	−0.220	•		•	•	This work
8946.260	2.85	−3.509				•	This work
8950.188	4.15	−2.425				•	This work
8975.401	2.99	−2.233	•		•		This work
8978.198	3.41	−3.457				•	This work
8984.886	5.10	−0.922	•		•	•	This work
8994.628	3.27	−3.189				•	This work
8999.556	2.83	−1.321		•		•	This work
9010.592	2.61	−2.953				•	This work
9013.977	2.28	−3.839				•	This work
9019.744	5.10	−0.988				•	This work
9057.971	3.05	−4.467				•	This work
9079.579	4.65	−0.809		•			This work
9080.386	4.96	−1.104		•			This work
9084.184	4.26	−2.240				•	This work
9089.404	2.95	−1.675				•	This work
9103.635	4.18	−1.921				•	This work
9210.024	2.85	−2.404	•				This work
9214.499	4.91	−0.743		•			This work
9258.267	4.61	−0.725	•	•			This work
9259.005	4.91	−0.749		•			This work
9800.308	5.09	−0.453		•			This work
9811.504	5.01	−1.362				•	This work
9820.241	2.42	−5.073				•	This work
9834.185	4.99	−1.214	•				This work
9847.457	4.58	−2.305				•	This work
9861.734	5.06	−0.142	•				This work
9868.186	5.09	−0.979	•	•		•	This work
9881.522	4.58	−1.711	•			•	This work
9886.081	5.01	−1.953				•	This work
9889.035	5.03	−0.446	•	•	•	•	This work
9913.180	4.99	−1.266	•		•	•	This work
9924.388	3.55	−3.127	•				This work
9944.207	5.01	−1.338	•	•	•	•	This work
9951.157	5.39	−1.267	•	•	•	•	This work
9953.470	5.45	−1.309				•	This work
9970.233	3.02	−4.818				•	This work
9977.641	5.06	−1.660	•		•		This work
9980.463	5.03	−1.379	•		•	•	This work
9999.924	5.50	−1.421				•	This work
10041.472	5.01	−1.772				•	This work
10065.045	4.83	−0.289	•	•	•	•	This work
10081.393	2.42	−4.537				•	And16
10086.242	2.95	−4.054				•	This work

TABLE B.4. *continued*

λ_{air} [Å]	χ_{I} [eV]	$\log gf$	Line list [a]				Reference [b]
			MRD	MPD	MRG	MPG	
10089.776	5.45	−1.247				•	This work
10114.014	2.76	−3.692	•	•	•	•	This work
10137.100	5.09	−1.708	•		•	•	And16
10142.844	5.06	−1.510	•		•		And16
10145.561	4.80	−0.177	•	•			This work
10155.162	2.18	−4.226	•	•	•	•	And16
10167.468	2.20	−4.117	•	•	•	•	And16
10195.105	2.73	−3.580	•		•	•	And16
10216.313	4.73	−0.063		•		•	This work
10218.408	3.07	−2.760		•		•	This work
10227.994	6.12	−0.354	•		•		And16
10230.795	6.12	−0.339	•		•	•	And16
10252.551	5.83	−1.026				•	This work
10262.471	5.48	−1.613				•	This work
10265.217	2.22	−4.537	•		•	•	And16
10307.454	4.59	−2.067				•	This work
10332.327	3.64	−2.938	•		•	•	And16
10333.184	4.59	−2.585				•	This work
10340.885	2.20	−3.577	•	•	•	•	And16
10347.965	5.39	−0.551	•	•	•	•	And16
10353.804	5.39	−0.819	•	•	•	•	And16
10364.062	5.45	−0.960	•		•	•	And16
10378.999	2.22	−4.148		•			And16
10388.744	5.45	−1.468				•	And16
10395.794	2.18	−3.393	•			•	This work
10423.027	2.69	−3.616		•		•	This work
10423.743	3.07	−2.918	•	•	•	•	And16
10435.355	4.73	−1.945				•	This work
10469.652	3.88	−1.184	•	•		•	This work
10532.234	3.93	−1.480	•	•	•	•	And16
10555.649	5.45	−1.108	•		•	•	And16
10577.139	3.30	−3.136	•	•	•	•	And16
10611.686	6.17	+0.021	•	•	•	•	And16
10616.721	3.27	−3.127	•	•	•	•	And16
10674.070	6.17	−0.466	•		•	•	And16
10742.550	3.64	−3.629				•	This work
10753.004	3.96	−1.845	•	•		•	This work
10754.753	2.83	−4.523				•	This work
10780.694	3.24	−3.289	•		•	•	And16
10783.050	3.11	−2.567	•	•		•	This work
10818.274	3.96	−1.948	•	•	•	•	And16
10849.465	5.54	−1.444				•	This work
10863.518	4.73	−0.895				•	This work
10881.758	2.85	−3.604		•		•	This work
10884.262	3.93	−1.925	•	•		•	This work
10888.606	2.28	−5.433				•	This work

TABLE B.4. *continued*

λ_{air} [Å]	χ_{I} [eV]	$\log gf$	MRD	MPD	MRG	MPG	Reference [b]
10896.299	3.07	−2.694	●			●	This work
11026.788	3.94	−2.805				●	And16
11045.599	5.59	−0.624				●	This work
11071.712	3.07	−4.281				●	This work
12053.082	4.56	−1.543	●		●	●	And16
12283.298	6.17	−0.537	●		●	●	And16
12485.492	2.42	−5.379				●	This work
12510.519	4.96	−1.605	●		●	●	And16
12545.946	4.08	−3.485				●	This work
12556.996	2.28	−3.626	●		●	●	And16
12615.928	4.64	−1.517	●		●		And16
12638.703	4.56	−0.783		●			This work
12648.741	4.61	−1.140		●			And16
12789.450	5.01	−1.514				●	This work
12807.152	3.64	−2.452	●	●	●	●	And16
12808.243	4.99	−1.362	●		●	●	And16
12824.859	3.02	−3.835	●		●	●	And16
12879.766	2.28	−3.458	●		●	●	This work
12933.006	5.02	−1.548	●		●	●	And16
12934.666	5.39	−0.948			●	●	And16
12946.532	3.25	−4.754				●	This work
13014.841	5.45	−1.693				●	And16
13098.876	5.01	−1.290				●	This work
13352.173	5.31	−0.521	●		●		And16
14939.644	6.47	−0.153				●	This work
14979.696	6.17	−0.451				●	And16
14982.801	6.26	−0.495	●		●		And16
14988.778	6.17	+0.186	●				This work
15013.771	6.22	+0.087				●	This work
15017.700	6.22	+0.062	●	●	●	●	And16
15160.503	6.34	−0.253	●		●		This work
15176.713	5.92	−0.497	●		●		And16
15194.490	2.22	−4.815	●		●	●	And16
15201.562	6.31	−0.161				●	And16
15207.526	5.39	+0.323	●	●	●	●	And16
15219.618	5.59	−0.825	●		●	●	And16
15224.729	5.96	−0.315	●		●	●	And16
15239.712	6.42	−0.032			●	●	And16
15244.973	5.59	−0.072				●	This work
15293.135	6.31	+0.143	●				This work
15294.560	5.31	+0.719	●	●		●	This work
15301.557	5.92	−0.687	●		●	●	This work
15335.383	5.41	+0.088	●				And16
15343.788	5.65	−0.582	●	●	●	●	This work
15348.966	5.95	−1.260	●		●		This work
15375.346	5.92	−0.991	●		●	●	And16

TABLE B.4. *continued*

λ_{air} [Å]	χ_I [eV]	$\log gf$	MRD	MPD	MRG	MPG	Reference [b]
				Line list [a]			
15394.673	5.62	+0.008	●		●	●	And16
15395.718	5.62	−0.126	●	●	●	●	And16
15514.279	6.29	−0.473	●				And16
15522.607	6.32	−1.118	●			●	And16
15524.308	5.79	−0.881	●		●	●	And16
15531.751	5.64	−0.243	●	●	●	●	And16
15534.245	5.64	−0.382	●	●	●	●	And16
15542.079	5.64	−0.337	●	●	●	●	And16
15550.436	6.32	−0.102	●		●	●	And16
15551.433	6.35	−0.371	●		●	●	And16
15560.784	6.35	−0.475	●		●		And16
15565.222	6.32	−0.557	●		●		And16
15566.725	6.35	−0.681			●	●	And16
15588.259	6.37	+0.419	●	●	●		And16
15590.046	6.24	−0.829	●			●	And16
15591.490	6.24	+0.874	●	●	●	●	And16
15593.749	5.03	−1.922	●		●		And16
15598.869	6.24	−0.236			●		And16
15604.220	6.24	+0.538	●	●	●	●	This work
15611.145	3.41	−3.768			●	●	And16
15621.654	5.54	+0.589	●	●		●	This work
15645.016	6.31	−0.390	●		●	●	This work
15648.510	5.43	−0.599	●	●	●	●	And16
15652.871	6.25	−0.161	●	●	●		And16
15662.013	5.83	+0.371	●	●	●	●	And16
15665.240	5.98	−0.337	●	●			This work
15682.513	6.37	−0.265	●		●	●	And16
15691.853	6.25	+0.649	●				And16
15723.586	5.62	−0.143	●	●	●		And16
15731.412	6.45	−0.337			●		And16
15733.509	6.25	−0.978	●				And16
15788.996	6.25	+0.490	●				And16
15920.642	6.26	+0.366	●		●		This work
15928.158	5.95	−0.680	●		●	●	And16
15929.472	6.31	−0.383	●			●	And16
15934.017	6.31	−0.294	●		●	●	And16
15938.918	6.37	+0.065				●	This work
15940.918	5.81	−1.594	●			●	And16
15941.848	6.36	+0.265	●	●	●		And16
15962.558	6.42	−0.078	●		●	●	This work
15964.865	5.92	+0.279	●	●	●	●	And16
15980.725	6.26	+0.958	●	●			And16
16009.610	5.43	−0.470	●	●			And16
16040.654	5.87	+0.317	●		●		And16
16051.734	6.26	−0.942	●		●		And16
16070.180	5.96	−0.569	●		●		And16

TABLE B.4. *continued*

λ_{air} [Å]	χ_{I} [eV]	$\log gf$	Line list [a]				Reference [b]
			MRD	MPD	MRG	MPG	
16071.397	6.27	+0.102	•				And16
16100.282	6.35	−0.043				•	And16
16102.408	5.87	+0.546	•		•		And16
16125.899	6.35	+0.860		•		•	This work
16156.557	5.96	−0.294	•			•	And16
16165.029	6.32	+0.988	•	•		•	And16
16171.930	6.38	−0.445	•		•	•	And16
16174.975	6.38	+0.185	•	•	•	•	And16
16177.991	6.38	−0.402		•	•	•	And16
16179.583	6.32	+0.261	•	•	•	•	And16
16180.900	6.28	+0.295	•	•	•	•	And16
16182.170	6.32	−0.708			•		This work
16185.799	6.39	+0.264		•			This work
16195.060	6.39	+0.467	•	•	•		And16
16198.502	5.41	−0.444	•	•	•	•	And16
16201.513	6.38	−0.329	•		•		This work
16207.744	6.32	+0.585	•	•	•		And16
16377.388	6.36	−0.465	•		•	•	And16
16384.141	6.36	−0.736			•	•	And16
16394.389	5.96	+0.358	•	•	•	•	And16
16396.306	6.28	−0.530	•				This work
16404.601	6.36	+0.581	•		•		And16
16407.786	6.29	+0.007	•	•			This work
16436.621	5.92	+0.007	•		•		And16
16440.394	6.29	−0.241	•		•		And16
16444.816	5.83	+0.663	•	•	•		And16
16466.921	6.39	+0.003	•	•	•	•	And16
16471.753	6.37	+0.030	•			•	And16
16474.077	6.02	−0.959	•	•		•	And16
16481.228	6.39	−0.162	•				This work
16486.666	5.83	+0.783	•		•	•	This work
16506.293	5.95	−0.463			•		This work
16537.994	6.29	−0.867	•				This work
16539.193	6.34	−0.119	•				And16
16544.667	6.34	−0.029	•		•	•	And16
16551.994	6.41	+0.338	•		•	•	And16
16557.148	6.41	−1.083				•	This work
16559.677	6.40	+0.210				•	And16
16561.764	5.98	+0.243		•			And16
16586.051	5.62	−0.753			•	•	And16
16612.761	6.40	+0.286	•		•		And16
16629.836	6.57	−0.435	•				This work
16645.874	5.96	−0.032	•	•	•	•	And16
16807.435	5.83	−1.301			•		And16
16833.052	5.96	−0.889	•		•	•	And16
16843.228	5.87	−1.321	•				And16

Table B.4. *continued*

λ_{air} [Å]	χ_{I} [eV]	$\log gf$	MRD	MPD	MRG	MPG	Reference [b]
16865.513	6.41	−0.749				•	And16
16869.950	6.41	−0.415			•		This work
16874.116	6.35	−0.159	•				And16
16892.384	6.31	−0.799	•		•	•	This work
16969.910	5.95	−0.069			•		This work
17005.450	6.07	+0.005		•		•	This work
17008.971	6.62	−0.301	•		•		This work
17011.095	5.95	+0.102	•			•	This work
17037.787	6.39	−0.852				•	And16

(Column header "Line list [a]" spans MRD, MPD, MRG, MPG.)

[a] Line lists. MRD: metal-rich dwarfs; MPD: metal-poor dwarfs; MRG: metal-rich giants; MPG: metal-poor giants.

[b] References. Sou08: Sousa et al. (2008); And16: Andreasen et al. (2016).

TABLE B.5. Merged Fe II line lists.

λ_{air} [Å]	χ_{II} [eV]	$\log gf$	Line list [a]				Reference [b]
			MRD	MPD	MRG	MPG	
5325.552	3.22	−3.160		•		•	Sou08
5414.070	3.22	−3.580			•		Sou08
5425.248	3.20	−3.220	•	•	•	•	Sou08
5534.838	3.24	−2.730		•			Sou08
5991.371	3.15	−3.540	•				Sou08
6084.102	3.20	−3.780	•		•		Sou08
6149.246	3.89	−2.720	•		•	•	Sou08
6238.386	3.89	−2.754		•	•		Sou08
6247.557	3.89	−2.310		•			Sou08
6369.459	2.89	−4.160	•			•	Sou08
6416.919	3.89	−2.650	•				Sou08
6432.676	2.89	−3.520	•	•	•		Sou08
6456.380	3.90	−2.100		•	•	•	Sou08
6516.077	2.89	−3.320	•	•			Sou08
7222.391	3.89	−3.360	•	•	•		This work
7224.478	3.89	−3.240	•	•	•		This work
7449.329	3.89	−3.090	•		•		This work
7479.693	3.89	−3.680	•		•		This work
7515.830	3.90	−3.460	•		•		This work
7533.368	3.90	−3.600	•		•		This work
7711.720	3.90	−2.500	•	•	•	•	This work
9997.598	5.48	−1.867	•		•		This work
10501.503	5.55	−2.086	•				And16

[a] Line lists. MRD: metal-rich dwarfs; MPD: metal-poor dwarfs; MRG: metal-rich giants; MPG: metal-poor giants.
[b] References. Sou08: Sousa et al. (2008); And16: Andreasen et al. (2016).
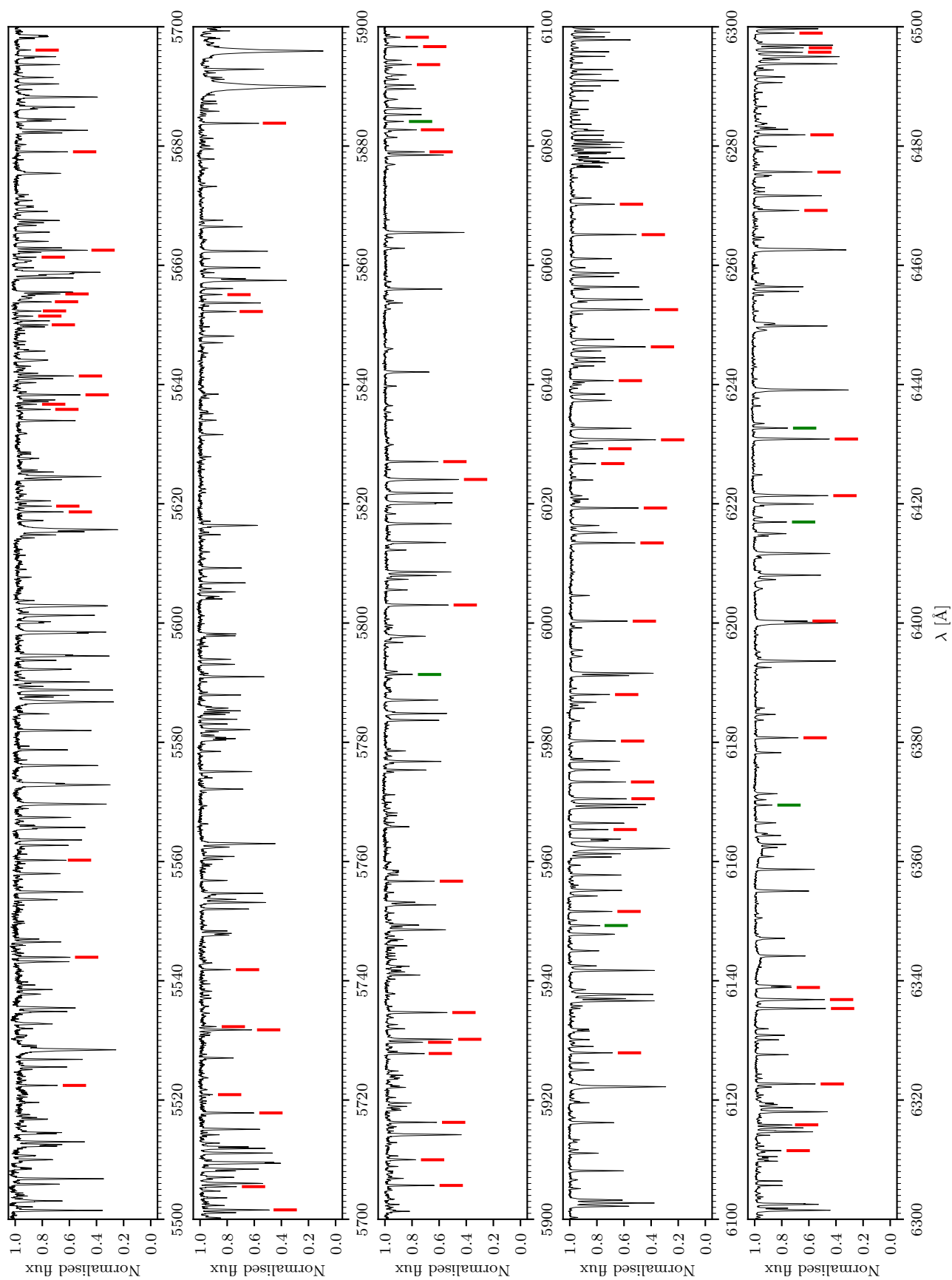
FIGURE B.1. CARMENES spectrum of 18 Sco. Fe I and Fe II lines are shown in red and green, respectively.
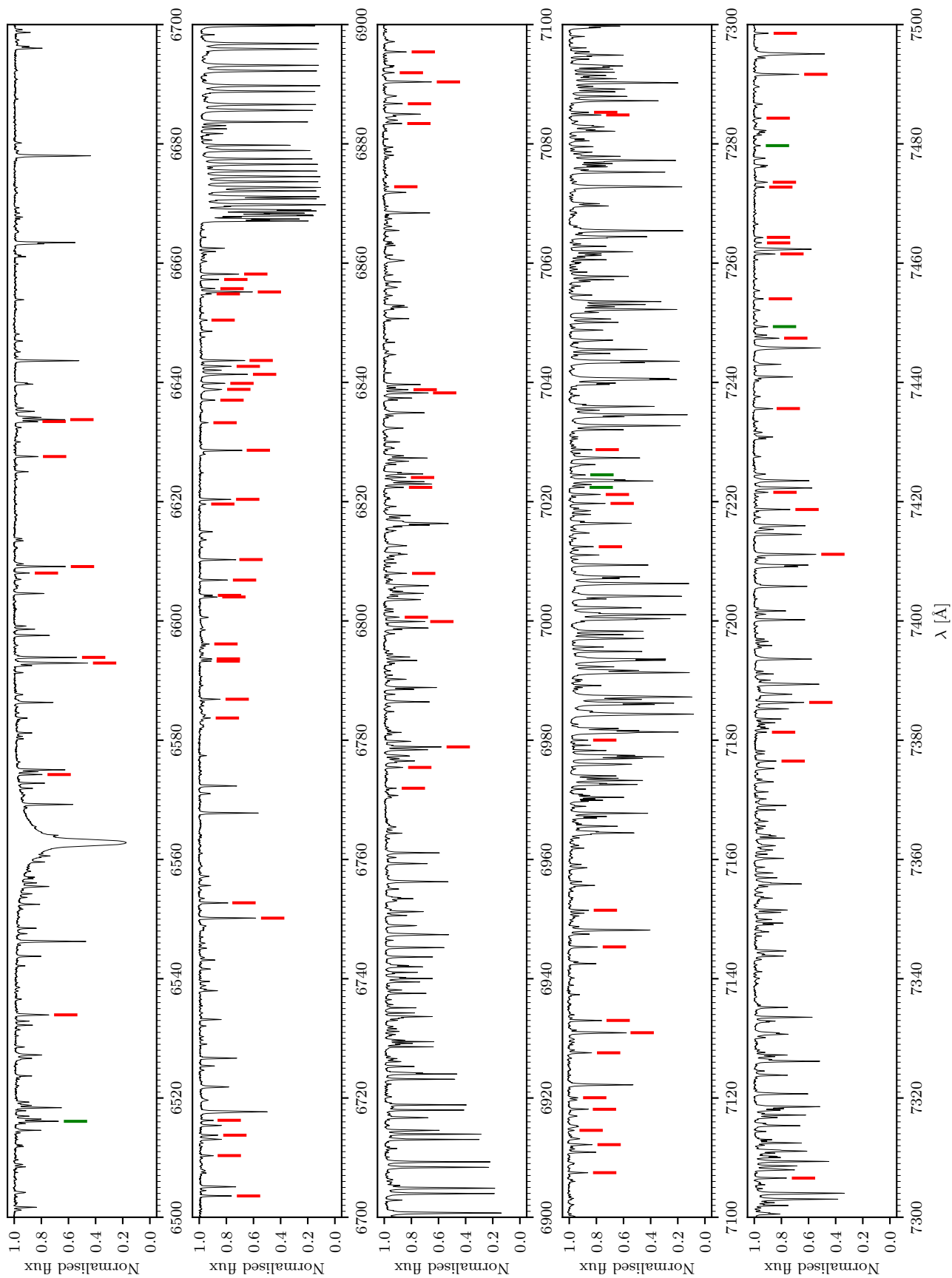
FIGURE B.1. *continued*
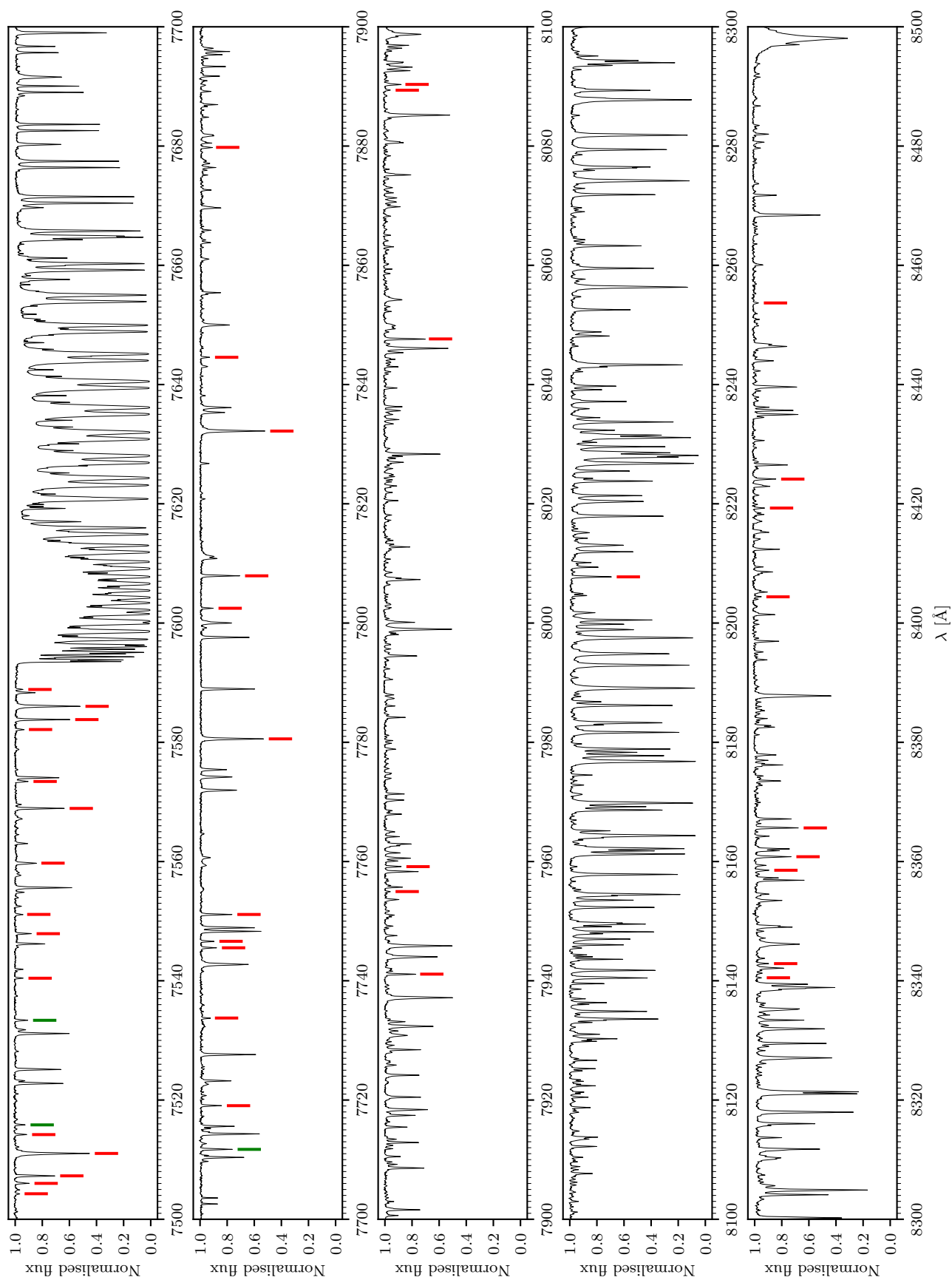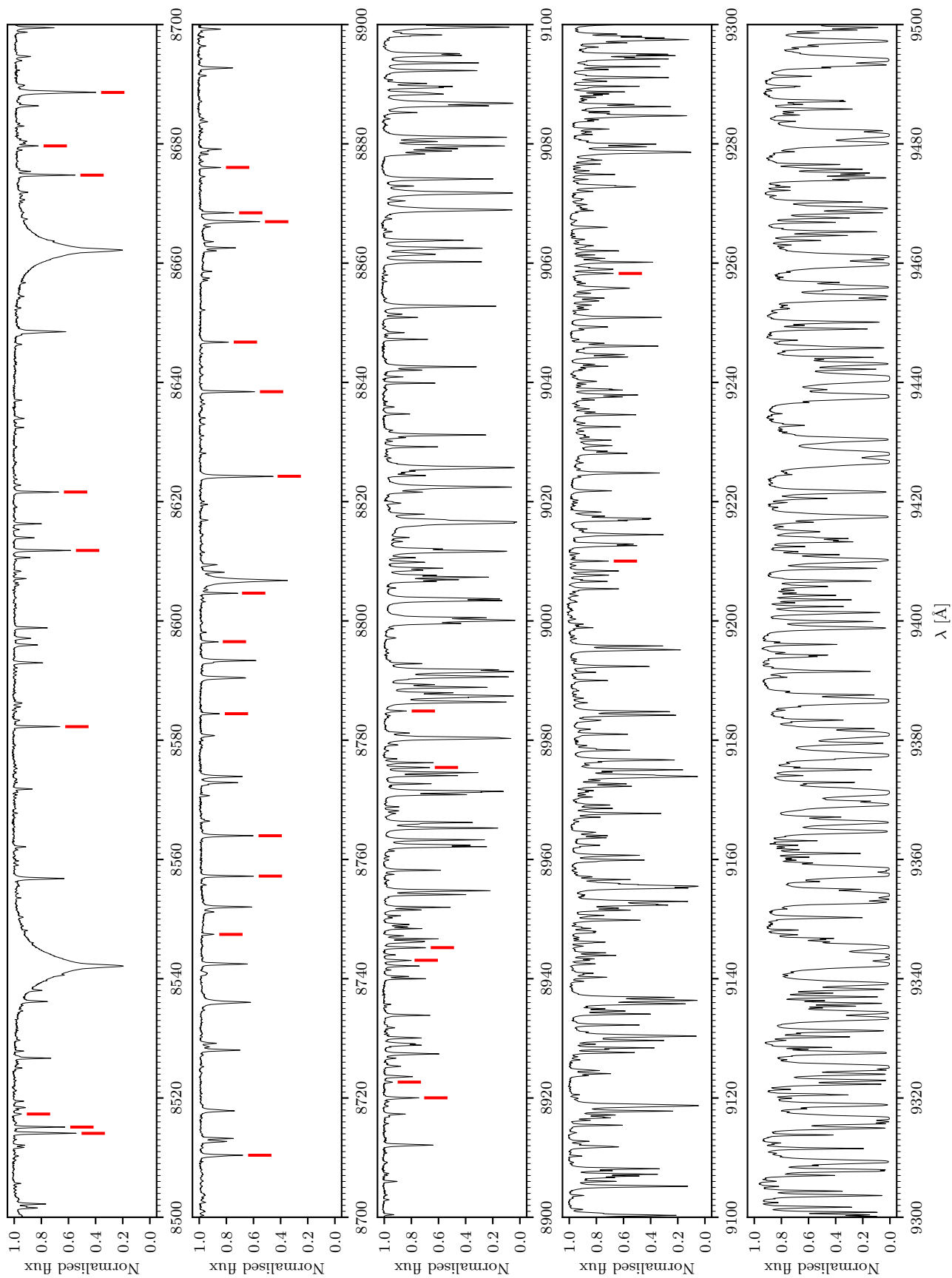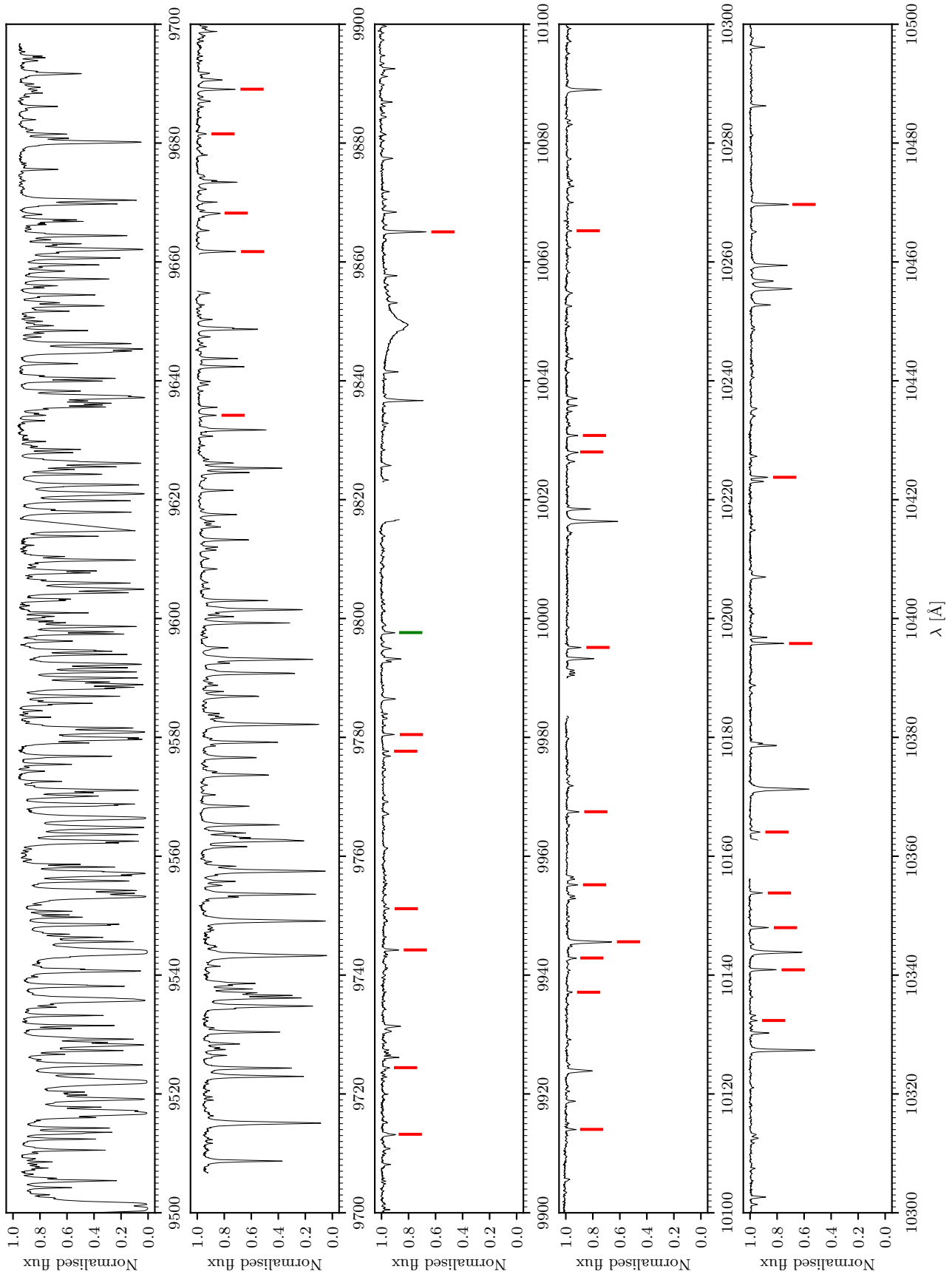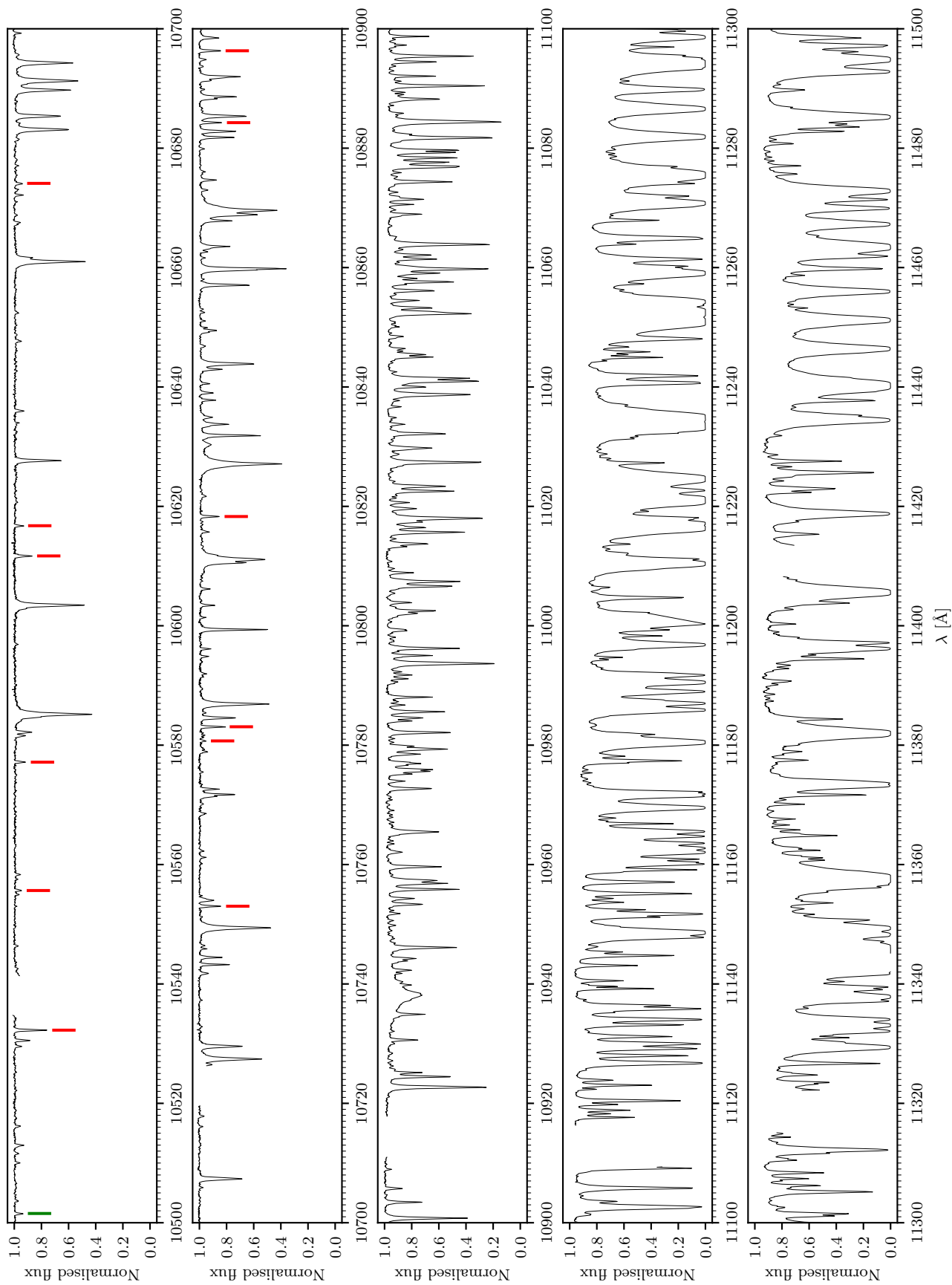
FIGURE B.1. *continued*

Figure B.1. *continued*

FIGURE B.1. *continued*
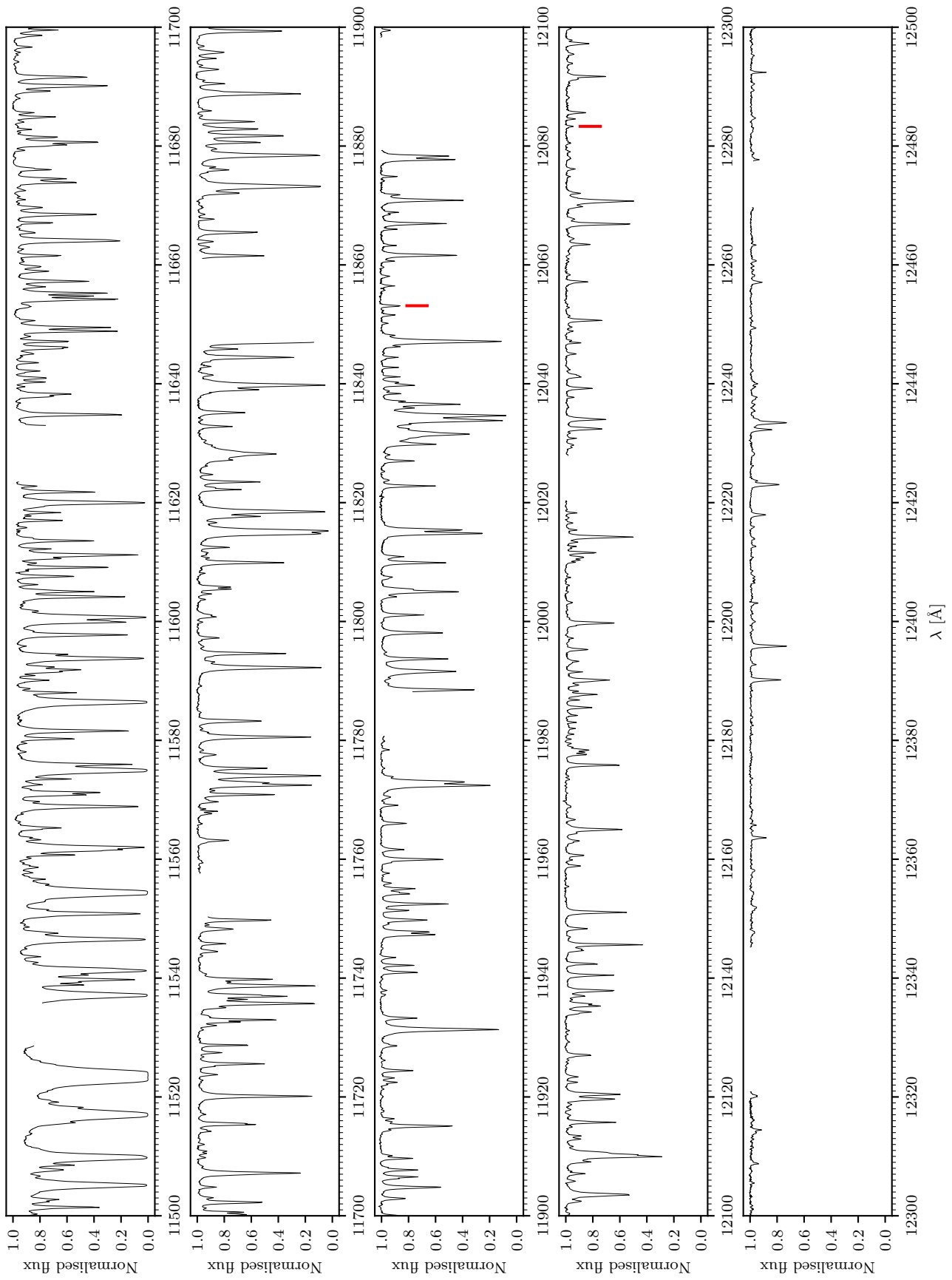
FIGURE B.1. *continued*

FIGURE B.1. *continued*
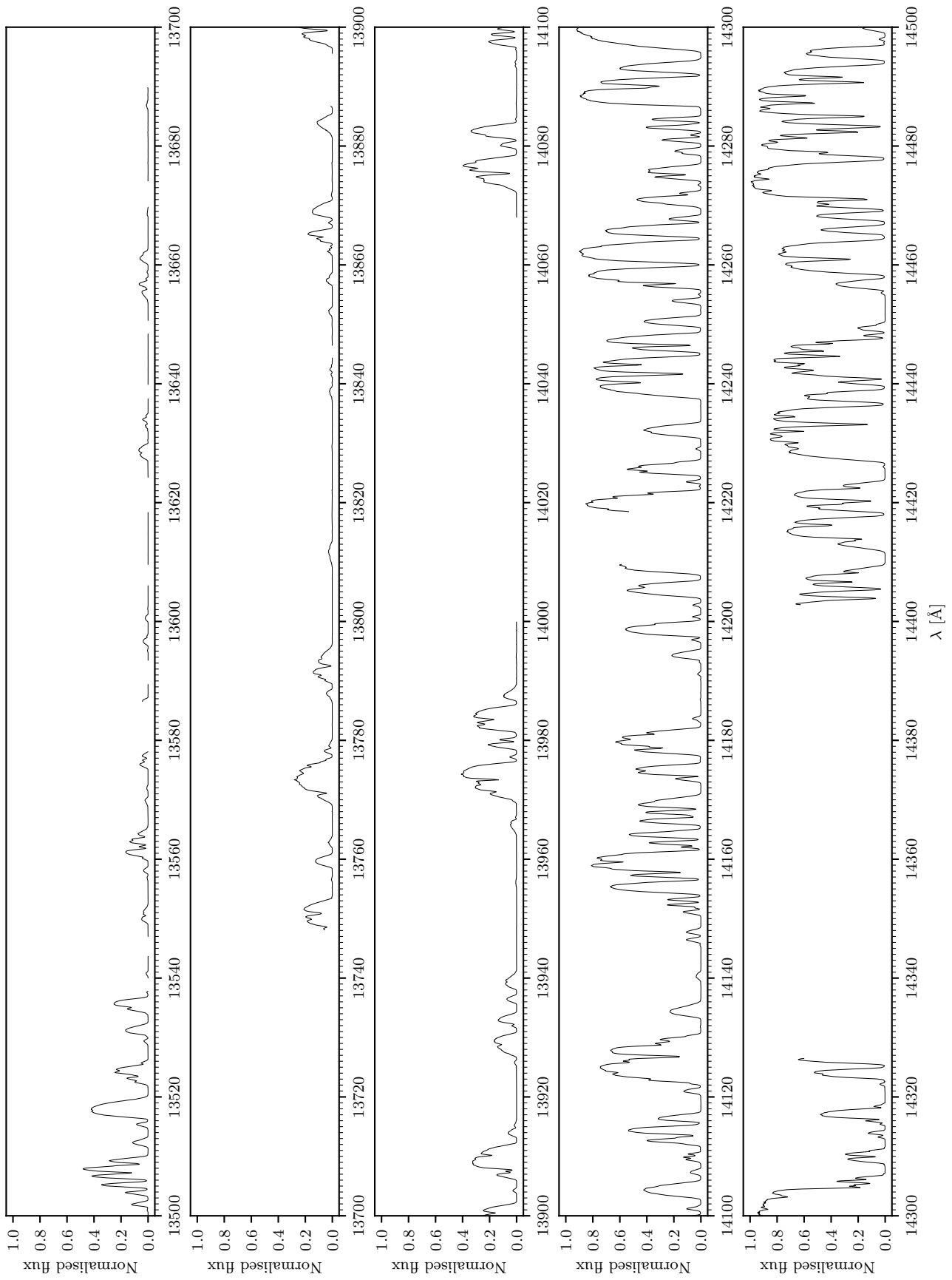
FIGURE B.1. *continued*
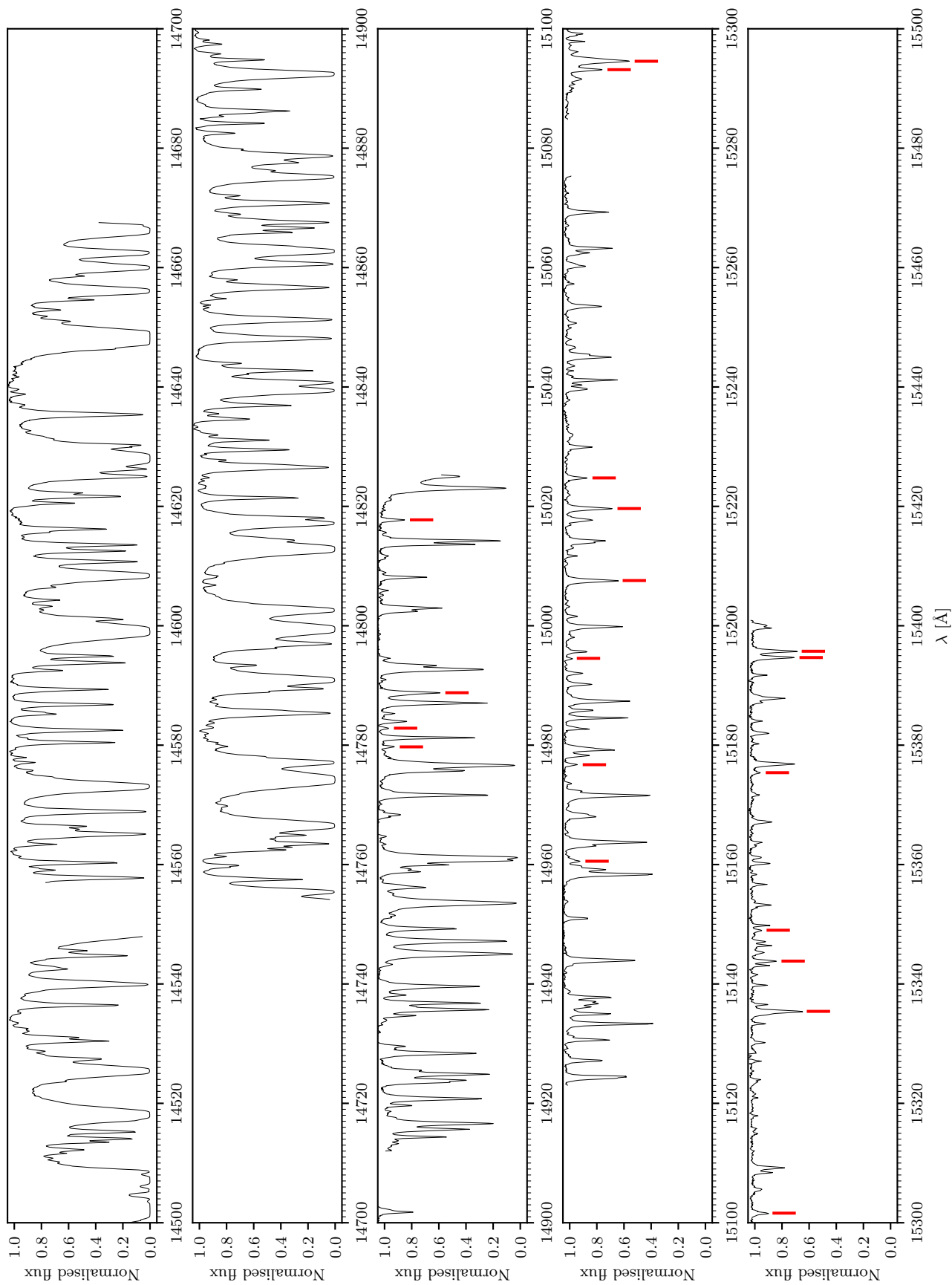
FIGURE B.1. *continued*

FIGURE B.1. *continued*
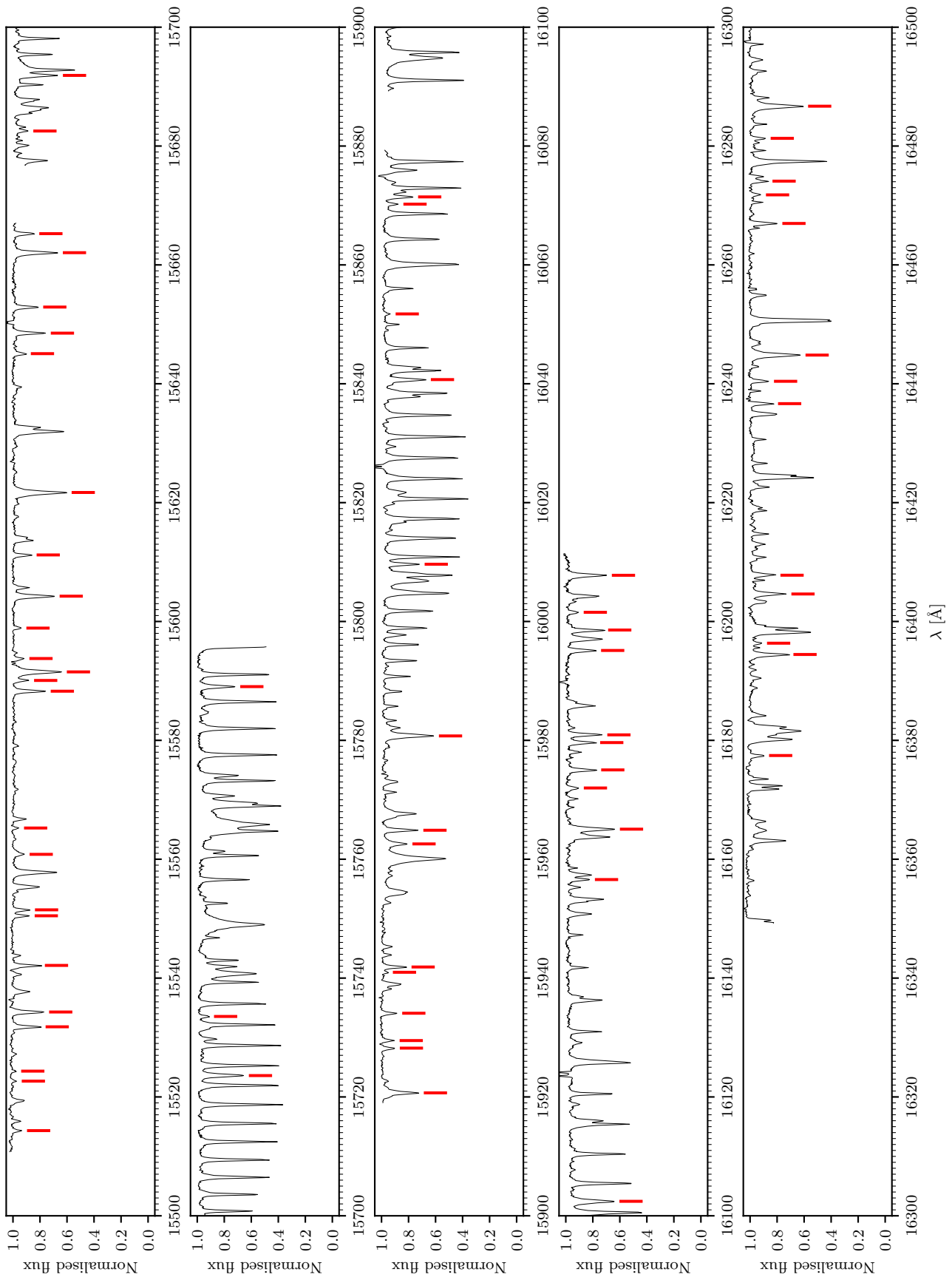
FIGURE B.1. *continued*
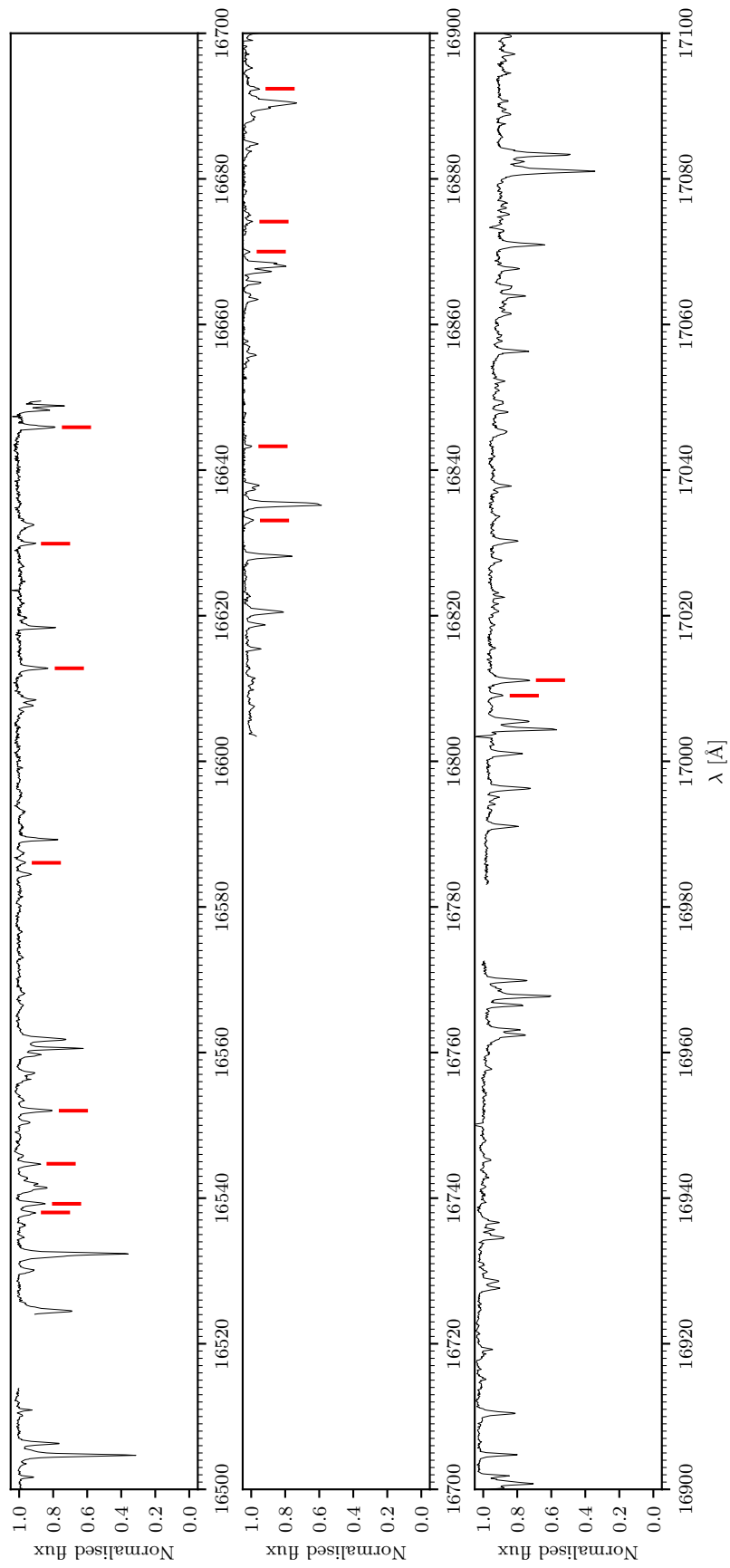
FIGURE B.1. *continued*

C Appendix of Chapter 4

This appendix contains the figures and tables referenced in Chapter 4.

- Figs. C.1, C.2, and C.3 show the marginalised posterior distributions in $T_{\rm eff}$, $\log g$, and [Fe/H] for the reference stars, namely GX And, Luyten's star, and Teegarden's star, respectively (see Table 4.2). The best synthetic fits for the atomic lines and molecular bands for these stars can be found in Figs. C.4, C.5, C.6, C.7, C.8, and C.9.

- Figs. C.10, C.11, C.12, C.13, C.14, C.15, C.16, C.17, and C.18 show the comparison between our results and those of Rojas-Ayala et al. (2012), Gaidos & Mann (2014), Maldonado et al. (2015), Mann et al. (2015), Passegger et al. (2018), Rajpurohit et al. (2018a), Schweitzer et al. (2019), Maldonado et al. (2020), and Passegger et al. (2020), respectively, as discussed in Sect. 4.4.

- Table C.1 contains the sample of 343 M dwarfs from the CARMENES GTO survey analysed in this work.

- Table C.2 displays the spectral ranges synthesised around the selected Fe I and Ti I lines according to the template spectra of GX And, Luyten's star, and Teegarden's star, as explained in Sect. 4.3.2.

- Table C.3 shows the adopted prior distributions in $T_{\rm eff}$ and $\log g$ along with the stellar atmospheric parameters of the sample computed with STEPARSYN, as discussed in Sects. 4.3.4 and 4.4.
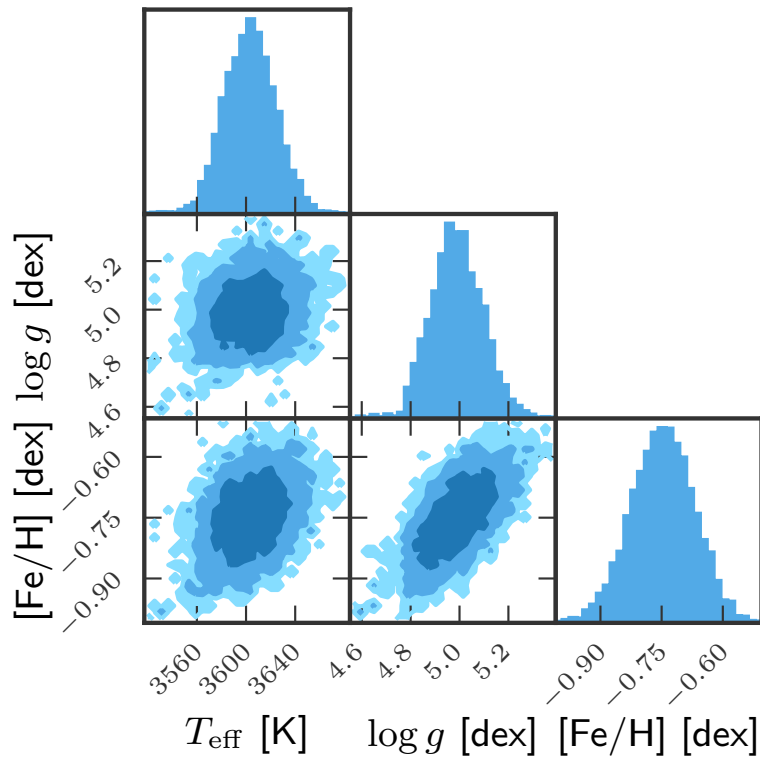
Figure C.1. Same as Fig. 4.5, but for GX And (M1.0 V, J00183+440). The retrieved parameters are $T_{\rm eff}$ = 3603 ± 24 K, $\log g = 4.99 \pm 0.14$ dex, and [Fe/H] = -0.75 ± 0.11 dex.
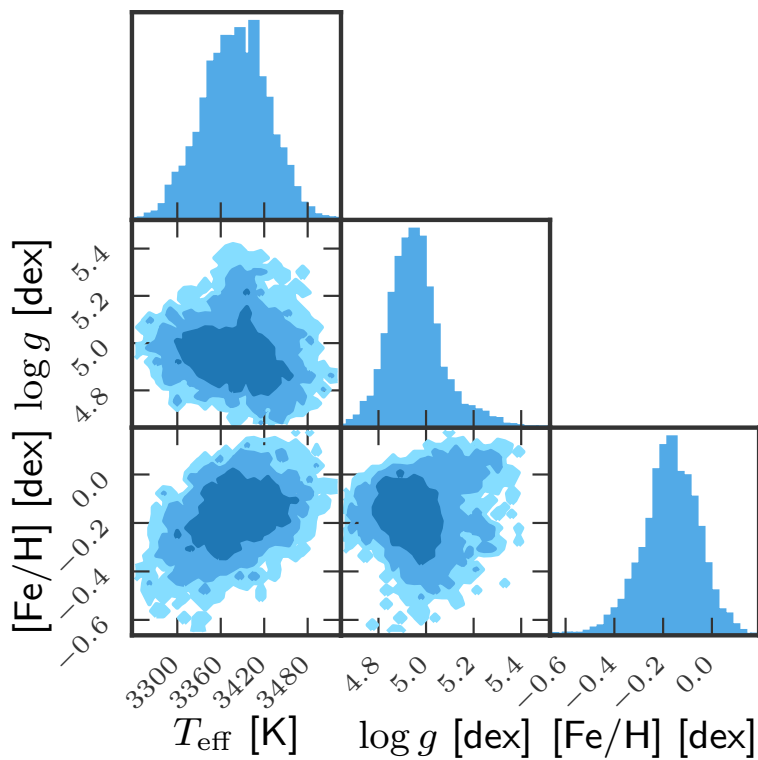
Figure C.2. Same as Fig. 4.5, but for Luyten's star (M3.5 V, J07274+052). The retrieved parameters are $T_{\rm eff}$ = 3380 ± 43 K, $\log g = 4.96 \pm 0.11$ dex, and [Fe/H] = -0.17 ± 0.11 dex.
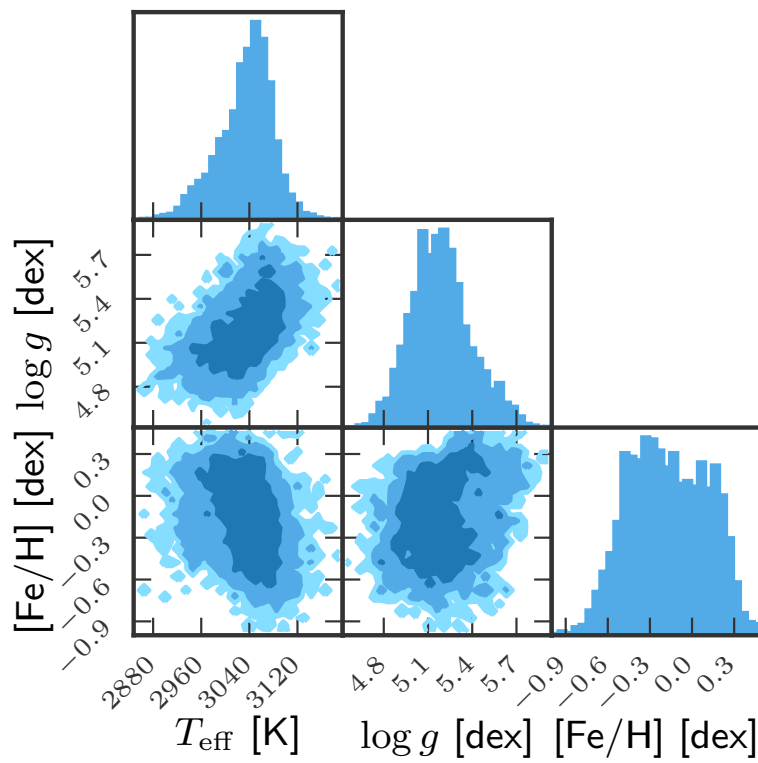
FIGURE C.3. Same as Fig. 4.5, but for Teegarden's star (M7.0 V, J02530+168). The retrieved parameters are $T_{\rm eff} = 3034 \pm 45$ K, $\log g = 5.19 \pm 0.20$ dex, and [Fe/H] $= -0.17 \pm 0.28$ dex.
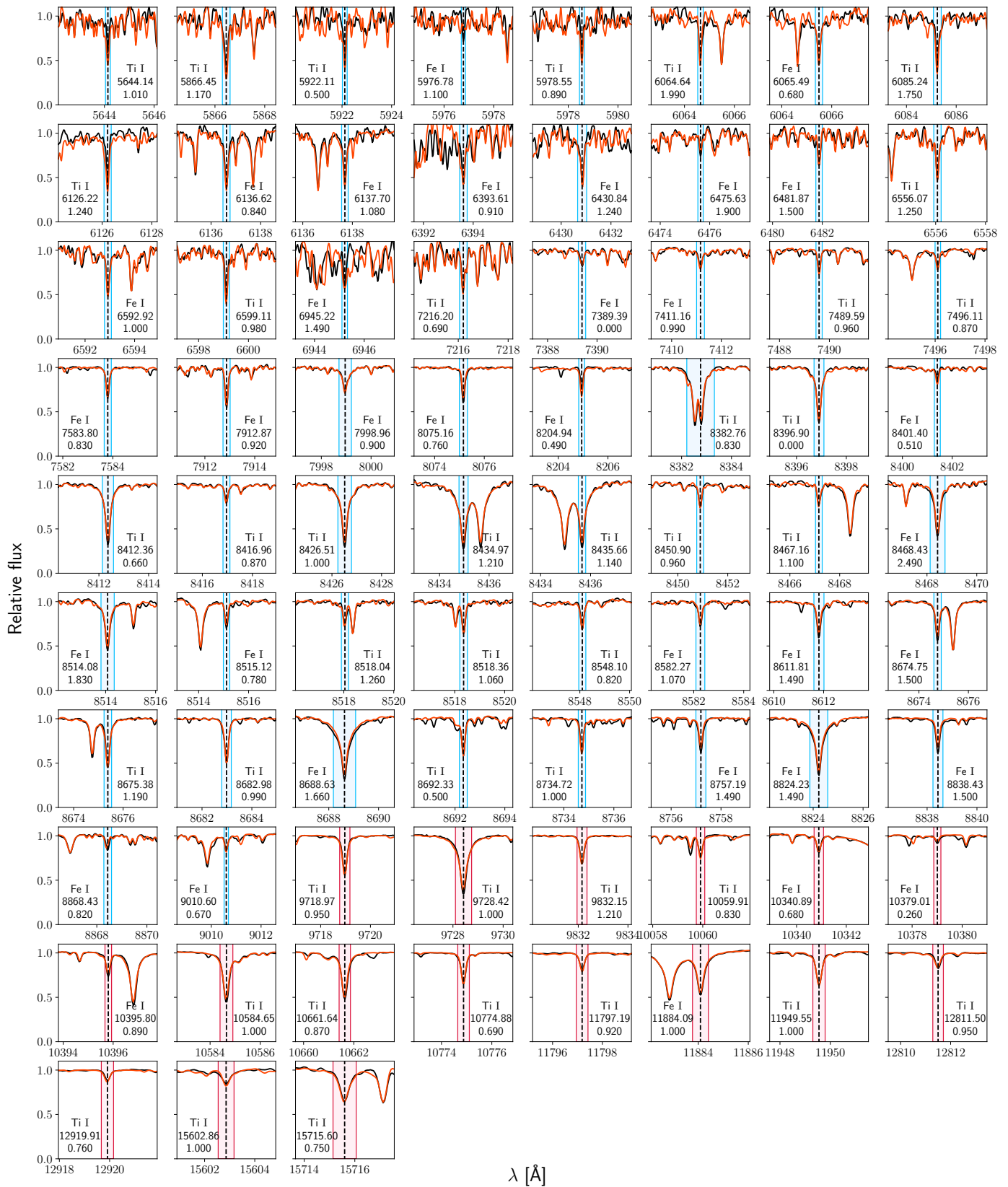
FIGURE C.4. Same as Fig. 4.6, but for GX And (M1.0 V, J00183+440).
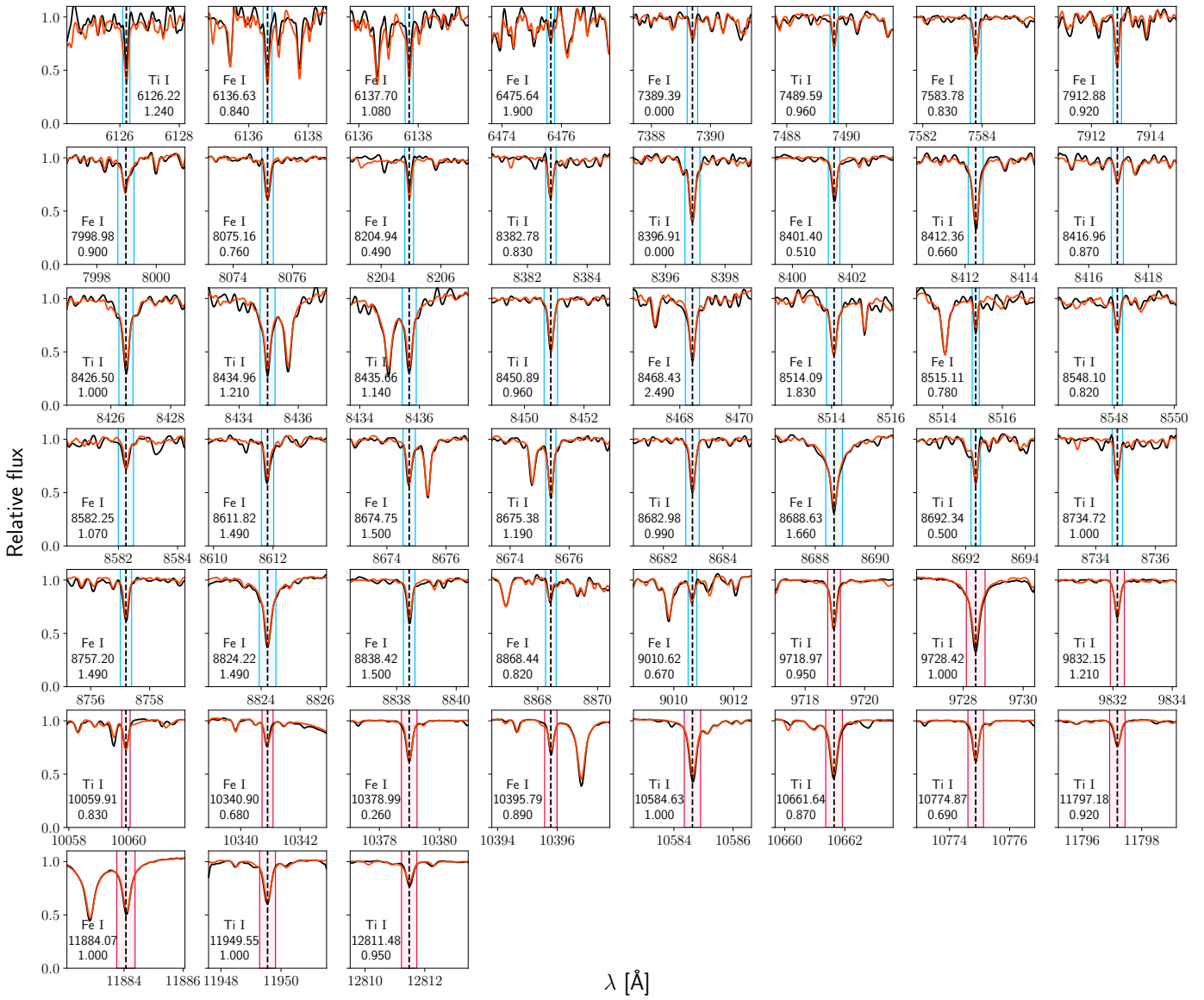
FIGURE C.5. Same as Fig. 4.6, but for Luyten's star (M3.5 V, J07274+052).
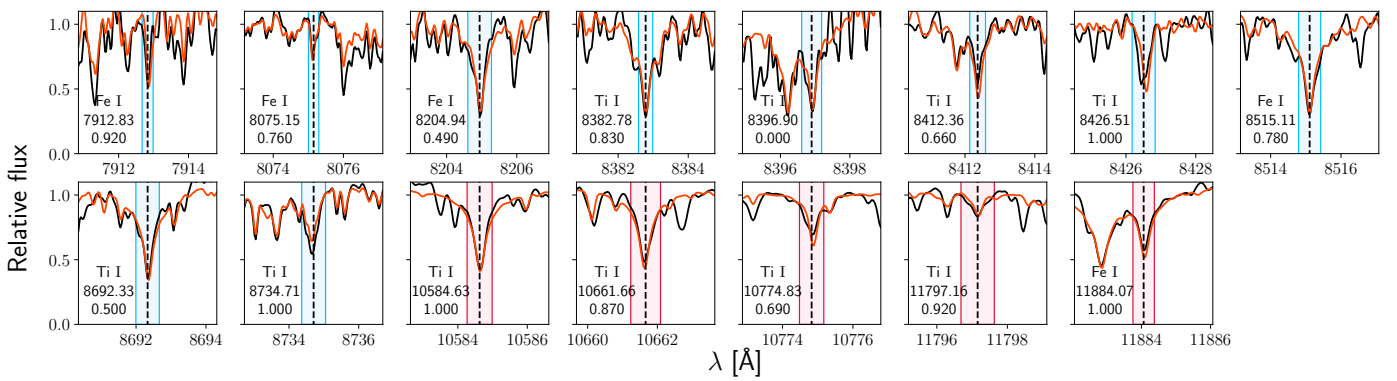
FIGURE C.6. Same as Fig. 4.6, but for Teegarden's star (M7.0 V, J02530+168).
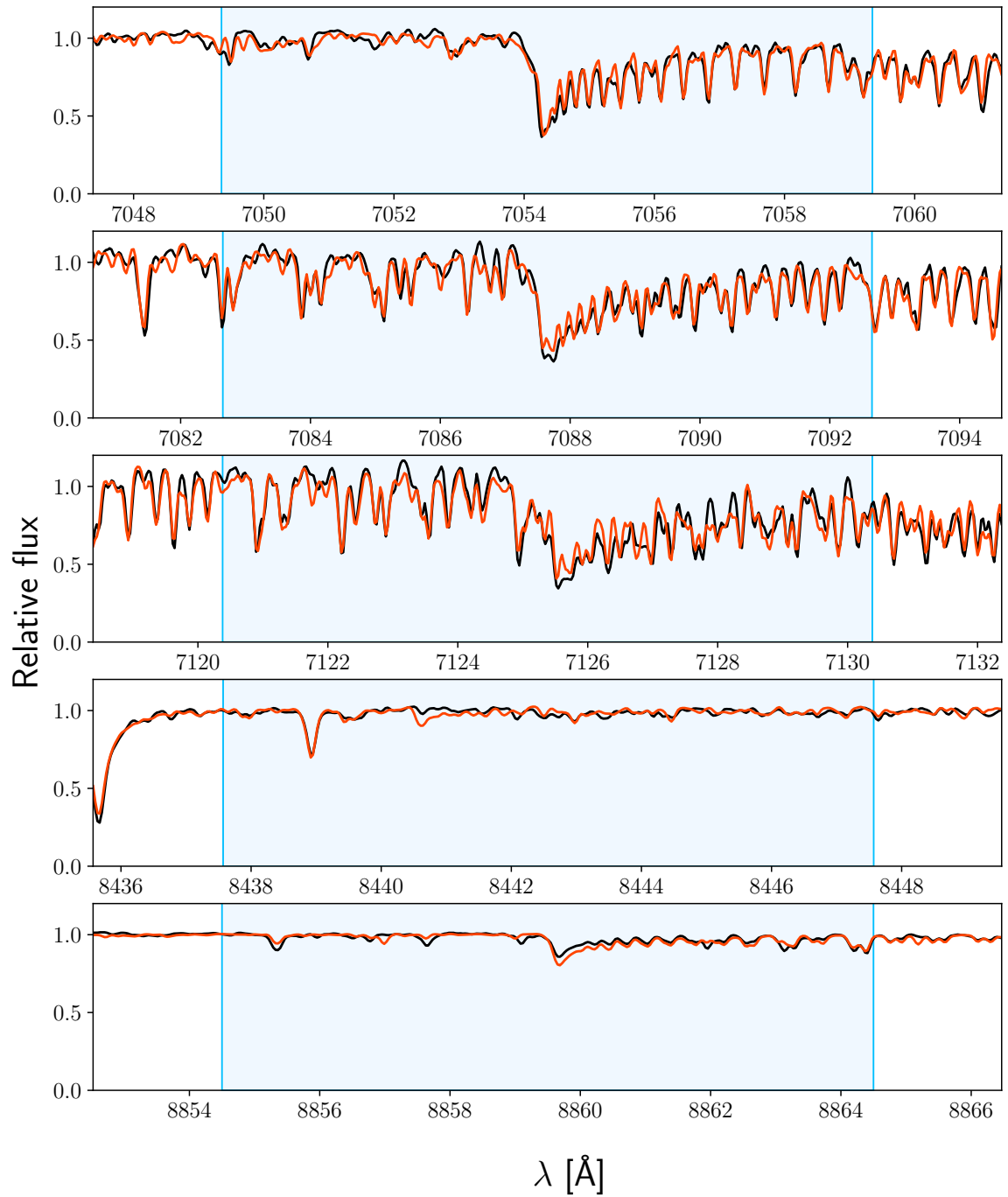
FIGURE C.7. Same as Fig. 4.7, but for GX And (M1.0 V, J00183+440).
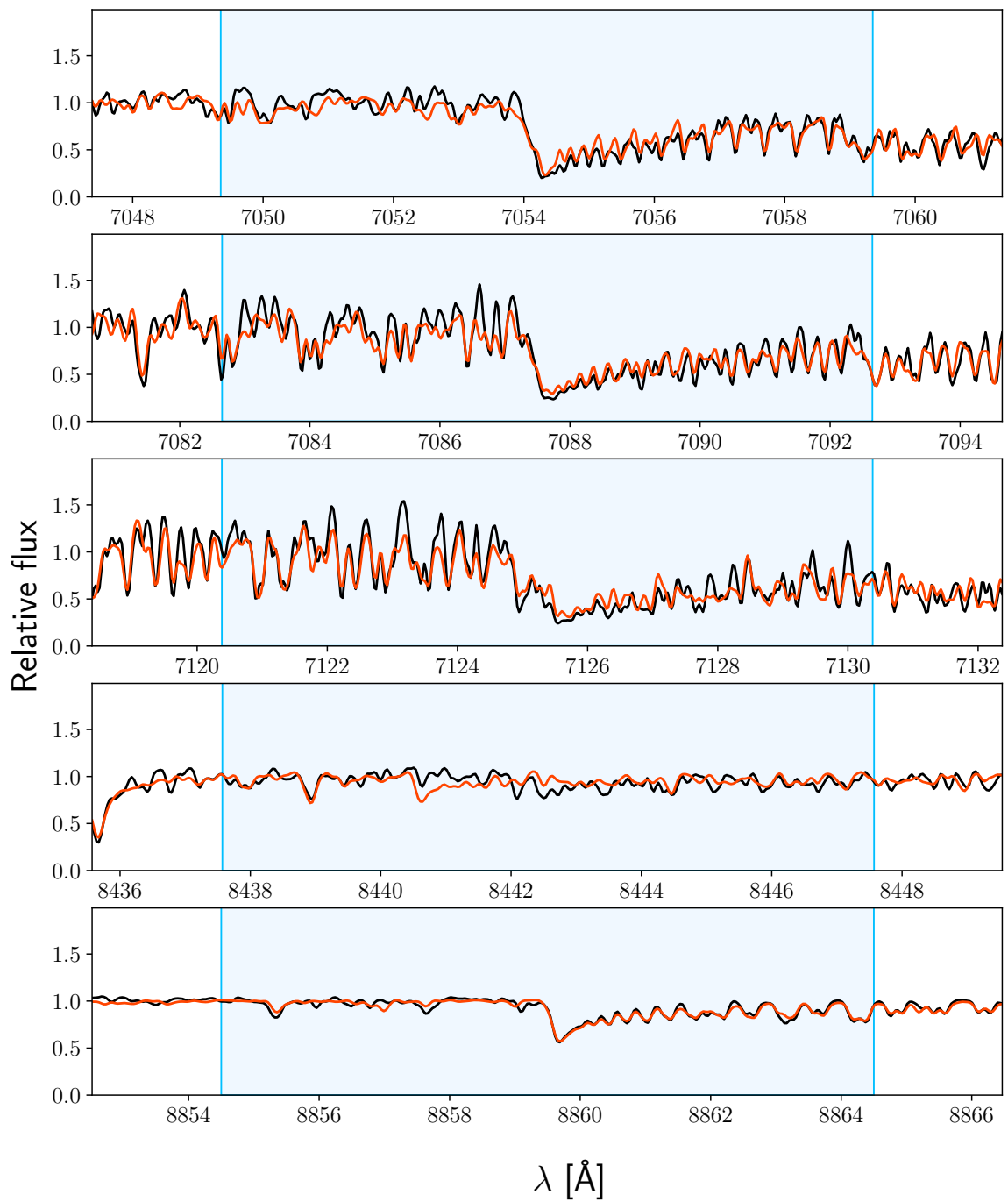
FIGURE C.8. Same as Fig. 4.7, but for Luyten's star (M3.5 V, J07274+052).
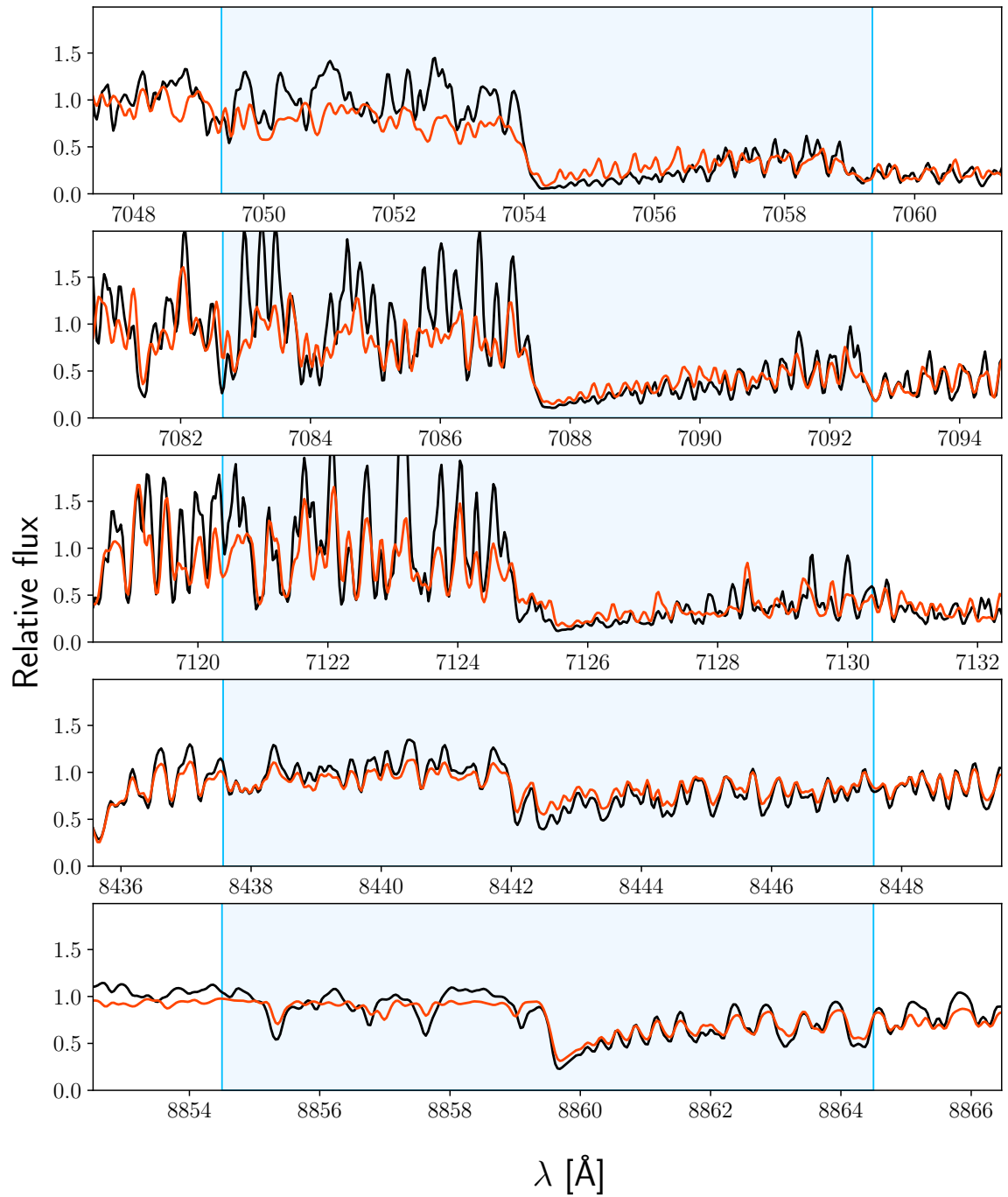
FIGURE C.9. Same as Fig. 4.7, but for Teegarden's star (M7.0 V, J02530+168).
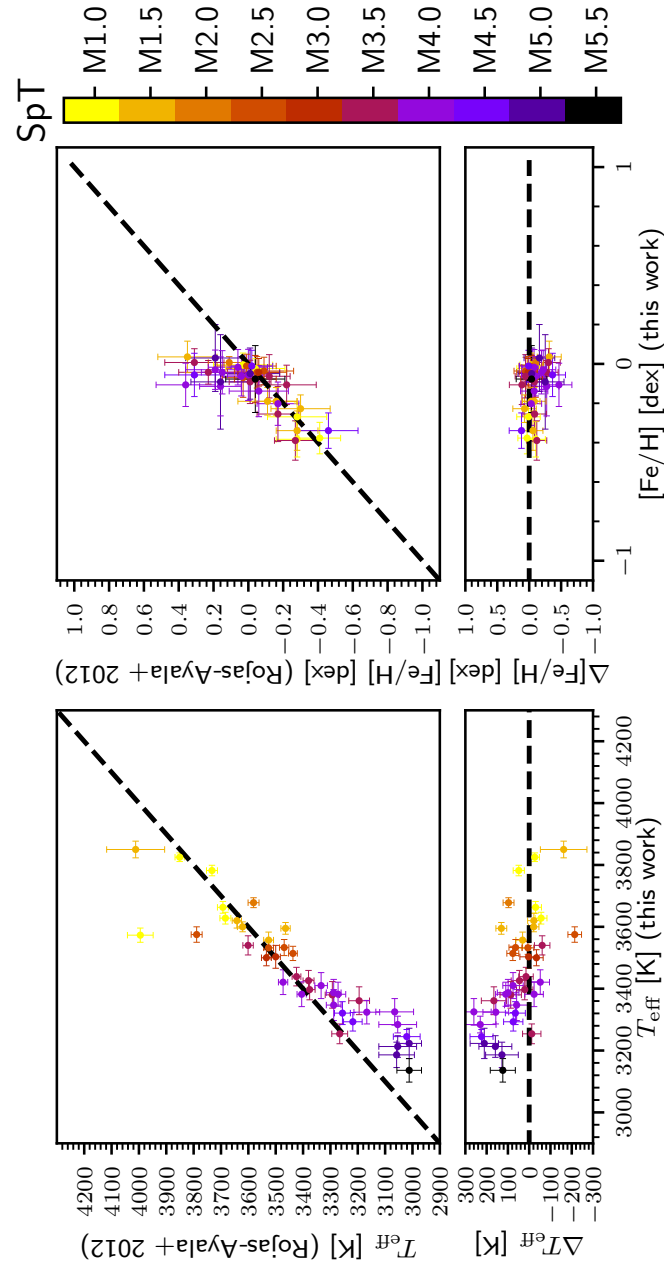
FIGURE C.10. Comparison between this work and Rojas-Ayala et al. (2012).
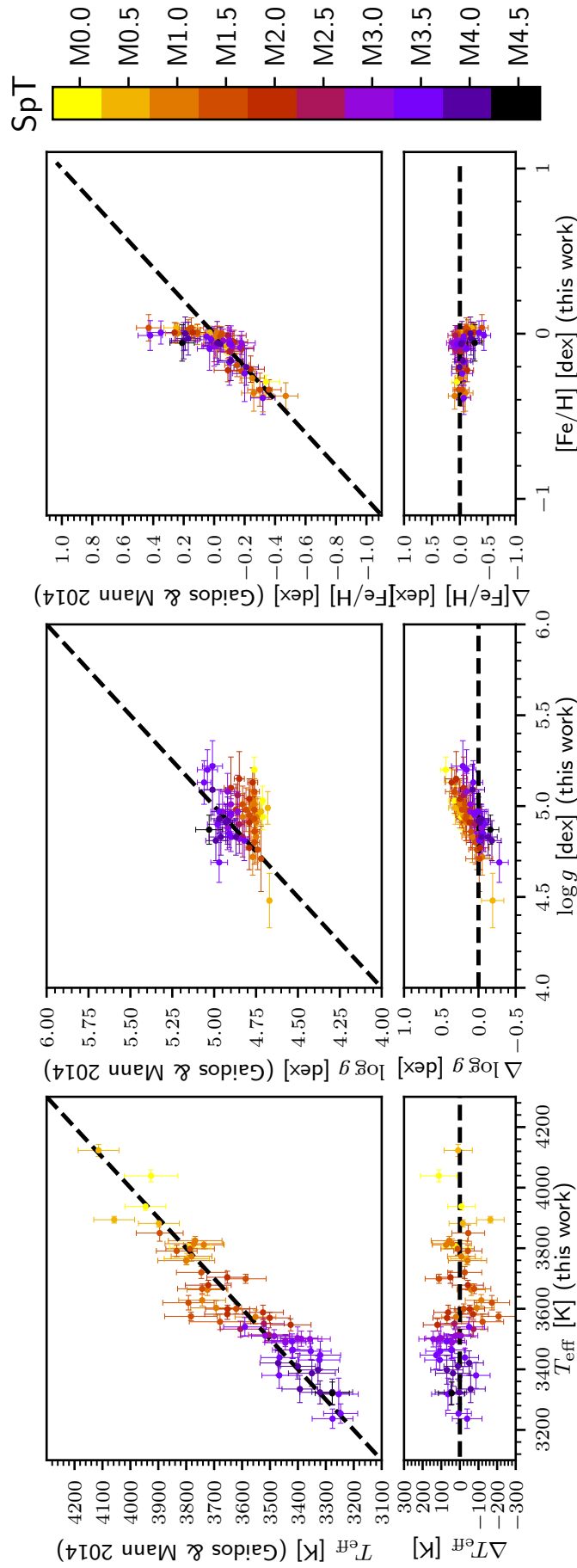
FIGURE C.11. Comparison between this work and Gaidos & Mann (2014).
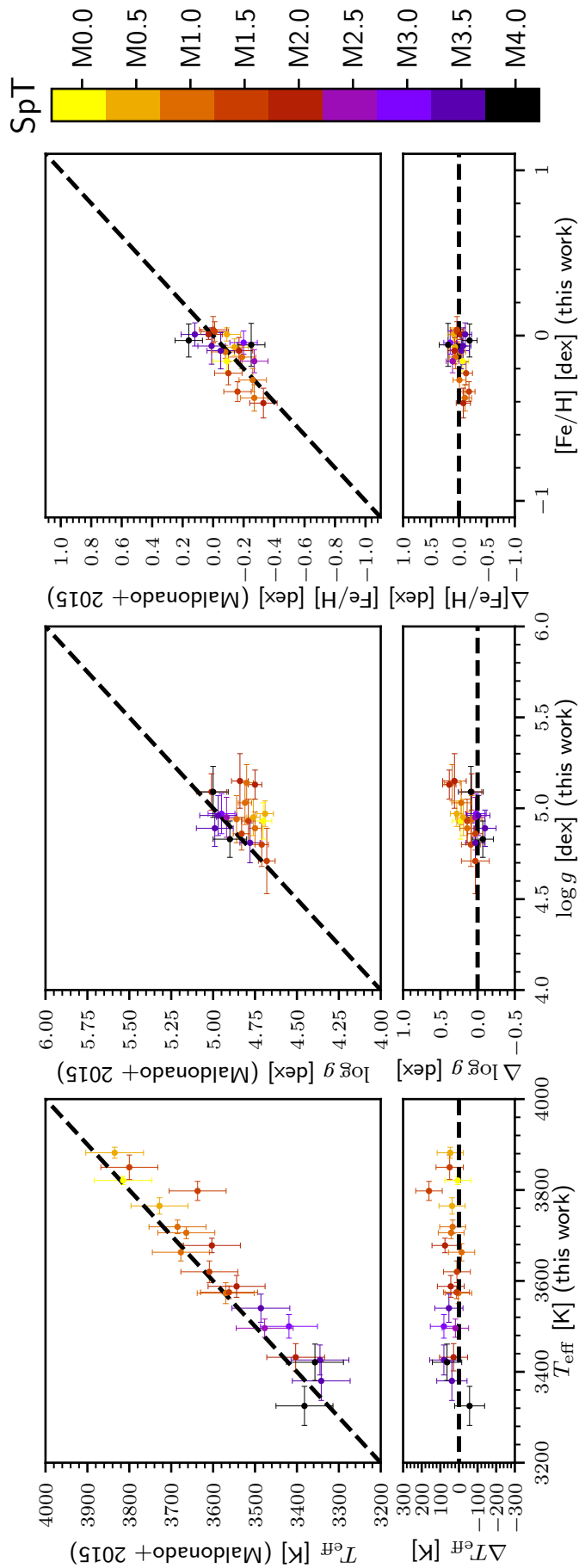
FIGURE C.12. Comparison between this work and Maldonado et al. (2015).
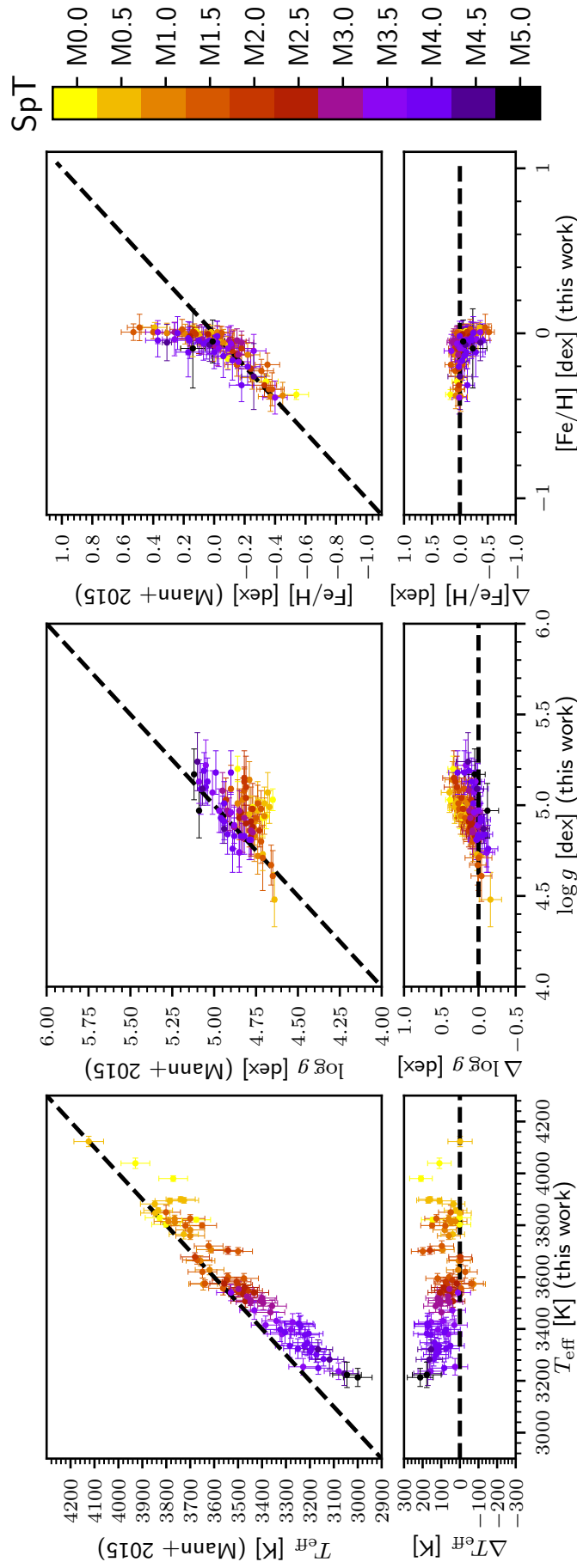
FIGURE C.13. Comparison between this work and Mann et al. (2015).
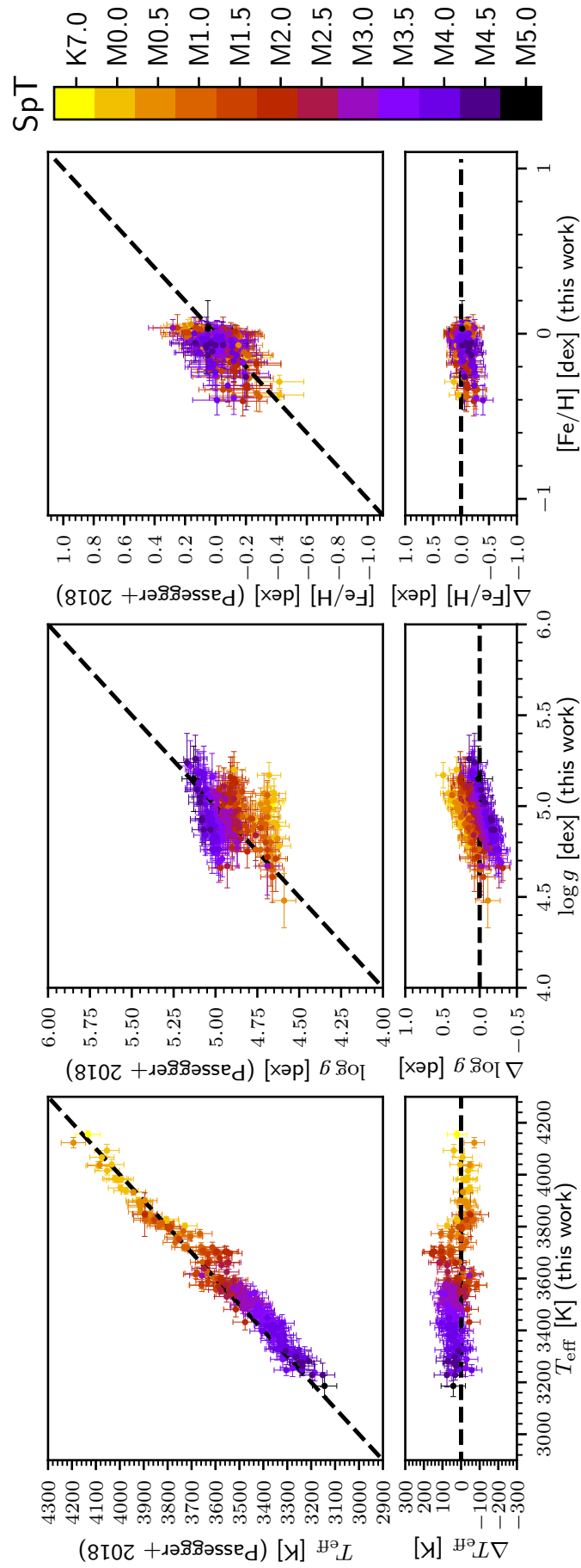
FIGURE C.14. Comparison between this work and Passegger et al. (2018).
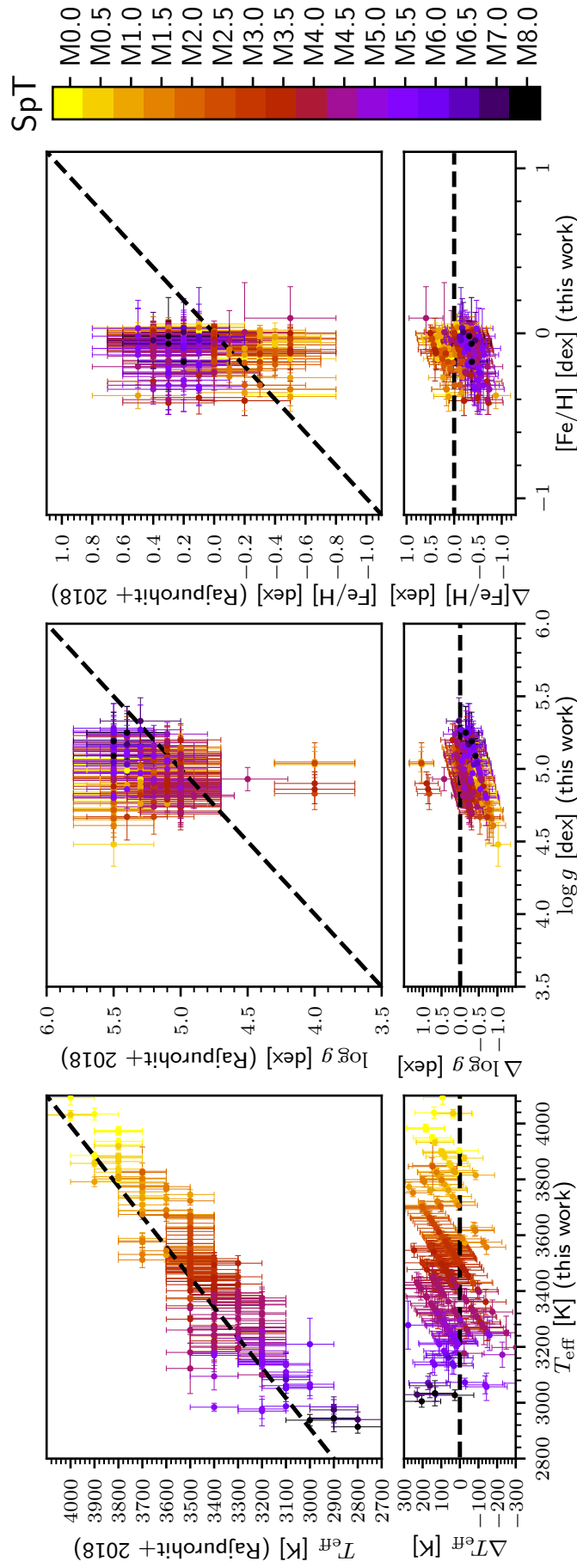
FIGURE C.15. Comparison between this work and Rajpurohit et al. (2018a).
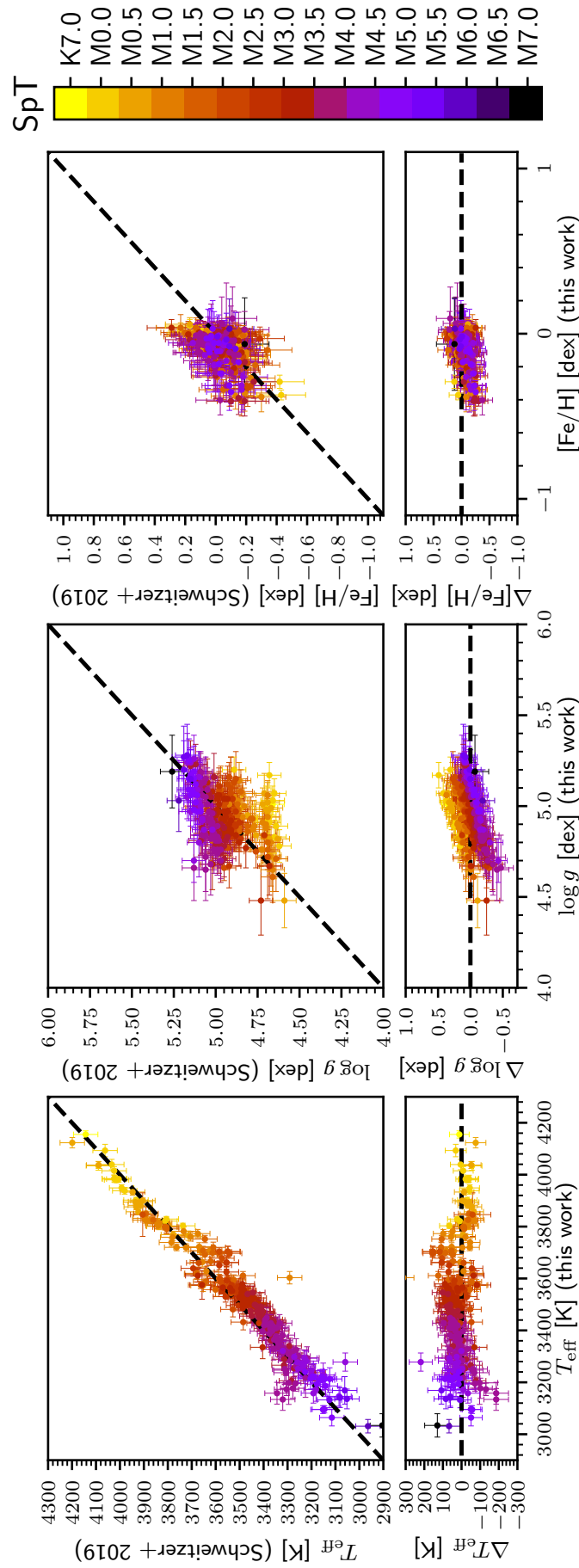
FIGURE C.16. Comparison between this work and Schweitzer et al. (2019).
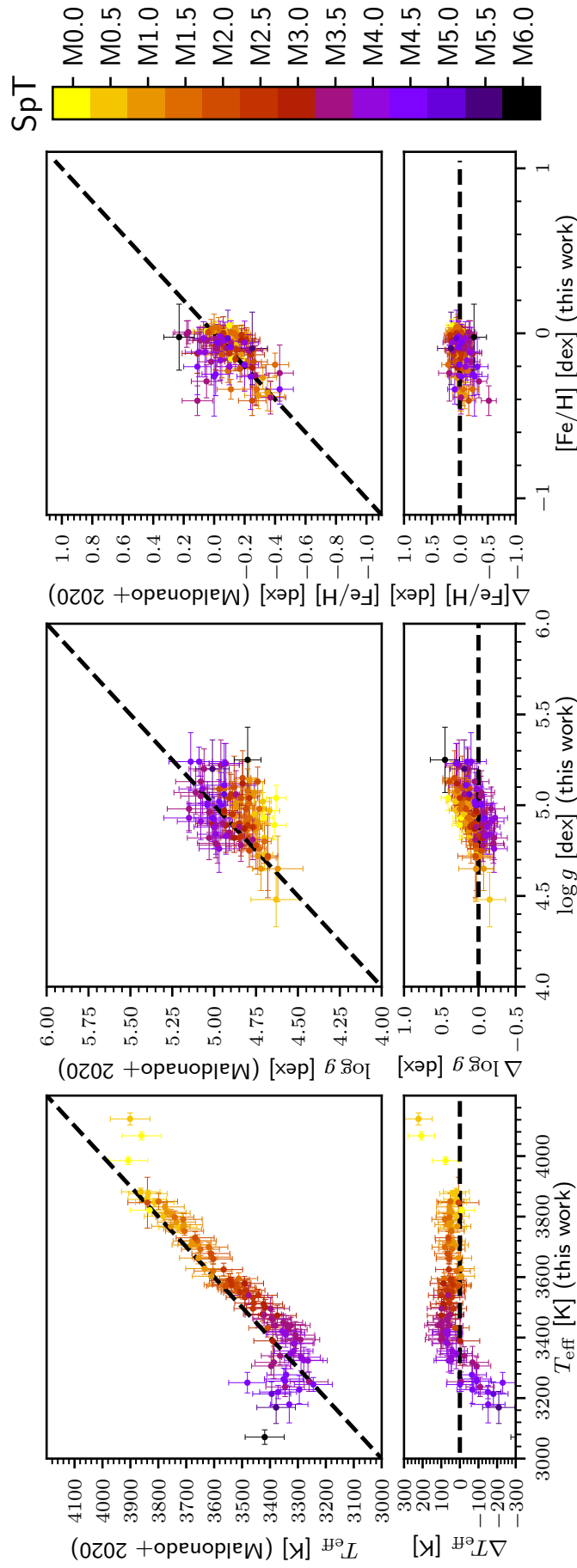
FIGURE C.17. Comparison between this work and Maldonado et al. (2020).
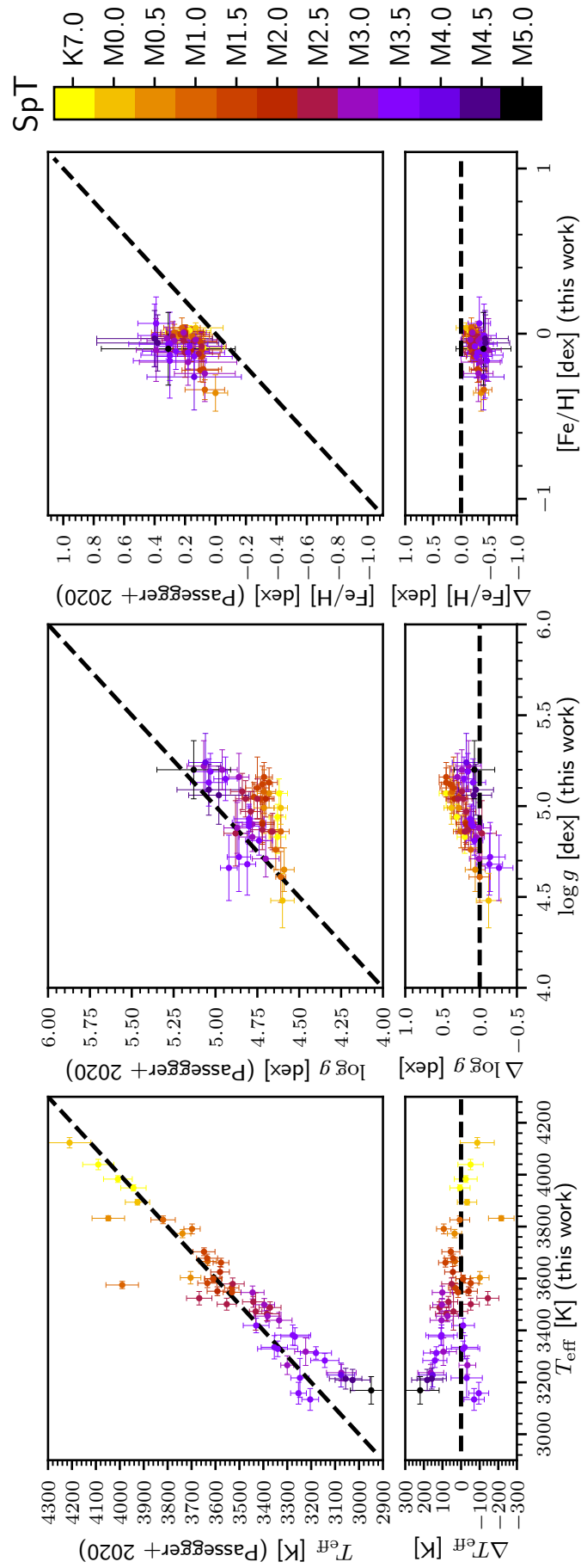
FIGURE C.18. Comparison between this work and Passegger et al. (2020).

TABLE C.1. Sample of M dwarfs from the CARMENES radial velocity survey analysed in this work.

Karmn	Name	SpT [a]	v_r [km s^{-1}]	Ref. [b]	$v \sin i$ [c] [km s^{-1}]	S/N	Hα flag [d]
J04167−120	LP 714-47	K7.0 V	−7.45 ± 0.05	This work	≤ 2.0	258	0
J11110+304E	HD 97101	K7.0 V	−16.00 ± 0.03	This work	≤ 2.0	422	0
J18198−019	HD 168442	K7.0 V	−14.03 ± 0.03	Laf20	≤ 3.0	1447	0
J03463+262	HD 23453	M0.0 V	35.59 ± 0.02	Laf20	3.3 ± 4.0	728	0
J04376+528	BD+52 857	M0.0 V	33.91 ± 0.01	Laf20	3.4 ± 1.5	1167	0
J04588+498	BD+49 1280	M0.0 V	−34.35 ± 0.02	Laf20	≤ 2.0	877	0
J05365+113	V2689 Ori	M0.0 V	21.51 ± 0.02	Laf20	3.8 ± 1.5	1291	1
J06371+175	HD 260655	M0.0 V	−58.75 ± 0.02	Laf20	≤ 2.0	780	0
J07393+021	BD+02 1729	M0.0 V	19.53 ± 0.02	Laf20	≤ 2.0	606	0
J09143+526	HD 79210	M0.0 V	10.69 ± 0.02	Laf20	≤ 3.0	681	0
J09144+526	HD 79211	M0.0 V	11.90 ± 0.02	Laf20	2.3 ± 1.5	1237	0
J09561+627	BD+63 869	M0.0 V	14.92 ± 0.02	Laf20	≤ 2.0	789	0
J12123+544S	HD 238090	M0.0 V	−17.67 ± 0.02	Laf20	≤ 2.0	1138	0
J13255+688	2MASS J13253177+6850106	M0.0 V	−16.97 ± 0.04	This work	≤ 2.0	212	0
J13450+176	BD+18 2776	M0.0 V	20.27 ± 0.02	Laf20	2.3 ± 1.5	581	0
J14257+236W	BD+24 2733 A	M0.0 V	8.88 ± 0.02	Laf20	≤ 2.0	823	0
J16167+672S	HD 147379	M0.0 V	−19.36 ± 0.02	Laf20	2.7 ± 1.5	1611	0
J17303+055	BD+05 3409	M0.0 V	−13.03 ± 0.02	Laf20	≤ 2.0	751	0
J19346+045	BD+04 4157	M0.0 V	−58.86 ± 0.02	Laf20	3.9 ± 1.5	789	0
J21474+627	TYC 4266-736-1	M0.0 V	−61.33 ± 0.23	This work	≤ 2.0	533	0
J02222+478	BD+47 612	M0.5 V	−38.51 ± 0.02	Laf20	≤ 2.0	663	0
J04290+219	BD+21 652	M0.5 V	−35.56 ± 0.01	Laf20	3.9 ± 1.5	1341	0
J06105−218	HD 42581 A	M0.5 V	4.18 ± 0.02	Laf20	≤ 2.0	446	0
J09511−123	BD−11 2741	M0.5 V	61.85 ± 0.02	Laf20	≤ 2.0	421	0
J10088+692	TYC 4384-1735-1	M0.5 V	−27.02 ± 0.04	This work	≤ 2.0	487	0
J12312+086	BD+09 2636	M0.5 V	18.59 ± 0.02	Laf20	≤ 2.0	712	0
J13299+102	BD+11 2576	M0.5 V	14.00 ± 0.02	Laf20	≤ 2.0	1810	0
J14257+236E	BD+24 2733 B	M0.5 V	7.96 ± 0.02	Laf20	≤ 2.0	697	0
J14307−086	BD−07 3856	M0.5 V	−22.53 ± 0.02	Laf20	2.4 ± 1.5	996	0
J17355+616	BD+61 1678 C	M0.5 V	−15.44 ± 0.02	Laf20	≤ 2.0	585	0
J18353+457	BD+45 2743	M0.5 V	−32.05 ± 0.02	Laf20	≤ 2.0	454	0
J18580+059	BD+05 3993	M0.5 V	9.87 ± 0.02	Laf20	≤ 2.0	585	0
J22021+014	BD+00 4810	M0.5 V	17.82 ± 0.02	Laf20	≤ 2.0	951	0
J22503−070	BD−07 5871	M0.5 V	−6.13 ± 0.02	Laf20	≤ 2.0	512	0
J00051+457	GJ 2	M1.0 V	−0.56 ± 0.02	Laf20	≤ 2.0	774	0
J00183+440	GX And	M1.0 V	11.48 ± 0.02	Laf20	≤ 2.0	1795	0
J02565+554W	Ross 364	M1.0 V	76.31 ± 0.02	Laf20	≤ 2.0	225	0
J05415+534	HD 233153	M1.0 V	1.82 ± 0.02	Laf20	≤ 2.0	1088	0
J07361−031	BD−02 2198	M1.0 V	−17.06 ± 0.06	This work	3.1 ± 1.5	676	1
J10023+480	BD+48 1829	M1.0 V	−10.11 ± 0.02	Laf20	≤ 2.0	439	0
J10251−102	BD−09 3070	M1.0 V	21.26 ± 0.02	Laf20	≤ 2.0	456	0
J11054+435	BD+44 2051 A	M1.0 V	68.58 ± 0.02	Laf20	≤ 2.0	1013	0
J13209+342	BD+35 2439	M1.0 V	−35.76 ± 0.02	Laf20	≤ 2.0	324	0
J14010−026	HD 122303	M1.0 V	−26.14 ± 0.02	Laf20	≤ 2.0	424	0
J14082+805	BD+81 465	M1.0 V	7.06 ± 0.02	Laf20	≤ 2.0	559	0
J15598−082	BD−07 4156	M1.0 V	−17.47 ± 0.02	Laf20	≤ 2.0	382	0
J16581+257	BD+25 3173	M1.0 V	3.99 ± 0.02	Laf20	≤ 2.0	773	0
J17378+185	BD+18 3421	M1.0 V	−9.85 ± 0.02	Laf20	≤ 2.0	1131	0
J18051−030	HD 165222	M1.0 V	32.34 ± 0.02	Laf20	≤ 2.0	728	0
J18409−133	BD−13 5069	M1.0 V	−33.30 ± 0.02	Laf20	≤ 2.0	461	0
J20451−313	AU Mic	M1.0 V	−4.78 ± 0.13	This work	7.5 ± 1.5	510	1
J20533+621	BD+61 2068	M1.0 V	−17.49 ± 0.02	Laf20	≤ 2.0	1366	0

TABLE C.1. *continued*

Karmn	Name	SpT [a]	v_r [km s^{-1}]	Ref. [b]	$v \sin i$ [c] [km s^{-1}]	S/N	Hα flag [d]
J21221+229	GSC 02187−00512	M1.0 V	5.35 ± 0.02	Laf20	≤ 2.0	1089	0
J22330+093	BD+08 4887	M1.0 V	−6.83 ± 0.02	Laf20	≤ 2.0	564	0
J22559+178	StkM 1−2065	M1.0 V	−32.24 ± 0.02	Laf20	≤ 2.0	295	0
J23245+578	BD+57 2735	M1.0 V	−33.52 ± 0.02	Laf20	≤ 2.0	596	0
J23492+024	BR Psc	M1.0 V	−71.47 ± 0.02	Laf20	≤ 2.0	1533	0
J01026+623	BD+61 195	M1.5 V	−6.30 ± 0.02	Laf20	≤ 2.0	904	0
J02123+035	BD+02 348	M1.5 V	−2.89 ± 0.02	Laf20	≤ 2.0	505	0
J03181+382	HD 275122	M1.5 V	−4.56 ± 0.02	Laf20	≤ 2.0	564	0
J04376−110	BD−11 916	M1.5 V	−7.11 ± 0.02	Laf20	≤ 2.0	333	0
J05314−036	HD 36395	M1.5 V	8.33 ± 0.02	Laf20	≤ 2.0	1020	0
J09163−186	LP 787-052	M1.5 V	14.57 ± 0.02	Laf20	≤ 2.0	115	1
J09411+132	Ross 85	M1.5 V	11.16 ± 0.02	Laf20	≤ 2.0	481	0
J09468+760	BD+76 3952	M1.5 V	−28.09 ± 0.02	Laf20	≤ 2.0	449	0
J10122−037	AN Sex	M1.5 V	7.60 ± 0.02	Laf20	≤ 2.0	776	0
J11033+359	Lalande 21185	M1.5 V	−85.02 ± 0.02	Laf20	≤ 2.0	1935	0
J11126+189	StkM 1−928	M1.5 V	31.22 ± 0.02	Laf20	≤ 2.0	468	0
J11511+352	BD+36 2219	M1.5 V	−0.06 ± 0.02	Laf20	≤ 2.0	1009	0
J13196+333	Ross 1007	M1.5 V	−12.03 ± 0.02	Laf20	≤ 2.0	161	0
J13457+148	HD 119850	M1.5 V	15.47 ± 0.02	Laf20	≤ 2.0	1541	0
J15218+209	OT Ser	M1.5 V	6.72 ± 0.02	Laf20	4.3 ± 1.5	678	1
J16254+543	GJ 625	M1.5 V	−13.38 ± 0.02	Laf20	≤ 2.0	526	0
J17052−050	Wolf 636	M1.5 V	34.48 ± 0.02	Laf20	≤ 2.0	574	0
J20450+444	BD+44 3567	M1.5 V	−25.03 ± 0.02	Laf20	≤ 2.0	604	0
J22057+656	G 264-018 A	M1.5 V	−46.90 ± 0.02	Laf20	≤ 2.0	839	0
J22565+165	HD 216899	M1.5 V	−27.66 ± 0.02	Laf20	≤ 2.0	2075	0
J00403+612	2MASS J00402129+6112490	M2.0 V	4.00 ± 0.07	This work	≤ 2.0	77	0
J01013+613	GJ 47	M2.0 V	7.24 ± 0.02	Laf20	≤ 2.0	255	0
J01433+043	GJ 70	M2.0 V	−26.23 ± 0.02	Laf20	≤ 2.0	391	0
J02358+202	BD+19 381	M2.0 V	0.66 ± 0.02	Laf20	≤ 2.0	359	0
J02489−145W	PM J02489−1432W	M2.0 V	32.27 ± 0.06	This work	≤ 2.0	218	1
J03213+799	GJ 133	M2.0 V	−13.59 ± 0.02	Laf20	≤ 2.0	376	0
J03217−066	G 077-046	M2.0 V	26.12 ± 0.02	Laf20	≤ 2.0	245	0
J04343+430	PM J04343+4302	M2.0 V	−43.21 ± 0.10	This work	≤ 2.0	273	0
J04429+189	HD 285968	M2.0 V	25.89 ± 0.02	Laf20	≤ 2.0	350	0
J04538−177	GJ 180	M2.0 V	−14.83 ± 0.02	Laf20	≤ 2.0	447	0
J05127+196	GJ 192	M2.0 V	−25.36 ± 0.02	Laf20	≤ 2.0	428	0
J06103+821	GJ 226	M2.0 V	−1.95 ± 0.02	Laf20	≤ 2.0	679	0
J07353+548	GJ 3452	M2.0 V	−15.27 ± 0.02	Laf20	≤ 2.0	180	0
J08161+013	GJ 2066	M2.0 V	61.87 ± 0.02	Laf20	≤ 2.0	706	0
J09425+700	GJ 360	M2.0 V	6.70 ± 0.02	Laf20	≤ 2.0	514	1
J10289+008	BD+01 2447	M2.0 V	8.01 ± 0.02	Laf20	≤ 2.0	819	0
J11026+219	DS Leo	M2.0 V	−14.24 ± 0.02	Laf20	2.6 ± 1.5	700	1
J11110+304W	HD 97101 B	M2.0 V	−15.69 ± 0.02	Laf20	≤ 2.0	641	0
J11201−104	LP 733-099	M2.0 V	12.03 ± 0.02	Laf20	3.6 ± 1.5	426	1
J12248−182	Ross 695	M2.0 V	50.85 ± 0.02	Laf20	≤ 2.0	317	0
J13119+658	PM J13119+6550	M2.0 V	−41.63 ± 0.06	This work	≤ 2.0	134	0
J14294+155	Ross 130	M2.0 V	7.51 ± 0.02	Laf20	≤ 2.0	129	0
J14524+123	G 066-037	M2.0 V	5.40 ± 0.02	Laf20	≤ 2.0	366	0
J15474−108	LP 743-031	M2.0 V	−0.88 ± 0.08	This work	3.0 ± 1.5	552	0
J17166+080	GJ 2128	M2.0 V	−30.93 ± 0.02	Laf20	≤ 2.0	193	0
J18174+483	TYC 3529-1437-1	M2.0 V	−24.24 ± 0.02	Laf20	≤ 2.0	793	1
J19070+208	Ross 730	M2.0 V	32.06 ± 0.02	Laf20	≤ 2.0	479	0
J19072+208	HD 349726	M2.0 V	31.83 ± 0.02	Laf20	≤ 2.0	526	0

TABLE C.1. *continued*

Karmn	Name	SpT [a]	v_r [km s^{-1}]	Ref. [b]	$v \sin i$ [c] [km s^{-1}]	S/N	Hα flag [d]
J22115+184	Ross 271	M2.0 V	-51.67 ± 0.02	Laf20	≤ 2.0	876	0
J23381−162	G 273-093	M2.0 V	20.47 ± 0.02	Laf20	≤ 2.0	644	0
J00389+306	Wolf 1056	M2.5 V	-0.63 ± 0.03	Laf20	≤ 2.0	471	0
J01518+644	G 244-037	M2.5 V	-13.06 ± 0.03	Laf20	≤ 2.0	368	0
J02489−145E	PM J02489−1432E	M2.5 V	32.40 ± 0.06	This work	≤ 2.0	164	1
J05337+019	V371 Ori	M2.5 V	-0.88 ± 1.65	This work	9.8 ± 1.5	379	1
J08293+039	2MASS J08292191+0355092	M2.5 V	22.50 ± 0.03	Laf20	≤ 2.0	365	0
J08358+680	G 234-037	M2.5 V	18.86 ± 0.03	Laf20	≤ 2.0	264	0
J09133+688	G 234-057	M2.5 V	13.65 ± 0.03	Laf20	≤ 2.0	351	1
J09360−216	GJ 357	M2.5 V	-34.83 ± 0.03	Laf20	≤ 2.0	497	0
J10396−069	GJ 399	M2.5 V	2.97 ± 0.03	Laf20	≤ 2.0	225	0
J11000+228	Ross 104	M2.5 V	2.89 ± 0.03	Laf20	≤ 2.0	641	0
J11302+076	K2-18	M2.5 V	0.20 ± 0.03	Laf20	≤ 2.0	302	0
J11421+267	Ross 905	M2.5 V	9.34 ± 0.03	Laf20	≤ 2.0	1036	0
J12350+098	GJ 476	M2.5 V	33.01 ± 0.03	Laf20	≤ 2.0	145	0
J14251+518	θ Boo B	M2.5 V	-10.38 ± 0.03	Laf20	≤ 2.0	308	0
J16462+164	LP 446-006	M2.5 V	18.54 ± 0.03	Laf20	≤ 2.0	292	0
J17198+417	GJ 671	M2.5 V	-19.77 ± 0.03	Laf20	≤ 2.0	347	0
J17578+465	G 204-039	M2.5 V	-31.63 ± 0.03	Laf20	≤ 2.0	335	0
J18480−145	G 155-042	M2.5 V	-4.78 ± 0.03	Laf20	≤ 2.0	135	0
J19169+051N	V1428 Aql	M2.5 V	35.61 ± 0.03	Laf20	≤ 2.0	1194	0
J20305+654	GJ 793	M2.5 V	10.33 ± 0.03	Laf20	≤ 2.0	669	0
J20567−104	Wolf 896	M2.5 V	34.98 ± 0.03	Laf20	≤ 2.0	364	0
J21019−063	Wolf 906	M2.5 V	-15.23 ± 0.03	Laf20	≤ 2.0	389	0
J23340+001	GJ 899	M2.5 V	-4.84 ± 0.03	Laf20	≤ 2.0	487	0
J23556−061	GJ 912	M2.5 V	17.53 ± 0.07	This work	≤ 2.0	483	0
J00570+450	G 172-030	M3.0 V	6.27 ± 0.03	Laf20	≤ 2.0	268	0
J01025+716	BD+70 68	M3.0 V	1.25 ± 0.03	Laf20	≤ 2.0	1078	0
J01066+192	LSMP J0106+1913	M3.0 V	11.58 ± 0.07	This work	≤ 2.0	159	0
J02015+637	G 244-047	M3.0 V	-84.39 ± 0.03	Laf20	≤ 2.0	469	0
J02442+255	VX Ari	M3.0 V	30.30 ± 0.03	Laf20	≤ 2.0	613	0
J03473−019	G 080-021	M3.0 V	17.88 ± 0.02	Laf20	5.2 ± 1.5	234	1
J03531+625	Ross 567	M3.0 V	-120.32 ± 0.03	Laf20	≤ 2.0	562	0
J05033−173	LP 776-049	M3.0 V	15.19 ± 0.03	Laf20	≤ 2.0	483	0
J06548+332	Wolf 294	M3.0 V	22.65 ± 0.03	Laf20	≤ 2.0	1431	0
J07044+682	GJ 258	M3.0 V	-50.77 ± 0.03	Laf20	≤ 2.0	302	0
J07287−032	GJ 1097	M3.0 V	1.18 ± 0.03	Laf20	≤ 2.0	383	0
J07386−212	LP 763-001	M3.0 V	-29.18 ± 0.03	Laf20	≤ 2.0	146	0
J09140+196	LP 427-016	M3.0 V	12.88 ± 0.03	Laf20	≤ 2.0	330	0
J09428+700	GJ 362	M3.0 V	6.35 ± 0.03	Laf20	≤ 2.0	461	1
J10167−119	GJ 386	M3.0 V	-10.81 ± 0.03	Laf20	≤ 2.0	295	0
J10196+198	AD Leo	M3.0 V	12.29 ± 0.02	Laf20	3.2 ± 1.5	402	1
J10350−094	LP 670-017	M3.0 V	14.32 ± 0.03	Laf20	≤ 2.0	317	0
J11044+304	LSPM J1104+3027	M3.0 V	-11.78 ± 0.12	This work	≤ 2.0	36	0
J11467−140	GJ 443	M3.0 V	20.20 ± 0.03	Laf20	≤ 2.0	309	0
J12111−199	LTT 4562	M3.0 V	-9.38 ± 0.03	Laf20	≤ 2.0	322	0
J12230+640	Ross 690	M3.0 V	8.86 ± 0.03	Laf20	≤ 2.0	1308	0
J12388+116	Wolf 433	M3.0 V	-4.49 ± 0.03	Laf20	≤ 2.0	200	0
J13283−023W	Ross 486 A	M3.0 V	-39.73 ± 0.03	Laf20	≤ 2.0	248	0
J13582+125	Ross 837	M3.0 V	-10.13 ± 0.03	Laf20	≤ 2.0	105	0
J14152+450	Ross 992	M3.0 V	13.88 ± 0.03	Laf20	≤ 2.0	233	0
J15013+055	G 015-002	M3.0 V	-6.27 ± 0.03	Laf20	≤ 2.0	303	0
J15095+031	Ross 1047	M3.0 V	-32.79 ± 0.03	Laf20	≤ 2.0	261	0

TABLE C.1. *continued*

Karmn	Name	SpT [a]	v_r [km s^{-1}]	Ref. [b]	$v \sin i$ [c] [km s^{-1}]	S/N	Hα flag [d]
J15194−077	HO Lib	M3.0 V	−9.66 ± 0.03	Laf20	≤ 2.0	654	0
J16092+093	G 137-084	M3.0 V	−45.13 ± 0.03	Laf20	≤ 2.0	185	0
J16102−193	K2-33	M3.0 V	−7.00 ± 0.03	Laf20	7.3 ± 1.5	67	1
J16167+672N	EW Dra	M3.0 V	−18.78 ± 0.03	Laf20	≤ 2.0	985	0
J16327+126	GJ 1203	M3.0 V	−33.07 ± 0.03	Laf20	≤ 2.0	183	0
J17071+215	Ross 863	M3.0 V	−51.06 ± 0.03	Laf20	≤ 2.0	302	0
J17364+683	BD+68 946	M3.0 V	−28.82 ± 0.08	This work	≤ 2.0	609	0
J18180+387E	G 204-058	M3.0 V	0.23 ± 0.03	Laf20	≤ 2.0	210	0
J18419+318	Ross 145	M3.0 V	−32.03 ± 0.03	Laf20	≤ 2.0	343	0
J18427+596N	HD 173739	M3.0 V	−0.75 ± 0.08	Laf20	≤ 2.0	781	0
J19084+322	G 207-019	M3.0 V	−1.98 ± 0.03	Laf20	≤ 2.0	407	0
J19251+283	Ross 164	M3.0 V	−40.77 ± 0.03	Laf20	≤ 2.0	355	0
J21152+257	LP 397-041	M3.0 V	−16.28 ± 0.03	Laf20	≤ 2.0	346	0
J21164+025	LSPM J2116+0234	M3.0 V	−22.31 ± 0.03	Laf20	≤ 2.0	764	0
J21348+515	Wolf 926	M3.0 V	−14.12 ± 0.03	Laf20	≤ 2.0	804	0
J22125+085	Wolf 1014	M3.0 V	8.46 ± 0.03	Laf20	≤ 2.0	831	0
J22518+317	GT Peg	M3.0 V	−2.44 ± 0.05	Laf20	13.4 ± 1.5	368	1
J23585+076	Wolf 1051	M3.0 V	−13.54 ± 0.08	This work	≤ 2.0	404	0
J00184+440	GQ And	M3.5 V	10.68 ± 0.03	Laf20	≤ 2.0	1352	0
J02002+130	TZ Ari	M3.5 V	−28.83 ± 0.03	Laf20	≤ 2.0	863	1
J02070+496	G 173-037	M3.5 V	18.73 ± 0.03	Laf20	≤ 2.0	305	1
J02088+494	G 173-039	M3.5 V	−9.73 ± 0.06	Laf20	24.1 ± 2.4	633	1
J04225+105	LSPM J0422+1031	M3.5 V	36.72 ± 0.03	Laf20	≤ 2.0	283	0
J04429+214	2MASS J04425586+2128230	M3.5 V	2.80 ± 0.03	Laf20	≤ 2.0	205	0
J04520+064	Wolf 1539	M3.5 V	−9.12 ± 0.03	Laf20	≤ 2.0	181	0
J05280+096	Ross 41	M3.5 V	60.30 ± 0.03	Laf20	≤ 2.0	279	0
J05348+138	Ross 46	M3.5 V	37.42 ± 0.03	Laf20	≤ 2.0	362	0
J06011+595	G 192-013	M3.5 V	1.69 ± 0.03	Laf20	≤ 2.0	769	0
J06421+035	G 108-021	M3.5 V	82.19 ± 0.03	Laf20	≤ 2.0	390	0
J07274+052	Luyten's star	M3.5 V	17.89 ± 0.03	Laf20	≤ 2.0	678	0
J07319+362N	BL Lyn	M3.5 V	−1.07 ± 0.03	Laf20	≤ 2.0	590	1
J07582+413	GJ 1105	M3.5 V	−21.34 ± 0.03	Laf20	≤ 2.0	399	0
J08402+314	LSPM J0840+3127	M3.5 V	66.69 ± 0.03	Laf20	≤ 2.0	227	0
J08409−234	LP 844-008	M3.5 V	87.55 ± 0.03	Laf20	≤ 2.0	294	0
J09307+003	GJ 1125	M3.5 V	45.87 ± 0.03	Laf20	≤ 2.0	390	0
J09423+559	GJ 363	M3.5 V	15.00 ± 0.03	Laf20	≤ 2.0	230	0
J09439+269	Ross 93	M3.5 V	34.18 ± 0.03	Laf20	≤ 2.0	168	0
J10125+570	LP 092-048	M3.5 V	−3.78 ± 0.03	Laf20	≤ 2.0	242	0
J10360+051	RY Sex	M3.5 V	20.81 ± 0.03	Laf20	2.9 ± 1.6	171	1
J11289+101	Wolf 398	M3.5 V	36.80 ± 0.03	Laf20	≤ 2.0	89	0
J11306−080	LP 672-042	M3.5 V	16.43 ± 0.03	Laf20	≤ 2.0	289	0
J11476+786	GJ 445	M3.5 V	−111.97 ± 0.03	Laf20	≤ 2.0	608	0
J12100−150	LP 734-032	M3.5 V	80.21 ± 0.03	Laf20	≤ 2.0	497	0
J12479+097	Wolf 437	M3.5 V	18.77 ± 0.03	Laf20	≤ 2.0	838	0
J13293+114	GJ 513	M3.5 V	27.98 ± 0.03	Laf20	≤ 2.0	68	0
J13427+332	Ross 1015	M3.5 V	6.45 ± 0.03	Laf20	≤ 2.0	339	0
J13458−179	LP 798-034	M3.5 V	4.63 ± 0.03	Laf20	≤ 2.0	116	0
J14310−122	Wolf 1478	M3.5 V	−2.08 ± 0.03	Laf20	≤ 2.0	175	0
J14544+355	Ross 1041	M3.5 V	−41.06 ± 0.03	Laf20	≤ 2.0	456	0
J15583+354	G 180-018	M3.5 V	9.54 ± 0.10	This work	≤ 2.0	328	0
J16303−126	V2306 Oph	M3.5 V	−21.56 ± 0.03	Laf20	≤ 2.0	841	0
J16554−083N	GJ 643	M3.5 V	15.50 ± 0.03	Laf20	≤ 2.0	433	0
J16570−043	LP 686-027	M3.5 V	−3.96 ± 0.05	Laf20	10.1 ± 1.5	405	1

TABLE C.1. *continued*

Karmn	Name	SpT [a]	v_r [km s^{-1}]	Ref. [b]	$v \sin i$ [c] [km s^{-1}]	S/N	Hα flag [d]
J17115+384	Wolf 654	M3.5 V	-44.78 ± 0.03	Laf20	≤ 2.0	653	0
J17578+046	Barnard's star	M3.5 V	-110.57 ± 0.02	Laf20	≤ 2.0	2007	0
J18319+406	G 205-028	M3.5 V	-19.32 ± 0.03	Laf20	≤ 2.0	307	0
J18346+401	LP 229-017	M3.5 V	12.18 ± 0.03	Laf20	≤ 2.0	822	0
J18427+596S	HD 173740	M3.5 V	1.02 ± 0.08	This work	≤ 2.0	817	0
J18498−238	GJ 729	M3.5 V	-10.80 ± 0.03	Laf20	3.0 ± 1.5	575	1
J22020−194	LP 819-017	M3.5 V	-23.60 ± 0.03	Laf20	≤ 2.0	182	0
J22096−046	BD−05 5715	M3.5 V	-15.59 ± 0.03	Laf20	≤ 2.0	679	0
J22468+443	EV Lac	M3.5 V	0.35 ± 0.03	Laf20	3.5 ± 1.5	944	1
J23113+085	NLTT 56083	M3.5 V	-10.73 ± 0.10	Laf20	≤ 2.0	643	0
J00162+198E	LP 404-062	M4.0 V	-1.62 ± 0.02	Laf20	≤ 2.0	224	0
J00286−066	GJ 1012	M4.0 V	-12.71 ± 0.02	Laf20	≤ 2.0	594	0
J01339−176	LP 768-113	M4.0 V	6.12 ± 0.02	Laf20	≤ 2.0	279	1
J01352−072	Barta 161 12	M4.0 V	9.34 ± 0.21	Laf20	59.8 ± 6.9	587	1
J02336+249	GJ 102	M4.0 V	-6.66 ± 0.02	Laf20	3.0 ± 1.5	303	1
J02362+068	BX Cet	M4.0 V	25.97 ± 0.02	Laf20	≤ 2.0	611	0
J02519+224	RBS 365	M4.0 V	9.14 ± 0.08	Laf20	27.2 ± 2.7	565	0
J04311+589	STN 2051A	M4.0 V	28.43 ± 0.02	Laf20	≤ 2.0	248	0
J05019+011	1RXS J050156.7+010845	M4.0 V	19.71 ± 0.03	Laf20	6.5 ± 1.5	296	1
J05019−069	LP 656-038	M4.0 V	41.97 ± 0.02	Laf20	≤ 2.0	204	1
J05062+046	RX J0506.2+0439	M4.0 V	19.08 ± 0.08	Laf20	24.9 ± 2.5	417	1
J05360−076	Wolf 1457	M4.0 V	29.09 ± 0.02	Laf20	≤ 2.0	327	0
J05366+112	2MASS J05363846+1117487	M4.0 V	21.53 ± 0.02	Laf20	2.4 ± 1.5	283	1
J05421+124	V1352 Ori	M4.0 V	105.67 ± 0.02	Laf20	≤ 2.0	591	0
J06000+027	G 099-049	M4.0 V	29.90 ± 0.03	Laf20	4.9 ± 1.5	201	1
J06246+234	Ross 64	M4.0 V	-11.66 ± 0.02	Laf20	≤ 2.0	144	0
J06396−210	LP 780-032	M4.0 V	-7.43 ± 0.02	Laf20	≤ 2.0	385	0
J06574+740	2MASS J06572616+7405265	M4.0 V	-2.69 ± 0.10	Laf20	27.1 ± 2.7	463	1
J07033+346	LP 255-011	M4.0 V	2.03 ± 0.02	Laf20	≤ 2.0	258	1
J07472+503	2MASS J07471385+5020386	M4.0 V	-14.77 ± 0.05	Laf20	10.1 ± 1.5	381	1
J08023+033	G 050-016 A	M4.0 V	-1.15 ± 0.25	This work	≤ 2.0	282	0
J08126−215	GJ 300	M4.0 V	8.68 ± 0.02	Laf20	≤ 2.0	450	0
J08315+730	LP 035-219	M4.0 V	-90.84 ± 0.02	Laf20	≤ 2.0	269	0
J09028+680	LP 060-179	M4.0 V	-25.01 ± 0.02	Laf20	≤ 2.0	237	0
J09161+018	RX J0916.1+0153	M4.0 V	-12.75 ± 0.05	Laf20	10.4 ± 1.5	255	1
J09447−182	GJ 1129	M4.0 V	8.34 ± 0.02	Laf20	≤ 2.0	237	0
J10185−117	LP 729-054	M4.0 V	-0.05 ± 0.33	This work	≤ 2.0	356	0
J10504+331	G 119-037	M4.0 V	-59.65 ± 0.11	Laf20	≤ 2.0	327	0
J10508+068	EE Leo	M4.0 V	-1.34 ± 0.02	Laf20	≤ 2.0	632	0
J11417+427	Ross 1003	M4.0 V	-9.34 ± 0.02	Laf20	≤ 2.0	812	0
J11476+002	LP 613-049 A	M4.0 V	5.94 ± 0.03	Laf20	2.4 ± 1.5	122	1
J11477+008	FI Vir	M4.0 V	-31.38 ± 0.02	Laf20	≤ 2.0	578	0
J12054+695	Ross 689	M4.0 V	5.26 ± 0.02	Laf20	≤ 2.0	59	0
J12156+526	StkM 2-809	M4.0 V	-9.55 ± 0.13	Laf20	35.3 ± 3.5	614	1
J12373−208	LP 795-038	M4.0 V	9.09 ± 0.02	Laf20	≤ 2.0	168	0
J12428+418	G 123-055	M4.0 V	-4.68 ± 0.02	Laf20	≤ 2.0	180	1
J13229+244	Ross 1020	M4.0 V	-19.56 ± 0.02	Laf20	≤ 2.0	647	0
J13536+776	RX J1353.6+7737	M4.0 V	-7.59 ± 0.02	Laf20	8.9 ± 1.5	412	1
J13591−198	LP 799-007	M4.0 V	-16.49 ± 0.03	Laf20	3.2 ± 1.5	195	1
J14342−125	HN Lib	M4.0 V	-1.74 ± 0.02	Laf20	≤ 2.0	806	0
J15369−141	Ross 802	M4.0 V	2.10 ± 0.02	Laf20	≤ 2.0	135	0
J16028+205	GJ 609	M4.0 V	6.18 ± 0.02	Laf20	≤ 2.0	320	0
J17542+073	GJ 1222	M4.0 V	-28.61 ± 0.02	Laf20	≤ 2.0	122	0

TABLE C.1. *continued*

Karmn	Name	SpT [a]	v_r [km s^{-1}]	Ref. [b]	$v \sin i$ [c] [km s^{-1}]	S/N	Hα flag [d]
J18131+260	LP 390-016	M4.0 V	-8.61 ± 0.09	Laf20	5.9 ± 1.5	198	1
J18221+063	Ross 136	M4.0 V	-43.97 ± 0.02	Laf20	≤ 2.0	128	0
J18224+620	GJ 1227	M4.0 V	-13.97 ± 0.02	Laf20	≤ 2.0	357	0
J18363+136	Ross 149	M4.0 V	-45.32 ± 0.02	Laf20	≤ 2.0	307	1
J19206+731S	TOI-1670	M4.0 V	-34.42 ± 0.51	This work	≤ 2.0	88	0
J19511+464	G 208-042	M4.0 V	-12.94 ± 0.06	Laf20	22.5 ± 2.3	493	1
J20336+617	GJ 1254	M4.0 V	-21.18 ± 0.02	Laf20	≤ 2.0	490	0
J20525−169	LP 816-060	M4.0 V	16.00 ± 0.02	Laf20	≤ 2.0	414	0
J21463+382	LSPM J2146+3813	M4.0 V	-83.01 ± 0.02	Laf20	≤ 2.0	495	0
J21466−001	Wolf 940	M4.0 V	-28.55 ± 0.02	Laf20	≤ 2.0	319	0
J21466+668	G 264-012	M4.0 V	-9.77 ± 0.02	Laf20	≤ 2.0	761	0
J22012+283	V374 Peg	M4.0 V	-3.25 ± 0.14	Laf20	35.4 ± 3.5	618	1
J22252+594	G 232-070	M4.0 V	3.87 ± 0.02	Laf20	≤ 2.0	639	0
J22298+414	G 215-050	M4.0 V	2.11 ± 0.02	Laf20	≤ 2.0	231	0
J22532−142	IL Aqr	M4.0 V	-1.80 ± 0.03	Laf20	≤ 2.0	645	0
J23216+172	LP 462-027	M4.0 V	-6.77 ± 0.02	Laf20	≤ 2.0	775	0
J23431+365	GJ 1289	M4.0 V	-2.98 ± 0.02	Laf20	≤ 2.0	308	1
J23505−095	LP 763-012	M4.0 V	-21.87 ± 0.02	Laf20	≤ 2.0	365	0
J23548+385	RX J2354.8+3831	M4.0 V	5.37 ± 0.03	Laf20	3.6 ± 1.5	200	1
J01125−169	YZ Cet	M4.5 V	27.85 ± 0.02	Laf20	≤ 2.0	821	1
J04153−076	o^{02} Eri C	M4.5 V	-43.58 ± 0.02	Laf20	2.1 ± 1.5	477	1
J07446+035	YZ CMi	M4.5 V	26.71 ± 0.03	Laf20	4.0 ± 1.5	542	1
J07558+833	GJ 1101	M4.5 V	7.64 ± 0.05	Laf20	12.1 ± 1.5	315	1
J08119+087	Ross 619	M4.5 V	14.42 ± 0.02	Laf20	≤ 2.0	285	0
J08526+283	ρ Cnc B	M4.5 V	27.18 ± 0.02	Laf20	≤ 2.0	223	0
J09005+465	GJ 1119	M4.5 V	1.99 ± 0.02	Laf20	≤ 2.0	49	1
J10416+376	GJ 1134	M4.5 V	-1.86 ± 0.02	Laf20	≤ 2.0	102	0
J11509+483	GJ 1151	M4.5 V	-35.61 ± 0.02	Laf20	≤ 2.0	429	0
J13005+056	FN Vir	M4.5 V	-25.33 ± 0.05	Laf20	16.4 ± 1.6	269	1
J17033+514	G 203-042	M4.5 V	37.18 ± 0.02	Laf20	≤ 2.0	330	0
J18075−159	GJ 1224	M4.5 V	-33.20 ± 0.02	Laf20	2.2 ± 1.5	144	1
J18189+661	LP 071-165	M4.5 V	5.36 ± 0.05	Laf20	15.3 ± 1.5	354	1
J19098+176	GJ 1232	M4.5 V	-14.26 ± 0.02	Laf20	≤ 2.0	256	0
J19216+208	GJ 1235	M4.5 V	4.52 ± 0.02	Laf20	≤ 2.0	256	0
J20405+154	GJ 1256	M4.5 V	-59.78 ± 0.02	Laf20	≤ 2.0	260	0
J22137−176	LP 819-052	M4.5 V	-24.48 ± 0.02	Laf20	≤ 2.0	418	0
J22231−176	LP 820-012	M4.5 V	-1.97 ± 0.02	Laf20	≤ 2.0	163	1
J01019+541	G 218-020	M5.0 V	-5.20 ± 0.13	Laf20	30.6 ± 3.1	426	1
J01033+623	V388 Cas	M5.0 V	-6.52 ± 0.08	Laf20	10.5 ± 1.5	392	1
J01048−181	GJ 1028	M5.0 V	11.37 ± 0.02	Laf20	≤ 2.0	203	0
J03133+047	CD Cet	M5.0 V	28.16 ± 0.02	Laf20	≤ 2.0	601	0
J04472+206	RX J0447.2+2038	M5.0 V	23.98 ± 0.31	Laf20	47.6 ± 26.8	429	1
J05084−210	2MASS J05082729−2101444	M5.0 V	22.21 ± 0.23	Laf20	25.2 ± 2.5	320	1
J06024+498	G 192-015	M5.0 V	20.26 ± 0.02	Laf20	≤ 2.0	260	0
J06318+414	LP 205-044	M5.0 V	4.35 ± 0.12	Laf20	58.4 ± 26.1	720	1
J06594+193	GJ 1093	M5.0 V	-29.51 ± 0.02	Laf20	≤ 2.0	263	1
J09449−123	G 161-071	M5.0 V	16.96 ± 0.36	Laf20	31.2 ± 3.1	412	1
J10584−107	LP 731-076	M5.0 V	10.78 ± 0.02	Laf20	3.2 ± 1.5	244	1
J11474+667	1RXS J114728.8+664405	M5.0 V	-9.40 ± 0.04	Laf20	2.7 ± 1.5	193	1
J12189+111	GL Vir	M5.0 V	5.68 ± 0.05	Laf20	15.5 ± 1.6	384	1
J13102+477	G 177-025	M5.0 V	-12.45 ± 0.02	Laf20	≤ 2.0	228	1
J14173+454	RX J1417.3+4525	M5.0 V	3.11 ± 0.06	Laf20	15.9 ± 1.6	242	1
J15499+796	LP 022-420	M5.0 V	-16.29 ± 0.10	Laf20	26.9 ± 2.7	286	1

Table C.1. *continued*

Karmn	Name	SpT [a]	v_r [km s^{-1}]	Ref. [b]	$v \sin i$ [c] [km s^{-1}]	S/N	Hα flag [d]
J16313+408	G 180-060	M5.0 V	-23.16 ± 0.04	Laf20	7.1 ± 1.5	150	1
J18022+642	LP 071-082	M5.0 V	-1.63 ± 0.05	Laf20	11.3 ± 1.5	449	1
J18027+375	GJ 1223	M5.0 V	3.67 ± 0.02	Laf20	≤ 2.0	218	0
J18165+048	G 140-051	M5.0 V	-53.52 ± 0.02	Laf20	≤ 2.0	224	0
J18482+076	G 141-036	M5.0 V	-34.45 ± 0.02	Laf20	2.4 ± 1.5	348	1
J19422−207	2MASS J19421282−2045477	M5.1 V	-2.09 ± 0.03	Laf20	6.2 ± 1.5	118	1
J20093−012	2MASS J20091824−0113377	M5.0 V	-53.97 ± 0.02	Laf20	4.3 ± 1.5	149	1
J20260+585	Wolf 1069	M5.0 V	-60.05 ± 0.02	Laf20	≤ 2.0	817	0
J20556−140S	GJ 810 B	M5.0 V	-142.04 ± 0.02	Laf20	≤ 2.0	195	0
J23419+441	HH And	M5.0 V	-78.07 ± 0.02	Laf20	≤ 2.0	774	1
J00067−075	GJ 1002	M5.5 V	-40.12 ± 0.02	Laf20	≤ 2.0	566	0
J08413+594	LP 090-018	M5.5 V	6.12 ± 0.02	Laf20	≤ 2.0	431	1
J11055+435	WX UMa	M5.5 V	69.16 ± 0.02	Laf20	8.2 ± 2.7	428	1
J15305+094	NLTT 40406	M5.5 V	1.43 ± 0.05	Laf20	16.3 ± 1.6	233	1
J17338+169	1RXS J173353.5+165515	M5.5 V	-21.87 ± 0.29	Laf20	41.5 ± 7.7	438	1
J22114+409	1RXS J221124.3+410000	M5.5 V	-16.88 ± 0.02	Laf20	≤ 2.0	227	1
J23351−023	GJ 1286	M5.5 V	-41.06 ± 0.02	Laf20	≤ 2.0	364	1
J07403−174	LP 783-002	M6.0 V	-28.81 ± 0.03	Laf20	≤ 2.0	146	0
J10564+070	CN Leo	M6.0 V	19.44 ± 0.03	Laf20	≤ 2.0	628	1
J14321+081	LP 560-035	M6.0 V	-22.02 ± 0.03	Laf20	6.3 ± 1.5	204	1
J08298+267	DX Cnc	M6.5 V	9.94 ± 0.05	Laf20	10.5 ± 1.5	500	1
J09003+218	LP 368-128	M6.5 V	8.11 ± 0.07	Laf20	14.3 ± 1.5	173	1
J10482−113	LP 731-058	M6.5 V	1.74 ± 0.03	Laf20	2.1 ± 1.5	348	1
J02530+168	Teegarden's star	M7.0 V	68.42 ± 0.03	Laf20	≤ 2.0	903	1
J09033+056	NLTT 20861	M7.0 V	-28.12 ± 0.04	Laf20	9.7 ± 1.5	139	1
J16555−083	vB 8	M7.0 V	14.41 ± 0.03	Laf20	5.4 ± 1.5	264	1
J05394+406 [e]	LSR J0539+4038	M8.0 V	-6.34 ± 0.03	Laf20	4.1 ± 1.5	61	1
J19169+051S [e]	V1298 Aql	M8.0 V	35.73 ± 0.03	Laf20	2.7 ± 2.2	173	1
J19255+096 [e]	LSPM J1925+0938	M8.0 V	-2.47 ± 9.87	This work	34.7 ± 3.5	120	1
J23064−050 [e]	2MUCD 12171	M8.0 V	-53.32 ± 0.03	Laf20	≤ 2.0	51	1
J04198+425 [e]	LSR J0419+4233	M8.5 V	21.49 ± 0.07	Laf20	3.6 ± 2.3	81	1
J18356+329 [e]	LSR J1835+3259	M8.5 V	0.64 ± 0.18	Laf20	49.2 ± 4.9	193	1
J08536−034 [e]	LP 666-009	M9.0 V	-7.22 ± 0.10	Laf20	9.3 ± 2.8	79	1

Notes. [a] Spectral types from Carmencita (Alonso-Floriano et al., 2015; Caballero et al., 2016a). [b] Radial velocities from Lafarga et al. (2020, Laf20) if available, or computed using `serval` (Zechmeister et al., 2018) otherwise. [c] Projected rotational velocities computed as in Reiners et al. (2018). [d] Hα-active stars following Schöfer et al. (2019) (1 if active). [e] M8.0 V or later (see Table 4.1).

TABLE C.2. Selection of Ti I and Fe I lines in the spectra of GX And (M1.0 V), Luyten's star (M3.5 V), and Teegarden's star (M7.0 V).

$\lambda_{\min}$ [Å]	$\lambda_{\max}$ [Å]	λ_{line} [Å]	Element	χ [eV]	$\log gf$	g_{eff}	Magnetically sensitive [b]	Ref. [c]	GX And	Luyten's star	Teegarden's star
5636.61	5651.65	5644.134	Ti I	2.2674	+0.120	1.010		This work	•		
5859.04	5874.01	5866.451	Ti I	1.0666	−0.790	1.170		This work	•		
5914.95	5929.51	5922.110	Ti I	1.0460	−1.380	0.500		This work	•		
5969.39	5985.75	5976.776	Fe I	3.9433	−1.236	1.100		This work	•		
		5978.541	Ti I	1.8732	−0.312	0.890		This work	•		
6056.60	6072.73	6064.626	Ti I	1.0460	−1.670	1.990		This work	•		
		6065.481	Fe I	2.6085	−1.530	0.680		This work	•		
6077.90	6092.38	6085.226	Ti I	1.0529	−1.331	1.750		This work	•		
6119.00	6145.00	6126.216	Ti I	1.0666	−1.206	1.240		This work	•	•	
		6136.615	Fe I	2.4534	−1.400	0.840		This work	•	•	
		6137.691	Fe I	2.5881	−1.403	1.080		This work	•	•	
6385.90	6400.63	6393.600	Fe I	2.4327	−1.432	0.910		This work	•		
6423.28	6438.23	6430.845	Fe I	2.1759	−2.006	1.240		This work	•		
6468.58	6489.05	6475.624	Fe I	2.5592	−2.942	1.900		This work	•	•	
		6481.869	Fe I	2.2786	−2.984	1.500		This work	•		
6548.73	6563.37	6556.062	Ti I	1.4601	−1.060	1.250		This work	•		
6585.30	6606.47	6592.912	Fe I	2.7275	−1.473	1.000		This work	•		
		6599.105	Ti I	0.8995	−1.715	0.980		This work	•		
6937.06	6953.09	6945.204	Fe I	2.4242	−2.482	1.490		This work	•		
7208.93	7223.18	7216.184	Ti I	1.4432	−1.200	0.690		This work	•		
7382.29	7396.59	7389.398	Fe I	4.3013	−0.460	0.000		This work	•	•	
7404.15	7418.15	7411.153	Fe I	4.2833	−0.299	0.990		This work	•		
7482.50	7503.00	7489.578	Ti I	2.2492	−0.910	0.960		This work	•	•	
		7496.102	Ti I	2.2363	−1.060	0.870		This work	•		
7576.46	7591.08	7583.788	Fe I	3.0176	−1.885	0.830		This work	•	•	
7905.87	7920.37	7912.866	Fe I	0.8590	−4.848	0.920	•	This work	•	•	•
7991.31	8006.60	7998.944	Fe I	4.3714	+0.151	0.900		This work	•	•	
8067.78	8082.27	8075.149	Fe I	0.9146	−5.062	0.760	•	This work	•	•	•
8197.77	8212.48	8204.936	Fe I	0.9582	−5.058	0.490	•	This work	•	•	•
8375.78	8457.72	8382.781	Ti I	0.8129	−1.710	0.830	•	This work	•	•	•
		8396.898	Ti I	0.8129	−1.633	0.000		This work	•	•	•
		8401.399	Fe I	2.4844	−3.163	0.510		This work	•	•	
		8412.358	Ti I	0.8181	−1.390	0.660	•	Pas19	•	•	•
		8416.950	Ti I	2.2363	−1.080	0.870		This work	•	•	
		8426.507	Ti I	0.8259	−1.200	1.000	•	Pas19	•	•	•
		8434.961	Ti I	0.8484	−0.830	1.210	•	Pas19	•	•	
		8435.653	Ti I	0.8360	−1.020	1.140	•	Pas19	•	•	
		8450.891	Ti I	2.2492	−0.800	0.960		This work	•	•	
8459.84	8476.15	8467.147	Ti I	2.1171	−1.101	1.100		Pas19	•		
		8468.406	Fe I	2.2227	−2.072	2.490	•	Pas19	•	•	
8506.00	8526.00	8514.071	Fe I	2.1979	−2.229	1.830	•	Pas19, Tab18	•	•	
		8515.108	Fe I	3.0176	−2.073	0.780	•	Tab18	•	•	•
		8518.028	Ti I	2.1344	−0.936	1.260		Tab18	•		
		8518.353	Ti I	1.8792	−1.050	1.060		Tab18	•		
8541.09	8555.21	8548.088	Ti I	1.8732	−1.160	0.820	•	This work	•	•	
8574.78	8590.67	8582.257	Fe I	2.9904	−2.134	1.070	•	Tab18	•	•	
8604.25	8619.48	8611.803	Fe I	2.8450	−1.926	1.490	•	Tab18	•	•	
8667.41	8699.33	8674.746	Fe I	2.8316	−1.800	1.500	•	Pas19	•	•	
		8675.372	Ti I	1.0666	−1.500	1.190	•	Pas19	•	•	
		8682.983	Ti I	1.0529	−1.790	0.990	•	Pas19, Tab18	•	•	
		8688.623	Fe I	2.1759	−1.212	1.660	•	Pas19, Tab18	•	•	
		8692.330	Ti I	1.0460	−2.130	0.500	•	Tab18	•	•	•
8727.71	8742.59	8734.710	Ti I	1.0529	−2.240	1.000	•	Tab18	•	•	•
8750.26	8764.42	8757.187	Fe I	2.8450	−2.059	1.490	•	Tab18	•	•	
8815.71	8845.95	8824.219	Fe I	2.1979	−1.540	1.490	•	Pas19, Tab18	•	•	
		8838.428	Fe I	2.8581	−2.050	1.500	•	Tab18	•	•	
8848.87	8875.78	8868.430	Fe I	3.0176	−2.909	0.820		This work	•	•	
9003.23	9018.33	9010.592	Fe I	2.6085	−2.953	0.670		This work	•	•	
9711.21	9737.14	9718.960	Ti I	1.5025	−1.181	0.950	•	Pas19	•	•	
		9728.407	Ti I	0.8181	−1.206	1.000	•	Pas19	•	•	
9825.15	9839.50	9832.140	Ti I	1.8871	−1.130	1.210	•	Pas19	•	•	
10052.60	10067.70	10059.904	Ti I	1.4298	−2.080	0.830		This work	•	•	
10333.30	10347.90	10340.885	Fe I	2.1979	−3.577	0.680	•	This work	•	•	
10371.50	10386.70	10378.999	Fe I	2.2227	−4.148	0.260		This work	•	•	
10388.90	10403.60	10395.794	Fe I	2.1759	−3.393	0.890	•	This work	•	•	
10576.90	10592.30	10584.633	Ti I	0.8259	−1.775	1.000	•	Pas19	•	•	•

Table C.2. *continued*

Range			Atomic line [a]				Magnetically	Ref. [c]	GX And	Luyten's	Teegarden's
λ_{min} [Å]	λ_{max} [Å]	λ_{line} [Å]	Element	χ [eV]	$\log gf$	g_{eff}	sensitive [b]			star	star
10654.40	10669.20	10661.623	Ti I	0.8181	−1.915	0.870	•	Pas19	•	•	•
10767.90	10781.90	10774.866	Ti I	0.8181	−2.666	0.690	•	Pas19	•	•	•
11789.90	11804.90	11797.186	Ti I	1.4298	−2.280	0.920	•	This work	•	•	•
11876.10	11891.90	11884.083	Fe I	2.2227	−2.083	1.000	•	This work	•	•	•
11942.20	11957.00	11949.547	Ti I	1.4432	−1.570	1.000	•	This work	•	•	
12804.50	12818.60	12811.478	Ti I	2.1603	−1.390	0.950	•	This work	•	•	
12912.90	12926.90	12919.899	Ti I	2.1535	−1.560	0.760		This work	•		
15595.50	15610.40	15602.842	Ti I	2.2674	−1.435	1.000	•	This work	•		
15707.80	15723.50	15715.578	Ti I	1.8732	−1.200	0.750	•	This work	•		

Notes. The corresponding wavelength ranges synthesised in this work are listed in the first two columns. χ, $\log gf$, and g_{eff} are the excitation potential, the oscillator strength, and the effective Landé factors of the lines, respectively. [a]Atomic line data from the VALD3 database (Ryabchikova et al., 2015). [b]Lines particularly affected by the stellar magnetic field (López-Gallifa et al. in prep.). [c]Lines employed in Tabernero et al. (2018, Tab18), and Passegger et al. (2019, Pas19).

TABLE C.3. Prior $T_{\rm eff}$ and log g distributions and stellar atmospheric parameters of the sample computed with STEPARSYN.

Karmn	Prior $T_{\rm eff}$ [a] [K]	Prior log g [a] [dex]	$T_{\rm eff}$ [K]	log g [dex]	[Fe/H] [dex]	[Fe/H]$_{\rm corr}$ [dex]	$T_{\rm eff,fixed}$ [K]	[Fe/H]$_{\rm fixed}$ [dex]	[Fe/H]$_{\rm corr,fixed}$ [dex]	Pop. [b]
K7.0 V										
J04167−120	3700 ± 200	4.62 ± 0.20	3961 ± 13	5.01 ± 0.09	0.15 ± 0.04	0.15 ± 0.04	3922 ± 14	0.00 ± 0.02	0.00 ± 0.02	D
J11110+304E	4100 ± 200	4.60 ± 0.20	4211 ± 13	4.98 ± 0.07	0.04 ± 0.03	0.04 ± 0.03	4195 ± 15	−0.07 ± 0.02	−0.04 ± 0.02	D
J18198−019	4000 ± 200	4.64 ± 0.20	4155 ± 14	5.01 ± 0.06	−0.21 ± 0.04	−0.14 ± 0.04	4215 ± 5	−0.33 ± 0.03	−0.22 ± 0.03	YD
M0.0 V										
J03463+262	3900 ± 200	4.67 ± 0.20	3949 ± 12	4.83 ± 0.09	0.01 ± 0.04	0.01 ± 0.04	3941 ± 12	−0.08 ± 0.02	−0.04 ± 0.02	YD
J04376+528	3900 ± 200	4.66 ± 0.20	4039 ± 20	4.94 ± 0.07	−0.21 ± 0.05	−0.14 ± 0.05	4005 ± 9	−0.42 ± 0.03	−0.28 ± 0.03	D
J04588+498	3900 ± 200	4.65 ± 0.20	3983 ± 13	5.07 ± 0.08	0.02 ± 0.03	0.02 ± 0.03	3981 ± 15	−0.21 ± 0.03	−0.14 ± 0.03	D
J05365+113	3900 ± 200	4.65 ± 0.20	4067 ± 14	5.04 ± 0.07	0.01 ± 0.03	0.01 ± 0.03	4001 ± 6	−0.22 ± 0.02	−0.15 ± 0.02	YD
J06371+175	3800 ± 200	4.80 ± 0.20	3803 ± 10	5.20 ± 0.07	−0.63 ± 0.04	−0.43 ± 0.04	3820 ± 11	−0.68 ± 0.04	−0.46 ± 0.04	TD-D
J07393+021	3800 ± 200	4.64 ± 0.20	3980 ± 11	5.03 ± 0.06	0.01 ± 0.03	0.01 ± 0.03	3984 ± 10	−0.17 ± 0.03	−0.11 ± 0.03	YD.
J09143+526	3900 ± 200	4.65 ± 0.20	4015 ± 16	4.91 ± 0.08	−0.19 ± 0.05	−0.12 ± 0.05	4004 ± 9	−0.35 ± 0.03	−0.23 ± 0.03	YD
J09144+526	3800 ± 200	4.64 ± 0.20	3983 ± 12	5.17 ± 0.07	−0.06 ± 0.04	−0.03 ± 0.04	3997 ± 15	−0.33 ± 0.03	−0.22 ± 0.03	YD
J09561+627	3800 ± 200	4.66 ± 0.20	3938 ± 13	5.03 ± 0.08	−0.03 ± 0.04	−0.01 ± 0.04	3943 ± 21	−0.16 ± 0.04	−0.10 ± 0.04	YD
J12123+544S	3800 ± 200	4.65 ± 0.20	3902 ± 11	4.99 ± 0.12	−0.14 ± 0.07	−0.08 ± 0.07	3889 ± 13	−0.37 ± 0.03	−0.25 ± 0.03	D
J13255+688	3900 ± 200	4.65 ± 0.20	4049 ± 41	4.96 ± 0.13	0.10 ± 0.04	0.10 ± 0.04	4016 ± 38	0.00 ± 0.06	0.00 ± 0.06	D
J13450+176	3900 ± 200	4.77 ± 0.20	3829 ± 10	4.99 ± 0.06	−0.79 ± 0.03	−0.54 ± 0.03	3849 ± 14	−0.78 ± 0.04	−0.54 ± 0.04	TD
J14257+236W	3800 ± 200	4.62 ± 0.20	3985 ± 13	4.89 ± 0.08	0.07 ± 0.04	0.07 ± 0.04	3954 ± 13	−0.05 ± 0.03	−0.02 ± 0.03	D
J16167+672S	4000 ± 200	4.64 ± 0.20	4034 ± 17	4.78 ± 0.09	0.00 ± 0.04	0.00 ± 0.04	4039 ± 12	−0.02 ± 0.03	−0.01 ± 0.03	D
J17303+055	3800 ± 200	4.72 ± 0.20	3821 ± 9	4.93 ± 0.10	−0.35 ± 0.06	−0.23 ± 0.06	3837 ± 7	−0.39 ± 0.03	−0.26 ± 0.03	YD
J19346+045	4000 ± 200	4.68 ± 0.20	4093 ± 24	4.92 ± 0.07	−0.34 ± 0.05	−0.22 ± 0.05	4165 ± 13	−0.47 ± 0.04	−0.32 ± 0.04	D
J21474+627	3900 ± 200	4.67 ± 0.20	4029 ± 13	4.98 ± 0.04	−0.03 ± 0.03	−0.01 ± 0.03	4001 ± 6	−0.25 ± 0.02	−0.17 ± 0.02	D
M0.5 V										
J02222+478	3900 ± 200	4.70 ± 0.20	3894 ± 11	4.99 ± 0.09	−0.01 ± 0.04	0.00 ± 0.04	3877 ± 10	−0.20 ± 0.03	−0.13 ± 0.03	D
J04290+219	4000 ± 200	4.59 ± 0.20	4123 ± 20	4.48 ± 0.15	0.05 ± 0.06	0.05 ± 0.03	4130 ± 21	0.06 ± 0.03	0.06 ± 0.03	D
J06105−218	3700 ± 200	4.70 ± 0.20	3801 ± 13	4.98 ± 0.09	−0.05 ± 0.05	−0.02 ± 0.05	3813 ± 11	−0.19 ± 0.04	−0.12 ± 0.04	YD
J09511−123	3700 ± 200	4.72 ± 0.20	3769 ± 13	4.84 ± 0.07	−0.34 ± 0.03	−0.23 ± 0.03	3778 ± 11	−0.37 ± 0.03	−0.25 ± 0.03	TD
J10088+692	3900 ± 200	4.63 ± 0.20	3952 ± 15	4.94 ± 0.08	−0.03 ± 0.04	−0.01 ± 0.04	3925 ± 15	−0.21 ± 0.03	−0.14 ± 0.03	D
J12312+086	3900 ± 200	4.71 ± 0.20	3896 ± 11	5.07 ± 0.11	−0.15 ± 0.05	−0.09 ± 0.05	3898 ± 14	−0.35 ± 0.03	−0.23 ± 0.03	D
J13299+102	3700 ± 200	4.75 ± 0.20	3765 ± 18	4.95 ± 0.10	−0.19 ± 0.05	−0.12 ± 0.05	3773 ± 16	−0.29 ± 0.04	−0.20 ± 0.04	D

TABLE C.3. *continued*

Karmn	Prior $T_{\rm eff}$ [a] [K]	Prior $\log g$ [a] [dex]	$T_{\rm eff}$ [K]	$\log g$ [dex]	[Fe/H] [dex]	[Fe/H]$_{\rm corr}$ [dex]	$T_{\rm eff, fixed}$ [K]	[Fe/H]$_{\rm fixed}$ [dex]	[Fe/H]$_{\rm corr, fixed}$ [dex]	Pop. [b]
J14257+236E	3800 ± 200	4.65 ± 0.20	3933 ± 12	4.71 ± 0.11	0.09 ± 0.04	0.09 ± 0.04	3873 ± 12	−0.08 ± 0.04	−0.04 ± 0.04	TD-D
J14307−086	4000 ± 200	4.64 ± 0.20	4037 ± 13	4.82 ± 0.07	0.01 ± 0.03	0.01 ± 0.03	4029 ± 12	−0.01 ± 0.02	0.00 ± 0.02	TD-D
J17355+616	3700 ± 200	4.68 ± 0.20	3847 ± 13	5.02 ± 0.11	−0.06 ± 0.06	−0.03 ± 0.06	3856 ± 11	−0.22 ± 0.03	−0.15 ± 0.03	D
J18353+457	3800 ± 200	4.66 ± 0.20	3876 ± 11	4.82 ± 0.09	−0.08 ± 0.08	−0.04 ± 0.08	3864 ± 8	−0.28 ± 0.02	−0.19 ± 0.02	D
J18580+059	3800 ± 200	4.68 ± 0.20	3857 ± 10	4.73 ± 0.09	−0.22 ± 0.05	−0.15 ± 0.05	3858 ± 7	−0.24 ± 0.02	−0.16 ± 0.02	D
J22021+014	3800 ± 200	4.68 ± 0.20	3882 ± 12	4.97 ± 0.07	−0.02 ± 0.04	0.00 ± 0.04	3869 ± 10	−0.29 ± 0.03	−0.20 ± 0.03	D
J22503−070	3800 ± 200	4.70 ± 0.20	3900 ± 10	5.01 ± 0.09	−0.13 ± 0.04	−0.08 ± 0.04	3904 ± 11	−0.34 ± 0.02	−0.23 ± 0.02	D
M1.0 V										
J00051+457	3600 ± 200	4.71 ± 0.20	3773 ± 16	5.07 ± 0.08	−0.07 ± 0.05	−0.04 ± 0.05	3770 ± 17	−0.23 ± 0.03	−0.15 ± 0.03	YD
J00183+440	3500 ± 200	4.79 ± 0.20	3603 ± 24	4.99 ± 0.14	−0.75 ± 0.11	−0.52 ± 0.11	3603 ± 23	−0.72 ± 0.07	−0.49 ± 0.10	D
J02565+554W	3700 ± 200	4.63 ± 0.20	3832 ± 10	4.65 ± 0.12	−0.07 ± 0.04	−0.04 ± 0.04	3830 ± 10	−0.09 ± 0.02	−0.05 ± 0.02	D
J05415+534	3800 ± 200	4.71 ± 0.20	3825 ± 14	4.94 ± 0.10	−0.04 ± 0.06	−0.02 ± 0.06	3829 ± 14	−0.20 ± 0.04	−0.13 ± 0.04	YD
J07361−031	3700 ± 200	4.70 ± 0.20	3825 ± 12	5.06 ± 0.08	−0.07 ± 0.05	−0.04 ± 0.05	3841 ± 9	−0.30 ± 0.03	−0.20 ± 0.03	D
J10023+480	3700 ± 200	4.67 ± 0.20	3739 ± 15	4.76 ± 0.08	−0.21 ± 0.04	−0.14 ± 0.04	3744 ± 13	−0.26 ± 0.02	−0.18 ± 0.02	TD
J10251−102	3700 ± 200	4.73 ± 0.20	3759 ± 14	4.91 ± 0.07	−0.02 ± 0.04	0.00 ± 0.04	3763 ± 15	−0.13 ± 0.02	−0.08 ± 0.02	YD
J11054+435	3400 ± 200	4.83 ± 0.20	3628 ± 19	5.01 ± 0.13	−0.82 ± 0.09	−0.56 ± 0.09	3715 ± 15	−0.52 ± 0.04	−0.36 ± 0.04	TD-D
J13209+342	3700 ± 200	4.71 ± 0.20	3720 ± 13	4.76 ± 0.09	−0.22 ± 0.04	−0.15 ± 0.04	3732 ± 11	−0.28 ± 0.03	−0.19 ± 0.03	D
J14010−026	3700 ± 200	4.74 ± 0.20	3719 ± 15	4.89 ± 0.09	−0.24 ± 0.04	−0.16 ± 0.04	3726 ± 13	−0.32 ± 0.03	−0.21 ± 0.03	D
J14082+805	3700 ± 200	4.65 ± 0.20	3803 ± 12	4.80 ± 0.09	−0.04 ± 0.05	−0.02 ± 0.05	3805 ± 12	−0.11 ± 0.03	−0.06 ± 0.03	D
J15598−082	3600 ± 200	4.75 ± 0.20	3707 ± 14	5.05 ± 0.07	−0.04 ± 0.04	−0.02 ± 0.04	3731 ± 17	−0.25 ± 0.04	−0.17 ± 0.04	D
J16581+257	3600 ± 200	4.71 ± 0.20	3782 ± 17	4.87 ± 0.09	−0.09 ± 0.05	−0.05 ± 0.05	3785 ± 14	−0.20 ± 0.04	−0.13 ± 0.04	D
J17378+185	3700 ± 200	4.82 ± 0.20	3663 ± 19	5.03 ± 0.12	−0.58 ± 0.07	−0.40 ± 0.07	3710 ± 15	−0.48 ± 0.05	−0.33 ± 0.05	D
J18051−030	3700 ± 200	4.80 ± 0.20	3706 ± 13	5.14 ± 0.10	−0.30 ± 0.06	−0.20 ± 0.07	3709 ± 15	−0.41 ± 0.04	−0.28 ± 0.04	D
J18409−133	3700 ± 200	4.70 ± 0.20	3799 ± 12	4.88 ± 0.08	−0.04 ± 0.05	−0.02 ± 0.05	3801 ± 12	−0.14 ± 0.04	−0.08 ± 0.04	D
J20451−313	3600 ± 200	4.54 ± 0.20	3768 ± 20	4.65 ± 0.18	0.01 ± 0.06	0.01 ± 0.06	3799 ± 13	−0.17 ± 0.03	−0.11 ± 0.03	YD
J20533+621	3700 ± 200	4.70 ± 0.20	3815 ± 16	4.83 ± 0.14	−0.16 ± 0.08	−0.10 ± 0.08	3814 ± 15	−0.24 ± 0.04	−0.16 ± 0.04	D
J21221+229	3700 ± 200	4.75 ± 0.20	3761 ± 17	5.00 ± 0.10	−0.27 ± 0.05	−0.18 ± 0.08	3776 ± 14	−0.36 ± 0.05	−0.24 ± 0.05	D.
J22330+093	3700 ± 200	4.78 ± 0.20	3722 ± 16	4.98 ± 0.11	−0.30 ± 0.05	−0.20 ± 0.05	3721 ± 14	−0.41 ± 0.04	−0.28 ± 0.04	YD
J22559+178	3700 ± 200	4.69 ± 0.20	3814 ± 12	4.90 ± 0.08	0.02 ± 0.03	0.02 ± 0.03	3813 ± 9	−0.18 ± 0.03	−0.11 ± 0.03	D
J23245+578	3600 ± 200	4.66 ± 0.20	3811 ± 13	4.72 ± 0.10	−0.03 ± 0.06	−0.01 ± 0.06	3810 ± 12	−0.13 ± 0.04	−0.08 ± 0.04	D
J23492+024	3700 ± 200	4.84 ± 0.20	3573 ± 23	4.94 ± 0.13	−0.80 ± 0.08	−0.55 ± 0.08	3562 ± 21	−0.85 ± 0.06	−0.58 ± 0.06	TD

TABLE C.3. *continued*

Karmn	Prior $T_{\rm eff}$ [a] [K]	Prior $\log g$ [a] [dex]	$T_{\rm eff}$ [K]	$\log g$ [dex]	[Fe/H] [dex]	[Fe/H]$_{\rm corr}$ [dex]	$T_{\rm eff, fixed}$ [K]	[Fe/H]$_{\rm fixed}$ [dex]	[Fe/H]$_{\rm corr, fixed}$ [dex]	Pop. [b]
M1.5 V										
J01026+623	3600 ± 200	4.69 ± 0.20	3791 ± 19	4.76 ± 0.11	0.05 ± 0.06	0.05 ± 0.06	3782 ± 18	−0.08 ± 0.04	−0.04 ± 0.04	YD
J02123+035	3700 ± 200	4.81 ± 0.20	3575 ± 14	4.86 ± 0.09	−0.72 ± 0.06	−0.49 ± 0.06	3571 ± 14	−0.75 ± 0.04	−0.52 ± 0.04	TD
J03181+382	3600 ± 200	4.63 ± 0.20	3826 ± 15	4.61 ± 0.14	−0.02 ± 0.05	0.00 ± 0.05	3825 ± 14	−0.01 ± 0.03	0.00 ± 0.03	D
J04376−110	3600 ± 200	4.78 ± 0.20	3666 ± 16	5.08 ± 0.12	−0.08 ± 0.06	−0.04 ± 0.06	3682 ± 17	−0.25 ± 0.04	−0.17 ± 0.04	D
J05314−036	3700 ± 200	4.66 ± 0.20	3850 ± 27	4.71 ± 0.18	0.05 ± 0.08	0.05 ± 0.08	3833 ± 17	0.02 ± 0.04	0.02 ± 0.04	D
J09163−186	3600 ± 200	4.78 ± 0.20	3697 ± 14	5.11 ± 0.16	−0.06 ± 0.06	−0.03 ± 0.06	3700 ± 13	−0.19 ± 0.04	−0.12 ± 0.04	YD
J09411+132	3600 ± 200	4.77 ± 0.20	3699 ± 15	5.01 ± 0.10	−0.03 ± 0.04	−0.01 ± 0.04	3688 ± 20	−0.20 ± 0.04	−0.13 ± 0.04	YD
J09468+760	3700 ± 200	4.75 ± 0.20	3616 ± 17	4.93 ± 0.10	−0.47 ± 0.04	−0.32 ± 0.04	3601 ± 14	−0.55 ± 0.05	−0.38 ± 0.05	TD
J10122−037	3600 ± 200	4.72 ± 0.20	3720 ± 20	4.98 ± 0.10	0.00 ± 0.05	0.00 ± 0.05	3714 ± 21	−0.12 ± 0.03	−0.07 ± 0.03	YD
J11033+359	3500 ± 200	4.86 ± 0.20	3557 ± 26	4.95 ± 0.14	−0.72 ± 0.10	−0.49 ± 0.10	3537 ± 26	−0.76 ± 0.06	−0.52 ± 0.06	TD
J11126+189	3600 ± 200	4.70 ± 0.20	3752 ± 14	4.88 ± 0.07	−0.02 ± 0.03	0.00 ± 0.03	3759 ± 15	−0.13 ± 0.02	−0.08 ± 0.02	D
J11511+352	3600 ± 200	4.78 ± 0.20	3692 ± 21	4.91 ± 0.15	−0.38 ± 0.08	−0.25 ± 0.08	3703 ± 18	−0.34 ± 0.05	−0.23 ± 0.05	D
J13196+333	3600 ± 200	4.66 ± 0.20	3799 ± 11	4.67 ± 0.11	−0.02 ± 0.04	0.00 ± 0.04	3799 ± 11	−0.03 ± 0.03	−0.01 ± 0.03	YD
J13457+148	3600 ± 200	4.74 ± 0.20	3620 ± 24	4.93 ± 0.12	−0.49 ± 0.07	−0.34 ± 0.07	3591 ± 17	−0.69 ± 0.05	−0.47 ± 0.05	D
J15218+209	3500 ± 200	4.67 ± 0.20	3611 ± 16	4.81 ± 0.11	−0.24 ± 0.09	−0.16 ± 0.09	3697 ± 9	−0.35 ± 0.03	−0.23 ± 0.03	D
J16254+543	3600 ± 200	4.94 ± 0.20	3595 ± 19	5.09 ± 0.13	−0.42 ± 0.07	−0.28 ± 0.07	3573 ± 20	−0.67 ± 0.06	−0.46 ± 0.06	YD
J17052−050	3500 ± 200	4.74 ± 0.20	3587 ± 14	4.89 ± 0.10	−0.57 ± 0.07	−0.39 ± 0.07	3583 ± 13	−0.60 ± 0.05	−0.41 ± 0.05	TD-D
J20450+444	3600 ± 200	4.83 ± 0.20	3600 ± 16	4.98 ± 0.12	−0.42 ± 0.07	−0.28 ± 0.07	3603 ± 18	−0.48 ± 0.06	−0.33 ± 0.06	YD
J22057+656	3700 ± 200	4.77 ± 0.20	3707 ± 17	4.86 ± 0.11	−0.30 ± 0.06	−0.20 ± 0.06	3715 ± 19	−0.32 ± 0.04	−0.21 ± 0.04	D
J22565+165	3600 ± 200	4.68 ± 0.20	3798 ± 21	4.80 ± 0.12	0.03 ± 0.06	0.03 ± 0.06	3799 ± 19	−0.07 ± 0.04	−0.04 ± 0.04	D
M2.0 V										
J00403+612	3700 ± 200	4.77 ± 0.20	3709 ± 11	5.01 ± 0.09	−0.02 ± 0.03	0.00 ± 0.03	3715 ± 10	−0.18 ± 0.03	−0.11 ± 0.03	YD
J01013+613	3500 ± 200	4.84 ± 0.20	3564 ± 19	5.05 ± 0.08	−0.24 ± 0.07	−0.16 ± 0.07	3545 ± 10	−0.24 ± 0.04	−0.16 ± 0.04	D
J01433+043	3500 ± 200	4.83 ± 0.20	3547 ± 20	5.10 ± 0.17	−0.15 ± 0.07	−0.09 ± 0.07	3539 ± 13	−0.22 ± 0.04	−0.15 ± 0.04	D
J02358+202	3500 ± 200	4.70 ± 0.20	3703 ± 15	4.86 ± 0.09	−0.04 ± 0.04	−0.02 ± 0.04	3696 ± 16	−0.14 ± 0.03	−0.08 ± 0.03	YD
J02489−145W	3500 ± 200	4.74 ± 0.20	3655 ± 25	4.98 ± 0.10	0.04 ± 0.05	0.04 ± 0.05	3674 ± 20	−0.13 ± 0.04	−0.08 ± 0.04	YD
J03213+799	3500 ± 200	4.81 ± 0.20	3599 ± 14	5.12 ± 0.10	−0.32 ± 0.07	−0.21 ± 0.08	3580 ± 13	−0.41 ± 0.05	−0.28 ± 0.05	D
J03217−066	3600 ± 200	4.77 ± 0.20	3661 ± 17	5.16 ± 0.08	0.01 ± 0.04	0.01 ± 0.04	3683 ± 18	−0.19 ± 0.04	−0.12 ± 0.04	YD
J04343+430	3400 ± 200	4.74 ± 0.20	3525 ± 25	4.86 ± 0.11	−0.14 ± 0.09	−0.08 ± 0.09	3533 ± 22	−0.19 ± 0.06	−0.12 ± 0.06	D
J04429+189	3500 ± 200	4.73 ± 0.20	3678 ± 16	5.13 ± 0.08	−0.01 ± 0.03	0.00 ± 0.03	3667 ± 16	−0.18 ± 0.03	−0.11 ± 0.03	D

TABLE C.3. *continued*

Karmn	Prior $T_{\rm eff}$ [a] [K]	Prior $\log g$ [a] [dex]	$T_{\rm eff}$ [K]	$\log g$ [dex]	[Fe/H] [dex]	[Fe/H]$_{\rm corr}$ [dex]	$T_{\rm eff, fixed}$ [K]	[Fe/H]$_{\rm fixed}$ [dex]	[Fe/H]$_{\rm corr, fixed}$ [dex]	Pop. [b]
J04538−177	3500 ± 200	4.81 ± 0.20	3582 ± 17	5.04 ± 0.11	−0.47 ± 0.08	−0.32 ± 0.08	3569 ± 16	−0.62 ± 0.06	−0.42 ± 0.06	D
J05127+196	3500 ± 200	4.78 ± 0.20	3599 ± 13	4.91 ± 0.11	−0.48 ± 0.07	−0.33 ± 0.07	3697 ± 14	−0.22 ± 0.03	−0.15 ± 0.03	D
J06103+821	3500 ± 200	4.81 ± 0.20	3554 ± 20	4.95 ± 0.13	−0.24 ± 0.07	−0.16 ± 0.07	3547 ± 13	−0.24 ± 0.05	−0.16 ± 0.05	D
J07353+548	3500 ± 200	4.86 ± 0.20	3564 ± 17	5.03 ± 0.11	−0.42 ± 0.07	−0.28 ± 0.07	3572 ± 13	−0.42 ± 0.05	−0.28 ± 0.05	YD
J08161+013	3600 ± 200	4.81 ± 0.20	3570 ± 18	4.98 ± 0.14	−0.25 ± 0.07	−0.17 ± 0.07	3564 ± 14	−0.30 ± 0.06	−0.20 ± 0.06	D
J09425+700	3400 ± 200	4.71 ± 0.20	3547 ± 23	5.02 ± 0.12	0.00 ± 0.03	0.00 ± 0.03	3556 ± 18	−0.29 ± 0.06	−0.20 ± 0.06	YD
J10289+008	3600 ± 200	4.82 ± 0.20	3588 ± 24	5.15 ± 0.15	−0.22 ± 0.08	−0.15 ± 0.08	3578 ± 17	−0.39 ± 0.06	−0.26 ± 0.06	YD
J11026+219	3700 ± 200	4.68 ± 0.20	3846 ± 84	4.72 ± 0.23	−0.30 ± 0.14	−0.20 ± 0.14	3833 ± 8	−0.40 ± 0.03	−0.27 ± 0.03	D
J11110+304W	3600 ± 200	4.68 ± 0.20	3730 ± 20	4.78 ± 0.13	−0.09 ± 0.07	−0.05 ± 0.07	3730 ± 22	−0.13 ± 0.04	−0.08 ± 0.04	D
J11201−104	3600 ± 200	4.72 ± 0.20	3697 ± 9	4.66 ± 0.07	−0.39 ± 0.06	−0.26 ± 0.06	3697 ± 9	−0.36 ± 0.04	−0.24 ± 0.04	YD
J12248−182	3500 ± 200	5.00 ± 0.20	3432 ± 30	5.09 ± 0.10	−0.88 ± 0.09	−0.60 ± 0.09	3414 ± 17	−0.93 ± 0.05	−0.63 ± 0.05	TD
J13119+658	3600 ± 200	4.80 ± 0.20	3686 ± 16	4.83 ± 0.07	−0.43 ± 0.05	−0.29 ± 0.05	3672 ± 35	−0.36 ± 0.09	−0.24 ± 0.09	D
J14294+155	3500 ± 200	4.70 ± 0.20	3660 ± 17	4.75 ± 0.09	−0.24 ± 0.06	−0.16 ± 0.06	3687 ± 14	−0.18 ± 0.03	−0.11 ± 0.03	TD
J14524+123	3500 ± 200	4.70 ± 0.20	3703 ± 21	4.88 ± 0.13	0.04 ± 0.07	0.04 ± 0.07	3689 ± 15	−0.04 ± 0.03	−0.02 ± 0.03	D
J15474−108	3500 ± 200	4.76 ± 0.20	3481 ± 29	5.00 ± 0.14	−0.70 ± 0.11	−0.48 ± 0.11	3459 ± 21	−0.84 ± 0.06	−0.57 ± 0.06	D
J17166+080	3500 ± 200	4.82 ± 0.20	3567 ± 19	4.89 ± 0.11	−0.38 ± 0.09	−0.25 ± 0.09	3573 ± 16	−0.37 ± 0.07	−0.25 ± 0.07	YD
J18174+483	3500 ± 200	4.68 ± 0.20	3605 ± 29	4.87 ± 0.17	−0.47 ± 0.11	−0.32 ± 0.11	3633 ± 41	−0.46 ± 0.12	−0.31 ± 0.12	YD
J19070+208	3600 ± 200	4.94 ± 0.20	3543 ± 21	5.03 ± 0.12	−0.68 ± 0.07	−0.46 ± 0.07	3538 ± 20	−0.75 ± 0.06	−0.52 ± 0.06	D
J19072+208	3600 ± 200	4.94 ± 0.20	3558 ± 19	5.06 ± 0.10	−0.67 ± 0.06	−0.46 ± 0.06	3548 ± 19	−0.75 ± 0.05	−0.52 ± 0.05	D
J22115+184	3500 ± 200	4.69 ± 0.20	3704 ± 20	4.77 ± 0.12	−0.01 ± 0.06	0.00 ± 0.06	3696 ± 20	−0.05 ± 0.03	−0.02 ± 0.03	D
J23381−162	3500 ± 200	4.85 ± 0.20	3570 ± 22	5.07 ± 0.12	−0.51 ± 0.08	−0.35 ± 0.08	3557 ± 21	−0.63 ± 0.06	−0.43 ± 0.06	D
M2.5 V										
J00389+306	3500 ± 200	4.81 ± 0.20	3551 ± 17	4.90 ± 0.11	−0.24 ± 0.07	−0.16 ± 0.07	3563 ± 15	−0.28 ± 0.06	−0.19 ± 0.06	D
J01518+644	3500 ± 200	4.75 ± 0.20	3625 ± 21	5.04 ± 0.10	−0.03 ± 0.05	−0.01 ± 0.05	3611 ± 20	−0.14 ± 0.05	−0.08 ± 0.05	YD
J02489−145E	3500 ± 200	4.79 ± 0.20	3572 ± 27	4.94 ± 0.12	0.00 ± 0.04	0.00 ± 0.04	3549 ± 24	−0.10 ± 0.03	−0.06 ± 0.03	YD
J05337+019	3400 ± 200	4.80 ± 0.20	3428 ± 32	4.98 ± 0.10	−0.10 ± 0.07	−0.06 ± 0.07	3440 ± 29	−0.16 ± 0.05	−0.10 ± 0.05	YD
J08293+039	3500 ± 200	4.73 ± 0.20	3651 ± 17	4.97 ± 0.13	−0.06 ± 0.06	−0.03 ± 0.06	3658 ± 13	−0.19 ± 0.04	−0.12 ± 0.04	YD
J08358+680	3400 ± 200	4.85 ± 0.20	3496 ± 16	5.11 ± 0.10	−0.07 ± 0.05	−0.04 ± 0.05	3480 ± 20	−0.16 ± 0.04	−0.10 ± 0.04	D
J09133+688	3500 ± 200	4.65 ± 0.20	3662 ± 26	4.67 ± 0.12	−0.38 ± 0.09	−0.25 ± 0.09	3653 ± 23	−0.35 ± 0.06	−0.23 ± 0.06	YD
J09360−216	3400 ± 200	4.87 ± 0.20	3496 ± 20	4.95 ± 0.11	−0.35 ± 0.07	−0.23 ± 0.07	3485 ± 19	−0.40 ± 0.04	−0.27 ± 0.04	D
J10396−069	3400 ± 200	4.73 ± 0.20	3592 ± 19	4.89 ± 0.11	−0.14 ± 0.07	−0.08 ± 0.07	3581 ± 17	−0.20 ± 0.03	−0.13 ± 0.03	YD

TABLE C.3. *continued*

Karmn	Prior $T_{\rm eff}$ [a] [K]	Prior $\log g$ [a] [dex]	$T_{\rm eff}$ [K]	$\log g$ [dex]	[Fe/H] [dex]	[Fe/H]$_{\rm corr}$ [dex]	$T_{\rm eff, fixed}$ [K]	[Fe/H]$_{\rm fixed}$ [dex]	[Fe/H]$_{\rm corr, fixed}$ [dex]	Pop. [b]
J11000+228	3400 ± 200	4.83 ± 0.20	3532 ± 21	5.04 ± 0.14	−0.12 ± 0.07	−0.07 ± 0.07	3521 ± 20	−0.18 ± 0.04	−0.11 ± 0.04	YD
J11302+076	3400 ± 200	4.76 ± 0.20	3563 ± 25	4.93 ± 0.10	−0.13 ± 0.10	−0.08 ± 0.10	3565 ± 23	−0.19 ± 0.05	−0.12 ± 0.05	D
J11421+267	3400 ± 200	4.79 ± 0.20	3533 ± 26	4.83 ± 0.11	−0.19 ± 0.10	−0.12 ± 0.10	3507 ± 22	−0.22 ± 0.08	−0.15 ± 0.08	D
J12350+098	3500 ± 200	4.74 ± 0.20	3556 ± 16	4.82 ± 0.07	−0.28 ± 0.07	−0.19 ± 0.07	3536 ± 18	−0.31 ± 0.05	−0.21 ± 0.05	D
J14251+518	3400 ± 200	4.80 ± 0.20	3551 ± 22	4.90 ± 0.10	−0.21 ± 0.06	−0.14 ± 0.06	3550 ± 12	−0.25 ± 0.04	−0.17 ± 0.04	D
J16462+164	3400 ± 200	4.78 ± 0.20	3560 ± 21	4.90 ± 0.10	−0.15 ± 0.07	−0.09 ± 0.07	3547 ± 15	−0.20 ± 0.04	−0.13 ± 0.04	D
J17198+417	3400 ± 200	4.84 ± 0.20	3540 ± 20	4.96 ± 0.12	−0.30 ± 0.07	−0.20 ± 0.07	3540 ± 16	−0.28 ± 0.06	−0.19 ± 0.06	D
J17578+465	3300 ± 200	4.79 ± 0.20	3507 ± 23	4.93 ± 0.09	−0.04 ± 0.06	−0.02 ± 0.06	3509 ± 18	−0.11 ± 0.05	−0.06 ± 0.05	YD
J18480−145	3400 ± 200	4.83 ± 0.20	3540 ± 29	4.92 ± 0.11	−0.20 ± 0.06	−0.13 ± 0.06	3544 ± 15	−0.23 ± 0.05	−0.15 ± 0.05	D
J19169+051N	3400 ± 200	4.72 ± 0.20	3575 ± 25	4.88 ± 0.12	−0.14 ± 0.08	−0.08 ± 0.08	3597 ± 28	−0.22 ± 0.06	−0.15 ± 0.06	D
J20305+654	3400 ± 200	4.83 ± 0.20	3514 ± 23	5.06 ± 0.11	−0.06 ± 0.06	−0.03 ± 0.06	3525 ± 13	−0.15 ± 0.04	−0.09 ± 0.04	D
J20567−104	3300 ± 200	4.70 ± 0.20	3560 ± 27	4.91 ± 0.09	−0.07 ± 0.06	−0.04 ± 0.06	3547 ± 16	−0.21 ± 0.04	−0.14 ± 0.04	TD
J21019−063	3400 ± 200	4.74 ± 0.20	3568 ± 20	4.95 ± 0.10	−0.07 ± 0.06	−0.04 ± 0.06	3554 ± 18	−0.21 ± 0.04	−0.14 ± 0.04	D
J23340+001	3400 ± 200	4.77 ± 0.20	3530 ± 21	4.91 ± 0.09	−0.38 ± 0.08	−0.25 ± 0.08	3548 ± 15	−0.30 ± 0.04	−0.20 ± 0.04	D
J23556−061	3400 ± 200	4.80 ± 0.20	3639 ± 30	4.84 ± 0.14	−0.04 ± 0.08	−0.02 ± 0.08	3643 ± 23	−0.04 ± 0.05	−0.02 ± 0.05	D
M3.0 V										
J00570+450	3300 ± 200	4.86 ± 0.20	3488 ± 22	5.04 ± 0.10	−0.04 ± 0.05	−0.02 ± 0.05	3491 ± 21	−0.17 ± 0.06	−0.11 ± 0.06	YD
J01025+716	3400 ± 200	4.74 ± 0.20	3524 ± 26	4.86 ± 0.10	−0.08 ± 0.07	−0.04 ± 0.09	3516 ± 21	−0.14 ± 0.06	−0.08 ± 0.06	D
J01066+192	3400 ± 200	4.88 ± 0.20	3496 ± 25	5.00 ± 0.11	−0.08 ± 0.07	−0.04 ± 0.07	3495 ± 22	−0.09 ± 0.05	−0.05 ± 0.05	YD
J02015+637	3400 ± 200	4.77 ± 0.20	3579 ± 23	4.87 ± 0.11	−0.14 ± 0.08	−0.08 ± 0.08	3549 ± 22	−0.16 ± 0.05	−0.10 ± 0.05	D
J02442+255	3400 ± 200	4.86 ± 0.20	3510 ± 21	4.97 ± 0.11	−0.14 ± 0.08	−0.08 ± 0.08	3512 ± 20	−0.18 ± 0.06	−0.11 ± 0.06	YD
J03473−019	3400 ± 200	4.73 ± 0.20	3473 ± 72	4.85 ± 0.18	−0.26 ± 0.15	−0.18 ± 0.15	3437 ± 76	−0.26 ± 0.18	−0.18 ± 0.18	YD
J03531+625	3500 ± 200	4.88 ± 0.20	3501 ± 23	5.04 ± 0.11	−0.28 ± 0.10	−0.19 ± 0.10	3506 ± 22	−0.26 ± 0.09	−0.18 ± 0.09	TD
J05033−173	3300 ± 200	4.95 ± 0.20	3464 ± 27	5.08 ± 0.10	−0.20 ± 0.09	−0.13 ± 0.09	3475 ± 26	−0.16 ± 0.06	−0.10 ± 0.06	YD
J06548+332	3400 ± 200	4.87 ± 0.20	3503 ± 37	4.88 ± 0.12	−0.20 ± 0.12	−0.13 ± 0.12	3497 ± 33	−0.16 ± 0.09	−0.10 ± 0.09	YD
J07044+682	3400 ± 200	4.81 ± 0.20	3527 ± 21	4.82 ± 0.09	−0.16 ± 0.08	−0.10 ± 0.08	3527 ± 19	−0.18 ± 0.06	−0.11 ± 0.06	D
J07287−032	3300 ± 200	4.81 ± 0.20	3511 ± 21	4.82 ± 0.08	−0.20 ± 0.07	−0.13 ± 0.07	3519 ± 18	−0.22 ± 0.06	−0.15 ± 0.06	D
J07386−212	3300 ± 200	4.92 ± 0.20	3488 ± 24	4.95 ± 0.09	−0.16 ± 0.07	−0.10 ± 0.07	3490 ± 21	−0.14 ± 0.06	−0.08 ± 0.06	D
J09140+196	3400 ± 200	4.72 ± 0.20	3561 ± 19	5.04 ± 0.11	−0.04 ± 0.05	−0.02 ± 0.05	3553 ± 17	−0.24 ± 0.04	−0.16 ± 0.04	YD
J09428+700	3400 ± 200	4.79 ± 0.20	3504 ± 30	5.06 ± 0.12	0.02 ± 0.05	0.02 ± 0.05	3503 ± 20	−0.07 ± 0.05	−0.04 ± 0.05	YD
J10167−119	3500 ± 200	4.75 ± 0.20	3552 ± 20	4.84 ± 0.09	−0.10 ± 0.06	−0.06 ± 0.06	3539 ± 15	−0.17 ± 0.04	−0.11 ± 0.04	D

TABLE C.3. *continued*

Karmn	Prior $T_{\rm eff}$ [a] [K]	Prior $\log g$ [a] [dex]	$T_{\rm eff}$ [K]	$\log g$ [dex]	[Fe/H] [dex]	[Fe/H]$_{\rm corr}$ [dex]	$T_{\rm eff, fixed}$ [K]	[Fe/H]$_{\rm fixed}$ [dex]	[Fe/H]$_{\rm corr, fixed}$ [dex]	Pop. [b]
J10196+198	3300 ± 200	4.77 ± 0.20	3477 ± 23	5.12 ± 0.12	−0.28 ± 0.12	−0.19 ± 0.12	3449 ± 54	−0.61 ± 0.24	−0.41 ± 0.24	YD
J10350−094	3300 ± 200	4.81 ± 0.20	3512 ± 20	4.85 ± 0.08	−0.15 ± 0.08	−0.09 ± 0.08	3514 ± 20	−0.16 ± 0.06	−0.10 ± 0.06	D
J11044+304	3200 ± 200	4.83 ± 0.20	3534 ± 97	4.84 ± 0.21	−0.72 ± 0.17	−0.49 ± 0.17	3513 ± 91	−0.76 ± 0.12	−0.52 ± 0.12	YD
J11467−140	3400 ± 200	4.69 ± 0.20	3565 ± 20	4.77 ± 0.11	−0.01 ± 0.05	0.00 ± 0.05	3597 ± 16	−0.03 ± 0.03	−0.01 ± 0.03	D
J12111−199	3400 ± 200	4.86 ± 0.20	3517 ± 18	4.92 ± 0.09	−0.19 ± 0.06	−0.12 ± 0.06	3522 ± 16	−0.19 ± 0.05	−0.12 ± 0.05	YD
J12230+640	3500 ± 200	4.74 ± 0.20	3563 ± 28	4.80 ± 0.13	−0.24 ± 0.10	−0.16 ± 0.10	3562 ± 28	−0.27 ± 0.07	−0.18 ± 0.07	D
J12388+116	3300 ± 200	4.73 ± 0.20	3525 ± 26	4.85 ± 0.09	−0.01 ± 0.06	0.00 ± 0.06	3521 ± 21	−0.06 ± 0.04	−0.03 ± 0.04	D
J13283−023W	3400 ± 200	4.77 ± 0.20	3554 ± 28	4.86 ± 0.13	−0.12 ± 0.09	−0.07 ± 0.09	3535 ± 16	−0.13 ± 0.04	−0.08 ± 0.04	D
J13582+125	3300 ± 200	5.03 ± 0.20	3442 ± 27	5.13 ± 0.13	−0.14 ± 0.09	−0.08 ± 0.09	3461 ± 29	−0.08 ± 0.06	−0.04 ± 0.06	D
J14152+450	3400 ± 200	4.77 ± 0.20	3516 ± 16	4.85 ± 0.06	−0.07 ± 0.05	−0.04 ± 0.05	3515 ± 13	−0.13 ± 0.04	−0.08 ± 0.04	D
J15013+055	3300 ± 200	4.85 ± 0.20	3502 ± 22	4.98 ± 0.09	−0.05 ± 0.05	−0.02 ± 0.05	3503 ± 18	−0.10 ± 0.04	−0.06 ± 0.04	D
J15095+031	3400 ± 200	4.78 ± 0.20	3545 ± 17	4.86 ± 0.09	−0.14 ± 0.07	−0.08 ± 0.07	3544 ± 16	−0.19 ± 0.04	−0.12 ± 0.04	D
J15194−077	3300 ± 200	4.90 ± 0.20	3500 ± 26	4.97 ± 0.11	−0.14 ± 0.07	−0.08 ± 0.07	3495 ± 26	−0.17 ± 0.08	−0.11 ± 0.08	YD
J16092+093	3300 ± 200	4.82 ± 0.20	3517 ± 18	5.06 ± 0.10	−0.03 ± 0.04	−0.01 ± 0.04	3525 ± 11	−0.14 ± 0.03	−0.08 ± 0.03	D
J16102−193	3100 ± 200	4.41 ± 0.20	3575 ± 55	4.48 ± 0.19	−0.04 ± 0.07	−0.02 ± 0.07	3552 ± 46	−0.02 ± 0.06	0.00 ± 0.06	YD
J16167+672N	3400 ± 200	4.74 ± 0.20	3569 ± 32	4.97 ± 0.11	−0.04 ± 0.06	−0.02 ± 0.06	3532 ± 32	−0.08 ± 0.05	−0.04 ± 0.05	YD
J16327+126	3500 ± 200	4.84 ± 0.20	3486 ± 21	4.92 ± 0.09	−0.28 ± 0.07	−0.19 ± 0.07	3492 ± 18	−0.26 ± 0.06	−0.18 ± 0.06	TD-D
J17071+215	3400 ± 200	4.82 ± 0.20	3534 ± 30	4.94 ± 0.13	−0.22 ± 0.11	−0.15 ± 0.11	3545 ± 16	−0.21 ± 0.05	−0.14 ± 0.05	D
J17364+683	3300 ± 200	4.84 ± 0.20	3389 ± 81	4.89 ± 0.15	−0.10 ± 0.13	−0.06 ± 0.13	3385 ± 79	−0.14 ± 0.12	−0.08 ± 0.12	D
J18180+387E	3200 ± 200	4.87 ± 0.20	3495 ± 20	5.01 ± 0.10	−0.21 ± 0.07	−0.14 ± 0.07	3430 ± 47	−0.62 ± 0.19	−0.42 ± 0.19	D
J18419+318	3300 ± 200	4.84 ± 0.20	3519 ± 20	4.93 ± 0.10	−0.30 ± 0.08	−0.20 ± 0.08	3521 ± 16	−0.23 ± 0.06	−0.15 ± 0.06	D
J18427+596N	3300 ± 200	4.84 ± 0.20	3473 ± 34	4.90 ± 0.11	−0.46 ± 0.12	−0.31 ± 0.12	3466 ± 31	−0.44 ± 0.13	−0.30 ± 0.13	D
J19084+322	3300 ± 200	4.85 ± 0.20	3501 ± 25	4.92 ± 0.09	−0.13 ± 0.07	−0.08 ± 0.07	3503 ± 21	−0.17 ± 0.06	−0.11 ± 0.06	YD
J19251+283	3300 ± 200	4.84 ± 0.20	3472 ± 29	4.90 ± 0.08	−0.09 ± 0.07	−0.05 ± 0.07	3476 ± 26	−0.10 ± 0.05	−0.06 ± 0.05	D
J21152+257	3400 ± 200	4.65 ± 0.20	3611 ± 25	4.67 ± 0.16	0.05 ± 0.05	0.05 ± 0.05	3682 ± 18	0.08 ± 0.03	0.08 ± 0.03	D
J21164+025	3400 ± 200	4.79 ± 0.20	3550 ± 23	4.88 ± 0.11	−0.13 ± 0.09	−0.08 ± 0.09	3533 ± 21	−0.17 ± 0.06	−0.11 ± 0.06	YD
J21348+515	3400 ± 200	4.76 ± 0.20	3525 ± 23	4.87 ± 0.10	−0.15 ± 0.08	−0.09 ± 0.08	3528 ± 19	−0.22 ± 0.05	−0.15 ± 0.05	YD
J22125+085	3400 ± 200	4.84 ± 0.20	3528 ± 25	4.90 ± 0.13	−0.30 ± 0.09	−0.20 ± 0.09	3534 ± 23	−0.26 ± 0.07	−0.18 ± 0.07	D
J22518+317	3300 ± 200	4.74 ± 0.20	3335 ± 44	4.68 ± 0.14	−0.45 ± 0.18	−0.31 ± 0.18	3407 ± 20	−0.34 ± 0.13	−0.23 ± 0.13	YD
J23585+076	3300 ± 200	4.84 ± 0.20	3496 ± 20	4.97 ± 0.08	−0.10 ± 0.06	−0.06 ± 0.06	3496 ± 19	−0.16 ± 0.04	−0.10 ± 0.04	D

TABLE C.3. *continued*

Karmn	Prior $T_{\rm eff}$ [a] [K]	Prior $\log g$ [a] [dex]	$T_{\rm eff}$ [K]	$\log g$ [dex]	[Fe/H] [dex]	[Fe/H]$_{\rm corr}$ [dex]	$T_{\rm eff,fixed}$ [K]	[Fe/H]$_{\rm fixed}$ [dex]	[Fe/H]$_{\rm corr,fixed}$ [dex]	Pop. [b]
					M3.5 V					
J00184+440	3200 ± 200	5.12 ± 0.20	3318 ± 53	5.20 ± 0.11	−0.53 ± 0.17	−0.36 ± 0.17	3302 ± 61	−0.55 ± 0.25	−0.38 ± 0.25	D
J02002+130	3100 ± 200	5.16 ± 0.20	3237 ± 32	5.22 ± 0.14	−0.38 ± 0.14	−0.25 ± 0.14	3210 ± 27	−0.51 ± 0.28	−0.35 ± 0.28	D
J02070+496	3400 ± 200	4.90 ± 0.20	3455 ± 22	5.16 ± 0.13	−0.12 ± 0.06	−0.07 ± 0.06	3471 ± 22	−0.10 ± 0.03	−0.06 ± 0.03	YD
J02088+494	3300 ± 200	4.83 ± 0.20	3266 ± 36	4.88 ± 0.14	−0.24 ± 0.19	−0.16 ± 0.19	3270 ± 37	−0.14 ± 0.18	−0.08 ± 0.18	YD
J04225+105	3300 ± 200	4.75 ± 0.20	3546 ± 25	4.71 ± 0.10	−0.10 ± 0.07	−0.06 ± 0.07	3536 ± 24	−0.07 ± 0.04	−0.04 ± 0.04	YD
J04429+214	3400 ± 200	4.85 ± 0.20	3499 ± 24	4.90 ± 0.08	−0.02 ± 0.04	0.00 ± 0.04	3495 ± 20	−0.02 ± 0.03	0.00 ± 0.03	D
J04520+064	3200 ± 200	4.82 ± 0.20	3439 ± 30	4.83 ± 0.08	−0.13 ± 0.06	−0.08 ± 0.06	3447 ± 30	−0.10 ± 0.06	−0.06 ± 0.06	D
J05280+096	3300 ± 200	5.02 ± 0.20	3440 ± 27	5.05 ± 0.11	−0.24 ± 0.09	−0.16 ± 0.09	3438 ± 23	−0.23 ± 0.08	−0.15 ± 0.08	D
J05348+138	3300 ± 200	4.85 ± 0.20	3464 ± 28	4.85 ± 0.08	−0.12 ± 0.07	−0.07 ± 0.07	3463 ± 28	−0.12 ± 0.07	−0.07 ± 0.07	YD
J06011+595	3300 ± 200	4.98 ± 0.20	3431 ± 35	4.97 ± 0.12	−0.22 ± 0.13	−0.15 ± 0.13	3389 ± 40	−0.11 ± 0.09	−0.06 ± 0.09	YD
J06421+035	3300 ± 200	4.82 ± 0.20	3475 ± 27	4.88 ± 0.08	−0.13 ± 0.08	−0.08 ± 0.08	3485 ± 26	−0.15 ± 0.07	−0.09 ± 0.07	D
J07274+052	3200 ± 200	4.91 ± 0.20	3380 ± 43	4.96 ± 0.11	−0.17 ± 0.11	−0.11 ± 0.11	3382 ± 45	−0.19 ± 0.11	−0.12 ± 0.11	D
J07319+362N	3200 ± 200	4.79 ± 0.20	3289 ± 32	5.10 ± 0.13	−0.15 ± 0.09	−0.09 ± 0.09	3248 ± 19	−0.93 ± 0.05	−0.63 ± 0.05	YD
J07582+413	3200 ± 200	4.95 ± 0.20	3431 ± 28	4.87 ± 0.10	−0.22 ± 0.08	−0.15 ± 0.08	3438 ± 26	−0.23 ± 0.10	−0.15 ± 0.10	D
J08402+314	3300 ± 200	4.94 ± 0.20	3426 ± 23	4.88 ± 0.09	−0.20 ± 0.07	−0.13 ± 0.07	3428 ± 23	−0.15 ± 0.07	−0.09 ± 0.07	TD-D
J08409−234	3300 ± 200	4.78 ± 0.20	3496 ± 37	4.78 ± 0.09	−0.05 ± 0.08	−0.02 ± 0.08	3489 ± 35	−0.05 ± 0.05	−0.02 ± 0.05	TD-D
J09307+003	3300 ± 200	4.91 ± 0.20	3460 ± 27	4.90 ± 0.08	−0.18 ± 0.08	−0.11 ± 0.08	3460 ± 26	−0.12 ± 0.07	−0.07 ± 0.07	D
J09423+559	3300 ± 200	4.83 ± 0.20	3439 ± 29	4.79 ± 0.06	−0.11 ± 0.06	−0.06 ± 0.06	3439 ± 29	−0.07 ± 0.06	−0.04 ± 0.06	D
J09439+269	3300 ± 200	4.82 ± 0.20	3492 ± 23	4.84 ± 0.06	−0.10 ± 0.05	−0.06 ± 0.05	3494 ± 21	−0.08 ± 0.04	−0.04 ± 0.04	D
J10125+570	3300 ± 200	4.91 ± 0.20	3474 ± 24	4.90 ± 0.08	−0.14 ± 0.06	−0.08 ± 0.06	3461 ± 24	−0.13 ± 0.06	−0.08 ± 0.06	YD
J10360+051	3200 ± 200	4.86 ± 0.20	3268 ± 16	5.14 ± 0.08	−0.91 ± 0.07	−0.62 ± 0.07	3323 ± 55	−0.77 ± 0.24	−0.53 ± 0.24	D
J11289+101	3300 ± 200	4.96 ± 0.20	3405 ± 33	4.86 ± 0.10	−0.27 ± 0.10	−0.18 ± 0.10	3383 ± 32	−0.32 ± 0.10	−0.21 ± 0.10	D
J11306−080	3300 ± 200	4.85 ± 0.20	3486 ± 28	4.90 ± 0.08	−0.03 ± 0.05	−0.01 ± 0.05	3469 ± 29	−0.04 ± 0.03	−0.02 ± 0.03	YD
J11476+786	3300 ± 200	4.99 ± 0.20	3361 ± 45	4.93 ± 0.12	−0.55 ± 0.14	−0.38 ± 0.14	3353 ± 40	−0.53 ± 0.14	−0.36 ± 0.14	TD
J12100−150	3200 ± 200	4.82 ± 0.20	3415 ± 35	4.74 ± 0.11	−0.12 ± 0.10	−0.07 ± 0.10	3391 ± 31	−0.10 ± 0.10	−0.06 ± 0.10	TD
J12479+097	3200 ± 200	4.88 ± 0.20	3408 ± 45	4.82 ± 0.12	−0.23 ± 0.13	−0.15 ± 0.13	3413 ± 33	−0.23 ± 0.12	−0.15 ± 0.12	D
J13293+114	3400 ± 200	4.94 ± 0.20	3455 ± 24	4.83 ± 0.07	−0.17 ± 0.06	−0.11 ± 0.06	3458 ± 23	−0.17 ± 0.05	−0.11 ± 0.05	TD
J13427+332	3200 ± 200	4.78 ± 0.20	3430 ± 28	4.88 ± 0.09	−0.21 ± 0.09	−0.14 ± 0.09	3427 ± 33	−0.16 ± 0.07	−0.10 ± 0.07	D
J13458−179	3300 ± 200	4.88 ± 0.20	3443 ± 29	4.78 ± 0.10	−0.16 ± 0.09	−0.10 ± 0.09	3435 ± 29	−0.15 ± 0.09	−0.09 ± 0.09	D
J14310−122	3200 ± 200	4.87 ± 0.20	3450 ± 28	4.79 ± 0.08	−0.23 ± 0.07	−0.15 ± 0.07	3448 ± 30	−0.20 ± 0.08	−0.13 ± 0.08	YD

TABLE C.3. *continued*

Karmn	Prior T_{eff} [a] [K]	Prior $\log g$ [a] [dex]	T_{eff} [K]	$\log g$ [dex]	[Fe/H] [dex]	[Fe/H]$_{\mathrm{corr}}$ [dex]	$T_{\mathrm{eff,\,fixed}}$ [K]	[Fe/H]$_{\mathrm{fixed}}$ [dex]	[Fe/H]$_{\mathrm{corr,\,fixed}}$ [dex]	Pop. [b]
J14544+355	3300 ± 200	4.86 ± 0.20	3433 ± 29	4.82 ± 0.12	−0.13 ± 0.08	−0.08 ± 0.08	3432 ± 29	−0.09 ± 0.07	−0.05 ± 0.07	D
J15583+354	3300 ± 200	4.91 ± 0.20	3478 ± 32	4.91 ± 0.10	−0.16 ± 0.08	−0.10 ± 0.08	3472 ± 29	−0.16 ± 0.08	−0.10 ± 0.08	D
J16303−126	3300 ± 200	4.93 ± 0.20	3426 ± 33	4.89 ± 0.10	−0.22 ± 0.11	−0.15 ± 0.11	3426 ± 36	−0.21 ± 0.11	−0.14 ± 0.11	YD
J16554−083N	3300 ± 200	5.06 ± 0.20	3397 ± 33	5.07 ± 0.12	−0.25 ± 0.10	−0.17 ± 0.10	3413 ± 25	−0.27 ± 0.10	−0.18 ± 0.10	D
J16570−043	3300 ± 200	5.02 ± 0.20	3206 ± 14	4.81 ± 0.08	−0.89 ± 0.03	−0.60 ± 0.03	3204 ± 8	−0.94 ± 0.04	−0.64 ± 0.04	YD
J17115+384	3300 ± 200	4.81 ± 0.20	3472 ± 35	4.74 ± 0.08	−0.13 ± 0.08	−0.08 ± 0.08	3475 ± 32	−0.12 ± 0.07	−0.07 ± 0.07	D
J17578+046	3200 ± 200	5.12 ± 0.20	3254 ± 32	5.13 ± 0.12	−0.84 ± 0.10	−0.57 ± 0.10	3240 ± 27	−0.86 ± 0.09	−0.59 ± 0.09	TD
J18319+406	3300 ± 200	4.85 ± 0.20	3492 ± 25	4.92 ± 0.09	−0.07 ± 0.06	−0.04 ± 0.06	3489 ± 24	−0.07 ± 0.04	−0.04 ± 0.04	YD
J18346+401	3200 ± 200	4.76 ± 0.20	3447 ± 46	4.69 ± 0.11	−0.06 ± 0.09	−0.03 ± 0.09	3458 ± 47	0.02 ± 0.06	0.02 ± 0.06	D
J18427+596S	3300 ± 200	4.90 ± 0.20	3393 ± 48	4.98 ± 0.12	−0.56 ± 0.18	−0.38 ± 0.18	3440 ± 49	−0.39 ± 0.20	−0.26 ± 0.20	D
J18498−238	3200 ± 200	5.10 ± 0.20	3340 ± 30	5.23 ± 0.11	−0.63 ± 0.10	−0.43 ± 0.10	3268 ± 17	−0.97 ± 0.03	−0.66 ± 0.03	D
J22020−194	3300 ± 200	4.88 ± 0.20	3474 ± 23	4.85 ± 0.07	−0.17 ± 0.07	−0.11 ± 0.07	3471 ± 24	−0.15 ± 0.08	−0.09 ± 0.08	D
J22096−046	3400 ± 200	4.75 ± 0.20	3540 ± 31	4.81 ± 0.11	−0.02 ± 0.07	0.00 ± 0.07	3531 ± 32	−0.04 ± 0.05	−0.02 ± 0.05	YD
J22468+443	3200 ± 200	4.87 ± 0.20	3306 ± 30	5.06 ± 0.13	−0.89 ± 0.09	−0.60 ± 0.09	3342 ± 49	−0.81 ± 0.19	−0.55 ± 0.19	D
J23113+085	3300 ± 200	4.90 ± 0.20	3477 ± 38	4.81 ± 0.10	−0.12 ± 0.09	−0.07 ± 0.09	3472 ± 42	−0.09 ± 0.10	−0.05 ± 0.10	D
M4.0 V										
J00162+198E	3200 ± 200	4.94 ± 0.20	3329 ± 30	4.93 ± 0.07	−0.18 ± 0.09	−0.11 ± 0.09	3327 ± 25	−0.19 ± 0.07	−0.12 ± 0.07	TD-D
J00286−066	3300 ± 200	4.86 ± 0.20	3419 ± 28	4.81 ± 0.08	−0.17 ± 0.08	−0.11 ± 0.08	3412 ± 35	−0.21 ± 0.10	−0.14 ± 0.10	D
J01339−176	3200 ± 200	4.94 ± 0.20	3376 ± 34	5.15 ± 0.12	−0.20 ± 0.08	−0.13 ± 0.08	3424 ± 19	−0.06 ± 0.03	−0.03 ± 0.03	YD
J01352−072	3200 ± 200	4.60 ± 0.20	3052 ± 12	4.73 ± 0.15	−0.04 ± 0.08	−0.02 ± 0.08	3033 ± 7	−0.12 ± 0.09	−0.07 ± 0.09	YD
J02336+249	3100 ± 200	5.01 ± 0.20	3313 ± 24	5.19 ± 0.10	−0.27 ± 0.10	−0.18 ± 0.10	3335 ± 22	−0.06 ± 0.05	−0.03 ± 0.05	D
J02362+068	3200 ± 200	4.96 ± 0.20	3335 ± 45	4.91 ± 0.10	−0.36 ± 0.12	−0.24 ± 0.12	3338 ± 40	−0.34 ± 0.11	−0.23 ± 0.11	D
J02519+224	3200 ± 200	4.71 ± 0.20	3158 ± 42	4.68 ± 0.17	−0.06 ± 0.19	−0.03 ± 0.19	3176 ± 33	−0.15 ± 0.16	−0.09 ± 0.16	YD
J04311+589	3200 ± 200	4.94 ± 0.20	3382 ± 39	4.89 ± 0.10	−0.25 ± 0.11	−0.17 ± 0.11	3365 ± 35	−0.24 ± 0.10	−0.16 ± 0.10	D
J05019+011	3200 ± 200	4.66 ± 0.20	3217 ± 75	4.66 ± 0.18	−0.29 ± 0.26	−0.20 ± 0.26	3207 ± 80	−0.30 ± 0.25	−0.20 ± 0.25	YD
J05019−069	3100 ± 200	5.09 ± 0.20	3284 ± 27	5.13 ± 0.13	−0.32 ± 0.13	−0.21 ± 0.13	3296 ± 26	−0.08 ± 0.04	−0.04 ± 0.04	D
J05062+046	3100 ± 200	4.68 ± 0.20	3134 ± 42	4.72 ± 0.19	0.10 ± 0.16	0.10 ± 0.16	3116 ± 38	0.10 ± 0.16	0.10 ± 0.16	YD
J05360−076	3200 ± 200	4.87 ± 0.20	3422 ± 29	4.81 ± 0.08	−0.19 ± 0.06	−0.12 ± 0.06	3384 ± 19	−0.29 ± 0.08	−0.20 ± 0.08	D
J05366+112	3200 ± 200	4.94 ± 0.20	3355 ± 23	5.17 ± 0.16	−0.29 ± 0.10	−0.20 ± 0.10	3411 ± 18	−0.04 ± 0.03	−0.02 ± 0.03	YD
J05421+124	3200 ± 200	5.01 ± 0.20	3324 ± 38	4.93 ± 0.08	−0.44 ± 0.11	−0.30 ± 0.11	3295 ± 35	−0.44 ± 0.10	−0.30 ± 0.10	TD
J06000+027	3200 ± 200	5.01 ± 0.20	3296 ± 19	5.12 ± 0.14	−0.29 ± 0.13	−0.20 ± 0.13	3323 ± 17	−0.04 ± 0.03	−0.02 ± 0.03	YD

TABLE C.3. *continued*

Karmn	Prior $T_{\rm eff}$ [a] [K]	Prior $\log g$ [a] [dex]	$T_{\rm eff}$ [K]	$\log g$ [dex]	[Fe/H] [dex]	[Fe/H]$_{\rm corr}$ [dex]	$T_{\rm eff, fixed}$ [K]	[Fe/H]$_{\rm fixed}$ [dex]	[Fe/H]$_{\rm corr, fixed}$ [dex]	Pop. [b]
J06246+234	3200 ± 200	5.14 ± 0.20	3249 ± 24	5.10 ± 0.09	−0.67 ± 0.10	−0.46 ± 0.10	3253 ± 21	−0.63 ± 0.09	−0.43 ± 0.09	D
J06396−210	3200 ± 200	4.94 ± 0.20	3428 ± 33	5.09 ± 0.12	−0.08 ± 0.07	−0.04 ± 0.07	3438 ± 27	−0.07 ± 0.06	−0.04 ± 0.06	D
J06574+740	3200 ± 200	4.94 ± 0.20	3173 ± 24	5.06 ± 0.13	−0.10 ± 0.06	−0.06 ± 0.06	3133 ± 11	−0.01 ± 0.01	0.00 ± 0.01	D
J07033+346	3200 ± 200	4.98 ± 0.20	3310 ± 26	5.13 ± 0.12	−0.36 ± 0.11	−0.24 ± 0.11	3386 ± 30	−0.03 ± 0.03	−0.01 ± 0.03	D
J07472+503	3200 ± 200	4.97 ± 0.20	3251 ± 59	4.92 ± 0.18	−0.14 ± 0.18	−0.08 ± 0.18	3255 ± 50	−0.20 ± 0.25	−0.13 ± 0.25	D
J08023+033	3300 ± 200	4.86 ± 0.20	3422 ± 26	4.72 ± 0.09	−0.36 ± 0.09	−0.24 ± 0.09	3416 ± 27	−0.24 ± 0.08	−0.16 ± 0.08	TD
J08126−215	3100 ± 200	4.93 ± 0.20	3356 ± 44	4.88 ± 0.12	−0.26 ± 0.15	−0.18 ± 0.15	3334 ± 32	−0.22 ± 0.10	−0.15 ± 0.10	D
J08315+730	3300 ± 200	4.96 ± 0.20	3364 ± 42	4.90 ± 0.10	−0.30 ± 0.10	−0.20 ± 0.10	3358 ± 25	−0.32 ± 0.10	−0.21 ± 0.10	D
J09028+680	3300 ± 200	4.98 ± 0.20	3328 ± 42	4.96 ± 0.08	−0.40 ± 0.13	−0.27 ± 0.13	3317 ± 34	−0.45 ± 0.11	−0.31 ± 0.11	D
J09161+018	3200 ± 200	4.91 ± 0.20	3237 ± 60	4.84 ± 0.19	−0.13 ± 0.21	−0.08 ± 0.21	3251 ± 51	−0.09 ± 0.28	−0.05 ± 0.28	D
J09447−182	3200 ± 200	4.93 ± 0.20	3417 ± 31	4.84 ± 0.11	−0.14 ± 0.09	−0.08 ± 0.09	3390 ± 36	−0.15 ± 0.11	−0.09 ± 0.11	TD-D
J10185−117	3300 ± 200	4.83 ± 0.20	3434 ± 28	4.74 ± 0.10	−0.27 ± 0.10	−0.18 ± 0.10	3433 ± 29	−0.21 ± 0.10	−0.14 ± 0.10	D
J10504+331	3200 ± 200	4.78 ± 0.20	3441 ± 34	4.74 ± 0.07	−0.06 ± 0.06	−0.03 ± 0.06	3435 ± 33	−0.05 ± 0.06	−0.02 ± 0.06	TD
J10508+068	3200 ± 200	4.96 ± 0.20	3410 ± 42	4.92 ± 0.13	−0.14 ± 0.11	−0.08 ± 0.11	3372 ± 40	−0.25 ± 0.13	−0.17 ± 0.13	YD
J11417+427	3200 ± 200	4.84 ± 0.20	3387 ± 43	4.83 ± 0.10	−0.17 ± 0.10	−0.11 ± 0.10	3380 ± 41	−0.18 ± 0.11	−0.11 ± 0.11	YD
J11476+002	3200 ± 200	4.88 ± 0.20	3282 ± 19	5.16 ± 0.10	−0.51 ± 0.12	−0.35 ± 0.12	3229 ± 13	−0.98 ± 0.02	−0.67 ± 0.02	YD
J11477+008	3100 ± 200	5.08 ± 0.20	3325 ± 43	5.09 ± 0.14	−0.16 ± 0.13	−0.10 ± 0.13	3306 ± 41	−0.19 ± 0.14	−0.12 ± 0.14	D
J12054+695	3200 ± 200	4.91 ± 0.20	3339 ± 41	4.91 ± 0.10	−0.10 ± 0.11	−0.06 ± 0.11	3332 ± 34	−0.11 ± 0.09	−0.06 ± 0.09	YD
J12156+526	3300 ± 200	4.69 ± 0.20	3360 ± 43	4.65 ± 0.17	−0.28 ± 0.14	−0.19 ± 0.14	3384 ± 39	−0.19 ± 0.14	−0.12 ± 0.14	D
J12373−208	3200 ± 200	4.77 ± 0.20	3431 ± 36	4.70 ± 0.10	−0.06 ± 0.07	−0.03 ± 0.07	3434 ± 34	0.03 ± 0.05	0.03 ± 0.05	D
J12428+418	3200 ± 200	4.82 ± 0.20	3328 ± 25	5.05 ± 0.14	−0.14 ± 0.09	−0.08 ± 0.09	3250 ± 14	−0.07 ± 0.07	−0.04 ± 0.07	YD
J13229+244	3200 ± 200	4.95 ± 0.20	3327 ± 44	4.93 ± 0.09	−0.44 ± 0.13	−0.30 ± 0.13	3331 ± 37	−0.36 ± 0.10	−0.24 ± 0.10	D
J13536+776	3200 ± 200	4.94 ± 0.20	3198 ± 83	4.94 ± 0.21	−0.01 ± 0.30	0.00 ± 0.30	3192 ± 80	−0.01 ± 0.25	0.00 ± 0.25	D
J13591−198	3100 ± 200	4.95 ± 0.20	3261 ± 20	5.12 ± 0.10	−0.22 ± 0.07	−0.15 ± 0.07	3292 ± 16	−0.04 ± 0.03	−0.02 ± 0.03	YD
J14342−125	3100 ± 200	4.89 ± 0.20	3347 ± 50	4.76 ± 0.13	−0.26 ± 0.15	−0.18 ± 0.15	3330 ± 35	−0.22 ± 0.13	−0.15 ± 0.13	D
J15369−141	3200 ± 200	4.89 ± 0.20	3428 ± 33	4.75 ± 0.08	−0.11 ± 0.07	−0.06 ± 0.07	3400 ± 36	−0.10 ± 0.10	−0.06 ± 0.10	D
J16028+205	3200 ± 200	4.98 ± 0.20	3362 ± 34	4.97 ± 0.10	−0.16 ± 0.12	−0.10 ± 0.12	3346 ± 39	−0.19 ± 0.11	−0.12 ± 0.11	TD-D
J17542+073	3200 ± 200	4.92 ± 0.20	3312 ± 30	4.86 ± 0.08	−0.19 ± 0.09	−0.12 ± 0.09	3289 ± 31	−0.39 ± 0.12	−0.26 ± 0.12	D
J18131+260	3200 ± 200	4.89 ± 0.20	3271 ± 63	4.83 ± 0.16	−0.52 ± 0.13	−0.36 ± 0.13	3268 ± 53	−0.54 ± 0.13	−0.37 ± 0.13	D
J18221+063	3400 ± 200	4.96 ± 0.20	3397 ± 28	4.89 ± 0.09	−0.50 ± 0.11	−0.35 ± 0.11	3388 ± 25	−0.53 ± 0.09	−0.36 ± 0.09	TD
J18224+620	3100 ± 200	5.13 ± 0.20	3294 ± 43	5.12 ± 0.15	−0.10 ± 0.11	−0.06 ± 0.11	3278 ± 37	−0.26 ± 0.18	−0.18 ± 0.18	D

TABLE C.3. *continued*

Karmn	Prior T_{eff} [a] [K]	Prior $\log g$ [a] [dex]	T_{eff} [K]	$\log g$ [dex]	[Fe/H] [dex]	[Fe/H]$_{\text{corr}}$ [dex]	$T_{\text{eff, fixed}}$ [K]	[Fe/H]$_{\text{fixed}}$ [dex]	[Fe/H]$_{\text{corr, fixed}}$ [dex]	Pop. [b]
J18363+136	3200 ± 200	4.94 ± 0.20	3335 ± 28	5.18 ± 0.12	−0.15 ± 0.08	−0.09 ± 0.08	3398 ± 37	−0.04 ± 0.03	−0.02 ± 0.03	YD
J19206+731S	3200 ± 200	4.94 ± 0.20	3448 ± 77	4.82 ± 0.16	−0.11 ± 0.12	−0.06 ± 0.12	3447 ± 98	−0.06 ± 0.14	−0.03 ± 0.14	D
J19511+464	3200 ± 200	4.98 ± 0.20	3177 ± 39	5.00 ± 0.15	0.16 ± 0.19	0.16 ± 0.19	3213 ± 34	0.10 ± 0.14	0.10 ± 0.14	YD
J20336+617	3200 ± 200	4.80 ± 0.20	3406 ± 32	4.76 ± 0.14	−0.16 ± 0.12	−0.10 ± 0.12	3401 ± 32	−0.05 ± 0.09	−0.02 ± 0.09	D
J20525−169	3100 ± 200	4.97 ± 0.20	3382 ± 40	5.01 ± 0.12	−0.07 ± 0.09	−0.04 ± 0.09	3374 ± 41	−0.07 ± 0.08	−0.04 ± 0.08	D
J21463+382	3300 ± 200	5.10 ± 0.20	3247 ± 21	4.84 ± 0.11	−0.86 ± 0.09	−0.59 ± 0.09	3265 ± 27	−0.69 ± 0.10	−0.47 ± 0.10	TD
J21466−001	3200 ± 200	4.94 ± 0.20	3408 ± 29	4.82 ± 0.09	−0.21 ± 0.08	−0.14 ± 0.08	3381 ± 28	−0.20 ± 0.10	−0.13 ± 0.10	D
J21466+668	3200 ± 200	4.91 ± 0.20	3409 ± 38	4.85 ± 0.11	−0.15 ± 0.11	−0.09 ± 0.11	3396 ± 38	−0.20 ± 0.13	−0.13 ± 0.13	YD
J22012+283	3200 ± 200	4.92 ± 0.20	3195 ± 29	5.00 ± 0.16	0.03 ± 0.11	0.03 ± 0.11	3195 ± 29	0.00 ± 0.10	0.00 ± 0.10	YD
J22252+594	3200 ± 200	4.77 ± 0.20	3448 ± 40	4.76 ± 0.10	−0.06 ± 0.08	−0.03 ± 0.08	3446 ± 41	−0.04 ± 0.06	−0.02 ± 0.06	D
J22298+414	3200 ± 200	4.98 ± 0.20	3332 ± 32	4.88 ± 0.07	−0.26 ± 0.10	−0.18 ± 0.10	3314 ± 25	−0.30 ± 0.11	−0.20 ± 0.11	D
J22532−142	3200 ± 200	4.87 ± 0.20	3421 ± 40	4.83 ± 0.10	−0.11 ± 0.10	−0.06 ± 0.10	3409 ± 40	−0.17 ± 0.12	−0.11 ± 0.12	YD
J23216+172	3200 ± 200	4.81 ± 0.20	3398 ± 47	4.81 ± 0.11	−0.03 ± 0.10	−0.01 ± 0.10	3399 ± 39	−0.03 ± 0.08	−0.01 ± 0.08	D
J23431+365	3100 ± 200	5.01 ± 0.20	3301 ± 30	5.18 ± 0.12	−0.16 ± 0.10	−0.10 ± 0.10	3295 ± 26	−0.06 ± 0.06	−0.03 ± 0.06	YD
J23505−095	3100 ± 200	4.88 ± 0.20	3377 ± 34	4.83 ± 0.10	−0.14 ± 0.10	−0.08 ± 0.10	3366 ± 37	−0.10 ± 0.09	−0.06 ± 0.09	D
J23548+385	3200 ± 200	4.91 ± 0.20	3263 ± 16	5.13 ± 0.10	−0.81 ± 0.09	−0.55 ± 0.09	3265 ± 19	−0.91 ± 0.07	−0.62 ± 0.07	D
M4.5 V										
J01125−169	3100 ± 200	5.18 ± 0.20	3228 ± 46	5.24 ± 0.16	−0.57 ± 0.20	−0.39 ± 0.20	3225 ± 43	−0.65 ± 0.22	−0.44 ± 0.22	D
J04153−076	3100 ± 200	4.98 ± 0.20	3179 ± 61	5.00 ± 0.18	−0.44 ± 0.17	−0.30 ± 0.17	3180 ± 69	−0.41 ± 0.18	−0.28 ± 0.18	TD-D
J07446+035	3100 ± 200	4.87 ± 0.20	3251 ± 34	5.11 ± 0.14	−0.57 ± 0.24	−0.39 ± 0.24	3248 ± 36	−0.63 ± 0.17	−0.43 ± 0.17	YD
J07558+833	3200 ± 200	4.98 ± 0.20	3252 ± 55	4.80 ± 0.19	−0.36 ± 0.21	−0.24 ± 0.21	3253 ± 50	−0.23 ± 0.19	−0.15 ± 0.19	YD
J08119+087	3200 ± 200	5.17 ± 0.20	3245 ± 23	5.24 ± 0.08	−0.72 ± 0.09	−0.49 ± 0.09	3225 ± 16	−0.80 ± 0.07	−0.55 ± 0.07	TD
J08526+283	3100 ± 200	4.94 ± 0.20	3321 ± 37	4.87 ± 0.08	−0.16 ± 0.11	−0.10 ± 0.11	3308 ± 39	−0.24 ± 0.12	−0.16 ± 0.12	YD
J09005+465	3100 ± 200	5.04 ± 0.20	3293 ± 30	5.16 ± 0.14	−0.06 ± 0.08	−0.03 ± 0.08	3286 ± 32	−0.12 ± 0.12	−0.07 ± 0.12	YD
J10416+376	3200 ± 200	5.05 ± 0.20	3298 ± 27	4.87 ± 0.08	−0.29 ± 0.12	−0.20 ± 0.12	3272 ± 31	−0.38 ± 0.14	−0.25 ± 0.14	D
J11509+483	3100 ± 200	5.11 ± 0.20	3282 ± 38	5.09 ± 0.09	−0.19 ± 0.10	−0.12 ± 0.10	3277 ± 41	−0.25 ± 0.15	−0.17 ± 0.15	D
J13005+056	3000 ± 200	5.06 ± 0.20	3158 ± 38	4.70 ± 0.12	−0.53 ± 0.11	−0.36 ± 0.11	3140 ± 39	−0.07 ± 0.17	−0.04 ± 0.17	D
J17033+514	3000 ± 200	5.04 ± 0.20	3273 ± 32	4.92 ± 0.14	−0.19 ± 0.17	−0.12 ± 0.17	3249 ± 33	−0.30 ± 0.18	−0.20 ± 0.18	D
J18075−159	3000 ± 200	5.10 ± 0.20	3220 ± 22	5.23 ± 0.11	−0.54 ± 0.13	−0.37 ± 0.13	3192 ± 19	−0.78 ± 0.06	−0.54 ± 0.06	D
J18189+661	3100 ± 200	5.17 ± 0.20	3172 ± 45	4.97 ± 0.15	−0.68 ± 0.16	−0.46 ± 0.16	3146 ± 44	−0.66 ± 0.19	−0.45 ± 0.19	D
J19098+176	3100 ± 200	5.07 ± 0.20	3277 ± 34	4.93 ± 0.13	−0.21 ± 0.16	−0.14 ± 0.16	3281 ± 53	−0.18 ± 0.19	−0.11 ± 0.19	D

TABLE C.3. *continued*

Karmn	Prior $T_{\rm eff}$ [a] [K]	Prior log g [a] [dex]	$T_{\rm eff}$ [K]	log g [dex]	[Fe/H] [dex]	[Fe/H]$_{\rm corr}$ [dex]	$T_{\rm eff, fixed}$ [K]	[Fe/H]$_{\rm fixed}$ [dex]	[Fe/H]$_{\rm corr, fixed}$ [dex]	Pop. [b]
J19216+208	3100 ± 200	5.05 ± 0.20	3278 ± 35	5.05 ± 0.12	−0.25 ± 0.13	−0.17 ± 0.13	3279 ± 35	−0.26 ± 0.12	−0.18 ± 0.12	D
J20405+154	3100 ± 200	5.07 ± 0.20	3263 ± 36	5.02 ± 0.12	−0.16 ± 0.11	−0.10 ± 0.11	3281 ± 37	−0.18 ± 0.15	−0.11 ± 0.15	D
J22137−176	3100 ± 200	5.09 ± 0.20	3256 ± 41	5.00 ± 0.10	−0.41 ± 0.16	−0.28 ± 0.16	3262 ± 41	−0.40 ± 0.14	−0.27 ± 0.14	D
J22231−176	3000 ± 200	5.08 ± 0.20	3228 ± 19	5.26 ± 0.13	−0.19 ± 0.10	−0.12 ± 0.14	3231 ± 19	−0.15 ± 0.10	−0.09 ± 0.10	D
M5.0 V										
J01019+541	2900 ± 200	5.15 ± 0.20	3070 ± 13	5.12 ± 0.03	−0.30 ± 0.06	−0.20 ± 0.06	3072 ± 15	−0.34 ± 0.04	−0.23 ± 0.04	D
J01033+623	3000 ± 200	5.02 ± 0.20	3057 ± 49	5.12 ± 0.18	−0.36 ± 0.24	−0.24 ± 0.24	3045 ± 58	−0.37 ± 0.13	−0.25 ± 0.13	YD
J01048−181	3000 ± 200	5.16 ± 0.20	3209 ± 41	5.09 ± 0.14	−0.16 ± 0.17	−0.10 ± 0.17	3200 ± 33	−0.22 ± 0.17	−0.15 ± 0.17	D
J03133+047	3000 ± 200	5.11 ± 0.20	3214 ± 40	5.06 ± 0.16	−0.10 ± 0.17	−0.06 ± 0.17	3208 ± 39	−0.21 ± 0.15	−0.14 ± 0.15	D
J04472+206	3000 ± 200	4.82 ± 0.20	3096 ± 14	5.12 ± 0.07	−0.11 ± 0.04	−0.06 ± 0.04	3075 ± 12	−0.59 ± 0.04	−0.40 ± 0.04	YD
J05084−210	3000 ± 200	4.59 ± 0.20	3233 ± 22	4.52 ± 0.10	−0.55 ± 0.07	−0.38 ± 0.07	3244 ± 19	−0.52 ± 0.06	−0.36 ± 0.06	YD
J06024+498	3000 ± 200	5.17 ± 0.20	3213 ± 35	5.17 ± 0.14	−0.15 ± 0.13	−0.09 ± 0.13	3201 ± 32	−0.20 ± 0.14	−0.13 ± 0.14	YD
J06318+414	3000 ± 200	4.81 ± 0.20	3084 ± 13	4.88 ± 0.07	−0.06 ± 0.05	−0.03 ± 0.05	3026 ± 12	−0.14 ± 0.05	−0.08 ± 0.05	YD
J06594+193	2800 ± 200	5.17 ± 0.20	3146 ± 38	5.09 ± 0.17	−0.16 ± 0.19	−0.10 ± 0.19	3158 ± 33	−0.10 ± 0.22	−0.06 ± 0.22	D
J09449−123	2900 ± 200	4.86 ± 0.20	3068 ± 15	5.05 ± 0.05	−0.21 ± 0.07	−0.14 ± 0.07	3032 ± 13	−0.22 ± 0.06	−0.15 ± 0.06	YD
J10584−107	3100 ± 200	5.07 ± 0.20	3218 ± 23	5.23 ± 0.11	−0.45 ± 0.17	−0.31 ± 0.17	3200 ± 39	−0.55 ± 0.15	−0.38 ± 0.15	YD
J11474+667	3000 ± 200	4.91 ± 0.20	3219 ± 35	4.98 ± 0.18	−0.62 ± 0.19	−0.42 ± 0.19	3211 ± 37	−0.73 ± 0.20	−0.50 ± 0.20	YD
J12189+111	2900 ± 200	5.14 ± 0.20	3064 ± 32	5.06 ± 0.17	−0.40 ± 0.22	−0.27 ± 0.22	3079 ± 28	−0.40 ± 0.19	−0.27 ± 0.19	YD
J13102+477	3000 ± 200	5.11 ± 0.20	3221 ± 21	5.25 ± 0.12	−0.37 ± 0.13	−0.25 ± 0.13	3226 ± 35	−0.34 ± 0.18	−0.23 ± 0.18	D
J14173+454	3100 ± 200	4.94 ± 0.20	3222 ± 24	5.19 ± 0.07	−0.74 ± 0.07	−0.51 ± 0.07	3150 ± 28	−0.10 ± 0.07	−0.06 ± 0.07	D
J15499+796	3000 ± 200	4.93 ± 0.20	3095 ± 15	5.07 ± 0.09	−0.25 ± 0.09	−0.17 ± 0.09	3066 ± 17	−0.20 ± 0.14	−0.13 ± 0.14	YD
J16313+408	2900 ± 200	5.10 ± 0.20	3170 ± 42	4.86 ± 0.13	−0.69 ± 0.11	−0.47 ± 0.11	3298 ± 49	−0.73 ± 0.12	−0.50 ± 0.12	YD
J18022+642	3000 ± 200	5.09 ± 0.20	3213 ± 43	5.15 ± 0.12	−0.67 ± 0.15	−0.46 ± 0.15	3198 ± 37	−0.69 ± 0.12	−0.47 ± 0.12	D
J18027+375	3000 ± 200	5.15 ± 0.20	3210 ± 39	5.02 ± 0.18	−0.08 ± 0.17	−0.04 ± 0.17	3186 ± 27	−0.22 ± 0.21	−0.15 ± 0.21	D
J18165+048	3000 ± 200	5.07 ± 0.20	3240 ± 36	4.97 ± 0.13	−0.26 ± 0.14	−0.18 ± 0.14	3258 ± 38	−0.22 ± 0.22	−0.15 ± 0.22	D
J18482+076	2900 ± 200	5.14 ± 0.20	3175 ± 39	5.10 ± 0.16	−0.19 ± 0.13	−0.12 ± 0.13	3169 ± 32	−0.14 ± 0.14	−0.08 ± 0.14	YD
J19422−207	3100 ± 200	5.04 ± 0.20	3241 ± 54	4.81 ± 0.15	−0.71 ± 0.10	−0.49 ± 0.10	3341 ± 41	−0.77 ± 0.09	−0.53 ± 0.09	YD
J20093−012	3000 ± 200	5.12 ± 0.20	3301 ± 90	4.96 ± 0.17	−0.74 ± 0.15	−0.51 ± 0.15	3388 ± 79	−0.80 ± 0.13	−0.55 ± 0.13	D
J20260+585	3000 ± 200	5.11 ± 0.20	3223 ± 49	4.97 ± 0.15	−0.23 ± 0.24	−0.15 ± 0.24	3216 ± 47	−0.16 ± 0.23	−0.10 ± 0.23	D
J20556−140S	3100 ± 200	5.16 ± 0.20	3193 ± 23	4.98 ± 0.10	−0.53 ± 0.11	−0.36 ± 0.11	3205 ± 21	−0.45 ± 0.08	−0.31 ± 0.08	TD
J23419+441	3000 ± 200	5.16 ± 0.20	3186 ± 41	5.15 ± 0.18	0.04 ± 0.17	0.04 ± 0.17	3175 ± 36	0.01 ± 0.16	0.01 ± 0.16	TD-D

TABLE C.3. *continued*

Karmn	Prior $T_{\rm eff}$ [a] [K]	Prior $\log g$ [a] [dex]	$T_{\rm eff}$ [K]	$\log g$ [dex]	[Fe/H] [dex]	[Fe/H]$_{\rm corr}$ [dex]	$T_{\rm eff, fixed}$ [K]	[Fe/H]$_{\rm fixed}$ [dex]	[Fe/H]$_{\rm corr, fixed}$ [dex]	Pop. [b]
					M5.5 V					
J00067−075	2900 ± 200	5.22 ± 0.20	3169 ± 53	5.20 ± 0.16	−0.22 ± 0.22	−0.15 ± 0.22	3137 ± 36	−0.37 ± 0.18	−0.25 ± 0.18	D
J08413+594	3000 ± 200	5.23 ± 0.20	3141 ± 38	5.28 ± 0.17	−0.12 ± 0.16	−0.07 ± 0.16	3124 ± 35	−0.14 ± 0.15	−0.08 ± 0.15	D
J11055+435	2900 ± 200	5.29 ± 0.20	3278 ± 86	5.25 ± 0.20	−0.52 ± 0.25	−0.36 ± 0.25	3167 ± 56	−0.63 ± 0.21	−0.43 ± 0.21	TD-D
J15305+094	3000 ± 200	5.26 ± 0.20	3073 ± 15	5.16 ± 0.05	−0.43 ± 0.08	−0.29 ± 0.08	3085 ± 13	−0.39 ± 0.08	−0.26 ± 0.08	D
J17338+169	2900 ± 200	4.86 ± 0.20	3048 ± 11	4.95 ± 0.13	−0.05 ± 0.06	−0.02 ± 0.06	3017 ± 10	−0.09 ± 0.05	−0.05 ± 0.05	YD
J22114+409	3000 ± 200	5.14 ± 0.20	3132 ± 30	5.15 ± 0.16	−0.07 ± 0.12	−0.04 ± 0.12	3145 ± 27	−0.12 ± 0.14	−0.07 ± 0.14	YD
J23351−023	3000 ± 200	5.25 ± 0.20	3136 ± 38	5.27 ± 0.17	−0.20 ± 0.17	−0.13 ± 0.17	3149 ± 40	−0.22 ± 0.18	−0.15 ± 0.18	D
					M6.0 V					
J07403−174	2800 ± 200	5.29 ± 0.20	3031 ± 26	5.03 ± 0.17	0.04 ± 0.18	0.04 ± 0.18	3050 ± 22	0.20 ± 0.11	0.20 ± 0.11	D
J10564+070	2800 ± 200	5.23 ± 0.20	3071 ± 24	5.25 ± 0.18	−0.09 ± 0.20	−0.05 ± 0.20	3060 ± 18	−0.15 ± 0.18	−0.09 ± 0.18	D
J14321+081	2800 ± 200	5.14 ± 0.20	3161 ± 86	5.04 ± 0.21	−0.13 ± 0.32	−0.08 ± 0.32	3187 ± 77	−0.17 ± 0.25	−0.11 ± 0.25	YD
					M6.5 V					
J08298+267	2700 ± 200	5.28 ± 0.20	2997 ± 49	5.16 ± 0.18	0.01 ± 0.19	0.01 ± 0.19	3054 ± 30	−0.16 ± 0.16	−0.10 ± 0.16	YD
J09003+218	2700 ± 200	5.28 ± 0.20	3061 ± 43	5.17 ± 0.21	−0.02 ± 0.18	0.00 ± 0.18	3088 ± 36	−0.10 ± 0.15	−0.06 ± 0.15	YD
J10482−113	2700 ± 200	5.30 ± 0.20	3029 ± 25	5.33 ± 0.16	−0.13 ± 0.17	−0.08 ± 0.17	3032 ± 19	−0.19 ± 0.16	−0.12 ± 0.16	D
					M7.0 V					
J02530+168	2800 ± 200	5.31 ± 0.20	3034 ± 45	5.19 ± 0.20	−0.17 ± 0.28	−0.11 ± 0.28	3031 ± 34	0.01 ± 0.25	0.01 ± 0.25	TD
J09033+056	2800 ± 200	5.14 ± 0.20	3027 ± 19	5.09 ± 0.12	−0.38 ± 0.12	−0.25 ± 0.12	3001 ± 18	−0.21 ± 0.10	−0.14 ± 0.10	D
J16555−083	2600 ± 200	5.29 ± 0.20	3005 ± 21	5.25 ± 0.18	−0.08 ± 0.09	−0.04 ± 0.09	2989 ± 20	0.00 ± 0.11	0.00 ± 0.11	D
					M8.0 V					
J05394+406	2500 ± 200	5.27 ± 0.20	...	...	...	...	...	...	...	D
J19169+051S	2500 ± 200	5.29 ± 0.20	...	...	...	...	...	...	...	D
J19255+096	2400 ± 200	5.12 ± 0.20	...	...	...	...	...	...	...	YD
J23064−050	2500 ± 200	5.29 ± 0.20	...	...	...	...	...	...	...	D
					M8.5 V					
J04198+425	2400 ± 200	5.29 ± 0.20	...	...	...	...	...	...	...	D
J18356+329	2400 ± 200	5.36 ± 0.20	...	...	...	...	...	...	...	D

TABLE C.3. *continued*

Karmn	Prior $T_{\rm eff}$ [a] [K]	Prior $\log g$ [a] [dex]	$T_{\rm eff}$ [K]	$\log g$ [dex]	[Fe/H] [dex]	[Fe/H]$_{\rm corr}$ [dex]	$T_{\rm eff,fixed}$ [K]	[Fe/H]$_{\rm fixed}$ [dex]	[Fe/H]$_{\rm corr,fixed}$ [dex]	Pop. [b]
J08536−034	2300 ± 200	5.33 ± 0.20	...	...	M9.0 V	...	...	...	...	D

Notes. [a] Adopted from Cifuentes et al. (2020). [b] Galactic populations, including the thick disc (TD), the thick disc-thin disc transition (TD-D), the thin disc (D), and the young disc (YD) (Cortés-Contreras et al. in prep.).

Bibliography

Abia, C., Tabernero, H. M., Korotin, S. A., et al. 2020, A&A, 642, A227

Adibekyan, V. Z., González Hernández, J. I., Delgado Mena, E., et al. 2014, A&A, 564, L15

Adibekyan, V. Z., Sousa, S. G., Santos, N. C., et al. 2012, A&A, 545, A32

Allard, F., Hauschildt, P. H., Alexander, D. R., Tamanai, A., & Schweitzer, A. 2001, ApJ, 556, 357

Allard, F., Homeier, D., & Freytag, B. 2012, Phil. Trans. R. Soc. A, 370, 2765

Allende-Prieto, C. 2015, 225th AAS Meeting, 422.07

Allende Prieto, C. 2016, Living Rev. Sol. Phys., 13, 1

Allende Prieto, C. 2021, Nature Astronomy, 5, 105

Allende Prieto, C., Barklem, P. S., Lambert, D. L., & Cunha, K. 2004, A&A, 420, 183

Allende Prieto, C., Beers, T. C., Wilhelm, R., et al. 2006, ApJ, 636, 804

Allende Prieto, C., Majewski, S. R., Schiavon, R., et al. 2008, Astron. Nachr., 329, 1018

Alonso-Floriano, F. J., Morales, J. C., Caballero, J. A., et al. 2015, A&A, 577, A128

Alonso-Floriano, F. J., Sánchez-López, A., Snellen, I. A. G., et al. 2019, A&A, 621, A74

Alonso-Santiago, J., Negueruela, I., Marco, A., et al. 2019, A&A, 631, A124

Alvarez, R. & Plez, B. 1998, A&A, 330, 1109

Andreasen, D. T., Sousa, S. G., Delgado Mena, E., et al. 2016, A&A, 585, A143

Andreasen, D. T., Sousa, S. G., Tsantaki, M., et al. 2017, A&A, 600, A69

Antoniadis-Karnavas, A., Sousa, S. G., Delgado-Mena, E., et al. 2020, A&A, 636, A9

Artigau, É., Kouach, D., Donati, J.-F., et al. 2014, SPIE Conf. Ser., Vol. 9147, 914715

Asplund, M., Grevesse, N., Sauval, A. J., & Scott, P. 2009, ARA&A, 47, 481

Aurière, M. 2003, EAS Publications Series, Vol. 9, 105

Auvergne, M., Bodin, P., Boisnard, L., et al. 2009, A&A, 506, 411

Bagnulo, S., Jehin, E., Ledoux, C., et al. 2003, The Messenger, 114, 10

Baraffe, I., Chabrier, G., Allard, F., & Hauschildt, P. H. 1998, A&A, 337, 403

Baratella, M., D'Orazi, V., Carraro, G., et al. 2020, A&A, 634, A34

Barber, C. B., Dobkin, D. P., & Huhdanpaa, H. T. 1996, ACM Trans. Math. Softw., 22, 469

Barber, R. J., Tennyson, J., Harris, G. J., & Tolchenov, R. N. 2006, MNRAS, 368, 1087

Barklem, P. S., Anstee, S. D., & O'Mara, B. J. 1998, PASA, 15, 336

Baroch, D., Morales, J. C., Ribas, I., et al. 2018, A&A, 619, A32

Baroch, D., Morales, J. C., Ribas, I., et al. 2021, A&A, 653, A49

Barrado y Navascués, D., Stauffer, J. R., & Jayawardhana, R. 2004, ApJ, 614, 386

Bauer, F. F., Zechmeister, M., Kaminski, A., et al. 2020, A&A, 640, A50

Bayo, A., Rodrigo, C., Barrado Y Navascués, D., et al. 2008, A&A, 492, 277

Bell, C. P. M., Mamajek, E. E., & Naylor, T. 2015, MNRAS, 454, 593

Bensby, T., Feltzing, S., & Lundström, I. 2003, A&A, 410, 527

Bensby, T., Feltzing, S., Lundström, I., & Ilyin, I. 2005, A&A, 433, 185

Bensby, T., Feltzing, S., & Oey, M. S. 2014, A&A, 562, A71

Bergemann, M., Collet, R., Schönrich, R., et al. 2017, ApJ, 847, 16

Bertelli, G., Nasi, E., Girardi, L., & Marigo, P. 2009, A&A, 508, 355

Bertone, E., Buzzoni, A., Chávez, M., & Rodríguez-Merino, L. H. 2008, A&A, 485, 823

Birky, J., Hogg, D. W., Mann, A. W., & Burgasser, A. 2020, ApJ, 892, 31

Blanco-Cuaresma, S. 2019, MNRAS, 486, 2075

Blanco-Cuaresma, S., Soubiran, C., Heiter, U., & Jofré, P. 2014a, A&A, 569, A111

Blanco-Cuaresma, S., Soubiran, C., Heiter, U., & Jofré, P. 2014b, iSpec: Stellar atmospheric parameters and chemical abundances, Astrophysics Source Code Library, ascl:1409.006

Blanco-Cuaresma, S., Soubiran, C., Jofré, P., & Heiter, U. 2014c, A&A, 566, A98

Bochanski, J. J., Hawley, S. L., Covey, K. R., et al. 2010, AJ, 139, 2679

Bochanski, J. J., Munn, J. A., Hawley, S. L., et al. 2007, AJ, 134, 2418

Bocquet, S. & Carter, F. W. 2016, JOSS, 1, 46

Bonfils, X., Delfosse, X., Udry, S., et al. 2013, A&A, 549, A109

Borsa, F. & Zannoni, A. 2018, A&A, 617, A134

Borsa, F., Allart, R., Casasayas-Barris, N., et al. 2021, A&A, 645, A24

Borucki, W. J., Koch, D., Basri, G., et al. 2010, Science, 327, 977

Bouchy, F., Doyon, R., Artigau, É., et al. 2017, The Messenger, 169, 21

Boyajian, T. S., McAlister, H. A., van Belle, G., et al. 2012a, ApJ, 746, 101

Boyajian, T. S., von Braun, K., van Belle, G., et al. 2012b, ApJ, 757, 112

Bressan, A., Marigo, P., Girardi, L., et al. 2012, MNRAS, 427, 127

Brewer, J. M., Fischer, D. A., Valenti, J. A., & Piskunov, N. 2016, ApJS, 225, 32

Bruzual, G. & Charlot, S. 2003, MNRAS, 344, 1000

Buchhave, L. A., Latham, D. W., Johansen, A., et al. 2012, Nature, 486, 375

Burrows, A., Marley, M., Hubbard, W. B., et al. 1997, ApJ, 491, 856

Caballero, J. A., Cortés-Contreras, M., Alonso-Floriano, F. J., et al. 2016a, 19th Cambridge Workshop on Cool Stars, Stellar Systems, and the Sun (CS19), 148

Caballero, J. A., Guàrdia, J., López del Fresno, M., et al. 2016b, SPIE Conf. Ser., Vol. 9910, 99100E

Cargile, P. A., Conroy, C., Johnson, B. D., et al. 2020, ApJ, 900, 28

Carrasco, E., Mollá, M., García-Vargas, M. L., et al. 2021, MNRAS, 501, 3568

Casagrande, L., Flynn, C., & Bessell, M. 2008, MNRAS, 389, 585

Casasayas-Barris, N., Pallé, E., Yan, F., et al. 2020, A&A, 635, A206

Cenarro, A. J., Cardiel, N., Gorgas, J., et al. 2001, MNRAS, 326, 959

Cenarro, A. J., Peletier, R. F., Sánchez-Blázquez, P., et al. 2007, MNRAS, 374, 664

Chen, Y.-P., Trager, S. C., Peletier, R. F., et al. 2014, A&A, 565, A117

Cifuentes, C., Caballero, J. A., Cortés-Contreras, M., et al. 2020, A&A, 642, A115

Claudi, R., Benatti, S., Carleo, I., et al. 2018, SPIE Conf. Ser., Vol. 10702, 107020Z

Clough, S. A., Shephard, M. W., Mlawer, E. J., et al. 2005, JQRSA, 91, 233

Coelho, P., Bruzual, G., Charlot, S., et al. 2007, MNRAS, 382, 498

Conroy, C., Gunn, J. E., & White, M. 2009, ApJ, 699, 486

Cortés-Contreras, M., Béjar, V. J. S., Caballero, J. A., et al. 2017, A&A, 597, A47

Cortés-Contreras, M. 2016, PhD thesis, Universidad Complutense de Madrid, E-Prints Complutense

Cosentino, R., Lovis, C., Pepe, F., et al. 2012, SPIE Conf. Ser., Vol. 8446, 84461V

Crane, J. D., Shectman, S. A., Butler, R. P., et al. 2010, SPIE Conf. Ser., Vol. 7735, 773553

Cui, X.-Q., Zhao, Y.-H., Chu, Y.-Q., et al. 2012, RAA, 12, 1197

Czesla, S., Klocová, T., Khalafinejad, S., Wolter, U., & Schmitt, J. H. M. M. 2015, A&A, 582, A51

da Silva, L., Girardi, L., Pasquini, L., et al. 2006, A&A, 458, 609

da Silva, R., Milone, A. d. C., & Rocha-Pinto, H. J. 2015, A&A, 580, A24

Dalton, G., Trager, S., Abrams, D. C., et al. 2018, SPIE Conf. Ser., Vol. 10702, 107021B

Damiani, F., Prisinzano, L., Micela, G., et al. 2014, A&A, 566, A50

Dawson, K. S., Schlegel, D. J., Ahn, C. P., et al. 2013, AJ, 145, 10

de Jong, R. S., Agertz, O., Berbel, A. A., et al. 2019, The Messenger, 175, 3

de Laverny, P., Recio-Blanco, A., Worley, C. C., & Plez, B. 2012, A&A, 544, A126

De Medeiros, J. R., do Nascimento, J. D., J., Sankarankutty, S., Costa, J. M., & Maia, M. R. G. 2000, A&A, 363, 239

De Medeiros, J. R., Udry, S., Burki, G., & Mayor, M. 2002, A&A, 395, 97

De Silva, G. M., Freeman, K. C., Bland-Hawthorn, J., et al. 2015, MNRAS, 449, 2604

Dekker, H., D'Odorico, S., Kaufer, A., Delabre, B., & Kotzlowski, H. 2000, SPIE Conf. Ser., Vol. 4008, 534

Delfosse, X., Forveille, T., Perrier, C., & Mayor, M. 1998, A&A, 331, 581

Delgado Mena, E., Israelian, G., González Hernández, J. I., et al. 2010, ApJ, 725, 2349

Delgado Mena, E., Lovis, C., Santos, N. C., et al. 2018, A&A, 619, A2

Demangeon, O. D. S., Zapatero Osorio, M. R., Alibert, Y., et al. 2021, A&A, 653, A41

Demarque, P., Woo, J.-H., Kim, Y.-C., & Yi, S. K. 2004, ApJS, 155, 667

Deng, L.-C., Newberg, H. J., Liu, C., et al. 2012, RAA, 12, 735

Desidera, S., Gratton, R. G., Lucatello, S., & Claudi, R. U. 2006, A&A, 454, 581

Desidera, S., Gratton, R. G., Scuderi, S., et al. 2004, A&A, 420, 683

Diaz, A. I., Terlevich, E., & Terlevich, R. 1989, MNRAS, 239, 325

Díez Alonso, E., Caballero, J. A., Montes, D., et al. 2019, A&A, 621, A126

Donati, J. F., Morin, J., Petit, P., et al. 2008, MNRAS, 390, 545

Donati, J. F., Kouach, D., Moutou, C., et al. 2020, MNRAS, 498, 5684

Dorn, C., Khan, A., Heng, K., et al. 2015, A&A, 577, A83

Dorn, R. J., Follert, R., Bristow, P., et al. 2016, SPIE Conf. Ser., Vol. 9908, 99080I

dos Santos, L. A., Meléndez, J., do Nascimento, J.-D., et al. 2016, A&A, 592, A156

Dressing, C. D. & Charbonneau, D. 2013, ApJ, 767, 95

Drew, J. E., Greimel, R., Irwin, M. J., et al. 2005, MNRAS, 362, 753

Dulick, M., Bauschlicher, C. W., J., Burrows, A., et al. 2003, ApJ, 594, 651

Falcón-Barroso, J., Sánchez-Blázquez, P., Vazdekis, A., et al. 2011, A&A, 532, A95

Famaey, B., Jorissen, A., Luri, X., et al. 2005, A&A, 430, 165

Fioc, M. & Rocca-Volmerange, B. 1997, A&A, 500, 507

Foreman-Mackey, D., Hogg, D. W., Lang, D., & Goodman, J. 2013, PASP, 125, 306

Fortney, J. J. 2018, Astrophysics of Exoplanetary Atmospheres (Springer International Publishing), 51

Francis, P. J. & Wills, B. J. 1999, ASP Conf. Ser., Vol. 162, 363

Frasca, A., Alcalá, J. M., Covino, E., et al. 2003, A&A, 405, 149

Frasca, A., Guillout, P., Marilli, E., et al. 2006, A&A, 454, 301

Freeman, K. & Bland-Hawthorn, J. 2002, ARA&A, 40, 487

Fuhrmeister, B., Czesla, S., Schmitt, J. H. M. M., et al. 2018, A&A, 615, A14

Fuhrmeister, B., Czesla, S., Hildebrandt, L., et al. 2020, A&A, 640, A52

Gaia Collaboration, Brown, A. G. A., Vallenari, A., et al. 2018, A&A, 616, A1

Gaia Collaboration, Brown, A. G. A., Vallenari, A., et al. 2021, A&A, 649, A1

Gaidos, E. & Mann, A. W. 2014, ApJ, 791, 54

García Pérez, A. E., Allende Prieto, C., Holtzman, J. A., et al. 2016, AJ, 151, 144

Ghezzi, L., Cunha, K., Smith, V. V., et al. 2010, ApJ, 720, 1290

Gilbert, J., Bergmann, C., Bloxham, G., et al. 2018, SPIE Conf. Ser., Vol. 10702, 107020Y

Gilmore, G., Randich, S., Asplund, M., et al. 2012, The Messenger, 147, 25

Girardi, L., Bressan, A., Bertelli, G., & Chiosi, C. 2000, A&AS, 141, 371

Gizis, J. E., Reid, I. N., & Hawley, S. L. 2002, AJ, 123, 3356

Gonneau, A., Lançon, A., Trager, S. C., et al. 2016, A&A, 589, A36

Gonneau, A., Lyubenova, M., Lançon, A., et al. 2020, A&A, 634, A133

Gontcharov, G. A. 2006, Astron. Lett., 32, 759

Gonzalez, G. & Lambert, D. L. 1996, AJ, 111, 424

Gonzalez, G., Laws, C., Tyagi, S., & Reddy, B. E. 2001, AJ, 121, 432

González-Álvarez, E., Zapatero Osorio, M. R., Caballero, J. A., et al. 2020, A&A, 637, A93

González Hernández, J. I., Rebolo, R., Israelian, G., et al. 2004, ApJ, 609, 988

González Hernández, J. I., Ruiz-Lapuente, P., Tabernero, H. M., et al. 2012, Nature, 489, 533

Goorvitch, D. 1994, ApJS, 95, 535

Gordon, I. E., Rothman, L. S., Tan, Y., Kochanov, R. V., & Hill, C. 2017, 72nd International Symposium on Molecular Spectroscopy, TJ08

Gorgas, J., Faber, S. M., Burstein, D., et al. 1993, ApJS, 86, 153

Gray, D. F. 2008, The Observation and Analysis of Stellar Photospheres (Cambridge University Press)

Gray, D. F. 2018, ApJ, 869, 81

Gray, D. F. & Toner, C. G. 1986, ApJ, 310, 277

Gray, R. 2014, Determination of Atmospheric Parameters of B-, A-, F- and G-Type Stars (Springer, Cham), 75

Gray, R. O., Corbally, C. J., Garrison, R. F., et al. 2006, AJ, 132, 161

Gray, R. O. & Corbally, Christopher, J. 2009, Stellar Spectral Classification (Princeton University Press)

Gray, R. O., Corbally, C. J., De Cat, P., et al. 2016, AJ, 151, 13

Gunn, J. E. & Stryker, L. L. 1983, ApJS, 52, 121

Gustafsson, B., Edvardsson, B., Eriksson, K., et al. 2008, A&A, 486, 951

Hatzes, A. 2017, 230th AAS Meeting, 117.02

Hauschildt, P. H., Allard, F., Ferguson, J., Baron, E., & Alexander, D. R. 1999, ApJ, 525, 871

Hayes, C. R., Majewski, S. R., Shetrone, M., et al. 2018, ApJ, 852, 49

Heiter, U. & Eriksson, K. 2006, A&A, 452, 1039

Heiter, U., Jofré, P., Gustafsson, B., et al. 2015a, A&A, 582, A49

Heiter, U. & Luck, R. E. 2003, AJ, 126, 2015

Heiter, U., Lind, K., Asplund, M., et al. 2015b, Phys. Scr., 90, 054010

Heiter, U., Lind, K., Bergemann, M., et al. 2021, A&A, 645, A106

Hejazi, N., Lépine, S., Homeier, D., Rich, R. M., & Shara, M. M. 2020, AJ, 159, 30

Hekker, S. & Meléndez, J. 2007, A&A, 475, 1003

Henry, T. J., Jao, W.-C., Winters, J. G., et al. 2018, AJ, 155, 265

Hinkle, K., Wallace, L., Valenti, J., & Harmer, D. 2000, Visible and Near Infrared Atlas of the Arcturus Spectrum 3727-9300 Å (Astronomical Society of the Pacific)

Hintz, D., Fuhrmeister, B., Czesla, S., et al. 2019, A&A, 623, A136

Hintz, D., Fuhrmeister, B., Czesla, S., et al. 2020, A&A, 638, A115

Hoeijmakers, H. J., Ehrenreich, D., Heng, K., et al. 2018, Nature, 560, 453

Howard, A. W., Marcy, G. W., Bryson, S. T., et al. 2012, ApJS, 201, 15

Hubeny, I. & Mihalas, D. 2014, Theory of Stellar Atmospheres (Princeton University Press)

Husser, T.-O., Wende-von Berg, S., Dreizler, S., et al. 2013, A&A, 553, A6

Ishikawa, H. T., Aoki, W., Kotani, T., et al. 2020, PASJ, 72, 102

Ivanov, V. D., Rieke, M. J., Engelbracht, C. W., et al. 2004, ApJS, 151, 387

Jacoby, G. H., Hunter, D. A., & Christian, C. A. 1984, ApJS, 56, 257

Jaschek, C. & Jaschek, M. 1990, The Classification of Stars (Cambridge University Press)

Jeffers, S. V., Schöfer, P., Lamert, A., et al. 2018, A&A, 614, A76

Jofré, E., Petrucci, R., Saffe, C., et al. 2015a, A&A, 574, A50

Jofré, P., Heiter, U., & Soubiran, C. 2019, ARA&A, 57, 571

Jofré, P., Heiter, U., Tucci Maia, M., et al. 2018, RNAAS, 2, 152

Jofré, P., Heiter, U., Soubiran, C., et al. 2014, A&A, 564, A133

Jofré, P., Heiter, U., Soubiran, C., et al. 2015b, A&A, 582, A81

Jofré, P., Heiter, U., Worley, C. C., et al. 2017, A&A, 601, A38

Johnson, J. A., Aller, K. M., Howard, A. W., & Crepp, J. R. 2010, PASP, 122, 905

Johnson, J. A. & Apps, K. 2009, ApJ, 699, 933

Jones, J. E., Alloin, D. M., & Jones, B. J. T. 1984, ApJ, 283, 457

Jones, L. A. 1998, PhD thesis, The University of North Carolina at Chapel Hill, ADS link

Kang, W. & Lee, S.-G. 2012, MNRAS, 425, 3162

Karataş, Y., Bilir, S., Eker, Z., & Demircan, O. 2004, MNRAS, 349, 1069

Kasting, J. F., Whitmire, D. P., & Reynolds, R. T. 1993, Icarus, 101, 108

Katz, D., Soubiran, C., Cayrel, R., Adda, M., & Cautain, R. 1998, A&A, 338, 151

Kausch, W., Noll, S., Smette, A., et al. 2015, A&A, 576, A78

Keenan, P. C. & McNeil, R. C. 1989, ApJS, 71, 245

Khata, D., Mondal, S., Das, R., Ghosh, S., & Ghosh, S. 2020, MNRAS, 493, 4533

Kirkpatrick, J. D., Henry, T. J., & McCarthy, Donald W., J. 1991, ApJS, 77, 417

Koch, D. G., Borucki, W. J., Basri, G., et al. 2010, ApJ, 713, L79

Koleva, M., Prugniel, P., Bouchard, A., & Wu, Y. 2009, A&A, 501, 1269

Kopparapu, R. K., Ramirez, R., Kasting, J. F., et al. 2013, ApJ, 765, 131

Kotani, T., Tamura, M., Suto, H., et al. 2014, SPIE Conf. Ser., Vol. 9147, 914714

Kotani, T., Tamura, M., Nishikawa, J., et al. 2018, SPIE Conf. Ser., Vol. 10702, 1070211

Kunder, A., Kordopatis, G., Steinmetz, M., et al. 2017, AJ, 153, 75

Kupka, F., Piskunov, N., Ryabchikova, T. A., Stempels, H. C., & Weiss, W. W. 1999, A&AS, 138, 119

Kupka, F. G., Ryabchikova, T. A., Piskunov, N. E., Stempels, H. C., & Weiss, W. W. 2000, Balt. Astron., 9, 590

Kurucz, R. 1993, ATLAS9 Stellar Atmosphere Programs and 2 km/s grid, CD-ROM No. 13

Kurucz, R. L. 2005, Mem. S. A. It. Suppl., 8, 14

Kurucz, R. L. 2014, Determination of Atmospheric Parameters of B-, A-, F- and G-Type Stars. (Springer, Cham), 63

Lafarga, M., Ribas, I., Lovis, C., et al. 2020, A&A, 636, A36

Lançon, A. & Wood, P. R. 2000, A&AS, 146, 217

Lancon, A. & Rocca-Volmerange, B. 1992, A&AS, 96, 593

Landi Degl'Innocenti, E. & Landolfi, M. 2004, Polarization in Spectral Lines (Springer Netherlands)

Lanzafame, A. C., Frasca, A., Damiani, F., et al. 2015, A&A, 576, A80

Laughlin, G., Bodenheimer, P., & Adams, F. C. 1997, ApJ, 482, 420

Le Borgne, J. F., Bruzual, G., Pelló, R., et al. 2003, A&A, 402, 433

Lèbre, A., de Laverny, P., Do Nascimento, J. D., J., & de Medeiros, J. R. 2006, A&A, 450, 1173

Lebzelter, T., Seifahrt, A., Uttenthaler, S., et al. 2012, A&A, 539, A109

Ledrew, G. 2001, JRASC, 95, 32

Lee, Y. S., Beers, T. C., Sivarani, T., et al. 2008, AJ, 136, 2022

Lee, Y. S., Beers, T. C., An, D., et al. 2011, ApJ, 738, 187

Lépine, S., Hilton, E. J., Mann, A. W., et al. 2013, AJ, 145, 102

Li, J., Liu, C., Zhang, B., et al. 2021, ApJS, 253, 45

Liu, Y. J., Zhao, G., Shi, J. R., Pietrzyński, G., & Gieren, W. 2007, MNRAS, 382, 553

Lohr, M. E., Negueruela, I., Tabernero, H. M., et al. 2018, MNRAS, 478, 3825

Luck, R. E. 2014, AJ, 147, 137

Luck, R. E. 2017, AJ, 153, 21

Luck, R. E. & Heiter, U. 2007, AJ, 133, 2464

Luque, R., Pallé, E., Kossakowski, D., et al. 2019, A&A, 628, A39

Lyubimkov, L. S., Lambert, D. L., Kaminsky, B. M., et al. 2012, MNRAS, 427, 11

Lyubimkov, L. S., Lambert, D. L., Rostopchin, S. I., Rachkovskaya, T. M., & Poklad, D. B. 2010, MNRAS, 402, 1369

Magrini, L., Randich, S., Friel, E., et al. 2013, A&A, 558, A38

Mahadevan, S., Ramsey, L., Bender, C., et al. 2012, SPIE Conf. Ser., Vol. 8446, 84461S

Mahadevan, S., Ramsey, L. W., Terrien, R., et al. 2014, SPIE Conf. Ser., Vol. 9147, 91471G

Majewski, S. R., Schiavon, R. P., Frinchaboy, P. M., et al. 2017, AJ, 154, 94

Maldonado, J., Martínez-Arnáiz, R. M., Eiroa, C., Montes, D., & Montesinos, B. 2010, A&A, 521, A12

Maldonado, J., Affer, L., Micela, G., et al. 2015, A&A, 577, A132

Maldonado, J., Micela, G., Baratella, M., et al. 2020, A&A, 644, A68

Mamajek, E. E., Bartlett, J. L., Seifahrt, A., et al. 2013, AJ, 146, 154

Mann, A. W., Brewer, J. M., Gaidos, E., Lépine, S., & Hilton, E. J. 2013a, AJ, 145, 52

Mann, A. W., Deacon, N. R., Gaidos, E., et al. 2014, AJ, 147, 160

Mann, A. W., Feiden, G. A., Gaidos, E., Boyajian, T., & von Braun, K. 2015, ApJ, 804, 64

Mann, A. W., Gaidos, E., & Ansdell, M. 2013b, ApJ, 779, 188

Mann, A. W., Dupuy, T., Kraus, A. L., et al. 2019, ApJ, 871, 63

Marconi, A., Abreu, M., Adibekyan, V., et al. 2020, SPIE Conf. Ser., Vol. 11447, 1144726

Marfil, E., Tabernero, H. M., Montes, D., et al. 2020, MNRAS, 492, 5470

Marfil, E., Tabernero, H. M., Montes, D., et al. 2021, A&A, 656, A162

Marigo, P., Girardi, L., Bressan, A., et al. 2008, A&A, 482, 883

Martínez-Arnáiz, R., Maldonado, J., Montes, D., Eiroa, C., & Montesinos, B. 2010, A&A, 520, A79

Martins, L. P. & Coelho, P. 2007, MNRAS, 381, 1329

Massarotti, A., Latham, D. W., Stefanik, R. P., & Fogel, J. 2008, AJ, 135, 209

Masseron, T., Merle, T., & Hawkins, K. 2016, BACCHUS: Brussels Automatic Code for Characterizing High accUracy Spectra, Astrophysics Source Code Library, ascl:1605.004

Matsunaga, N., Jian, M., Taniguchi, D., & Elgueta, S. S. 2021, MNRAS, 506, 1031

Mayor, M., Pepe, F., Queloz, D., et al. 2003, The Messenger, 114, 20

McCarthy, K. & Wilhelm, R. J. 2014, AJ, 148, 70

McKemmish, L. K., Yurchenko, S. N., & Tennyson, J. 2016, MNRAS, 463, 771

McWilliam, A. 1990, ApJS, 74, 1075

Meléndez, J. & Barbuy, B. 2009, A&A, 497, 611

Mészáros, S. & Allende Prieto, C. 2013, MNRAS, 430, 3285

Milone, A. D. C., Sansom, A. E., & Sánchez-Blázquez, P. 2011, MNRAS, 414, 1227

Miret-Roig, N., Galli, P. A. B., Brandner, W., et al. 2020, A&A, 642, A179

Montes, D. 2013, Highlights of Spanish Astrophysics VII, 661

Montes, D., Fernández-Figueroa, M. J., De Castro, E., et al. 2000, A&AS, 146, 103

Montes, D., López-Santiago, J., Gálvez, M. C., et al. 2001, MNRAS, 328, 45

Montes, D. & Martin, E. L. 1998, A&AS, 128, 485

Montes, D., Martin, E. L., Fernandez-Figueroa, M. J., Cornide, M., & de Castro, E. 1997, A&AS, 123, 473

Montes, D., Ramsey, L. W., & Welty, A. D. 1999, ApJS, 123, 283

Montes, D., González-Peinado, R., Tabernero, H. M., et al. 2018, MNRAS, 479, 1332

Montes, D., López-Gallifa, A., Labarga, F., et al. 2020, XIV.0 Scientific Meeting (virtual) of the Spanish Astronomical Society, 168

Morales, J. C., Ribas, I., Jordi, C., et al. 2009, ApJ, 691, 1400

Morel, T., Miglio, A., Lagarde, N., et al. 2014, A&A, 564, A119

Morgan, W. W. & Keenan, P. C. 1973, ARA&A, 11, 29

Mortier, A., Sousa, S. G., Adibekyan, V. Z., Brandão, I. M., & Santos, N. C. 2014, A&A, 572, A95

Morton, D. C. 2000, ApJS, 130, 403

Mucciarelli, A., Pancino, E., Lovisi, L., Ferraro, F. R., & Lapenna, E. 2013, ApJ, 766, 78

Munari, U. & Tomasella, L. 1999, A&AS, 137, 521

Nagel, E. 2019, PhD thesis, Universität Hamburg, Staats- und Universitätbibliothek Hamburg

Neves, V., Bonfils, X., Santos, N. C., et al. 2014, A&A, 568, A121

Neves, V., Santos, N. C., Sousa, S. G., Correia, A. C. M., & Israelian, G. 2009, A&A, 497, 563

Neves, V., Bonfils, X., Santos, N. C., et al. 2012, A&A, 538, A25

Newton, E. R., Charbonneau, D., Irwin, J., et al. 2014, AJ, 147, 20

Nicholls, C. P., Lebzelter, T., Smette, A., et al. 2017, A&A, 598, A79

Nidever, D. L., Marcy, G. W., Butler, R. P., Fischer, D. A., & Vogt, S. S. 2002, ApJS, 141, 503

Nissen, P. E. & Gustafsson, B. 2018, A&A Rev., 26, 6

Nordström, B., Mayor, M., Andersen, J., et al. 2004, A&A, 418, 989

Nortmann, L., Pallé, E., Salz, M., et al. 2018, Science, 362, 1388

Olander, T., Heiter, U., & Kochukhov, O. 2021, A&A, 649, A103

Oliva, E., Sanna, N., Rainer, M., et al. 2018, SPIE Conf. Ser., Vol. 10702, 1070274

Önehag, A., Heiter, U., Gustafsson, B., et al. 2012, A&A, 542, A33

Origlia, L., Oliva, E., Baffa, C., et al. 2014, SPIE Conf. Ser., Vol. 9147, 91471E

Park, S., Lee, J.-E., Kang, W., et al. 2018, ApJS, 238, 29

Parmentier, V., Line, M. R., Bean, J. L., et al. 2018, A&A, 617, A110

Passegger, V. M., Wende-von Berg, S., & Reiners, A. 2016, A&A, 587, A19

Passegger, V. M., Reiners, A., Jeffers, S. V., et al. 2018, A&A, 615, A6

Passegger, V. M., Schweitzer, A., Shulyak, D., et al. 2019, A&A, 627, A161

Passegger, V. M., Bello-García, A., Ordieres-Meré, J., et al. 2020, A&A, 642, A22

Passegger, V. M., Bello-García, A., Ordieres-Meré, J., et al. 2021, A&A, in press

Pavlenko, Y. V., Jenkins, J. S., Jones, H. R. A., Ivanyuk, O., & Pinfield, D. J. 2012, MNRAS, 422, 542

Pepe, F., Cristiani, S., Rebolo, R., et al. 2021, A&A, 645, A96

Percival, S. M., Salaris, M., Cassisi, S., & Pietrinferni, A. 2009, ApJ, 690, 427

Perryman, M. 2018, The Exoplanet Handbook (Cambridge University Press)

Perryman, M. A. C., Lindegren, L., Kovalevsky, J., et al. 1997, A&A, 500, 501

Phillips, M. W., Tremblin, P., Baraffe, I., et al. 2020, A&A, 637, A38

Pickles, A. J. 1985, ApJS, 59, 33

Pickles, A. J. 1998, PASP, 110, 863

Piskunov, N. & Valenti, J. A. 2017, A&A, 597, A16

Piskunov, N. E., Kupka, F., Ryabchikova, T. A., Weiss, W. W., & Jeffery, C. S. 1995, A&AS, 112, 525

Piskunov, N. E. & Valenti, J. A. 2002, A&A, 385, 1095

Plez, B. 2012, Turbospectrum: Code for spectral synthesis, Astrophysics Source Code Library, ascl:1205.004

Pourbaix, D., Tokovinin, A. A., Batten, A. H., et al. 2004, A&A, 424, 727

Press, W. H., Teukolsky, S. A., Vetterling, W. T., & Flannery, B. P. 2002, Numerical recipes in C++: the art of scientific computing (Cambridge University Press)

Prugniel, P. & Soubiran, C. 2001, A&A, 369, 1048

Quirrenbach, A., Amado, P. J., Ribas, I., et al. 2018, SPIE Conf. Ser., Vol. 10702, 107020W

Quirrenbach, A., Amado, P. J., Ribas, I., et al. 2020, SPIE Conf. Ser., Vol. 11447, 114473C

Rajpurohit, A. S., Allard, F., Rajpurohit, S., et al. 2018a, A&A, 620, A180

Rajpurohit, A. S., Allard, F., Teixeira, G. D. C., et al. 2018b, A&A, 610, A19

Rajpurohit, A. S., Reylé, C., Allard, F., et al. 2013, A&A, 556, A15

Rajpurohit, A. S., Reylé, C., Allard, F., et al. 2014, A&A, 564, A90

Rajpurohit, A. S., Reylé, C., Schultheis, M., et al. 2012, A&A, 545, A85

Rayner, J., Tokunaga, A., Jaffe, D., et al. 2016, SPIE Conf. Ser., Vol. 9908, 990884

Rayner, J. T., Cushing, M. C., & Vacca, W. D. 2009, ApJS, 185, 289

Reid, I. N., Cruz, K. L., Kirkpatrick, J. D., et al. 2008, AJ, 136, 1290

Reid, I. N. & Hawley, S. L. 2005, New light on dark stars : red dwarfs, low-mass stars, brown dwarfs (Springer)

Reiners, A., Zechmeister, M., Caballero, J. A., et al. 2018, A&A, 612, A49

Reylé, C., Jardine, K., Fouqué, P., et al. 2021, A&A, 650, A201

Ricker, G. R., Winn, J. N., Vanderspek, R., et al. 2014, SPIE Conf. Ser., Vol. 9143, 914320

Rodrigues, T. S., Girardi, L., Miglio, A., et al. 2014, MNRAS, 445, 2758

Rodrigues, T. S., Bossini, D., Miglio, A., et al. 2017, MNRAS, 467, 1433

Rojas-Ayala, B., Covey, K. R., Muirhead, P. S., & Lloyd, J. P. 2012, ApJ, 748, 93

Rothman, L. S., Gordon, I. E., Barbe, A., et al. 2009, J. Quant. Spectr. Rad. Transf., 110, 533

Ryabchikova, T., Piskunov, N., Kurucz, R. L., et al. 2015, Phys. Scr., 90, 054005

Sabotta, S., Schlecker, M., Chaturvedi, P., et al. 2021, A&A, 653, A114

Saffe, C. 2011, Rev. Mexicana Astron. Astrofis., 47, 3

Sánchez-Blázquez, P., Peletier, R. F., Jiménez-Vicente, J., et al. 2006, MNRAS, 371, 703

Santos, N. C., Israelian, G., & Mayor, M. 2004, A&A, 415, 1153

Santos, N. C., Sousa, S. G., Mortier, A., et al. 2013, A&A, 556, A150

Sarmento, P., Rojas-Ayala, B., Delgado Mena, E., & Blanco-Cuaresma, S. 2021, A&A, 649, A147

Sarro, L. M., Ordieres-Meré, J., Bello-García, A., González-Marcos, A., & Solano, E. 2018, MNRAS, 476, 1120

Sato, B., Ando, H., Kambe, E., et al. 2003, ApJ, 597, L157

Sbordone, L., Caffau, E., Bonifacio, P., & Duffau, S. 2014, A&A, 564, A109

Scalo, J., Kaltenegger, L., Segura, A. G., et al. 2007, Astrobiology, 7, 85

Scarfe, C. D., Funakawa, H., Delaney, P. A., & Barlow, D. J. 1983, JRASC, 77, 126

Schäfer, S., Guenther, E. W., Reiners, A., et al. 2018, SPIE Conf. Ser., Vol. 10702, 1070276

Schöfer, P., Jeffers, S. V., Reiners, A., et al. 2019, A&A, 623, A44

Schwab, C., Rakich, A., Gong, Q., et al. 2016, SPIE Conf. Ser., Vol. 9908, 99087H

Schweitzer, A., Passegger, V. M., Cifuentes, C., et al. 2019, A&A, 625, A68

Seifahrt, A., Bean, J. L., Stürmer, J., et al. 2020, SPIE Conf. Ser., Vol. 11447, 114471F

Selsis, F., Kasting, J. F., Levrard, B., et al. 2007, A&A, 476, 1373

Shan, Y., Reiners, A., Fabbian, D., et al. 2021, A&A, 654, A118

Sharon, C., Hillenbrand, L., Fischer, W., & Edwards, S. 2010, AJ, 139, 646

Shulyak, D., Reiners, A., Nagel, E., et al. 2019, A&A, 626, A86

Silva, D. R. & Cornell, M. E. 1992, ApJS, 81, 865

Skrutskie, M. F., Cutri, R. M., Stiening, R., et al. 2006, AJ, 131, 1163

Smette, A., Sana, H., Noll, S., et al. 2015, A&A, 576, A77

Smiljanic, R., Korn, A. J., Bergemann, M., et al. 2014, A&A, 570, A122

Sneden, C. A. 1973, PhD thesis, The University of Texas at Austin, ADS link

Sota, A., Maíz Apellániz, J., Morrell, N. I., et al. 2014, ApJS, 211, 10

Sota, A., Maíz Apellániz, J., Walborn, N. R., et al. 2011, ApJS, 193, 24

Soto, M. G. & Jenkins, J. S. 2018, A&A, 615, A76

Soto, M. G., Jones, M. I., & Jenkins, J. S. 2021, A&A, 647, A157

Soubiran, C., Jasniewicz, G., Chemin, L., et al. 2013, A&A, 552, A64

Soubiran, C., Katz, D., & Cayrel, R. 1998, A&AS, 133, 221

Soubiran, C., Le Campion, J.-F., Brouillet, N., & Chemin, L. 2016, A&A, 591, A118

Sousa, S. G., Santos, N. C., Adibekyan, V., Delgado-Mena, E., & Israelian, G. 2015, A&A, 577, A67

Sousa, S. G., Santos, N. C., Israelian, G., Mayor, M., & Monteiro, M. J. P. F. G. 2007, A&A, 469, 783

Sousa, S. G., Santos, N. C., Mayor, M., et al. 2008, A&A, 487, 373

Sousa, S. G., Adibekyan, V., Delgado-Mena, E., et al. 2018, A&A, 620, A58

Souto, D., Cunha, K., Smith, V. V., et al. 2020, ApJ, 890, 133

Spada, F., Demarque, P., Kim, Y. C., Boyajian, T. S., & Brewer, J. M. 2017, ApJ, 838, 161

Spencer Jones, H. & Furner, H. H. 1937, MNRAS, 98, 92

Steinmetz, M., Zwitter, T., Siebert, A., et al. 2006, AJ, 132, 1645

Stetson, P. B. & Pancino, E. 2008, PASP, 120, 1332

Stix, M. 2003, Sol. Phys., 212, 3

Tabernero, H. M. 2014, PhD thesis, Universidad Complutense de Madrid, E-Prints Complutense

Tabernero, H. M., Dorda, R., Negueruela, I., & González-Fernández, C. 2018, MNRAS, 476, 3106

Tabernero, H. M., Dorda, R., Negueruela, I., & Marfil, E. 2021a, A&A, 646, A98

Tabernero, H. M., Marfil, E., Montes, D., & González Hernández, J. I. 2019, A&A, 628, A131

Tabernero, H. M., Marfil, E., Montes, D., & González Hernández, J. I. 2021b, A&A, in press

Tabernero, H. M., Montes, D., & González Hernández, J. I. 2012, A&A, 547, A13

Tabernero, H. M., Montes, D., González Hernández, J. I., & Ammler-von Eiff, M. 2017, A&A, 597, A33

Takeda, Y., Sato, B., & Murata, D. 2008, PASJ, 60, 781

Takeda, Y., Sato, B., Kambe, E., et al. 2005, PASJ, 57, 13

Tal-Or, L., Zechmeister, M., Reiners, A., et al. 2018, A&A, 614, A122

Terrien, R. C., Mahadevan, S., Bender, C. F., et al. 2012, ApJ, 747, L38

Thygesen, A. O., Frandsen, S., Bruntt, H., et al. 2012, A&A, 543, A160

Ting, Y.-S., Conroy, C., Rix, H.-W., & Cargile, P. 2019, ApJ, 879, 69

Tinney, C. G. & Reid, I. N. 1998, MNRAS, 301, 1031

Torres, G., Fischer, D. A., Sozzetti, A., et al. 2012, ApJ, 757, 161

Trifonov, T., Kürster, M., Zechmeister, M., et al. 2018, A&A, 609, A117

Trifonov, T., Lee, M. H., Kürster, M., et al. 2020, A&A, 638, A16

Tsantaki, M., Andreasen, D., & Teixeira, G. 2020, JOSS, 5, 2048

Tsantaki, M., Andreasen, D. T., Teixeira, G. D. C., et al. 2018, MNRAS, 473, 5066

Tsantaki, M., Santos, N. C., Sousa, S. G., et al. 2019, MNRAS, 569

Tsantaki, M., Sousa, S. G., Adibekyan, V. Z., et al. 2013, A&A, 555, A150

Tsantaki, M., Sousa, S. G., Santos, N. C., et al. 2014, A&A, 570, A80

Tsuji, T., Ohnaka, K., & Aoki, W. 1996, A&A, 305, L1

Tull, R. G. 1998, SPIE Conf. Ser., Vol. 3355, 387

Valdes, F., Gupta, R., Rose, J. A., Singh, H. P., & Bell, D. J. 2004, ApJS, 152, 251

Valenti, J. A. & Fischer, D. A. 2005, ApJS, 159, 141

Valenti, J. A. & Piskunov, N. 1996, A&AS, 118, 595

van Leeuwen, F. 2007, A&A, 474, 653

Van Rossum, G. 2020, The Python Library Reference, release 3.8.2 (Python Software Foundation)

Vazdekis, A., Ricciardelli, E., Cenarro, A. J., et al. 2012, MNRAS, 424, 157

Veyette, M. J., Muirhead, P. S., Mann, A. W., & Allard, F. 2016, ApJ, 828, 95

Veyette, M. J., Muirhead, P. S., Mann, A. W., et al. 2017, ApJ, 851, 26

Virtanen, P., Gommers, R., Oliphant, T. E., et al. 2020, Nature Methods, 17, 261

Vogt, S. S., Allen, S. L., Bigelow, B. C., et al. 1994, SPIE Conf. Ser., Vol. 2198, 362

von Braun, K., Boyajian, T. S., van Belle, G. T., et al. 2014, MNRAS, 438, 2413

Wallace, L. & Hinkle, K. 1996, ApJS, 107, 312

Wallace, L. & Hinkle, K. 1997, ApJS, 111, 445

Wehrhahn, A. 2021, The 20.5th Cambridge Workshop on Cool Stars, Stellar Systems, and the Sun (CS20.5), 1

Wildi, F., Blind, N., Reshetov, V., et al. 2017, SPIE Conf. Ser., Vol. 10400, 1040018

Wilson, J. C., Hearty, F., Skrutskie, M. F., et al. 2010, SPIE Conf. Ser., Vol. 7735, 77351C

Winn, J. N. & Fabrycky, D. C. 2015, ARA&A, 53, 409

Winters, J. G., Henry, T. J., Lurie, J. C., et al. 2015, AJ, 149, 5

Worek, T. F. & Beardsley, W. R. 1977, ApJ, 217, 134

Worthey, G. 1994, ApJS, 95, 107

Wright, J. T., Mahadevan, S., Hearty, F., et al. 2018, 231st AAS Meeting, 246.45

Wu, Y., Singh, H. P., Prugniel, P., Gupta, R., & Koleva, M. 2011, A&A, 525, A71

Yan, R., Chen, Y., Lazarz, D., et al. 2019, ApJ, 883, 175

Yee, S. W., Petigura, E. A., & von Braun, K. 2017, ApJ, 836, 77

Zamora, O., García-Hernández, D. A., Allende Prieto, C., et al. 2015, AJ, 149, 181

Zechmeister, M., Anglada-Escudé, G., & Reiners, A. 2014, A&A, 561, A59

Zechmeister, M., Reiners, A., Amado, P. J., et al. 2018, A&A, 609, A12

Zechmeister, M., Dreizler, S., Ribas, I., et al. 2019, A&A, 627, A49

Zechmeister, M., Reiners, A., Amado, P. J., et al. 2020, SERVAL: SpEctrum Radial Velocity AnaLyser, Astrophysics Source Code Library, ascl:2006.011

Zhang, F., Li, L., & Han, Z. 2005, MNRAS, 364, 503

Zhou, X. 1991, A&A, 248, 367